ATMOSPHERIC MILLIMETRE WAVE PROPAGATION

THESIS PRESENTED FOR EXAMINATION FOR THE DEGREE OF PH.D

IN THE UNIVERSITY OF LONDON

BY

HO KA-LEUNG

AUGUST 1977

ELECTRONIC AND ELECTRICAL
ENGINEERING DEPARTMENT,
UNIVERSITY COLLEGE LONDON.

" To My Mother and My Wife„

Abstract

The work described in this thesis is mainly confined to atmospheric propagation effects occuring in a town enviroment at a frequency of 36 GHz on a 4.1 Km link. Precipitation effects on a 110 GHz link on the same path have also been measured and are included.

Measurements have been made on the amplitude scintillations and the results, under different atmospheric conditions, are compared with the theoretical predictions of Tatarski. Direct meteorological measurements of the important atmospheric parameters are described and are correlated with the effects occuring on the link, and the values of these parameters deduced from the behaviour of the radio signals. Measurements of signal attenuation due to fog and snow have also been made and the study of some other anomalous scintillation phenomena are included. Long term statistics have been collected. Attempts have been made to verify the theoretical relation between the attenuation and rainfall rate at 36 and 110 GHz. A dual-frequency technique is used to investigate the validity of the Laws-Parsons raindrop size distribution. All the instrumentation and electronic processing used in this experiment are described.

CONTENTS

ACKNOWLEDGEMENTS

The author is indebted to his supervisor, Dr. R.S. Cole, for his continuous guidance, support and encourgement. He also wishes to express his gratitude to Professor A.L. Cullen for providing the research facilities.

It is a pleasure to thank Mr. N.D. Mavrokoukoulakis, the author's colleague, for his fruitfull discussions and happy cooperation and the technical staff of the College who gave the necessary technical assistance.

Thanks are due to the Appleton Laboratories, which loaned the 110 GHz equipment and to the U.K. Science Research Council, which provided the grant to finance this work. Sincere thanks are also due to the Commonwealth Scholarship Commission for the award of the Commonwealth Scholarship.

LIST OF FIGURES

CHAPTER 1 INTRODUCTION

1.1 General introduction

The lower atmosphere has become increasingly important as the transmission medium for radio waves since the introduction of "spark" transmission by Marconi (1901) three-quarters of a century ago. Although the effect of the atmosphere on radio propagation was not known in those days, radio transmission was carried out with little difficulty since the wavelengths used were relatively long (100 metres and longer). In order to explain the phenomenon of long distance radio communication, the prediction of the existence of the ionosphere by Heaviside (1902) and derivation of the solution of Maxwell's equations for surface waves by Zenneck (1907) were made soon after Marconi's historical transmission, but the effect of the atmospheric conditions on radio propagation was not considered seriously. However, because of the constant demand for more radio channels throughout the years, the frequencies used for signal transmission have been increased.

The growth in demand in the U.K. and in gereral, all over the world, for existing and new services is such that a substantial increase in the telecommunication network capacity will be required over the next decade or so. The development of the network should be such that it can readily accept traffic originating from variety of services such as telephony, view-phone, television and data etc. The trend of development is

accordingly to a general purpose network based on digital transmission.

Microwave radio-relay systems form a substantial part of the trunk network and their development in this country has been based so far on FM/FDM using frequency bands around 2, 4 and 6 GHz; saturation of these bands can be foreseen on some routes before the end of the decade. Further increases in capacity therefore will require exploitation of the allocated high frequency bands as well as the introduction of digital transmission.

The Post Office in the U.K. has carried out experiments on links at frequencies of 11, 20 and 36 GHz at Mendlesham, Suffolk, with transmission paths ranging from 4 Km to 29 Km. A practical link at 35 GHz using the H_{01} mode low-loss wave guide is now in operation. Research is in progress for the use of optical fibres for communication purposes.

It may be argued that the use of low-loss wave guides for millimetre wave transmission can avoid all the problems of atmospheric propagation (deep fades, scintillations etc.). However, the installation is very expensive and in practice, it would not be possible to lay such a link in town area, because the wave guide runs need to be very straight. The use of H_{01} mode wave guide looks as though it is likely to be confined to long distance links between large centres. The use of optical fibres is likely, in the future, to solve the problem of wide-

band communication along short paths in a town since optical fibre can use existing telephone cable ducts. However, it is still at the very early experimental stage and it is estimated that it will be at least fifteen years before it can be brought into engineering use. In the meantime, should increasing tele-communication traffic require the use of the millimetre part of the spectrum, it would be practicable to install line-of- sight links at these frequencies in the near future.

1.2 The atmosphere and radio propagation

As wave-lengths get shorter, the dimensions of the aerial for transmission and reception become comparable to or even larger than the wave-length, thus allowing narrow beam transmission. However as the wavelength becomes comparable with atmospheric inhomogeneities, a relatively large atmospheric effect on propagation might be expected.

The major obstacle faced in using the frequencies above 30 GHz for terrestial radio-relay applications is the influence of the atmospheric conditions on the propagation of the electro-magnetic waves. In particular, attenuation far in excess of that at longer wavelengths is experienced at these frequencies. The main causes for this excessive attenuation are the absorption due to oxygen and water vapour, atmospheric precipitation and under certain circumstances, refractive index variations. Of course, the atmospheric precipitation, in particular, the rainfall

has the most influence. Curves showing signal attenuation due to rain, water vapour and oxygen for various operating frequencies are presented in Figure 1.1 (CCIR 1975), Figure 1.2 and Figure 1.3 (Matthews 1965). It is clear from Figure 1.3(b) that "windows" exist at about 36GHz and 90GHz for minimum loss which the radio engineers can exploit.

1.3 Refractive Index and Refractivity

The refractive index n of the atmosphere is a random function of the coordinate $\vec{r}$ and the time t. The time dependence is due to the wind. The spatial structure as well as its evolution in time and space, are governed by complex laws of fluid mechanics. The fluctuations are small in comparison with the average value (close to unity) which is primarily dependent on the meteorological parameters (Smith and Weitraub 1953). To characterize these fluctuations, N units are used which are parts per million of the deviations of $n(\vec{r},t)$ from its mean value taken as unity. The dependence on the pressure, temperature and humidity is given by (Bean and Dutton 1968)

$$N = (n - 1) \times 10^6$$

$$= 77.6 \frac{P}{T} + 3.73 \times 10^5 \frac{e}{T^2} \qquad 1.2.1$$

where P is the pressure in millibars

T is the absolute temperature in Kelvin

e is the partial pressure of water vapour in mb.

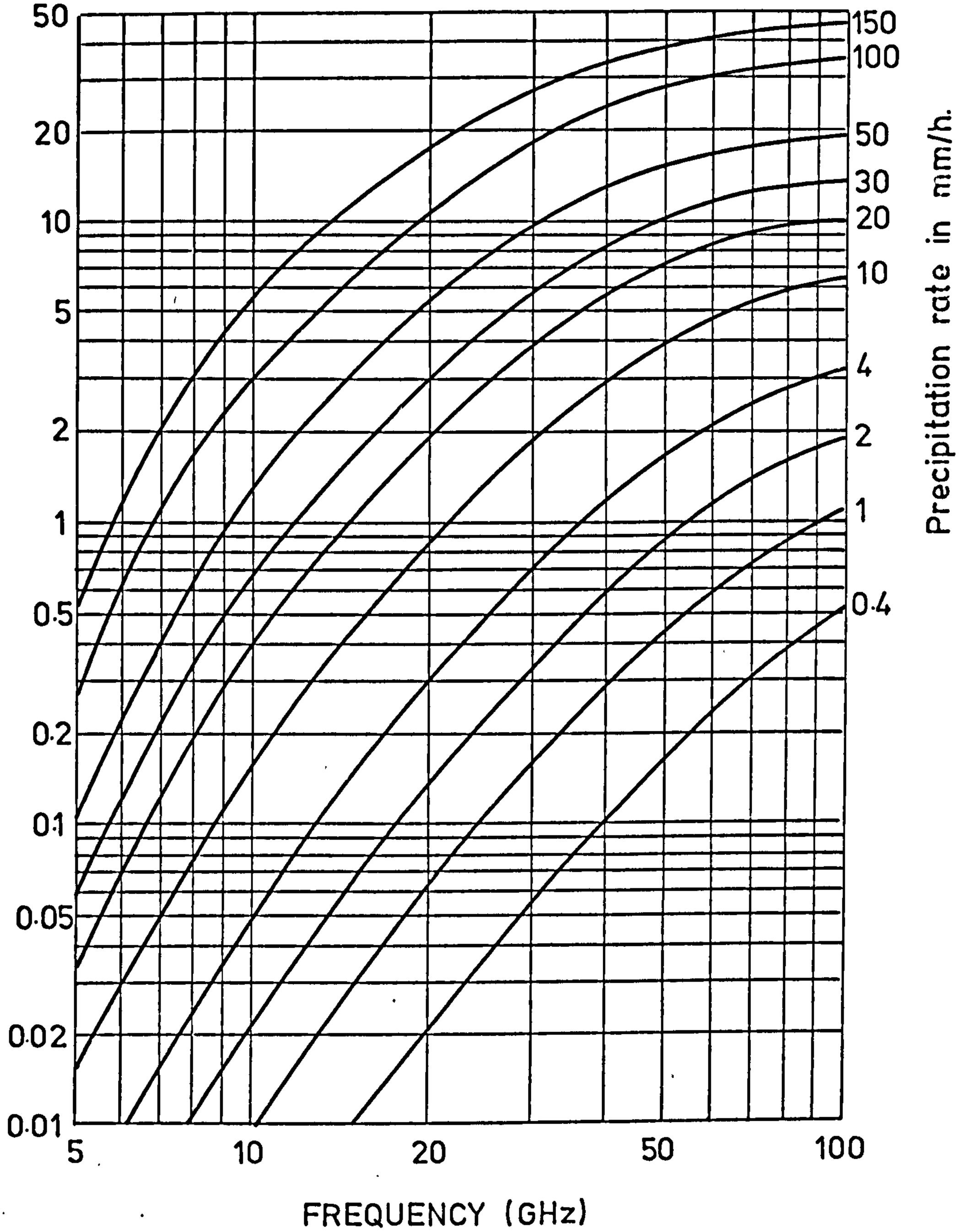

Fig. 1.1 Variation of attenuation with frequency.

These curves are based on the following assumptions:

---Laws and Parsons distribution of drop sizes

---Temperature 18°C

---Terminal velocity of the raindrops as measured by Gunn and Kinzer

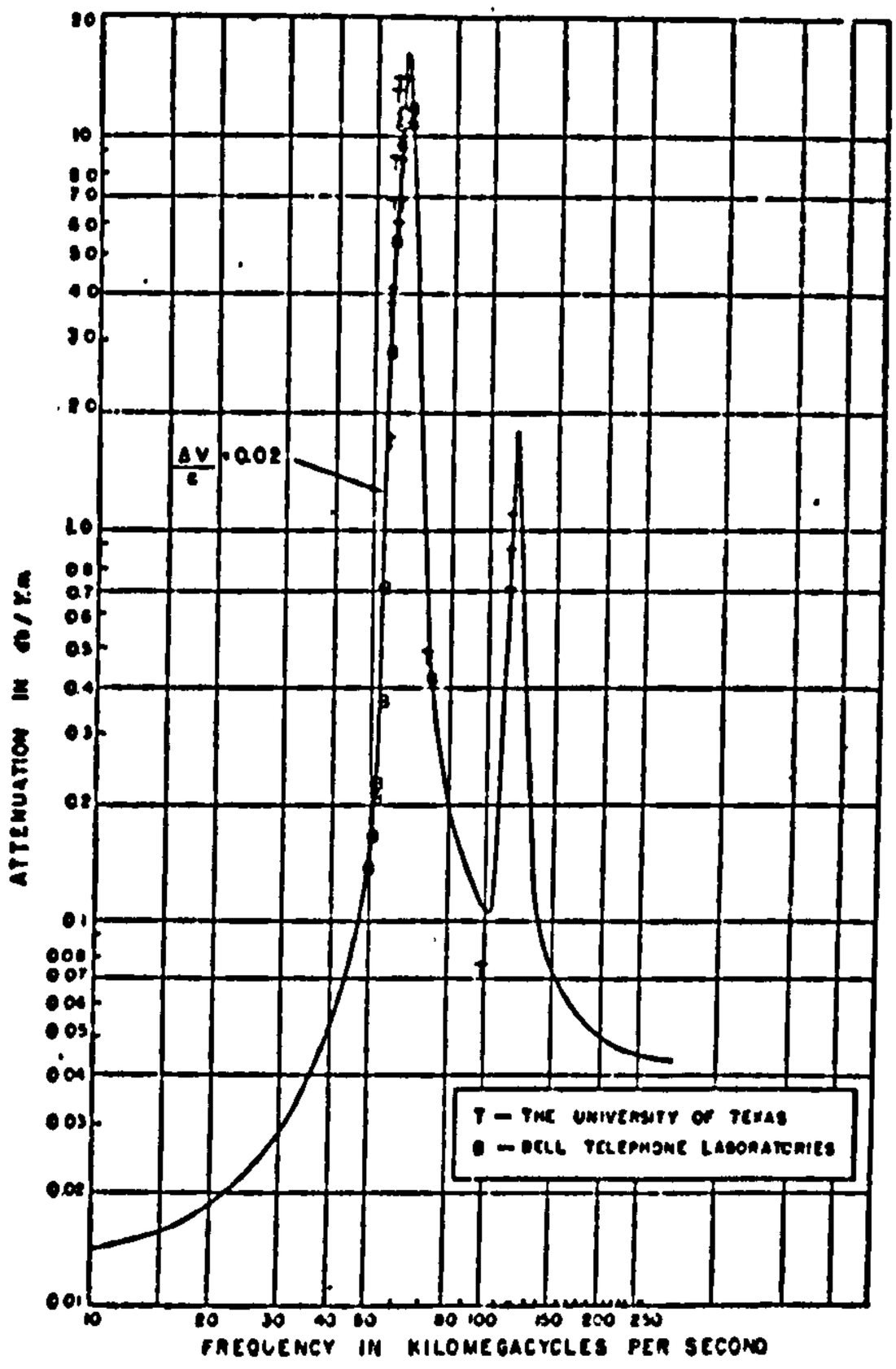

Fig. 1.2 Attenuation due to oxygen at one atmosphere.

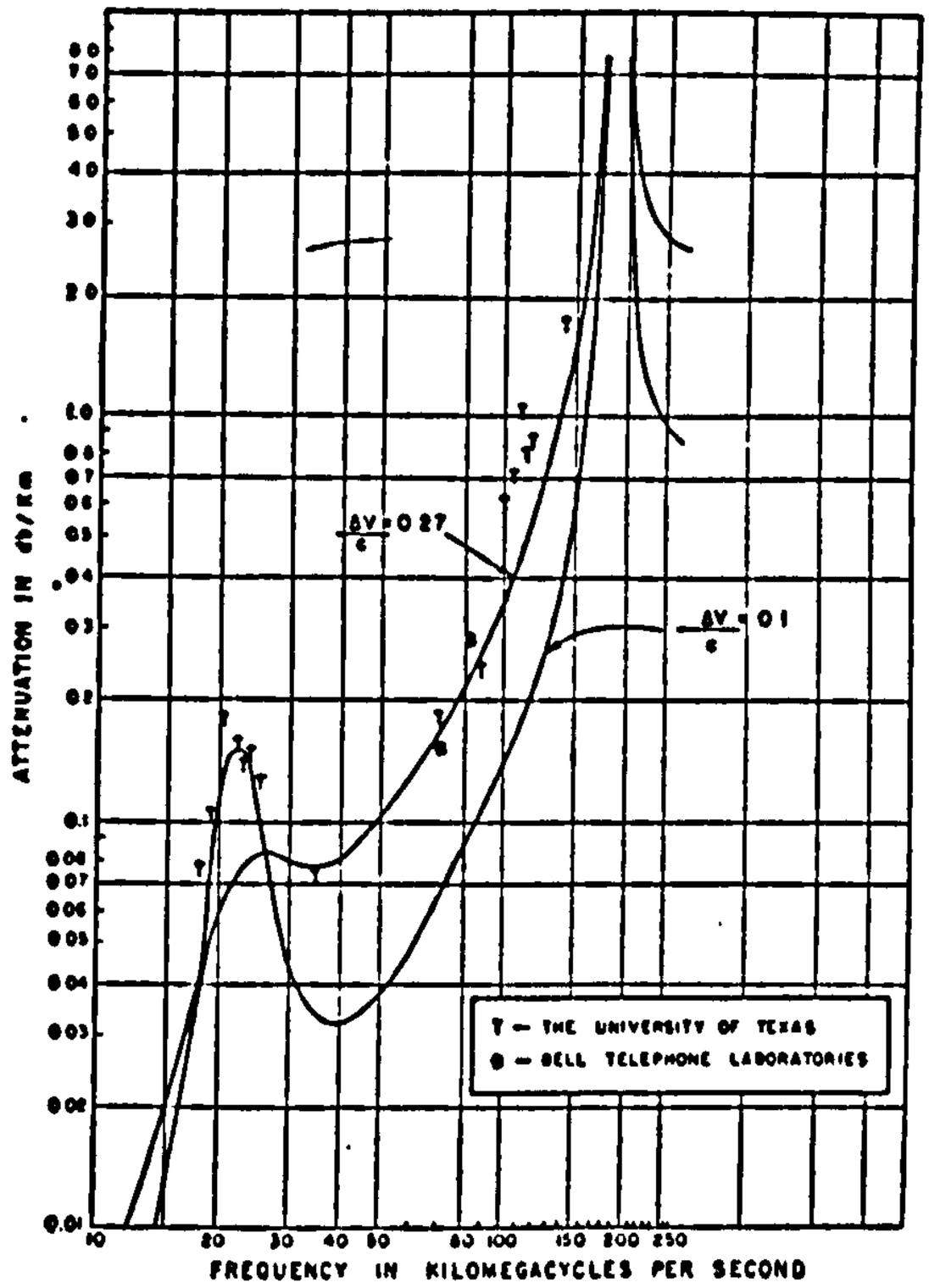

Water vapour attenuation for 7·5g/m³.

(a)

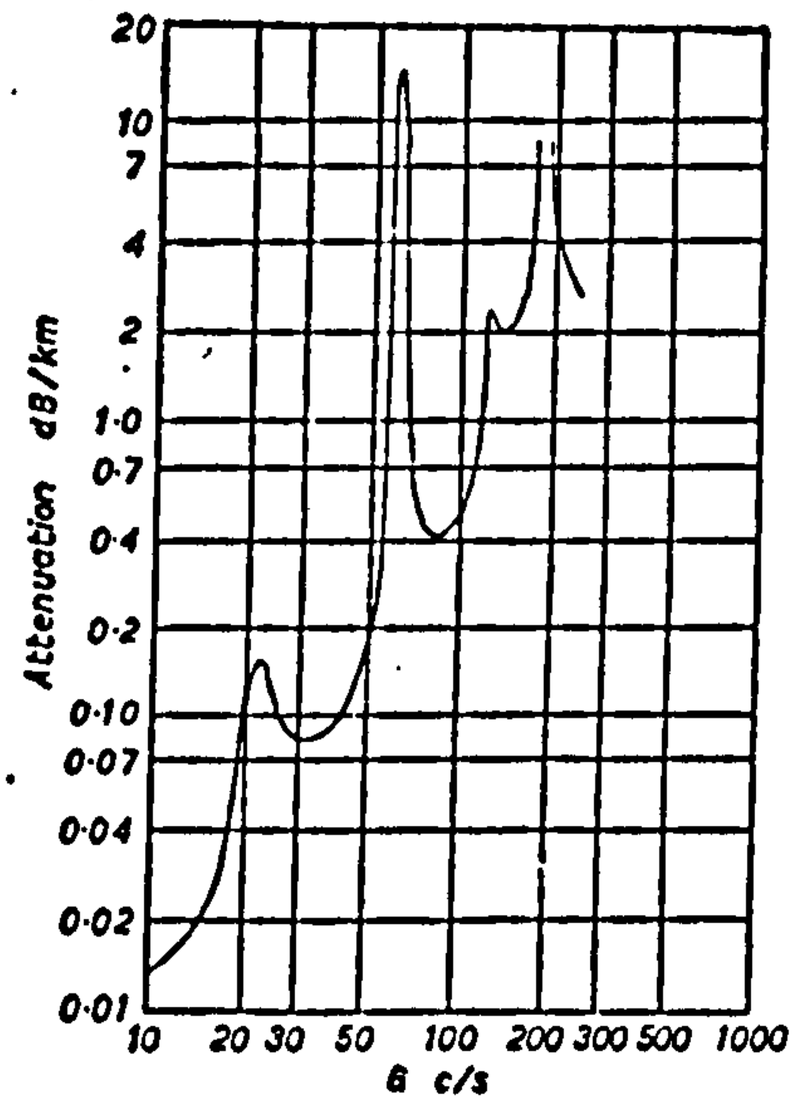

Total atmospheric attenuation in a standard atmosphere at sea level

(b)

Fig.1.3 (a) Water vapour attenuation.
(b) Total atmospheric attenuation.

The constants in Equation 1.2.1 vary slightly according to experiments and investigation reported.

Furthermore, it is now well-established that, in general the refractive index decays exponentially with altitude, up to several kilometres, according to

$$N = N_s \, e^{-h/\gamma} \qquad 1.2.2$$

where h is the height in kilometres

N_s is the refractivity at ground level

γ is a constant.

The CCIR has defined a basic reference atmosphere with $N_s = 289$, $\gamma = 7.35$ Km. These parameters have, however, substantial seasonal variations (Bean and Dutton 1968).

The dependence of the refractive index variations ΔN on pressure, temperature and water vapour pressure up to several kilometres is given approximately by

$$\Delta N = 0.3 \, \Delta P + 4.5 \, \Delta e - \Delta T \qquad 1.2.3$$

Again variations of these constants have been reported. Eqn. 1.2.3 shows that ΔN is very sensitive to Δe.

Electromagnetic waves are refracted by the variation of the refractive index through which they pass (Saxton et al 1964) Small scale variations in refractive index produce amplitude and phase scintillations in the beam whereas large scale variations may introduce other phenomena such as ducting and refraction.

1.4 The study of millimetre wave in town environment

Interest in the propagation of millimetre wave through the lower atmosphere arises both from the possible application of these frequencies in communications, despite their severe limitations,and from their use as a tool for studying atmospheric structures (Lee and Harp 1969). However, many published results are concerned mainly with gaseous absorption (Straiton and Tolbert 1960) (Tolbert and Straiton 1957) (IEEE 1966) and scintillations (Lee and Waterman 1968) (Lane et al 1967) either along a path at or near vertical incidence (between ground and outer space) or on a link with terminals located in rural environment. Little work has been done in town environment. It is clear that there is a strong need for quantitative millimetre wave observations. Of interest are:

a) attenuation due to precipitation as a function of frequency and rate of precipitation,

b) the amplitude of scintillations on line-of-sight links in a town environment,

c) absorption due to fog,

d) long term statistics,

and e) any other clear-air effects.

As expected, though the attenuation due to precipitation is increased at these high frequencies, the millimetre wave systems are still very useful and efficient for feeding main trunk networks and for short links between centres within towns.

It can be anticipated that the atmospheric structure

in a town environment may be very different from that in a rural area; hot air from air conditioning plants, heat radiation from huge buildings and even the exhausted gas from cars may cause interesting phenomena on millimetre wave propagation through the town area. It is in such circumstances that we would expect the largest variations of amplitude and phase in the wavefront both in space and in time as a result of irregular variations in refractive index. It is the purpose of this project to investigate the effects mentioned in the previous paragraph.

The project can be divided into two parts as follows:

A) <u>Clear-air scintillations</u>

The study of wave propagation in random media has been renewed with increased vigor in the past two decades. The works of Chernov (1960) and Tatarski (1961) in the Soviet Union during the 1950's rekindled interest and advanced the state of knowledge so that many previously unsolved problems became amenable to solution. For this reason, the monographs of Chernov and Tatarski aroused considerable interest and have served as a starting point for much theoretical and experimental work on wave propagation problems.

The atmospheric model based on the Kolmogorov theory of locally isotropic turbulence is the most well established theory and gives a sufficiently good description of the turbulent atmosphere. Attempts are made to compare the experimental results of amplitude fluctuations of millimetre waves with theoretical values given by theory. A dual frequency technique (36 and 110

GHz) is employed which is useful in eliminating undetermined constants (Section 5.4). Efforts are also made in the study of the atmospheric parameters such as temperature, refractive index and wind speed to correlate these parameters with the propagation scintillations (Chapter 6 and 7). Of course, it is impractical to measure the atmospheric parameters along the entire path, so the problem has been tackled from a statistical stand-point and attempts to evaluate certain statistics of the signal (mean, variance etc.) in terms of the statistics of the refractive index field $n(\vec{r})$ over the propagation path. Besides getting an idea how the scintillations are affected by the atmospheric structure, it is also hoped that the study of millimetre wave propagation phenomena can provide a powerful means of remote-probing of atmospheric structure.

As already mentioned, the atmospheric structure in a town environment may be very different from that in a rural environment. It is expected that under certain circumstances, for example, in the case where there are outputs from air-conditioning plants along the path, amplitude scintillations may be much higher than normal. This may be a contributory cause to the error rate of a digital communication system. Thus from a communications engineer's point of view, the study of the large scintillations in a town environment (Section 8.2) may be useful in the design of a millimetre wavelength digital communication system in a town area. Attention has also been given to the transit-time variation problem due to refractive index variations in millimetre wave propagation (Section 7.5).

The absorption due to fog has been studied (Section 8.3) and some other anomalous scintillation and fading effects are presented (Section 8.4).

B) Rain-induced attenuation

The limitation of the use of millimetre waves for communication purpose is mainly due to the high attenuation due to precipitation, particularly, rainfall. Thus to design and plan such links, it is desirable to have comprehensive information about the relationship between attenuation and rainfall characteristics. It is particularly useful to establish relationships between attenuation experienced over a link several kilometres in length and the rainfall rate measured at one point.

It is well established from Ryde's theory that the attenuation per unit path length is a function of the rainfall rate, the raindrop size distribution, the extinction cross-section of the drop and the terminal velocity of the drops. Corrections for the effects of departure of raindrop shapes from spherical, the effect of temperature on the complex refractive index of water and the effect of polarization was reported by Medhurst(1965).

However, the theoretical results are for uniform rainfall along the path between transmitting and receiving antennas. Prediction of the performance of the actual links depends on the knowledge of the way in which rainfall intensity tends to vary along the path.

Recent work has been done on the relation between the attenuation and rainfall rate at 36 GHz and 110 GHz (Norbury and White 1973) (Lane et al 1967) (Llewellyn and Zavody 1973) using rapid-response rain-gauges placed along short paths. Good agreement between experimental results and the theoretical values of microwave attenuation due to rainfall have been obtained. Attempts have been made to verify experimentally the theoretical relation between rain-induced attenuation and rainfall rate at 36 and 110 GHz. A dual-frequency approach is again used. Results obtained from the dual frequency measurements serve as a means to investigate the validity of the applications of the Laws and Parsons raindrop size distribution to the theory of rainfall attenuation. (Chapter 9)

It is, of course, the great interest of the communication engineers to know the reliability of line-of-sight telecommunication links especially at frequencies above 30 GHz so that the long-term rain-induced attenuation distribution at 36 GHz has been collected (Section 9.7).

CHAPTER 2 WAVE PROPAGATION IN A TURBULENT MEDIUM

This chapter contains a summary of the mechanism for for the microwave propagation problem (i.e. the random refractive index field). The considerations have been restricted to those required to explain the experimental results presented later and are mainly based on Tatarski's theory (1961). At the short wavelengths used in this experiment, only a line-of-sight communication system can be achieved. Further detail of the mechanism required to explain experimental results will be introduced in appropriate sections.

The atmosphere is usually in a state of turbulent motion and the meteorological quantities such as wind velocity, humidity, temperature and radio refractivity undergo irregular oscillations which differ in amplitude and frequency and are superimposed in a random manner. Statistical methods are used to describe the laws characterizing the structure of such fluctuating quantities.

2.1 Some statistical considerations

Of all the statistical characteristics of the random field $f(\vec{r})$, the most important and simplest is the mean value $\overline{f(\vec{r})}$. The next characteristic of the field is its correlation function $B(\vec{r}_1,\vec{r}_2)$ or the structure function $D(\vec{r}_1,\vec{r}_2)$. The following discussion will be treated in two parts; the first

being for a homogeneous and isotropic random field (Section 2.1.1) and the second being for a locally homogeneous and isotropic random field (Section 2.1.2)

2.1.1 Homogeneous and isotropic random fields

For a random field $f(\vec{r})$, such as the wind velocity vector field, the scalar fields of temperature, humidity etc. in the turbulent atmosphere, we can define the mean value $\overline{f(\vec{r})}$ and the correlation function $B_f(\vec{r}_1,\vec{r}_2)$,

where $$B_f(\vec{r}_1,\vec{r}_2) = \overline{\left[f(\vec{r}_1) - \overline{f(\vec{r}_1)}\right]\left[f(\vec{r}_2) - \overline{f(\vec{r}_2)}\right]} \qquad 2.1.1$$

A random field is called homogeneous if its mean value is constant and if its correlation function does not change when a pair of points $\vec{r}_1$ and $\vec{r}_2$ are both displaced by the same amount in the same direction, that is, if

$$\overline{f(\vec{r})} = \text{constant} \qquad 2.1.2$$

and $$B_f(\vec{r}_1,\vec{r}_2) = B_f(\vec{r}_1+\vec{r}_o,\vec{r}_2+\vec{r}_o)$$

Putting $\vec{r}_o = -\vec{r}_2$, then

$$B_f(\vec{r}_1,\vec{r}_2) = B_f(\vec{r}_1- \vec{r}_2) \qquad 2.1.3$$

that is, it depends only on $(\vec{r}_1- \vec{r}_2)$.

A homogeneous random field is isotropic if $B_f(\vec{r})$ depends

only on $\vec{r} = |\vec{r}|$, that is, the distance between the observation points.

Assuming $\overline{f(\vec{r})} = 0$, the correlation function of a homogeneous field can be expressed in terms of the three dimensional spectral density $\Phi(K)$, such that

$$B_f(\vec{r}_1 - \vec{r}_2) = \iiint_{-\infty}^{\infty} e^{i\vec{K}\cdot(\vec{r}_1 - \vec{r}_2)}\, \Phi(\vec{K})\, d\vec{K} \qquad 2.1.4$$

where $\vec{K}$ is the spatial wave number.

Since $\Phi(\vec{K}) = \Phi(-\vec{K})$ because $B_f(\vec{r}_1 - \vec{r}_2) = B_f(\vec{r}_2 - \vec{r}_1)$, hence Equation 2.1.4 can be written as

$$B_f(\vec{r}) = \iiint_{-\infty}^{\infty} \cos(\vec{K}\cdot\vec{r})\, \Phi(\vec{K})\, d\vec{K} \qquad 2.1.5$$

The function $\Phi(\vec{K})$ can be expressed in terms of $B_f(\vec{r})$ as

$$\Phi(\vec{K}) = \frac{1}{(2\pi)^3} \iiint_{-\infty}^{\infty} \cos(\vec{K}\cdot\vec{r})\, B_f(\vec{r})\, d\vec{r} \qquad 2.1.6$$

Thus the functions $B_f(\vec{r})$ and $\Phi(\vec{K})$ are Fourier Transforms of each other.

Introducing spherical coordinates for the isotropic field we have

$$\Phi(K) = \frac{1}{2\pi^2 K} \int_0^{\infty} r\, B_f(r)\, \sin(Kr)\, dr \qquad 2.1.7$$

and

$$B_f(r) = \frac{4\pi}{r} \int_0^{\infty} K\, \Phi(K)\, \sin(Kr)\, dK$$

The three dimensional spectral density $\Phi(K)$ of an isotropic random field is related to the one dimensional spectral density V(K) by the relation

$$\Phi(K) = -\frac{1}{2\pi K}\frac{d\,V(K)}{dK} \qquad 2.1.8$$

2.1.2 Locally homogeneous and isotropic random fields

It is a very rough approximation to regard actual meteorological fields as homogeneous and isotropic random fields. Atmospheric turbulence always contains large scale components which usually destroy the homogeneity and isotropy of the fields of the meteorological variables. Moreover, these large scale components cause the meteorological fields to be non-stationary. Therefore, in analysing the spatial structure of meteorological fields, it is appropriate to apply the method of structure functions. In fact, the difference between the values of the field $f(\vec{r})$ at two points $\vec{r}_1$ and $\vec{r}_2$ is mainly affected by inhomogeneities of the field $f(\vec{r})$ with dimensions which do not exceed the distance $|\vec{r}_1 - \vec{r}_2|$. If this distance is not too large, the largest inhomogeneities have no effect on $f(\vec{r}_1)-f(\vec{r}_2)$ and therefore the structure function

$$D_f(\vec{r}_1,\vec{r}_2) = \overline{[f(\vec{r}_1) - f(\vec{r}_2)]^2} \qquad 2.1.9$$

can depend only on $\vec{r}_1 - \vec{r}_2$.

Thus the random field $f(\vec{r})$ is called locally homogeneous

in the region R if the distribution function of the random variable $[f(\vec{r}_1)-f(\vec{r}_2)]$ is invariant with respect to shifts of the pair of points $\vec{r}_1$, $\vec{r}_2$, as long as these points are located in the region R. If the distribution function of the quantity $[f(\vec{r}_1)-f(\vec{r}_2)]$ is invariant with respect to rotations and mirror reflections of the vector $\vec{r}_1 - \vec{r}_2$, then as long as the points $\vec{r}_1$ and $\vec{r}_2$ are located in R, the locally homogeneous random field is locally isotropic in the region R as well.

Thus the structure function of a locally isotropic random field is given by

$$D_f(\vec{r}) = \overline{\left[f(\vec{r} + \vec{r}_1) - f(\vec{r}_1)\right]^2} = D_f(r) \qquad 2.1.10$$

Again, the structure function of a locally homogeneous random field can be expressed in terms of the three dimensional spectral density by the relation,

$$D_f(\vec{r}) = 2\iiint_{-\infty}^{\infty}(1 - \cos \vec{K}\cdot\vec{r})\, \Phi(\vec{K})\, d\vec{K} \qquad 2.1.11$$

In case of a locally isotropic field

$$D_f(r) = 8\pi\int_0^{\infty}\left[1 - \frac{\sin(Kr)}{Kr}\right]\Phi(K)\, K^2\, dK \qquad 2.1.12$$

Again, the three dimensional spectral density is related to the one dimensional spectral density by Equation 2.1.8.

In the study of amplitude and phase fluctuations, it is always convenient to express the structure function using two

dimensional expansions in the plane x = constant where x is the direction of propagation. In the case of local homogeneity and local isotropy in the plane x = constant,

$$D_f(\rho) = 4\pi \int_0^\infty [1 - J_0(K\rho)] F(K,0)\, K\, dK \qquad 2.1.13$$

where ρ is the distance of the observation point from the x axis on the plane x=constant

$K = \sqrt{K_2^2 + K_3^2}$ is root mean square value of the spatial wave number in the y and z directions.

F(K,O) is the two dimensional spectral density

If the field is homogeneous and isotropic in the plane x = constant, its correlation function in this plane can be expressed in terms of F(K,O) by using the formula

$$B_f(\rho) = 2\pi \int_0^\infty J_0(K\rho)\, F(K,0)\, K\, dK \qquad 2.1.14$$

The relationships between the two dimensional and three dimensional spectral density being given by

$$F(K_2,K_3,x) = \int_{-\infty}^{\infty} \cos(K_1 x)\, \Phi(K_1,K_2,K_3)\, dK_1$$

and $$2.1.15$$

$$\Phi(K_1,K_2,K_3) = \frac{1}{2\pi} \int_{-\infty}^{\infty} F(K_2,K_3,x)\, \cos(K_1 x)\, dx$$

2.2 Atmospheric turbulence

Winds, thermal currents etc. cause fluctuations in the

refractive index of the atmosphere. These sources give rise to stratifications or layers, sinusoidal waves or well mixed random variations. Generally, the atmosphere is not homogeneous so that whatever conditions exist at one point in the atmosphere do not exist at another. Unfortunately, there is only a well developed model for the atmosphere for the case of homogeneous and isotropic turbulence. Thus, the use of such a model in each practical problem must be carefully examined.

In the electromagnetic problem, the quantity of direct concern is the refractive index $n(\vec{r},t)$ of the atmosphere which is a random function of both space and time. However, in dealing with such problems, only the spatial variations are important and the time variations are suppressed. This assumption is clearly valid since the transit times for electromagnetic wave (order of microseconds) are much shorter than the characteristic decay times for the turbulent "blobs" of refractive index (order of seconds for small blobs to several seconds and longer for larger blobs) (Lumley and Panofsky 1964) (Liu 1961).

Thus, the correlation function and the spectrum of the refractive index are given by Equation 2.1.7 as

$$B_n(r) = \frac{4\pi}{r}\int_o^\infty \Phi_n(K)\, K \sin(Kr)\, dK \qquad 2.2.1a$$

and

$$\Phi_n(r) = \frac{1}{2\pi^2 K}\int_o^\infty B_n(r)\, r \sin(Kr)\, dr \qquad 2.2.1b$$

for a homogeneous and isotropic random refractive index field.

However, it can be shown (Tatarski 1961a) that in the atmosphere, when conditions for homogeneous turbulence exist, the form of the refractive index spectrum and velocity spectrum are the same, differing only by a constant. For this reason, it is easier to understand the form of the spectrum $\Phi_n(K)$ by discussing the velocity spectrum $\Phi_v(\vec{K})$. Although velocity is a vector, a single quantity $\Phi_v(K)$ contains all the information about the velocity fluctuations for isotropic turbulence.

It is common to interpret K, the spatial wave number as equal to $2\pi/l$, where l is the size of a turbulent eddy or blob. Then $\Phi_v(K)$ is the amount of energy in turbulent eddies of size l.

In the atmosphere, the energy is introduced into the turbulence from the largest scale sizes (smallest value of K). The source of this energy depends on the local climatology but the major sources can be taken as the wind shear and convective heating from the ground. It is clear that the form of the spectrum in the energy-producing wave numbers cannot be specified and this region of the spectrum is not well understood. Figure 2.1 shows a general form of the spectrum $\Phi_n(K)$. The energy producing eddies are assumed to be below some maximum wave number K_o. The scale length $L_o = 2\pi/K_o$ is called the outer scale of turbulence. At spatial wave numbers above K_o, the frequency of the spectrum is better understood. This region, known as the inertial sub-range, can be shown theoretically and experimentally to have a $K^{-11/3}$ form for $\Phi(K)$. Physically, the large eddies are unstable

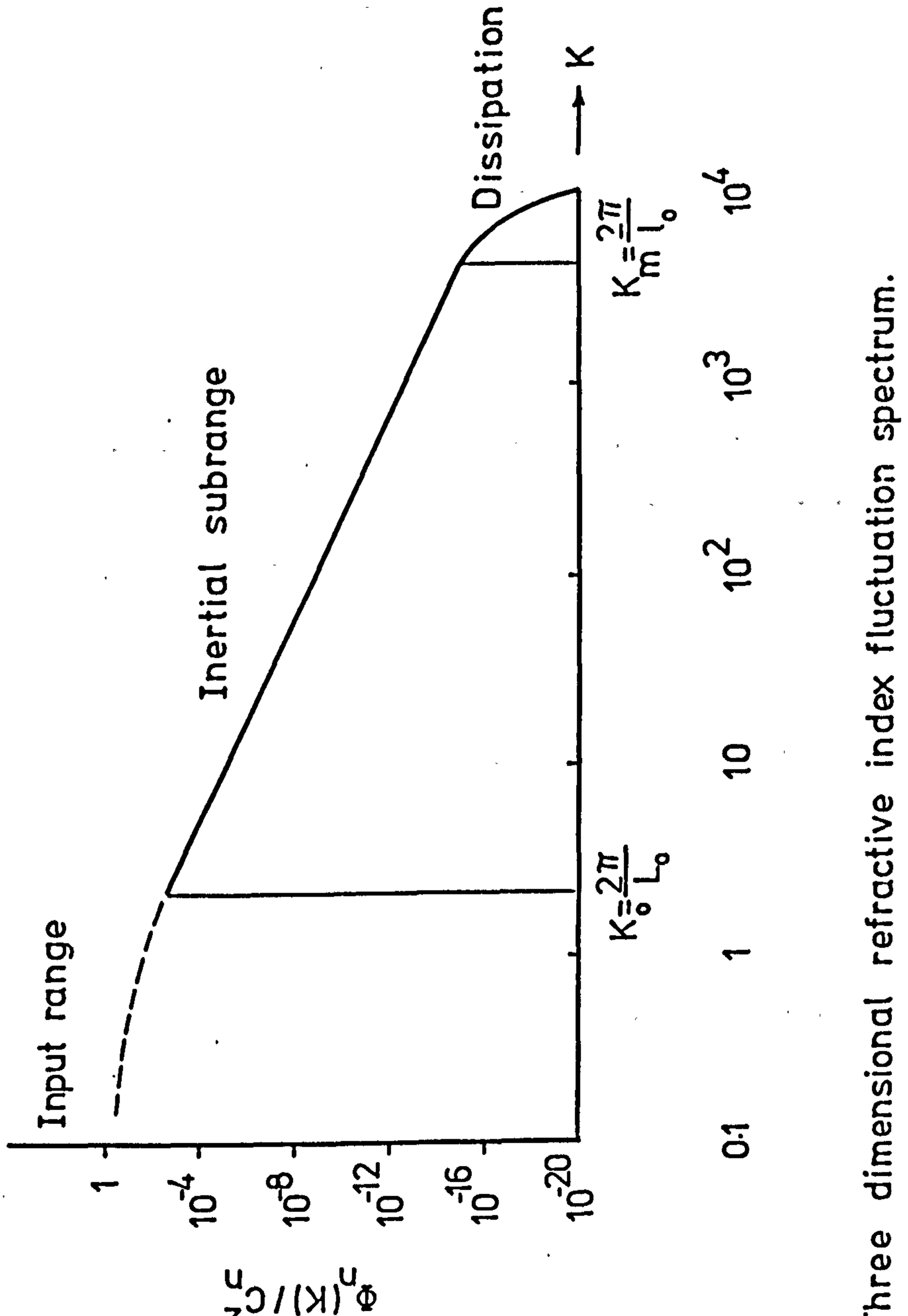

Fig 2.1 Three dimensional refractive index fluctuation spectrum.

and break up to form, and transfer energy, to smaller eddies (Tennekes and Lumley 1973). These eddies then form and transfer energy to still smaller eddies and so on. Eventually, for very small eddies, viscous effects become important and the energy is dissipated. The viscous dissipation range begins at a spatial wave number $K_m = 2\pi/l_o$ where l_o is called the inner scale of the turbulence.

In the dissipation range, the form of the spectrum $\Phi(K)$ is again not well understood, but it is known that the spectrum falls off more rapidly than $K^{-11/3}$.

A spectrum possessing all the above mentioned characteristics is called the "Kolmogorov's spectrum of turbulence".

Tatarski (1961a) tackled the problem by first investigating the velocity fluctuations in a highly developed turbulent flow and then carried out the analysis by considering temperature, humidity, refractive index and some other characteristics of the atmosphere to be conservative passive additives. (The problem of the microstructure of the concentration of a conservative passive additive was first considered by Obukhov and Yaglom for the case of the temperature field). The basic idea was as follows:

Concentration inhomogeneities with geometrical dimensions l appear as a result of the action of velocity field

perturbations with dimension l and characteristic velocity v_l. A certain number of inhomogeneities with this dimension are thus generated per unit time by means of turbulence. This generation of inhomogeneities of dimension l is to be levelled off by means of molecular diffusion action. If the rate of levelling off by molecular diffusion is smaller than the rate of generation by the turbulence action, then the inhomogeneities of dimension l which appear are not dissipated and can subsequently subdivide into smaller eddies. This process of subdivision proceeds until inhomogeneities of size l_o appear for which the generation rate by turbulence is equal to the levelling off rate by molecular diffusion action.

Dimensional considerations lead to the formulae

$$D_J(r) = a^2 \frac{\bar{N}}{\varepsilon^{1/3}} r^{2/3} \qquad \text{for } l_o \ll r \ll L_o \qquad 2.2.2a$$

and

$$D_J(r) = \frac{1}{3} \frac{\bar{N}}{D'} r^2 \qquad \text{for } r \ll l_o \qquad 2.2.2b$$

where

$D_J(r)$ is the structure function of the conservative passive additive.

a is a numerical constant

$\bar{N}$ is the dissipation rate of the additive due to molecular diffusion

ε is the corresponding dissipation rate caused by viscosity

D' is the molecular diffusion coefficient.

It can be seen that the 2/3 law holds for separation between inner (l_o) and outer (L_o) scales.

Thus the structure function $D_J(r)$ can be represented in the form

$$D_J(r) = \begin{cases} C_J^2 \, r^{2/3} & \text{for } l_o \ll r \ll L_o \\ C_J^2 \, l_o^{2/3} \, (\frac{r}{l_o})^2 & \text{for } r \ll l_o \end{cases} \qquad 2.2.3$$

The function $\Phi_J(K)$ which is the spectral density in the three dimensional space of wave number K_1, K_2, K_3 of the distribution of the amount of inhomogeneities in a unit volume can be obtained by using equation 2.1.11. Thus

$$D_J(\bar{r}) = 2 \iiint_{-\infty}^{\infty} (1 - \cos \vec{K} \cdot \vec{r}) \, \Phi_J(\vec{K}) \, d\vec{K} \qquad 2.2.4$$

In the case of isotropy, Equation 2.2.4 can be written from Equation 2.1.12 in the form

$$D_J(r) = 8\pi \int_o^{\infty} \left[1 - \frac{\sin Kr}{Kr}\right] \Phi_J(K) \, K^2 \, dK \qquad 2.2.5$$

Substituting $D_J(r)$ from Equation 2.23, $\Phi_J(K)$ is given by

$$\Phi_J(K) = 0.033 \, C_J^2 \, K^{-11/3} \qquad 2.2.6$$

However, we note that for $r \ll l_o$, the structure function $D_J(r)$ behaves quadratically, corresponding to a rapid decrease of $\Phi_J(K)$

for $K \gtrsim 1/l_o$. At present, the exact cutoff law of $\Phi_v(K)$ for $K \sim 1/l_o$ has not yet been ascertained exactly. So, for simplicity sake, a function $\Phi_v(K)$ which vanished for $K > K'_m$ is used. Thus

$$\Phi_v(K) = \begin{cases} 0.033\ C_v^2\ K^{-11/3} & \text{for } K < K'_m \\ 0 & \text{for } K > K'_m \end{cases} \qquad 2.2.7$$

where K'_m is given by

$$K'_m = 5.48/l_o \qquad 2.2.8$$

In particular, the spectral density of the refractive index of the atmosphere is given by

$$\Phi_n(K) = \begin{cases} 0.033\ C_n^2\ K^{-11/3} & \text{for } K < K'_m \\ 0 & \text{for } K > K'_m \end{cases} \qquad 2.2.9$$

and $$D_n(r) = \overline{\left[n(r_1) - n(r_1 + r)\right]^2} = C_n^2\ r^{2/3} \qquad 2.2.10$$

where C_n^2 is called the refractive index structure parameter.

In applying this spectrum to propagation problems, one must keep in mind that this spectrum is only valid for homogeneous turbulence. Under many conditions in the atmosphere, the form of the spectrum may be considerably different. Also the form of the spectrum for $K \lesssim K_o$ is at best a rough approximation and for $K > K'_m$ a good approximation. Therefore, if the electromagnetic problem is particularly sensitive to one or the other of these

regions, the use of these models must be carefully examined.

2.3 Millimetre wave propagation through turbulence

In general, a propagating electromagnetic wave can be perturbed by many different mechanisms. Different types of perturbation are treated analytically by very distinct techniques which are sometimes exact but very often approximate. Our propagation problem consists of millimetre wave propagating in a medium which has no small particles and is characterized by zero conductivity and certain average properties (composition, temperature, pressure, permittivity etc.) which may be slow varying functions of position. Also point to point values of the medium properties may exhibit small deviations from the average due to their random characteristic.

Physically, we consider that when a wave (e.g. plane wave) is launched into the turbulent medium, the small deviations in the medium properties, which result in correspondingly small refractive index fluctuations, cause the wave front to quickly become non-planar. For relatively short distances into the medium, the amplitude along constant phase surfaces remains essentially constant, although the wave front distortion grows progressively large. It should be clear that for long enough propagation paths, the warping of the equiphase surfaces will result in a shaping of the amplitude distribution across the wave. So, in general, one must solve for the complex-valued

field quantity u which satisfied the linear stochastic differential equation

$$\nabla^2 u + k^2 n^2 u = 0 \qquad 2.3.1$$

where the wave number $k = \frac{2\pi}{\lambda} = \frac{\omega}{c}$ and n is the refractive index.

The justification of using this equation is given in Section 2.4. The field u depends on position and time, that is, $n = n(\vec{r},t)$. However, as mentioned in Section 2.2, the time variation is normally suppressed. In principle, one can solve Equation 2.3.1 for each value of $n_i(\vec{r})$. However, it is impossible to obtain instantaneous values of n over the entire path. Instead, the problem should be approached from a statistical stand-point and an attempt made to evaluate certain statistics of u (mean, variances etc.) in terms of the statistics of the refractive index field $n(\vec{r})$ over the propagation path.

2.4 Theoretical approaches to the wave propagation problem

Solutions to the general problem of propagation through random media have been sought by many theoreticians using very different approaches, however, we shall restrict ourselves to those which are most widely accepted. When solving the problem of wave propagation in a turbulent medium, a number of approximations must normally be used. Though it is usually impossible to ascertain exactly what effect the approximation has on the solution, an attempt is made to put limits on significant parameters. These restrictions, if made correctly, are sufficient

conditions, that is, if the conditions are met, the solutions obtained should be valid. By valid, it is meant that the theoretical result will agree with experimental observations. It is quite possible, and often the case, that the conditions are very stringent.

In this section, three methods will be described. Brief descriptions will only be given of the Geometrical Optics and Born Approximation. More detail discussion will be made on Rytov's Method. Particular attention is paid to the validity of the approaches.

A common starting point is the solution of Maxwell's equations. We consider that the conductivity of the medium is zero and that the magnetic permeability is unity. Furthermore, we shall assume that the electromagnetic field under consideration has a time dependence given by the factor $e^{-i\omega t}$. Then the general vector wave equation which must be solved for propagation in a medium characterized by a random point function for the refractive index is given by

$$\nabla^2\vec{E} + k^2 n^2 \vec{E} = -2\nabla(\vec{E}\cdot\nabla \ln n) \qquad 2.4.1$$

where $\vec{E}$ is the electromagnetic field and n is the refractive index of the medium.

2.4.1 Geometrical optics

In the geometrical optics approach, it is assumed that $\lambda \ll l_o$ i.e. the wavelength of the propagating wave is small in comparison with the inner scale of the turbulence so that the scalar wave equation is used instead of the vector wave equation. Physically, this step is equivalent to assuming that the polarization fluctuations are negligible on the basis (Tatarski 1961) that the change of the refractive index is extremely small in a distance having the same order of the wavelength if $\lambda \ll l_o$. Diffraction effects are ignored in the geometrical optics approach and the additional restriction that $(\lambda L)^{1/2} \ll l_o$ ($\sqrt{\lambda L}$ is equivalent to the dimension of the first Fresnel zone of the propagation) is placed on the results. The phase fluctuations are calculated from the changes in velocity as a ray passes through regions of different refractive index variations. Amplitude fluctuations are attributed to the focusing and defocusing of the rays by curvature of the turbulent eddies along the path. Under these conditions, the propagation of short waves ($\lambda \ll l_o$) in a homogeneous medium is described by the scalar equation.

$$\nabla^2 u + k^2 n^2 u = 0 \qquad 2.4.2$$

where u can denote any of the field components.

If we set $u = Ae^{iS}$ where A is the amplitude and S is the phase of the wave and put $n = 1 + n_1$, $S = S_o + S_1$ and $\ln A = \ln A_o + \chi$. n_1 is the deviation of n from unity such that $|n_1| \ll 1$ and $\chi = \ln(A/A_o)$ is the level of the amplitude fluctuations on a logarithmic scale. Putting these conditions in Equation 2.4.2

and neglecting second order of small terms, the amplitude and phase fluctuations at the point (L,y,z) can be expressed in the plane of the receiver antenna in terms of the refractive index fluctuations along the propagation path (Tatarski 1961b) as follows:

$$S_1(L,y,z) = k \int_o^L n_1(x,y,z)\, dx \qquad 2.4.3$$

$$\chi(L,y,z) = -\frac{1}{2} \int_o^L dx \int_o^x d\xi \left[\frac{\partial^2 n_1(\xi,y,z)}{\partial y^2} + \frac{\partial^2 n_1(\xi,y,z)}{\partial z^2} \right] \qquad 2.4.4$$

The assumption that $\lambda \ll l_o$ is not a sufficient condition for the validity of the geometrical optics approach. The application of such an approach is also limited by the length of the propagation path.

Consider an obstacle of geometrical dimensions l located on the propagation path of a plane wave. Thus at a distance L from this obstacle, its image occurs with the same dimension l. At the same time, diffraction of the wave by the obstacle will occur (Landau and Lifshitz 1959). The angle of divergence of the diffracted wave will be of the order $\theta \sim \frac{\lambda}{l}$ and the size of the diffracted bundle at a distance L from the obstacle will be of the order $\theta L \sim \frac{\lambda L}{l}$. In order that the geometrical image is not to be appreciably affected, $\frac{\lambda L}{l}$ must be much smaller than l i.e. $\lambda L \ll l^2$. Since l_o is the smallest size of the eddies, then, we obtain the sufficient conditions for the geometrical optics

approach as follows:

$$\lambda \ll l_o \quad \text{and} \quad \sqrt{\lambda L} \ll l_o \qquad 2.4.5$$

In other words, the application of geometrical optics approach to propagation problem is limited to path lengths satisfying the condition

$$L \ll L_{critical} = \frac{l_o^2}{\lambda} \qquad 2.4.6$$

2.4.2 Born theory

To include the diffraction effect, the Born approximation is applied to the wave equation (Equation 2.4.1). This is a perturbation technique and assumes that the field at the receiver can be calculated as a sum of the original incident field plus the field scattered once from a turbulent blob such that

$$\vec{E} = \vec{E}_o + \vec{E}_1 \qquad 2.4.7$$

where $\vec{E}_o$ is the field that would exist in the absence of turbulence.

Putting in $n(\vec{r}) = 1 + n_1(\vec{r})$ and substituting into Equation 2.4.1 we obtain

$$\nabla^2 \vec{E}_o + k^2 \vec{E}_o = 0 \qquad 2.4.8$$

$$\nabla^2 \vec{E}_1 + k^2 \vec{E}_1 = -2\, k^2\, n_1\, \vec{E}_o - 2\nabla\left[\vec{E}_o\, \nabla(n_1)\right] \qquad 2.4.9$$

Let $\vec{E}_o = \vec{A}_o e^{i\vec{k}\cdot\vec{r}}$ and $|n_1(\vec{r})| \ll 1$. Putting the limitation that $\lambda r \gg L_s^2$ where L_s is the dimensions of the scattering volume and introducing the unit vector $\vec{m} = \frac{\vec{r}}{|\vec{r}|}$ directed from the origin of coordinates, Tatarski (1961c) showed that

$$E_1(\vec{r}) = \frac{k^2 e^{ikr}}{2\pi r} C_1 \vec{A}_o + \frac{ike^{ikr}}{2\pi r} C_2 \vec{m} \qquad 2.4.10$$

where

$$C_1 = \int_V n_1(\vec{r}') \, e^{i(\vec{k} - k\vec{m})\cdot\vec{r}'} \, dV'$$

$$C_2 = \int_V \vec{A}_o \nabla n_1(\vec{r}') \, e^{i(\vec{k} - k\vec{m})\cdot\vec{r}'} \, dV'$$

r' is a variable vector ranging over the scattering volume V.

If it is assumed that $\lambda \ll l_o$ as in the case of geometrical optics approach, the last term in Equation 2.4.9 can be neglected and the wave equation becomes

$$\nabla^2\vec{E}_1 + k^2\vec{E}_1 = -2k^2 n_1 \vec{E}_o \qquad 2.4.11$$

The solution to Equation 2.4.11 is given by

$$E_1(\vec{r}) = \frac{1}{4\pi} \int_V 2k^2 n_1(\vec{r}) E_o(\vec{r}) \frac{e^{ik|\vec{r}-\vec{r}'|}}{|\vec{r}-\vec{r}'|} \, dV' \qquad 2.4.12$$

The Born approximation remains valid only as long as the amplitude fluctuations remain small. However, for most line-

of-sight propagation, multiple scattering is important and the field may be scattered from one blob and then re-scattered from a second and so on before reaching the receiver. A multiple scattering approach can be formulated from this theory by a series of expansions of $\vec{E}$ in the form

$$\vec{E} = \vec{E}_o + \vec{E}_1 + \vec{E}_2 + \ldots\ldots + \vec{E}_n \qquad 2.4.13$$

where $\vec{E}_i \sim n_1 |E_{i-1}|$ and a system of equations similar to Equation 2.4.9 can be obtained.

2.4.3 Rytov theory

Rytov's method is similar to the Born approximation in that it is a perturbation technique but applied to a transformation of the scalar wave equation. In the monographs of Chernov (1960) and Tatarski (1961), it was claimed that Rytov's method significantly relaxed the restrictions that were necessary to apply to the Born approximation or geometrical optics. The derivation starts with the transformed wave equation of Equation 2.4.2

$$\nabla^2 \ln E + |\nabla \ln E|^2 + k^2 n^2(\vec{r}) = 0 \qquad 2.4.14$$

with the unperturbed wave E_o represented by

$$E_o = A_o e^{iS_o} \qquad 2.4.15$$

and let $E = E_o + E_1$ where E_1 is the small perturbation. Replacing ln E by φ thus making $\mathrm{Re}\,\varphi = \ln A$, $\mathrm{Im}\,\varphi = S$ and substituting into Equation 2.4.14, we have

$$\nabla^2\varphi + |\nabla\varphi|^2 + k^2\left[1 + n_1(\vec{r})\right]^2 = 0 \qquad 2.4.16$$

Then put $\varphi = \varphi_o + \varphi_1$ where φ_o satisfies the equation

$$\nabla^2\varphi_o + |\nabla\varphi_o|^2 + k^2 = 0 \qquad 2.4.17$$

we obtain from Equation 2.4.16 the following form

$$\nabla^2\varphi_1 + 2\nabla\varphi_o\cdot\nabla\varphi_1 + 2k^2 n_1(\vec{r}) = 0 \qquad 2.4.18$$

for $|n_1(\vec{r})| \ll 1$ and $\lambda|\nabla\varphi_1| \ll 2\pi$

The solution to this equation was shown to be (Tatarski 1961d)

$$\varphi_1(\vec{r}) = \frac{1}{E_o(\vec{r})}\,\frac{k^2}{2\pi}\int_V n_1(\vec{r}')E_o(\vec{r}')\;\frac{e^{ik|\vec{r}-\vec{r}'|}}{|\vec{r}-\vec{r}'|}\,dV' \qquad 2.4.19$$

Since $\varphi_1 = \varphi - \varphi_o = \ln\frac{A}{A_o} + i(S-S_o)$

$$= \chi + iS_1 \qquad 2.4.20$$

where χ is termed as the logarithmic amplitude fluctuation of the field

S_1 is the phase fluctuation,

we get

$$\ln \frac{A}{A_o} = \chi = \mathrm{Re}\, \varphi_1 \qquad 2.4.21$$

and

$$S_1 = \mathrm{Im}\, \varphi_1 \qquad 2.4.22$$

However Equation 2.4.19 is too difficult to permit easy analysis and it must be simplified. If the x axis is along the direction of propagation of the incident wave, then

$$E_o(\vec{r}) = A_o e^{ikx}$$

and Equation 2.4.19 takes the form

$$\varphi_1(\vec{r}) = \frac{k^2}{2\pi} \int_V n_1(\vec{r}') \, e^{-ik(x-x')} \left[\frac{e^{ik|\vec{r}-\vec{r}'|}}{|\vec{r}-\vec{r}'|} \right] dV' \qquad 2.4.23$$

In order to simplify the Green's function in Equation 2.4.23 to make the mathematical manipulation possible, it must be assumed that λ is small in comparison with l_o, i.e. $\lambda \ll l_o$ and that the condition $\left[\lambda^3 L / l_o^4\right] \ll 1$ to be met. Thus Equation 2.4.23 can be reduced to the form

$$\varphi_1(r) = \frac{k^2}{2\pi} \int_V n_1(\vec{r}') \left[\frac{e^{ik \frac{(y-y')^2 + (z-z')^2}{2(x-x')}}}{(x-x')} \right] dV' \qquad 2.4.24$$

which is an exact solution of the equation

$$\frac{\partial^2 \varphi_1}{\partial y^2} + \frac{\partial^2 \varphi_1}{\partial z^2} + 2ik \frac{\partial \varphi_1}{\partial x} + 2k^2 n_1(\vec{r}) = 0 \qquad 2.4.25$$

Following the method of spectral expansions as given by Tatarski (1961d), it is possible to start with Equation 2.4.25 and solve for the structure functions and spectra of phase and logarithmic amplitudes. The solution for the phase and logarithmic amplitude spectra are, respectively

$$F_A(K,0) = \pi k^2 L \left[1 - \frac{k}{K^2 L} \sin \frac{K^2 L}{k}\right] \Phi_n(K) \qquad 2.4.26$$

and

$$F_S(K,0) = \pi k^2 L \left[1 + \frac{k}{K^2 L} \sin \frac{K^2 L}{k}\right] \Phi_n(K) \qquad 2.4.27$$

Equations 2.4.26 and 2.4.27 relate the two dimensional spectral density of the structure (correlation) functions of the amplitude and phase fluctuations of the wave in the plane x = L to the three-dimensional spectral density of the structure (correlation) function of the refractive index.

2.5 Validity of theoretical approaches to millimetre wave propagation

2.5.1 Geometrical optics

Consider geometrical optics first. This approach ignores the diffraction effects (Section 2.4.1) and the restriction $\sqrt{\lambda L} \ll l_o$ has been imposed. Immediately it can be seen that this approach cannot be applied to millimetre wave analysis because $\sqrt{\lambda L}$, in the millimetre wave propagation, is of the order of metres. Taylor

(1968a,1968b) has questioned the validity of this criterion and raised the possibility that the ray optics technique may have much greater validity at optical frequencies and the range can be extended to hundreds of metres instead of several metres according to the condition $\sqrt{\lambda L} \ll l_o$, i.e. an increase of a factor of hundreds. However, for millimetre waves, if the condition $\sqrt{\lambda L}$ is to be met, L is only of the order of millimetres. It can be realized that it is impossible to extend the range from millimetres to kilometres (the range for practical communication links).

2.5.2 Born theory

Single-scatter Born theory requires that $|E_1/E_o| \ll 1$ which can be generally met at millimetre wavelengths, and the multiple scattering effect is ignored. The negligence of the multiple scattering may have no effect on longer wavelengths in troposcatter propagation, but when the wavelength is comparable with the size of inhomogeneities and for a practical propagation path (say, several Km for millimetre wave propagation) the application of such a theory is limited because multiple scattering can no longer be ignored.

2.5.3 Rytov theory

Rytov theory seems to be the most realistic theory which exists at the present time. It includes the multiple scattering effect and has conditions which are much less stringent than

those in the geometrical optics approach. It contains one notable assumption that the complex phase changes little over distances of a wavelength, that is $\lambda|\nabla S_1| \ll 2\pi$ and the condition that $\lambda^3 L/l_o^4 \ll 1$ to ease the mathematical manipulation. However since l_o is of the order of a few millimetres, the validity of the theory is uncertain in the millimetre and longer wavelength range. The validity of this method applied to millimetre wavelengths has been questioned as reported by Strohbehn (1968). The condition $\lambda^3 L/l_o^4 \ll 1$ is a very weak restriction at optical frequencies where $\lambda \ll l_o$. At millimetre or longer wavelengths, however, the condition cannot be satisfied since it implies that the path length L must be a few millimetres or less.

In order to relax the restrictions imposed, we have to examine carefully why such restrictions are imposed and the effects if such restrictions are ignored.

In the first place, the application of the perturbation expansion approach to wave propagations is limited to small amplitude fluctuations. Though such an application may be doubtful at optical frequencies since the fluctuations in amplitude and phase are often very large, but in microwave cases, the fluctuations are much smaller (a ratio of the order of 10^5) and the validity of the perturbation expansion approach does not need to be doubted.

In the derivation given in Section 2.4.3, the assumption

that $\lambda \ll l_o$ is applied in two ways. First, it is used to argue that the depolarization term can be neglected in the vector wave equation. Second, when $\lambda \ll l_o$, the effective scattering cone, i.e. the volume of the atmosphere from which there is significant energy scattered to the receiver, has a vertex angle of the order of λ/l_o. The assumption that this scattering cone is small is used to make several approximations which result in simplifying the Green's function or equivalently, the differential equation that is solved.

The effect of dropping the depolarization term in the wave equation 2.4.7 was studied by Strohbehn (1968). He started with the vector wave equation and assumed that the incident electric field is a linearly polarized monchromatic plane wave propagating in the x direction and polarized in the z direction. He applied a perturbation techneque, assuming that

$$n = 1 + \sqrt{} n_1 \qquad 2.5.1$$

and $$\vec{E} = \vec{E}_o + \sqrt{}\vec{E}_1 + \sqrt{}^2\vec{E}_2 + \ldots\ldots + \sqrt{}^m\vec{E}_m \qquad 2.5.2$$

where $\sqrt{}$ is a dummy variable which shows the order of smallness of the various terms in equation. Substituting the above equations into the vector wave equation (Equation 2.4.7), equating equal powers of $\sqrt{}$, and separating orthogonal components of the field, the zeroth and first order terms are

$$\nabla^2 E_{oz} + k^2 E_{oz} = 0 \qquad 2.5.3a$$

$$\nabla^2 E_{1z} + k^2 E_{1z} + 2(k^2 n_1 + \frac{\partial^2 n_1}{\partial z^2}) E_{oz} = 0 \qquad 2.5.3b$$

$$\nabla^2 E_{1y} + k^2 E_{1y} + 2(\frac{\partial^2 n_1}{\partial y \partial z}) E_{oz} = 0 \qquad 2.5.3c$$

$$\nabla^2 E_{1x} + k^2 E_{1x} + 2(ik \frac{\partial n_1}{\partial z} + \frac{^2 n_1}{\partial x \partial z}) E_{oz} = 0 \qquad 2.5.3d$$

Then, he made use of the covariance function of the depolarized component found by Strohbehn and Clifford (1967) and assumed the three dimensional spectrum of the refractive index $\Phi_n(K)$ obeyed the Kolmogorov spectrum of turbulence, he came to the conclusion that the variance of the depolarized scattered field is given by

$$\overline{|E_{1y}|^2} \approx 0.0756 \frac{C_n^2 L K_m^{7/3}}{k^2} |E_o|^2 \qquad 2.5.4$$

Letting $C_n^2 \sim 4 \times 10^{-14}\ m^{-2/3}$, $l_o = 1$ mm and $L = 4 \times 10^3$ metres, it can be shown that the variance of the depolarized scattered field is about 80 dB and 87 dB respectively below the incident free-space wave at 8 mm and 3 mm wavelengths.

However, the validity of neglecting the polarized term when calculating the scattered field is the ratio of the depolarized component to the scattered polarized component. Strohbehn reckoned that the magnitude of the neglected term

$2\left(\frac{\partial^2 n_1}{\partial z^2}\right) E_{oz}$ is of the same order as $\overline{|E_{1y}|^2}$ and defined the term

$$R = \frac{\overline{|E_{1y}^2|}}{\overline{|E_{1z}^2|}} \qquad 2.5.5$$

which is calculated to be

$$R \approx 0.245 \frac{K_m^{7/3}}{L^{5/6} k^{19/6}} \qquad 2.5.6$$

This equation shows that for l_o= 1 mm to 10 mm, R remains much smaller than unity for millimetre wavelengths over all reasonable path lengths, i.e. the effect of neglecting the depolarization in Equation 2.5.3b is very small and the use of the scalar wave equation seems completely justified for millimetre wavelengths.

Concerning the wavelength restriction ($\lambda \ll l_o$) imposed on the solution of the wave equation, Clifford and Strohbehn (1970) showed that for almost all cases of practical interest in line-of-sight propagation at millimetre wavelengths and centimetre wavelengths, the result derived using the assumption that $\lambda \ll l_o$ is equally valid for $\lambda > l_o$. They solved the scalar wave equations (Equations 2.5.3a and 2.5.3b) without putting in any wavelength restriction and divided the spatial wave numbers into three regions. With the inclusion of the effects of the atmospheric absorption, they came to the following expressions for the two dimensional

amplitude and phase spectra:

$$\left.\begin{matrix} F_A(K,0) \\ \\ \\ E_S(K,0) \end{matrix}\right\} = \frac{\pi k^4 L}{(k^2 - K^2)} \left[1 \mp \frac{\sin\{2\left[k - (k^2 - K^2)^{1/2}\right]L\}}{2\left[k - (k^2 - K^2)^{1/2}\right]L} \right]$$

$$\cdot \Phi_n\left[k - (k^2 - K^2)^{1/2}, K_2, K_3\right] \quad \text{for } K < k$$

$$\text{and} \quad K = (K_2^2 + K_3^2)^{1/2}$$

2.5.7

$$F_A(K,0) = F_S(K,0) \leqslant \frac{\pi k^4 (1 - e^{-2bL})}{2b(a^2 + b^2)} \cdot \Phi_n(k,K) \quad \text{for } K \sim k$$

2.5.8

where

$$a = \frac{1}{(2)^{1/2}} \left\{ \left[(k^2 - K^2)^2 + 4k^2 \alpha^2 \right]^{1/2} + k^2 - K^2 \right\}^{1/2}$$

$$b = \frac{1}{(2)^{1/2}} \left\{ \left[(k^2 - K^2)^2 + 4k^2 \alpha^2 \right]^{1/2} - k^2 + K^2 \right\}^{1/2}$$

α is the absorption coefficient which is very small in comparison with k in practical cases.

$$F_A(K,0) = F_S(K,0) \leqslant \frac{\pi (k^2 - K_3^2)^2}{(K^2 - k^2)^{3/2}} \Phi_n(k,K) \cdot \left\{ 1 - e^{-2(K^2 - k^2)^{1/2} L} \right\}$$

for $K > k$

2.5.9

A typical two-dimensional spectrum of amplitude fluctuations is shown in Figure 2.2. It can be seen that without the wavelength restriction, a new peak at K = k occurs. However, it can be shown that the contribution of the new peak is insignificant in the range of millimetre wavelengths. (Clifford and Strohbehn 1970).

In order to see the effect of the new peak on the variance of amplitude fluctuations, Clifford and Strohbehn showed that the ratio of the contribution to the variance from the new peak to the variance as calculated from the optical formula is

$$\sigma^2_{\text{new peak}} / \sigma^2_{\text{optical}} \approx 0.29 \left(\frac{1}{k^{5/6} L^{11/6} \alpha} \right) \qquad 2.5.10$$

A curve showing this ratio at different wave numbers for a path length of 4 kilometres is given in Figure 2.3. It can be seen that the contribution of the new peak to the variance is insignificant in the range of millimetre wavelengths. Lee and Harp (1969) arrived at the same conclusion using an entirely different approach based on the technique of resolving the three dimensional refractivity field of the medium into thin slabs perpendicular to the propagation path and further resolving the two dimensional refractivity field with a slab into Fourier components of varying wave number and angle in polar coordinates. The effect produced upon the wave by one of these Fourier components is then determined. The resolution is then retraced and perturbations produced by Fourier components of differing

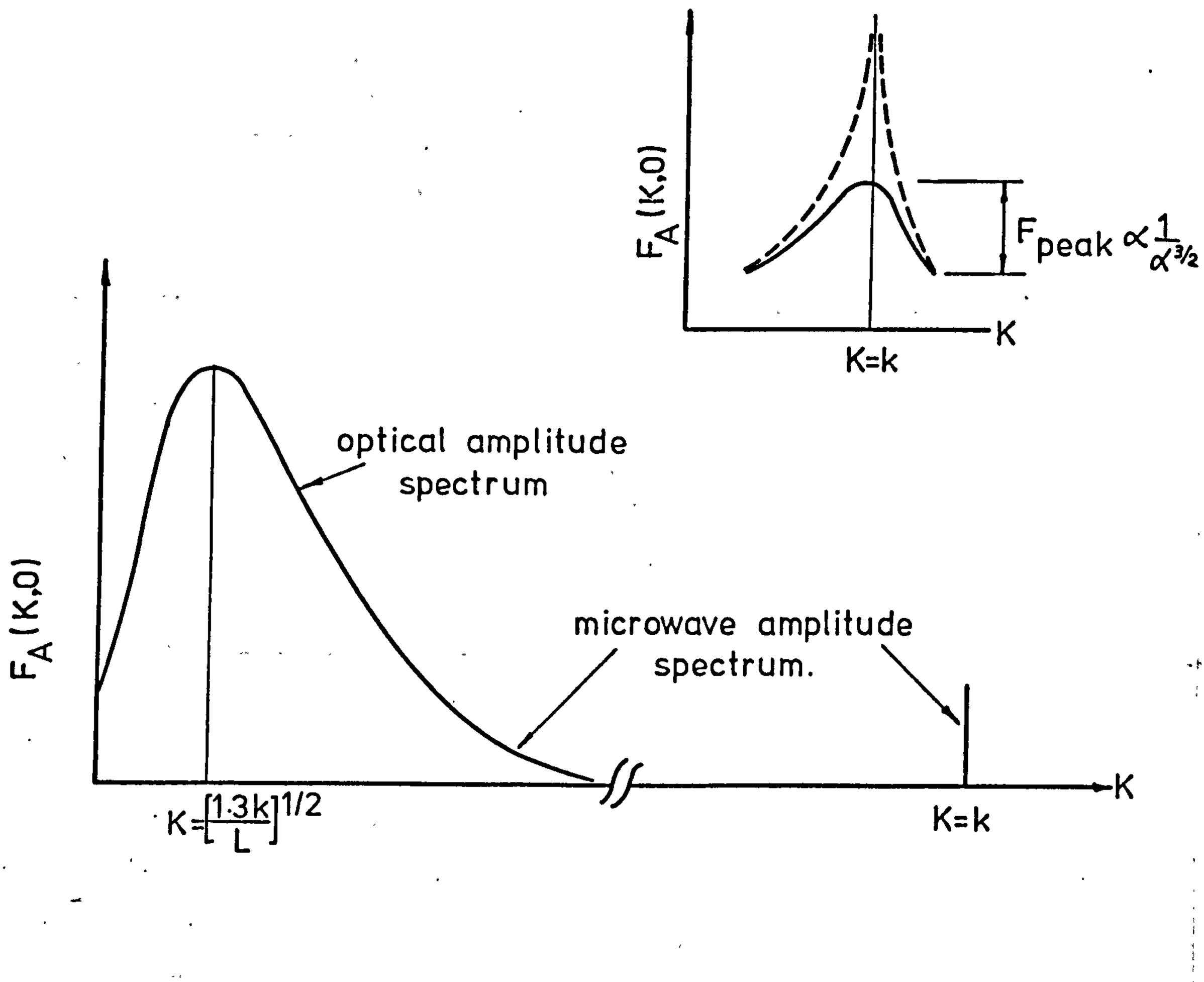

Fig. 2.2 Two dimensional spectrum for amplitude fluctuations of a line-of-sight microwave signal. The insert is an expansion of the narrow peak at $K=k$. The assumption here is $\Phi_n(K) = 0.033\, C_n^2\, K^{-11/3}$.

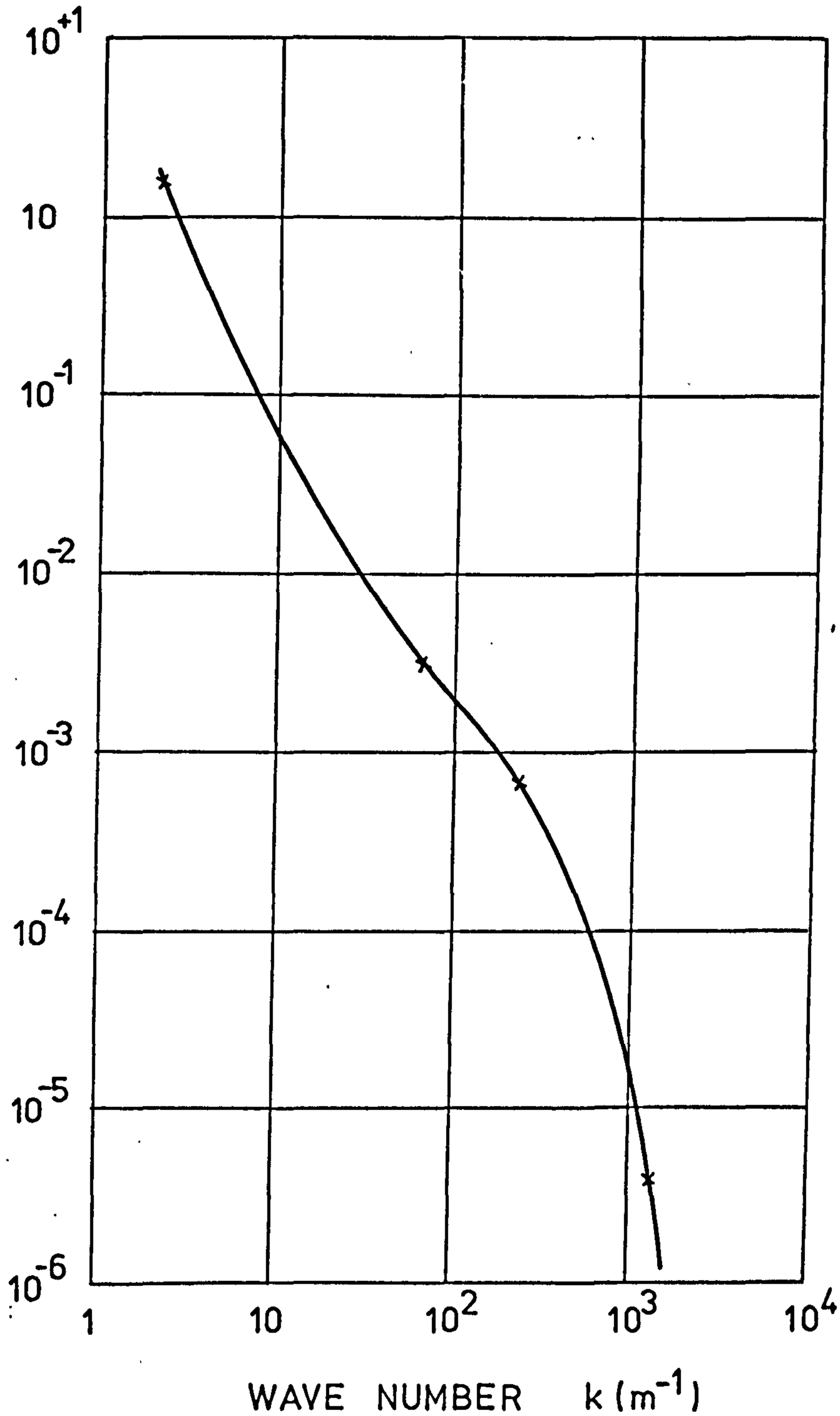

Fig. 2.3 The ratio of the contribution to the variance of the new peak of the microwave spectrum to the contribution from the peak calculated from optical formula.

wave number, angle and position along the path are summed statistically.

Based on the above conclusions, it is evident that the solutions of the wave field based on Rytov's theory developed for optical frequencies can also be applied to millimetre wavelengths without any significant error. Thus throughout the rest of this thesis, any calculations and further derivations will be based on these solutions.

CHAPTER 3 EXPERIMENTAL EQUIPMENT

This chapter deals with the description and characteristics of the equipment designed and built for measurements of the microwave link amplitude variations and the meteorological parameters. The chapter is divided into two parts. The first describes the system with some theoretical considerations regarding the detection of the amplitude fluctuations and the noise level of the system. The second part is mainly concerned with the description of the meteorological measurement devices with particular regard to the response characteristics of the sensors. Some of the descriptions are further detailed in the appendices.

PART I DESCRIPTION OF THE SYSTEM

3.1.1 The 36 GHz link

The link is a line-of-sight one way microwave path of length 4.1 kilometres at the nominal frequency of 36.1 GHz. The transmitter and receiver were located on the top of the Electrical Engineering Buildings at Imperial College and University College London respectively. The topography of the link is shown in Figure 3.1. The direction of University College London to Imperial College is 239.1° from the north. At about 1500 metres from the receiving end (around Bond Street Underground Station) the clearance of the path is reduced to a section of 10 x 10 metres which is still wide enough for the first Fresnel zone diameter $\sqrt{\lambda L}$ of 5.76 metres at this frequency. Another link with nominal frequency of 110 GHz also shares the same path ($\sqrt{\lambda L}$ = 3.3 metres).

The geographical situation of the links is a representative of an urban link in a modern city. The path passes over trees and open space (Hyde Park) and between tall buildings.

The two 36 GHz aerials are identical with a nominal (measured) gain of 44.4 dB. The transmitter power P_t is 15 mW. With the values above-stated, the received power at the plane of the receiving aerial can be calculated by using the relation:

$$P_r = P_t G^2 \left(\frac{\lambda_o}{4\pi L} \right)^2 \qquad 3.1.1.1$$

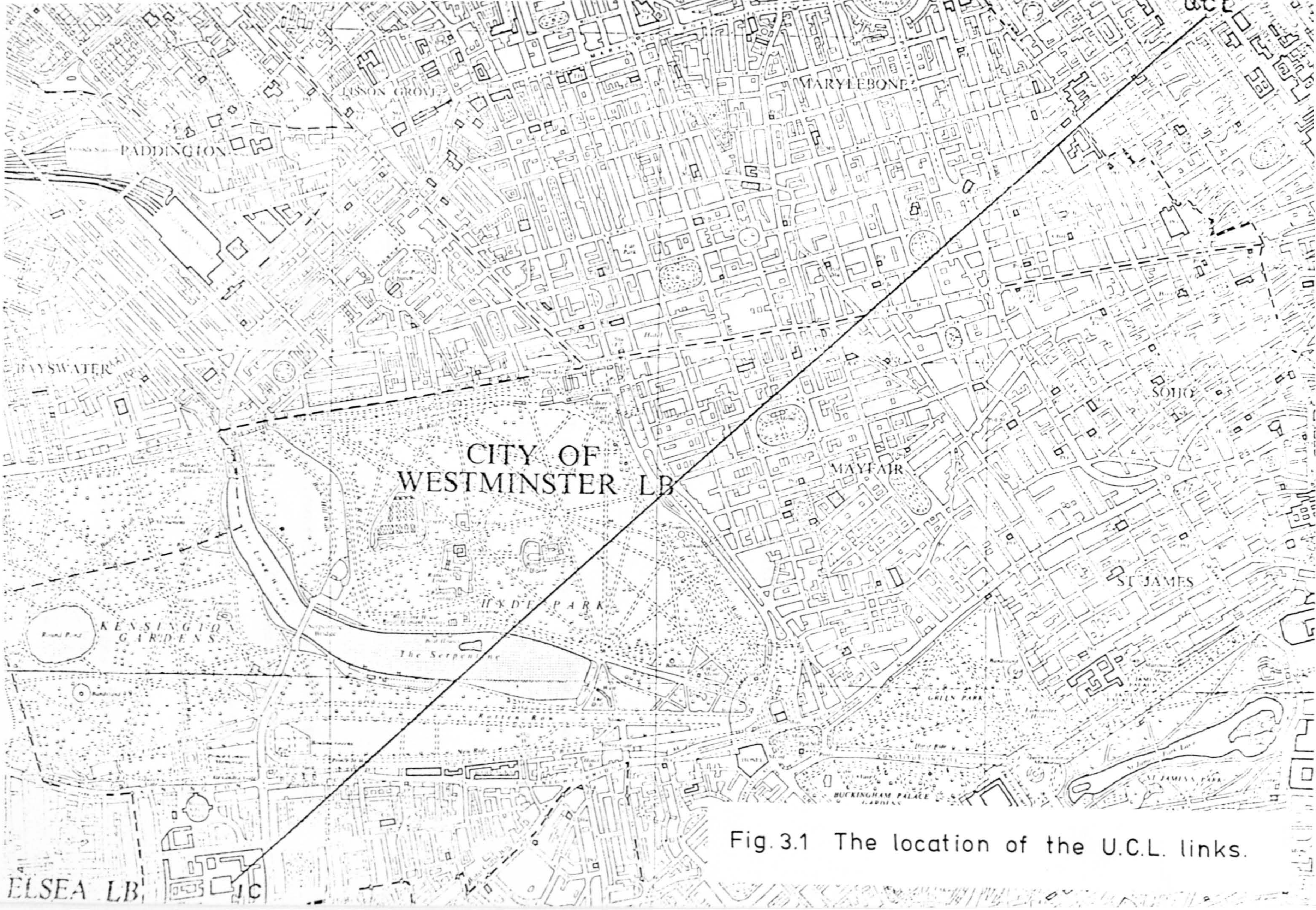

Fig. 3.1 The location of the U.C.L. links.

where G is the gain of the aerials = 2.754×10^4

λ_o is the free space wavelength = 8.33×10^{-3} metres

L is the path length = 4.1 kilometres

giving

$$P_r = 3.1024 \times 10^{-7} \text{ W.}$$

In other words, the free space attenuation is

$$10 \log_{10} \frac{15 \times 10^{-3}}{3.1024 \times 10^{-7}} = 46.84 \text{ dB}$$

The receiving aerial was linked to the receiver by 8 metres of waveguide introducing an attenuation of 2.5 dB thus making the total attenuation from transmitter to receiver 49.34 dB.

A rough experiment has been carried out to find the point at which the noise level was comparable with the signal level and it was found that this observable margin of the receiver with nominal power was better than 46 dB.

3.1.2 The aerials

The aerials used at both transmitter and receiver ends are shown in Figure 3.2. They were built of commerically available paraboloids (Vilar 1972). The basic characteristics required of the antenna system are axial symmetry, high gain and reasonably low side lobes. The aerial symmetry led to a Cassegrain configurature with a conical feeding horn. The

Figure 3.2 The 36 GHz receiving antenna, the 110 GHz receiving system and the wind measurement devices.

subreflector is hyperboloidal illuminated from a circular waveguide. The transition to rectangular waveguide is immediately behind the main dish.

The paraboloids have a diameter of 0.6 metre with an effective diameter of 0.57 metre due to round edges. The focal length is 20.3 cm. The nominal gain ($4S/\lambda^2$ where S is the effective area) at 36.1 GHz is estimated to be 46.5 dB whereas the measured gain is 44.4 dB. The measured polar diagram is shown in Figure 3.3.

The alignment of the antennas was carried out by means of a telescope mounted on one side of the antenna frame. The optical axis of the telescope was aligned with the mechanical axis of the antenna. However very fine alignment of the transmitter and receiver aerials was necessary to produce maximum signal.

3.1.3 The transmitter

The block diagram of the transmitter is shown in Figure 3.4(a). It is contained in a die-cast box 8"x10"x2½" in size and mounted on a rigidly erected mast on the roof of the engineering building at Imperial College (Figure 3.4b).

The Gunn diode is an EMI-Varian 9010 AA mounted on an invar cavity. The output power at the feeder is 15 mW. The

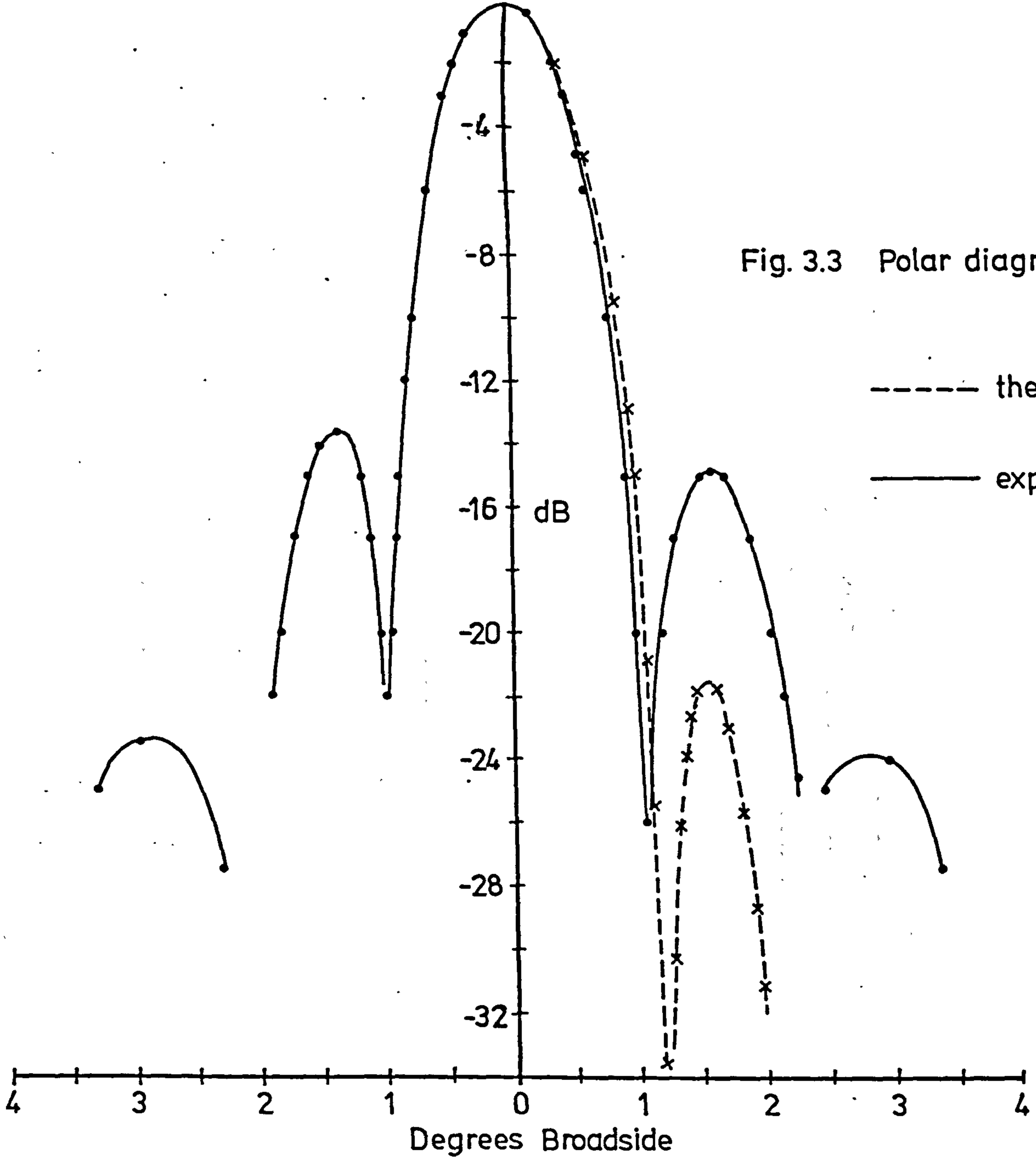

Fig. 3.3 Polar diagram of aerials

----- theoretical

——— experimental

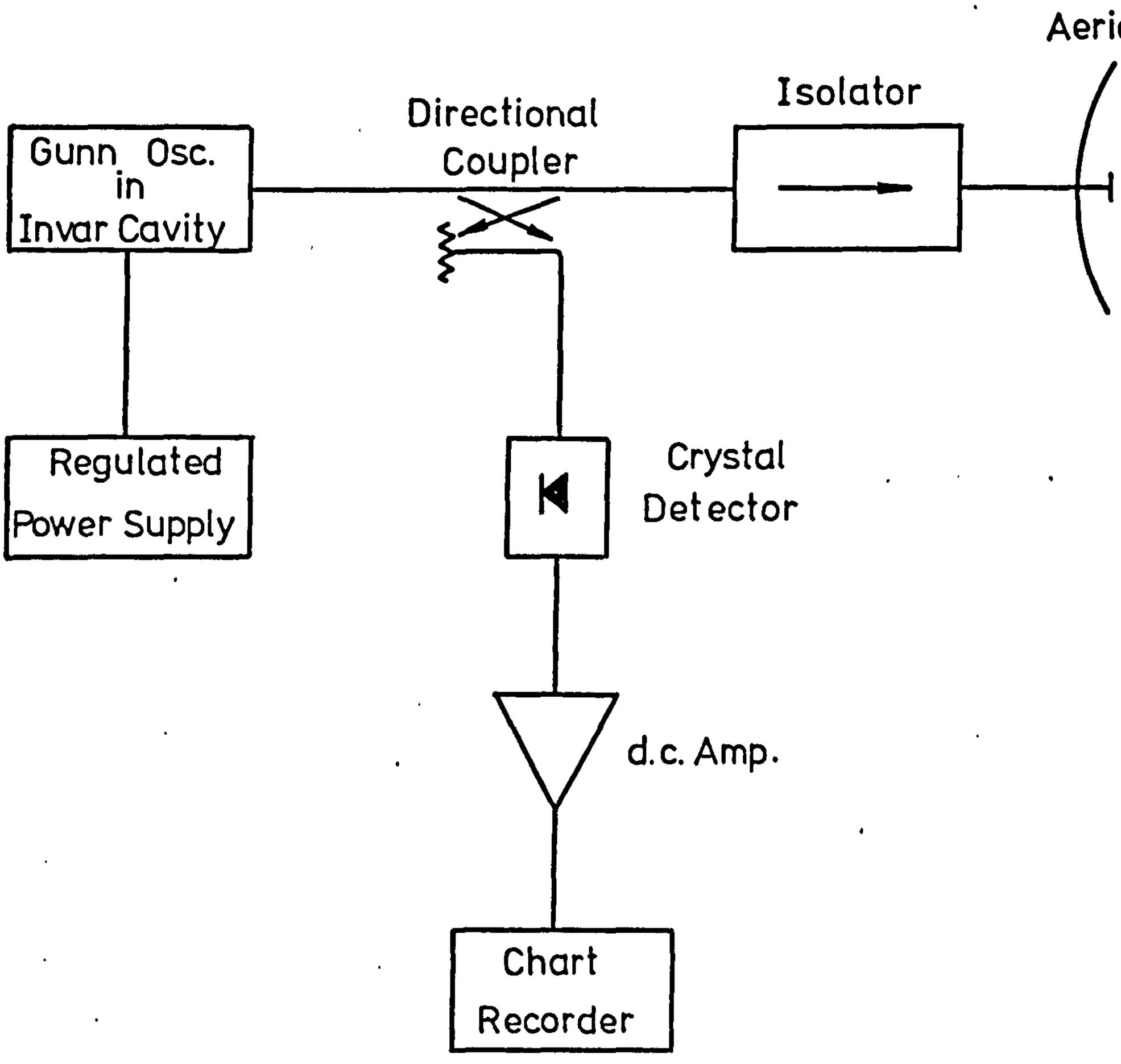

Fig. 3.4a Block diagram of the transmitter

Figure 3.4b The transmitters and the transmitting antennas at Imperial College.

power dependence on the temperature quoted by the manufacturer is negligible within a range of 0 to 50°C. The frequency temperature dependence is 0.35 MHz/°C and the frequency voltage dependence is 10 MHz/volt.

There is also facility for monitoring the power transmitted by means of a crystal detector, mounted on a directional coupler. The detected level was amplified and recorded on a chart recorder.

Though the oscillator specification seems to be relatively independent of temperature, however, the output from the regulated power supply associated with the transmitter may be affected slightly by temperature changes, so the whole transmitter including the regulated power supply unit, is completely enclosed in a temperature controlled chamber to ensure temperature stability.

3.1.4 The receiver

The receiver was constructed in two parts. The first part (Figure 3.5a) includes the mixer, the local oscillator, the i.f. pre-amplifier and the frequency control circuit, all as close to the aerial as possible. The block diagram is shown in Fig.3.5b. The 30 MHz i.f. signal is fed via a coaxial cable to the second part of the receiver in the laboratory (Figure 3.5c). This part includes the intermediate frequency main amplifier, the detector and the recording system.

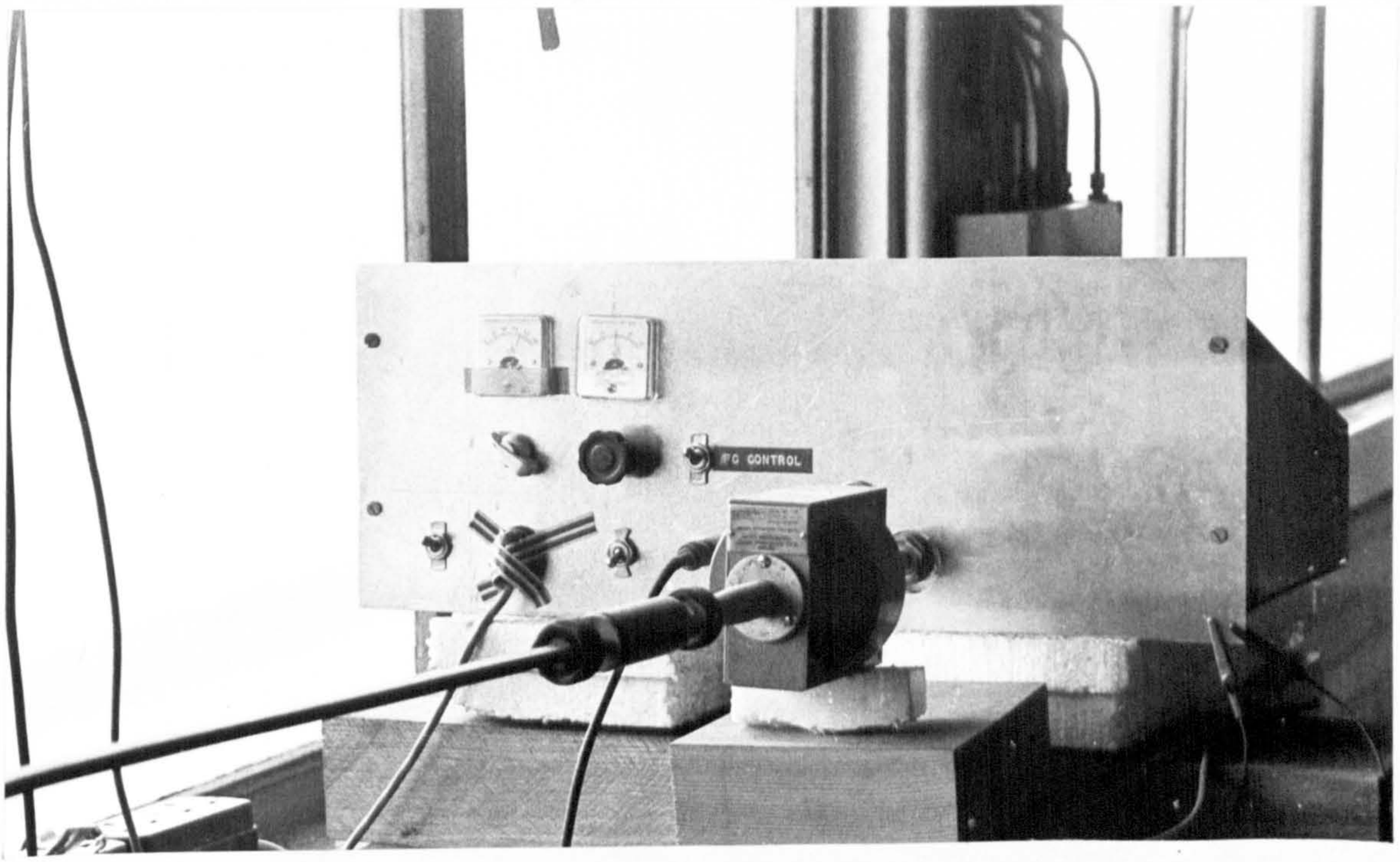

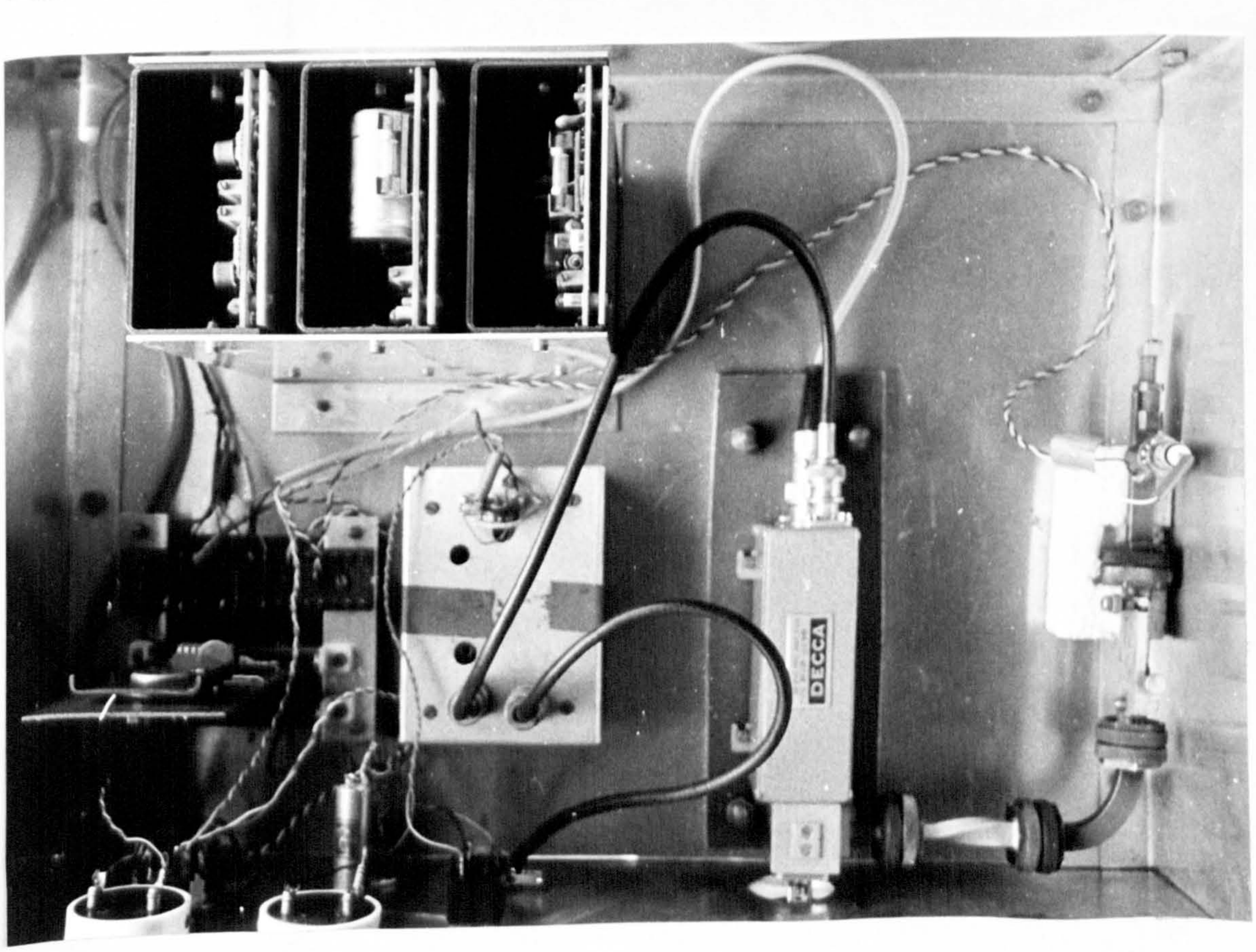

Figure 3.5a Front view and top view of the 36 GHz receiver

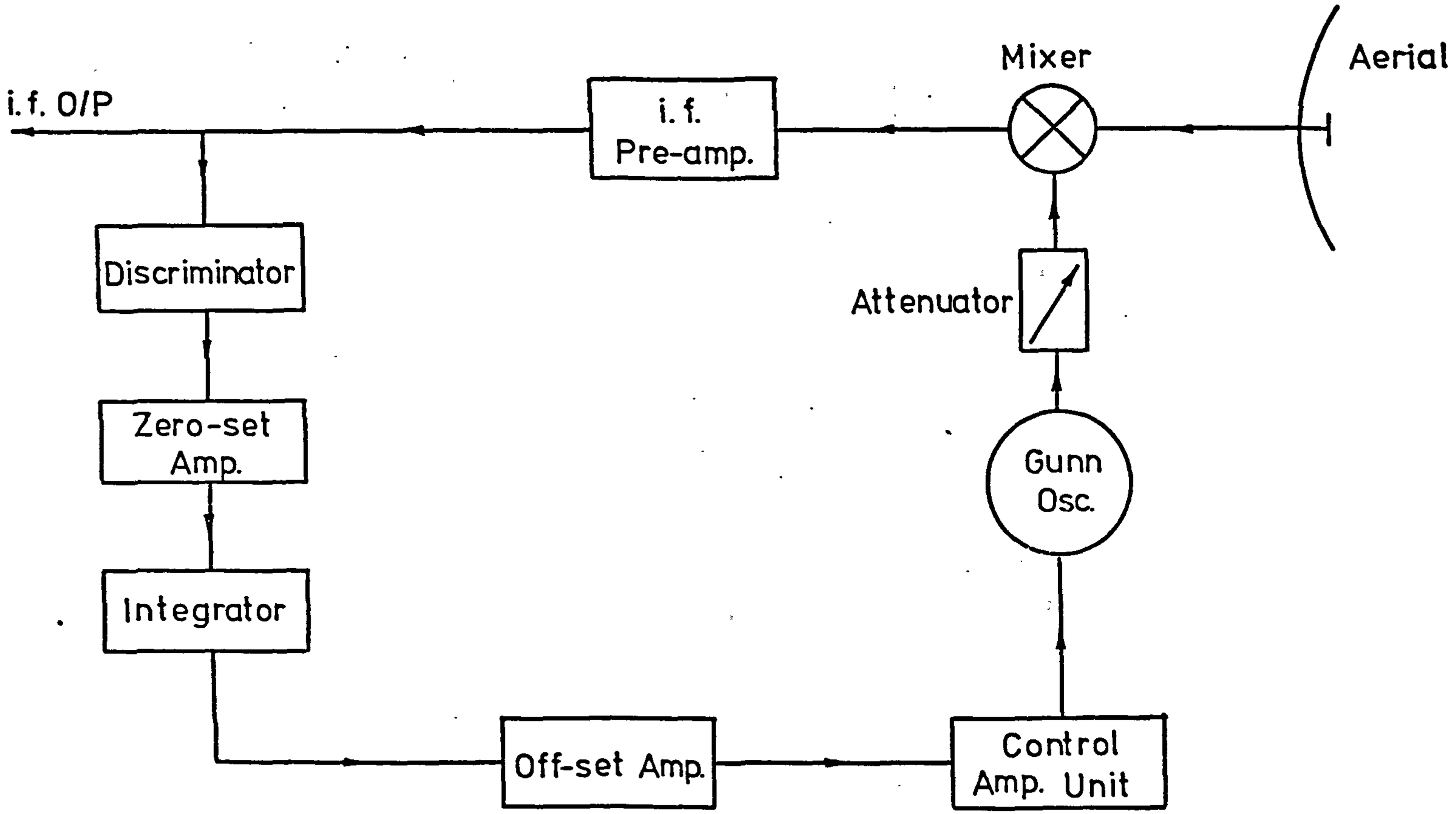

Fig. 3.5b Block diagram of the receiver (first part)

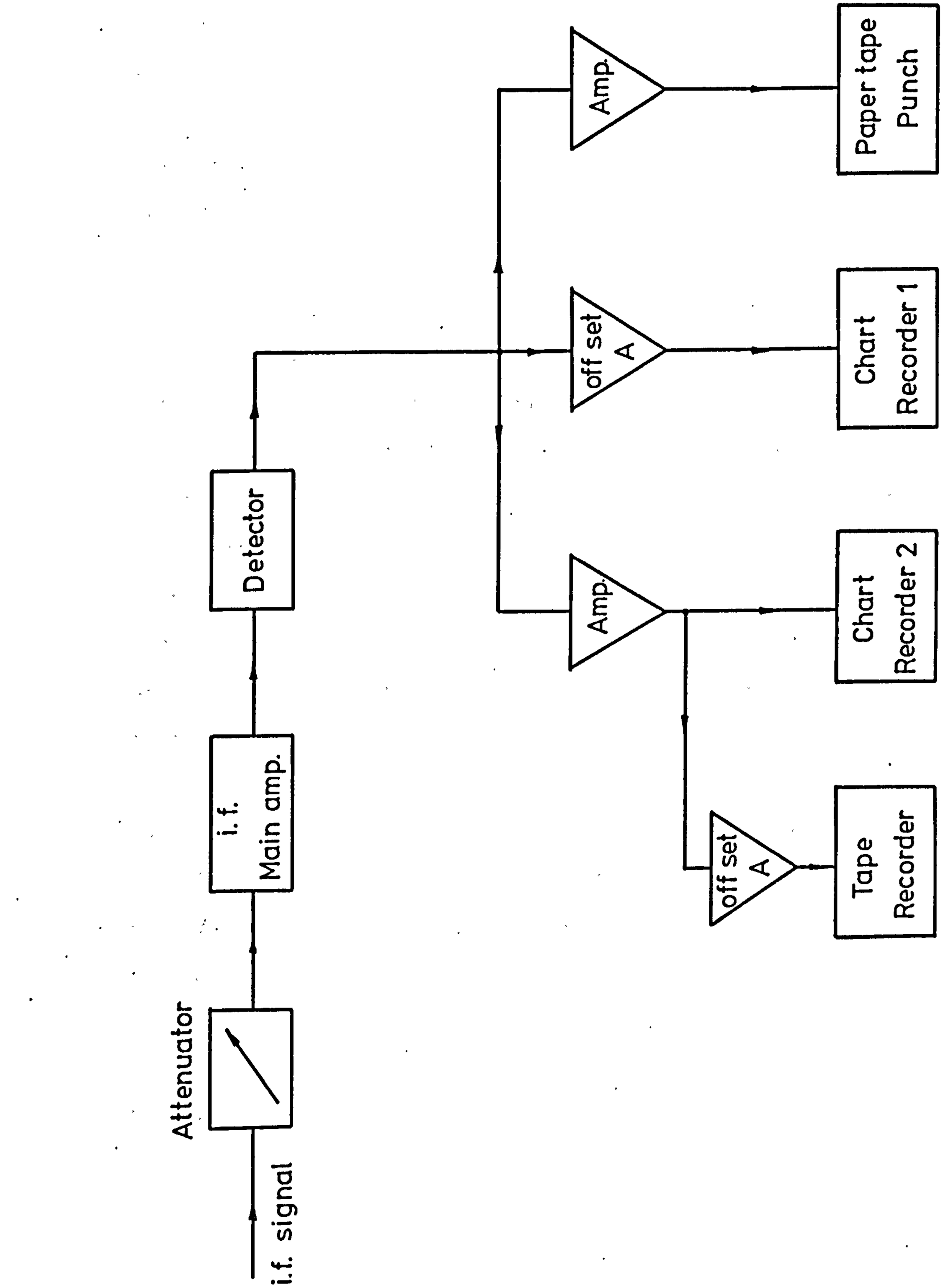

Fig.3.5c Block diagram of the receiver (second part)

The local oscillator uses a Plessey TE 042E Gunn diode mounted in a tunable resonant cavity. The local oscillator is electrically tuned by an automatic frequency control circuit so that the intermediate frequency remains at 30 MHz independent of the variations of the transmitter frequency or the operation conditions of the local oscillator.

The automatic frequency control system circuit is shown in Figures 3.6a and 3.6b. It operates by using a frequency discriminator to detect any change in the intermediate frequency from 30 MHz. The characteristics of the discriminator is shown in Figure 3.7. Changes in the intermediate frequency may be caused by either a change in the frequency of the received signal or a change in the local oscillator frequency. The output of the frequency discriminator is amplified and passed through an operational amplifier integrator. The integrator provides a long time constant in the control system, the output from which is passed through a further amplifier and control unit to provide suitable variations in the supply voltage of the Gunn diode. Assuming linear operation for the automatic frequency control system, it can be shown that the automatic frequency control system is always stable (Appendix 3.1).

The intermediate frequency signal which carries the information is obtained via a Decca MW 19-22-36 Q band balanced mixer. The local oscillator power fed into the mixer is 0.5 mW. The pre-amplifier and main-amplifier have gains of 45 dB and 50 dB respectively with centre frequency at 30 MHz and a

All resistors in ohms

All capacitors in uF

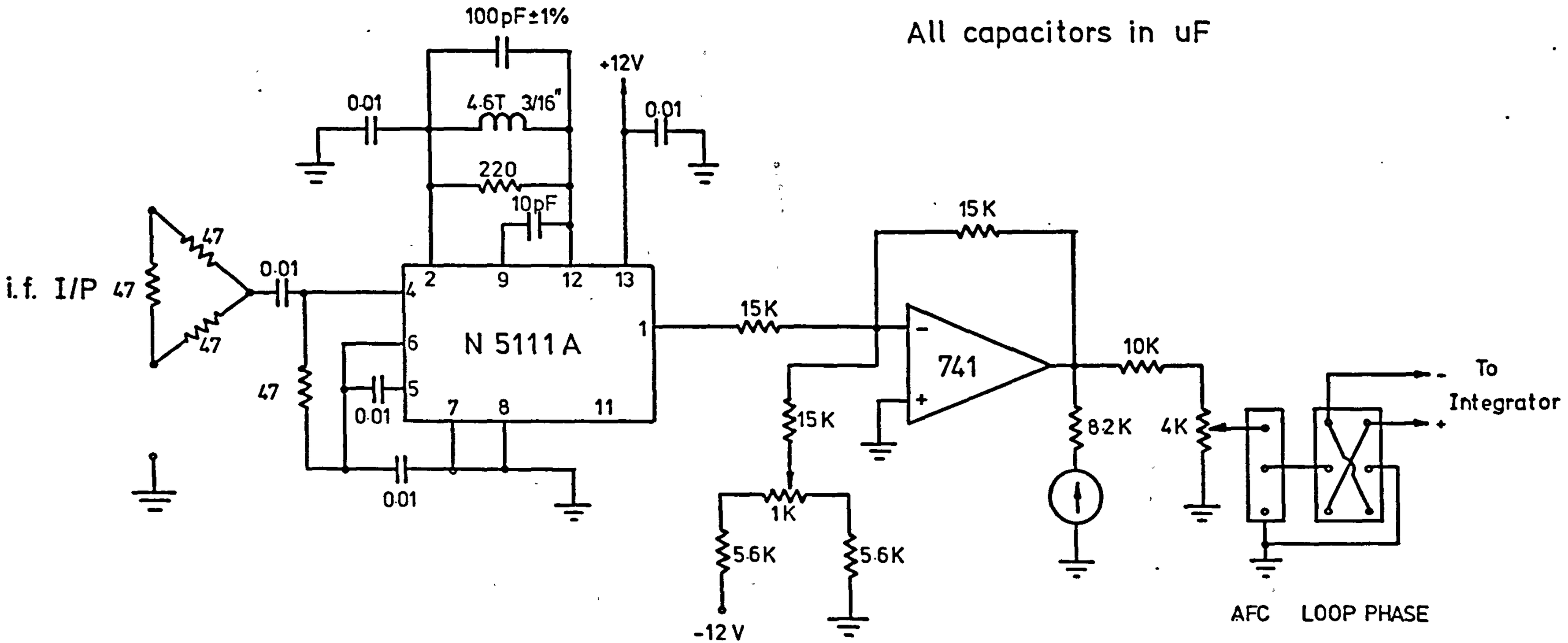

Discriminator

Zero setting amp.

Fig. 3.6a Automatic control of frequency (part 1)

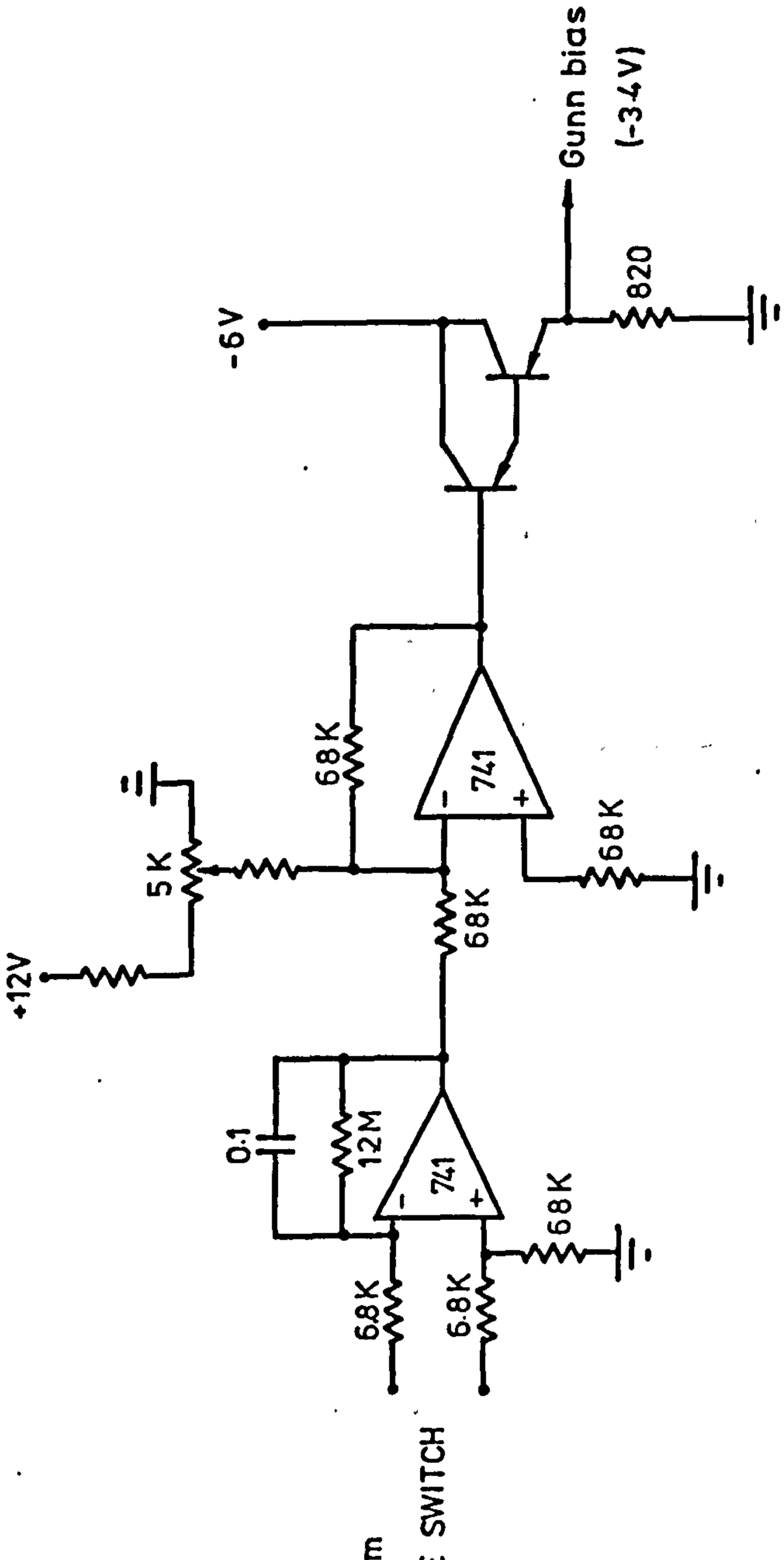

Fig.3.6b Automatic frequency control circuit (part 2)

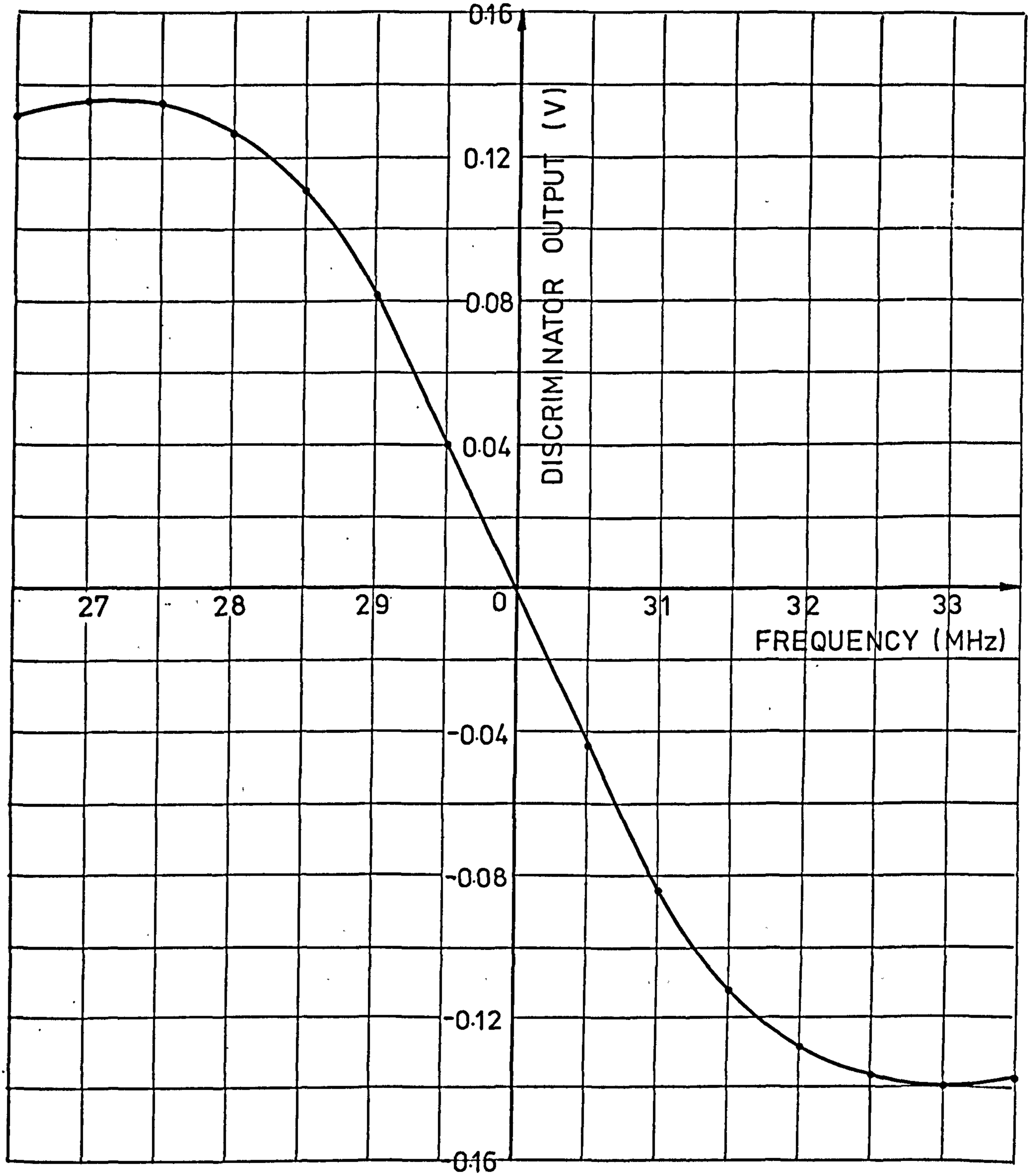

Fig. 3.7 Discriminator characteristics

bandwidth of 15 MHz.

The 30 MHz intermediate frequency signal is fed via coaxial cables into the second unit situated in the laboratory. The amplitude of the signal variation is obtained using a wideband efficient envelope detector. The circuit and characteristics of which is shown in Figure 3.8.

3.1.5 Detection of amplitude variations

The perturbation of the transmitted signal through the atmospheric medium can be represented as a random modulation g(t) of the carrier amplitude A_o. Under these conditions, the received amplitude can be written as

$$A_c\left[1 + g(t)\right] \qquad 3.1.5.1$$

The microwave signal frequency ω_c is reduced to the intermediate frequency $(\omega_c - \omega_o)$ by mixing it with the local oscillator frequency ω_o through the balanced mixer. Consider the local oscillator signal $A_o \cos \omega_o t$, then the output from the balanced mixer is given by

$$\left\{A_c\left[1 + g(t)\right]\cos \omega_c t\right\}\cdot\left\{A_o \cos \omega_o t\right\}$$

$$= \frac{A_c A_o}{2}\left[1 + g(t)\right]\left\{\cos (\omega_c - \omega_o)t + \cos (\omega_c + \omega_o)t\right\} \qquad 3.1.5.2$$

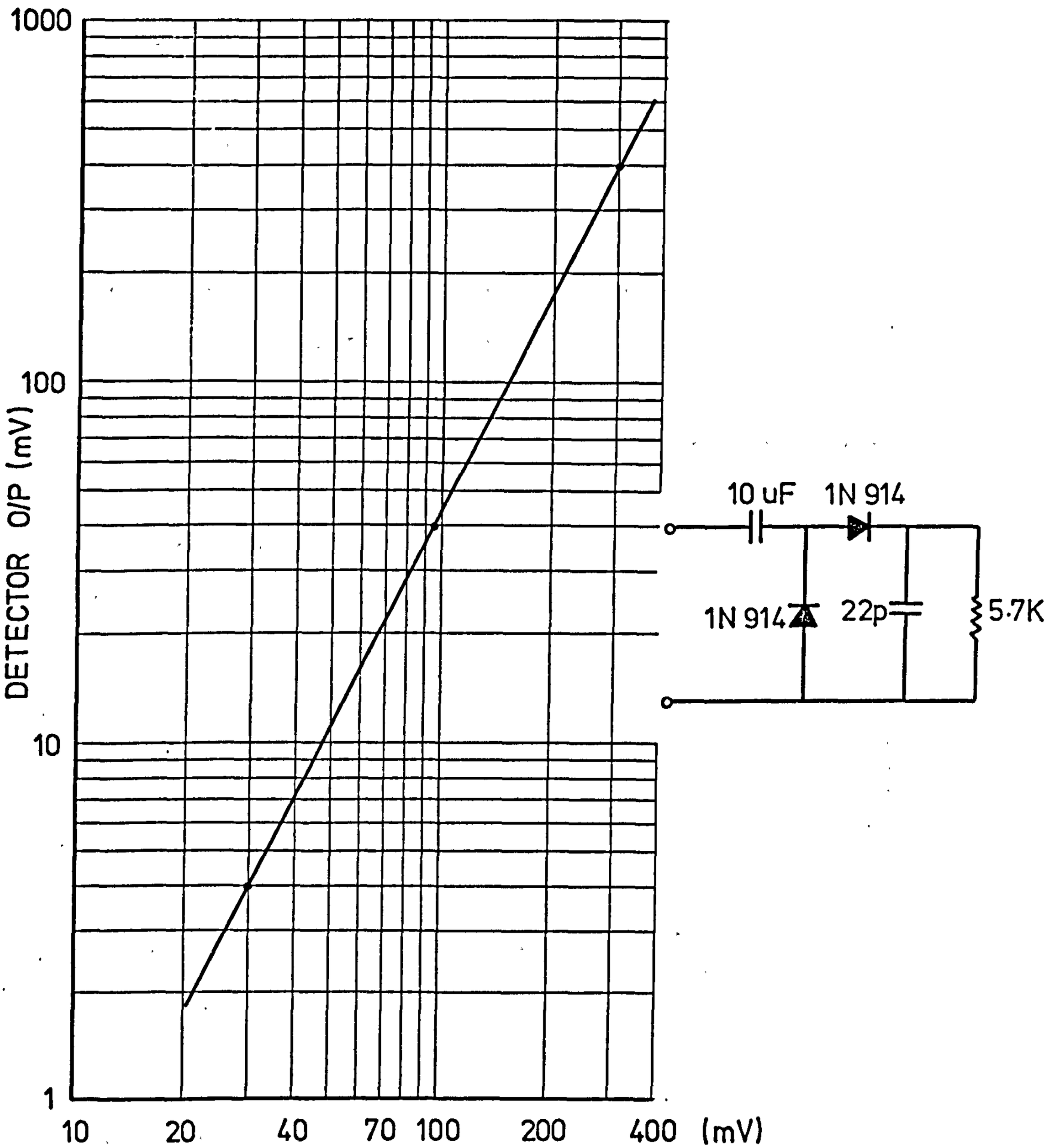

Fig. 3.8 Detector characteristics

The intermediate frequency amplifier acts as a band pass filter to eliminate the higher frequency component $(\omega_c + \omega_o)$. Thus the output from the intermediate frequency amplifier is

$$\frac{A_c A_o A}{2}\left[1 + g(t)\right]\cos(\omega_c - \omega_o)t \qquad 3.1.5.3$$

where A is the gain of the amplifier, and this output is the input to the envelope detector.

The analysis of the detector of Figure 3.8 can be carried out very simply by approximating the diode as a piece-wise linear device with switching occurring at the carrier frequency rate. Thus the output may be written as

$$\left\{\frac{A_c A_o A}{2}\left[1 + g(t)\right]\cos(\omega_c - \omega_o)t\right\}\cdot S(t) \qquad 3.1.5.4$$

with S(t), a switching function defined as

$$S(t) = b \qquad \text{for } -\tfrac{1}{4}T < t < \tfrac{T}{4} \quad \frac{2\pi}{(\omega_c - \omega_o)} = T$$

$$3.1.5.5$$

$$S(t) = 0 \qquad \text{for } t \text{ elsewhere}$$

and repeating at multiples of $T = \frac{2\pi}{(\omega_c - \omega_o)}$ seconds. S(t) is thus a periodic square switching function as shown in Figure 3.9 which may be expanded in its Fourier representation as

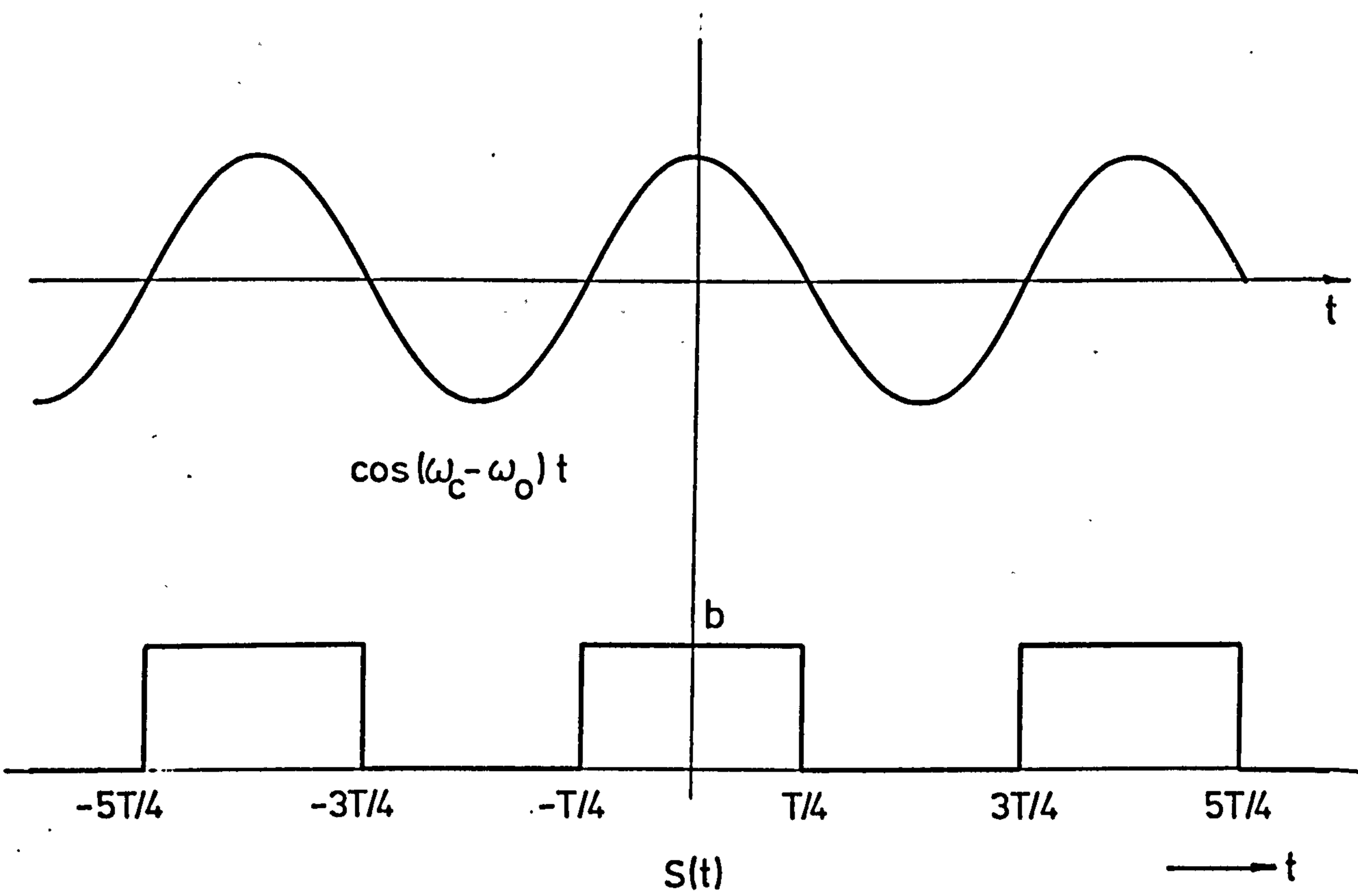

Fig. 3.9 Switching function

$$S(t) = b\left[\frac{1}{2} + \sum_{n=1}^{\infty} \frac{\sin\frac{n\pi}{2}}{\frac{n\pi}{2}} \cos n(\omega_c - \omega_o)t\right] \qquad 3.1.5.6$$

Substituting Equation 3.1.5.6 into Equation 3.1.5.4 and expanding, we get

$$\frac{A_c A_o A \cdot b}{2}\left\{\frac{1}{2}\left[1 + g(t)\right]\cos(\omega_c - \omega_o)t + \frac{1}{\pi}\left[1 + g(t)\right]\cdot\right.$$

$$\left[1 + \cos 2(\omega_c - \omega_o)t\right] + \left[1 + g(t)\right]\cdot$$

$$\left.\left[\sum_{n=1}^{\infty} \frac{\sin\frac{n\pi}{2}}{\frac{n\pi}{2}} \cos n(\omega_c - \omega_o)t\right]\right\} \qquad 3.1.5.7$$

It can be seen that the output from the detector contains a component proportional to g(t) and a d.c. level proportional to the amplitude of the carrier wave plus higher frequency terms (sum and difference frequencies of carrier and the random modulation g(t)).

The capacitor of Figure 3.8 serves to filter out these higher frequency terms. In our case, the cut-off frequency of the filter section is 1.27 MHz, so that the detector output contains only the components corresponding to the amplitude fluctuations and the mean level of the unperturbed level of the transmitted signal.

3.1.6 Noise in the receiver system

Since the bandwidths of both the pre-amplifier and the main amplifier are 15 MHz, therefore the thermal noise generated in the receiver is given by

$$P_{noise} = K \cdot T \cdot B \quad \text{watts} \qquad 3.1.6.1$$

where K is the Boltzman's constant = 1.38×10^{-23}

T is the absolute temperature in Kelvin

B is the bandwidth of the system in Hz.

Taking the normal temperature to be $20^{o}C$ ($293^{o}K$), the noise power is given by Equation 3.1.6.1 to be 6.05×10^{-14} watt. The received power at the receiving system was evaluated in Section 3.1.1 to be 3.1024×10^{-7} watt which after subtraction of 2.5 dB attenuation of the connecting waveguide will give a power value of 1.745×10^{-7} watt at the mixer input. Therefore the ratio of the signal to the noise power generated by the receiver system is 64 dB. Since the noise level is 64 dB below the nominal level (0 dB) of the signal and the weakest fluctuation measured in practice is of the order of 0.01 dB about the 0 dB level, thus, from this figure, we can see that even very small fluctuations of the received signal are not significantly disturbed by the presence of the noise in the receiving system.

3.2 The 110 GHz link (Mavrokoukoulakis 1977)

The transmitter is a CW klystron coupled directly onto the transmitting aerial which is a 45 cm parabolic dish with a

beam width of about 1.5°. The whole transmitter, including the aerial, is enclosed in a white box made from abestolux. A polystyrene foam window is situated in front of the aerial to prevent it being wetted by rain. The attenuation caused by the polystyrene is estimated to be of the order of 1 dB. The box also contains the klystron power supply and a heating and ventilation system to keep the temperature of the transmitter as constant as possible to reduce frequency drift and variation in the output power of the klystron.

The receiver is the heterodyne type using an harmonic mixer and a 55 GHz klystron as local oscillator. The construction of the receiver enclosure is the same as the transmitter. The received signal passes through a precision calibrated attenuator which is used for calibration purposes. The signal is amplitude modulated by a 1 KHz square wave. The amplitude of the modulating signal depends on the level of the signal and is achieved by means of a low noise amplifier and a phase sensitive detector loop. The signal from the local oscillator is mixed with the received signal and produces an output at 60 MHz. A wide band amplifier (d.c. to 200 MHz) is used to amplify the 60 MHz signal which is then detected at the receiver. The detected signal is linked to the laboratory via a sealed cable and recorded on chart recorders and paper tape. Figure 3.10 shows the block diagram of the receiver system.

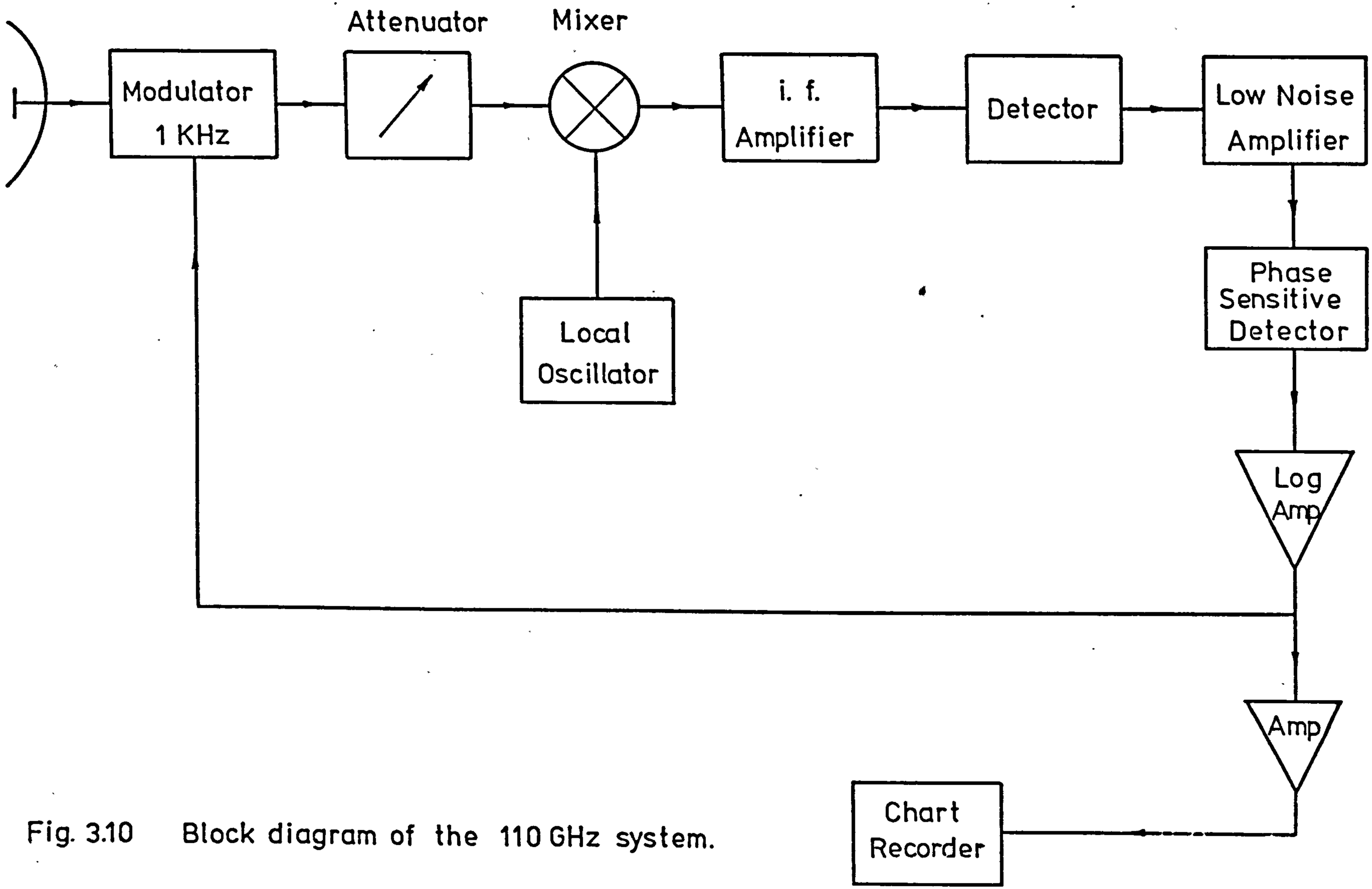

Fig. 3.10 Block diagram of the 110 GHz system.

PART II METEOROLOGICAL INSTRUMENTATION

In order to supplement the propagation measurements, measurements of the temperature, humidity, wind speed , wind direction, refractivity and rainfall rate are essential. The following gives a brief description of the sensors used to measure these parameters.

3.3.1 The thermometer

The sensor of the thermometer consists of a platinum resistance wire sensor wound non-inductively on a plastic former. Two versions of the thermometers were built; one using 25μm dia. platinum wire; the other using 10μm diameter wire. The construction of the first version was based on the design of the Meteorological Research Unit at Cardington. This version of thermometers has a frequency response of 15 Hz which is limited by the thickness and length (180 cm) of the platinum wire. The second version of the thermometer was designed at U.C.L. It uses a shorter length (30 cm) of 10μm diameter platinum wire which produces a response above 30 Hz.

The complete thermometer consists of the sensor and a bridge amplifier. The sensor forms one arm of the bridge. It can be shown that the sensitivity of the bridge amplifier (i.e. the output from the bridge circuit) depends on two parameters, namely, the voltage applied to the bridge and the ratio of the

resistance of the sensor to the resistances in the other arms. The higher the applied voltage, the higher the bridge output, thus the greater the sensitivity. Also the smaller the ratio of the resistances of the arms, the higher the resolution. However, too high a d.c. voltage applied to the bridge will cause the resistors to heat and thus change their resistance. An applied voltage of 6 volts was found to be satisfactory. The best resolution is obtained when the ratio of the resistances of the arms is approximately unity. It should also be pointed out that the output voltage from the bridge is only linear over a certain range of resistance change of the sensor. However, calibration of the thermometers shows that a linear output of 0.4729 volt/^{o}C can be obtained over a range of -7^{o}C to 40^{o}C. The complete electronic circuit is given in Figure 3.11.

The sensors were calibrated against a mercury thermometer having divisions in steps of 0.1^{o}C. The sensor and the mercury thermometer were immersed in white spirit which was varied in temperature by means of a heating element in the liquid. Care was taken to keep the white spirit continually stirred. The resistance of the sensor at different temperature was measured by a very accurate ohmmeter (accuracy 0.1 ohm). Thus a resistance versus temperature curve for the sensor was obtained.

The bridge amplifier was calibrated by means of standard resistances instead of the sensor directly. An output voltage to resistance curve was plotted.

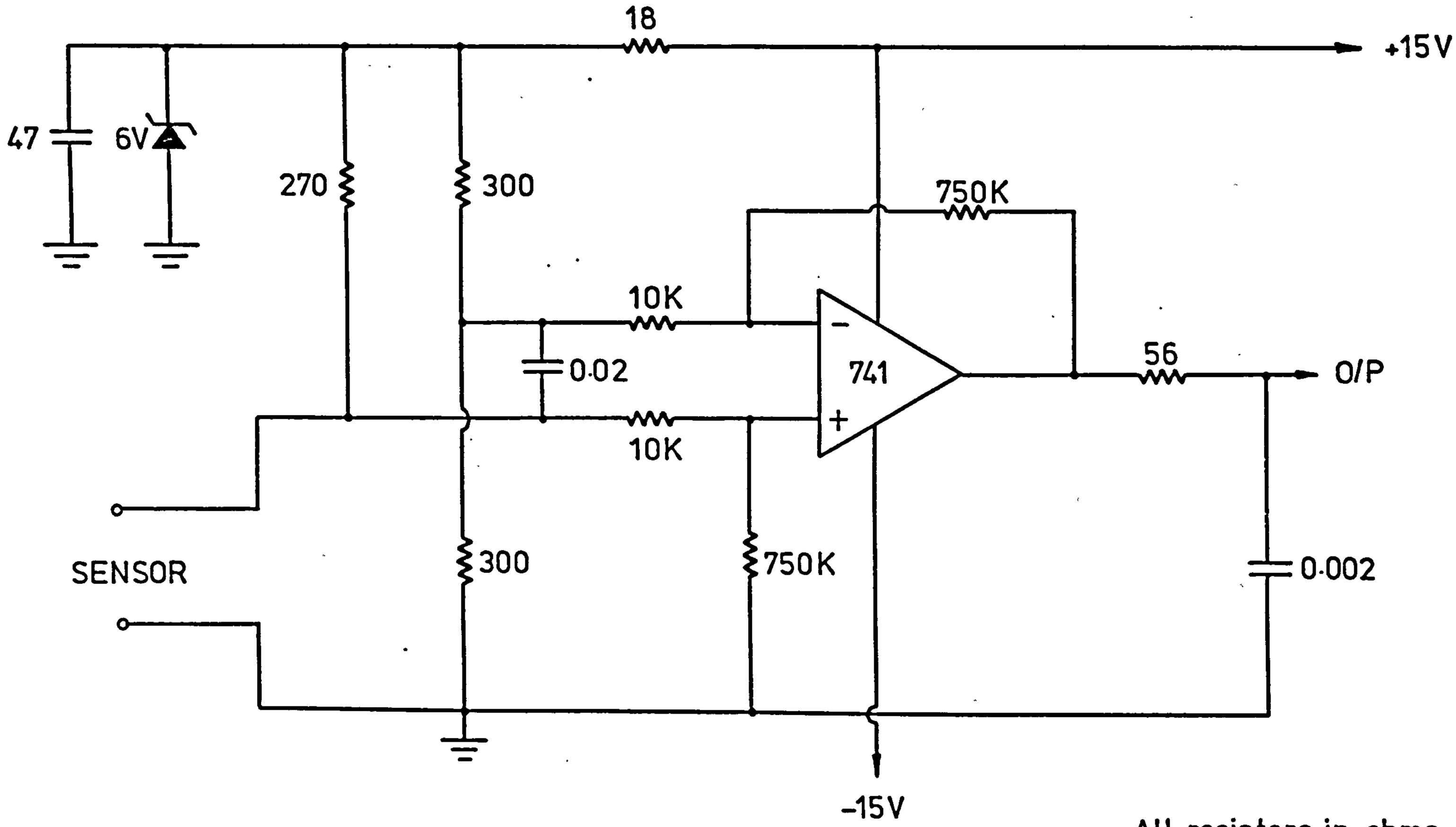

All resistors in ohms

All capacitors in uF

Fig. 3.11 Temperature head amplifier

In the construction of the sensors care has been taken to make the sensors as identical as possible and in practice, the largest difference between two sensors is less than 0.1 of an ohm.

These temperature sensors can also be used to measure the differential temperature between two points separated some distance in space. The principle is basically the same. Two identical sensors are connected to two arms of a differential amplifier which gives an output of 0.622 volt/degree C difference directly proportional to the difference in temperature. The circuit employed for this differential measurement is given in Appendix 3.2

3.3.2 Wind-rotating temperature sensor mount

Whenever any temperature measurements were made the sensors were mounted on a wind-rotating device as shown in Figure 3.12 which can rotate freely, being guided by the wind vane, so that the sensors are always facing the direction of the wind. This device was developed at U.C.L. Three sensors can be mounted on it; two for measurement of differential temperature and one for measurement of absolute temperature. The separation between two sensors for differential measurements is adjustable within the range from 3 cm to 30 cm. Such a range is well within the inertial subrange of the turbulence spectrum. In order to avoid any noise problem, the amplifiers are placed as close to the sensors as possible. These amplifiers are mounted on either

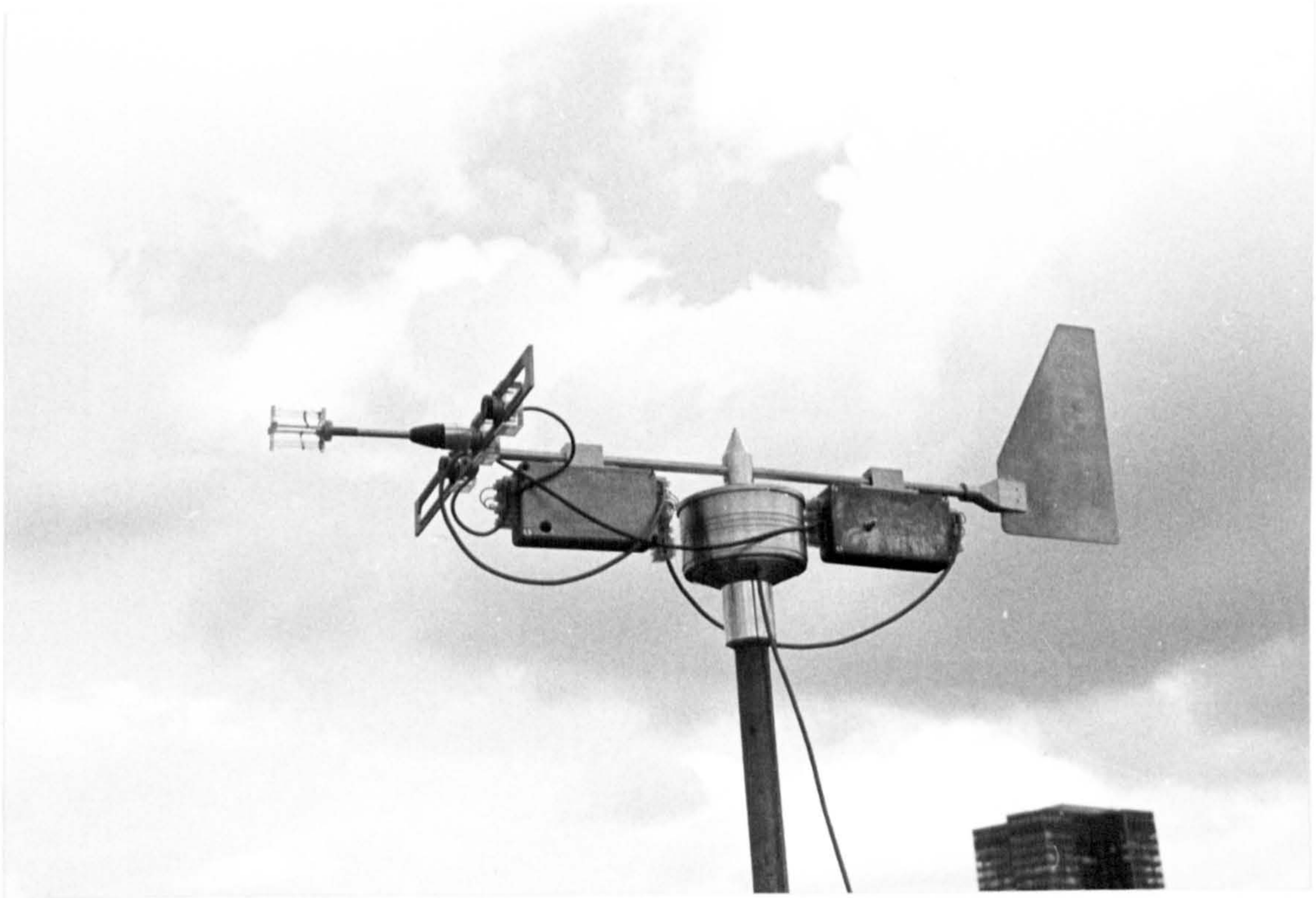

Figure 3.12 Temperature sensor on the wind rotating mount

side of the pilot point of the device so as to produce weight balance of the device. The output from the amplifiers as well as the power supply leads are connected through rotating contacts so that no wiring can hinder the free movement of the device. The signals are brought down to the laboratory through screened cables.

3.3.3 The relative humidity sensor

The sensor (the humicap) used is a commerical product which is based on the capacitance change in a thin film capacitor with a polymer dielectric. The sensor capacitance is nearly a linear function of the relative humidity with a very small temperature effect. The sensor capacitance is used to control the frequency of a multivibrator which has a nominal frequency of about 500 KHz. The two outputs from the multivibrator are compared by a differential amplifier with an offset facility. The amplifier gives a d.c. output which is a function of the relative humidity. A separate regulated supply is used for the oscillator to ensure amplitude and frequency stability. The complete electronic circuit diagram and a picture of the device are given in Figures 3.13 and 3.14.

The typical step response curves of the sensor at room temperature is shown in Figure 3.15. The first step of absorption occurs in less than one second. The time constant and amplitude of the second step are very dependent on the polymer material used. Usually, the second step is only a few percent of the total response.

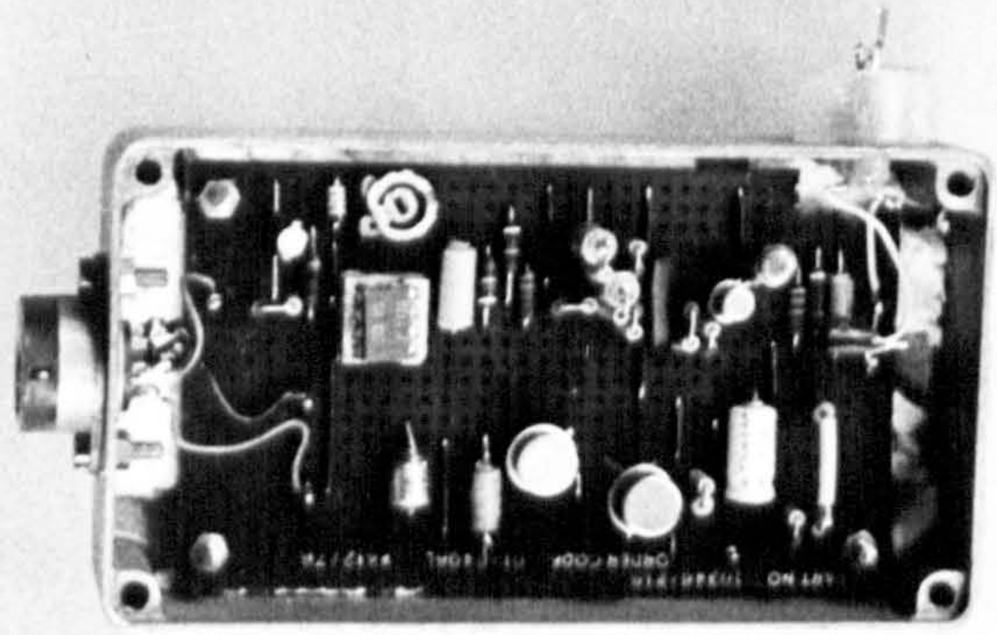

Figure 3.13 The relative humidity measuring device

BFY 50

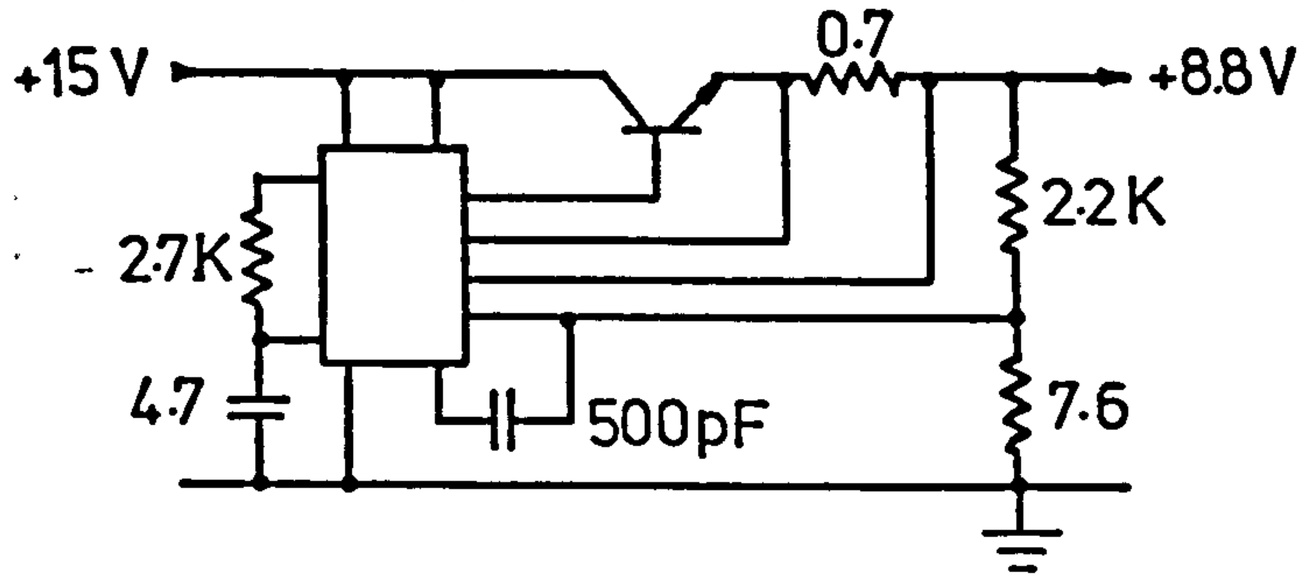

All resistors in ohms

All capacitors in uF

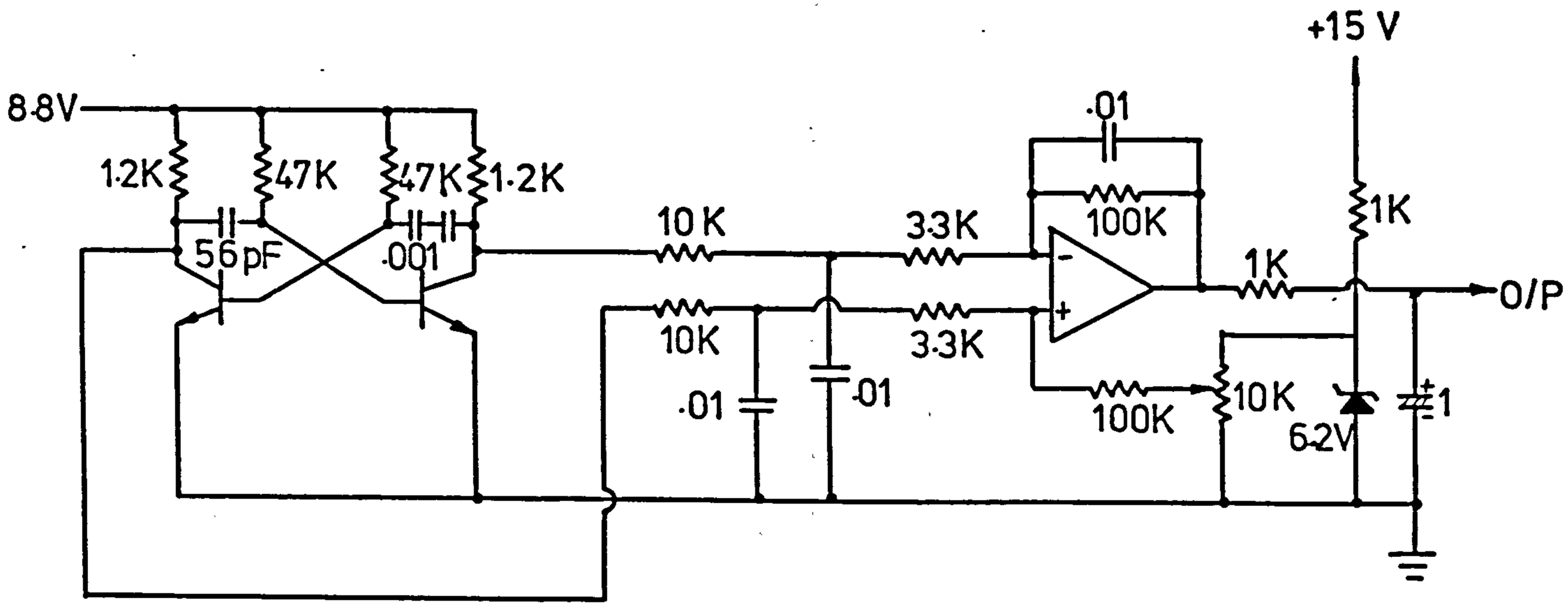

BSX 20 ×2

Fig. 3.14 Humidity device circuit

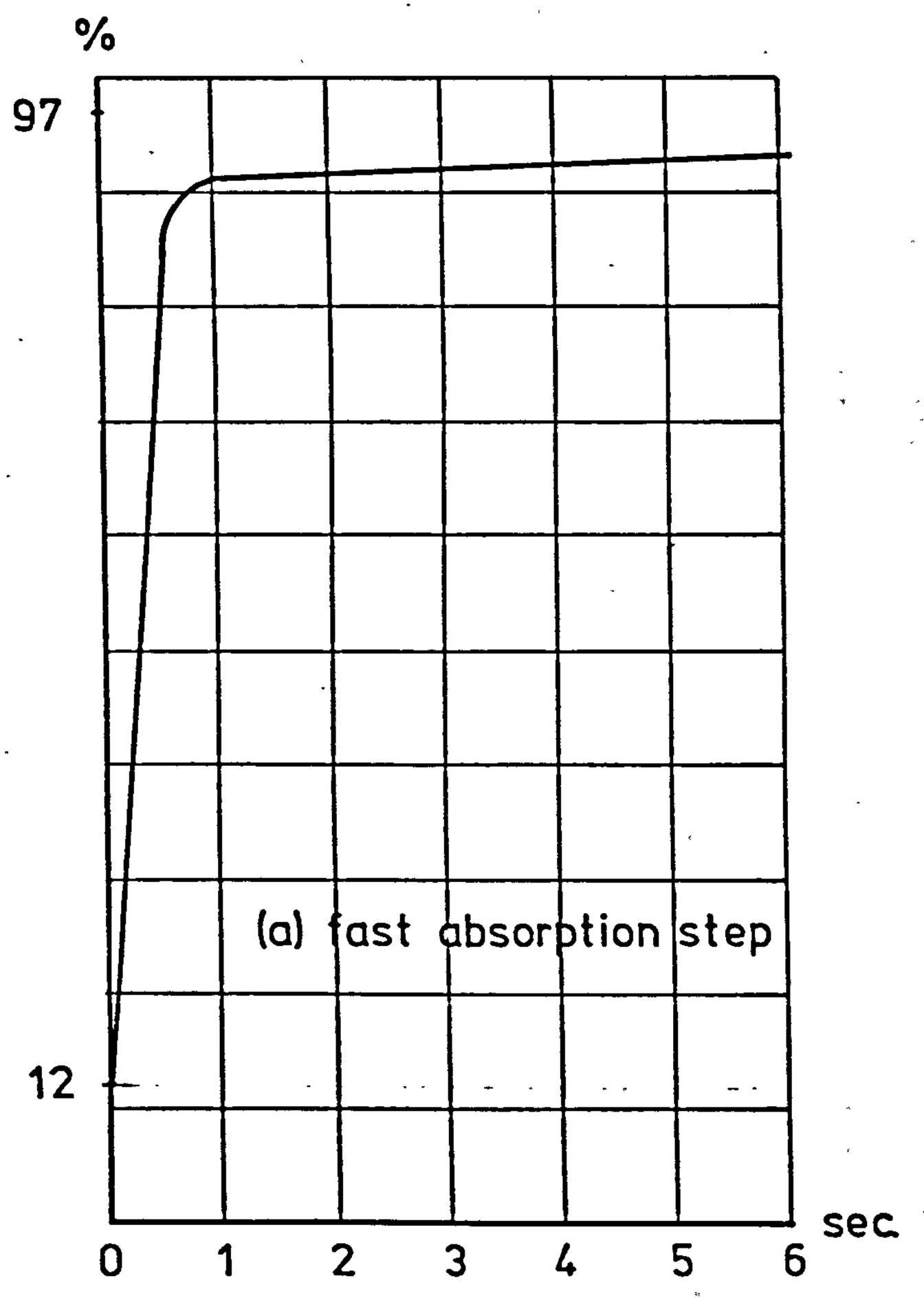

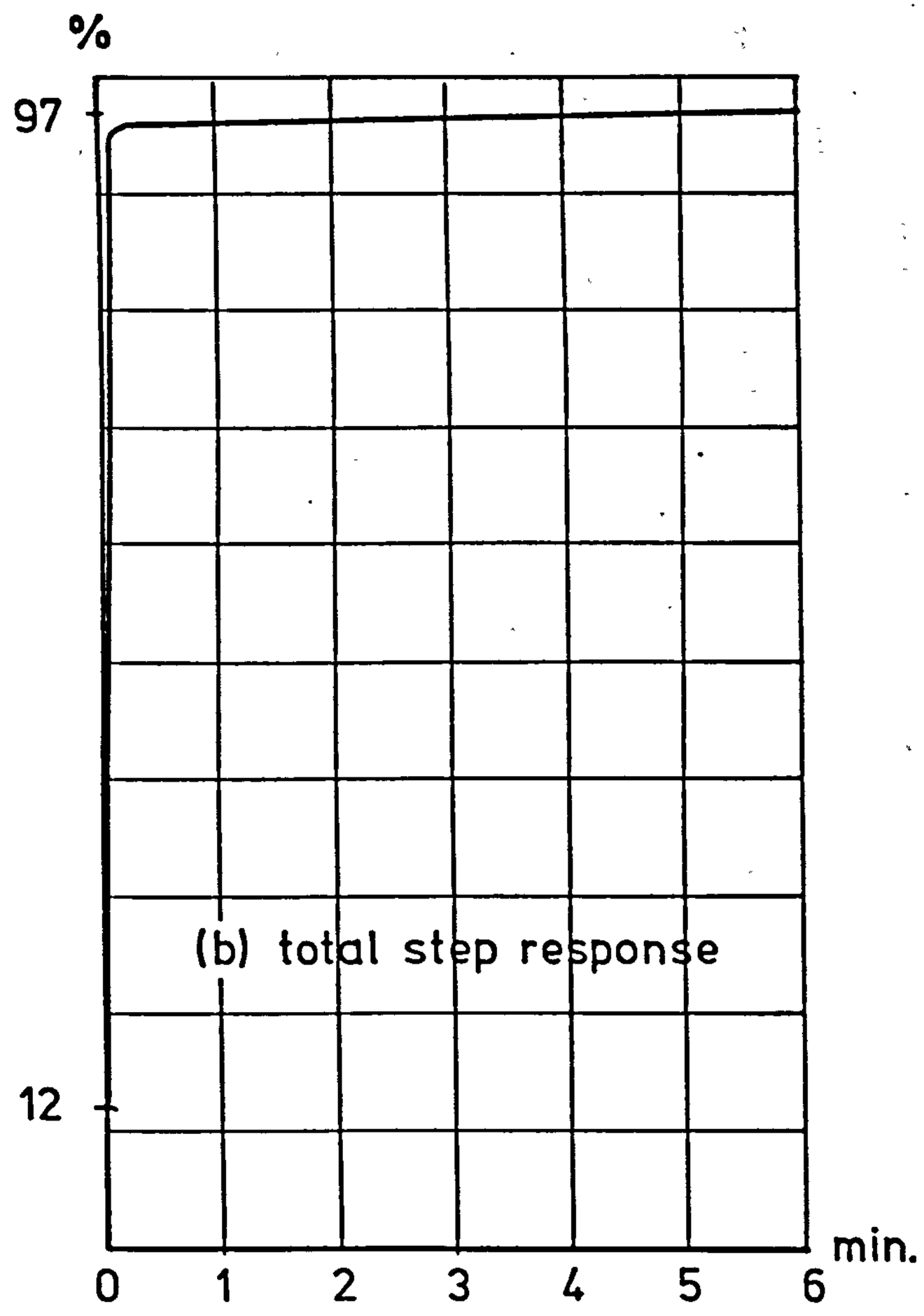

Fig.3.15 Step response of sensor from 12% to 97% at room temperature

However, the response time of the sensor is strongly dependent on temperature as indicated in Figure 3.16. At $0^{o}C$ the response time for 90% of the total response from 12% to 97% R.H. is about 4 seconds while at $30^{o}C$, it is only 0.2 second. Since, under normal condition, the humidity of the atmosphere can never change from 12% to 97% in a short period of time, the frequency response of the sensor is expected to be better. A frequency spectrum under a given set of experimental conditions was plotted in Figure 3.17.

3.3.4 Wind speed and wind direction measurements

The wind speed and wind direction measuring devices were both designed at U.C.L. for this experiment. The wind speed probe uses an aneomemeter fitted with a 3-cup metallic rotor which rotates a drum having 16 holes. A light bulb shinning through the holes and a photoelectric transitor (OCP 71) are used to provide 16 pulses per revolution. These pulses are converted to an anologue voltage by a rate-meter located in the laboratory. The circuit of the system is given in Figure 3.18.

The wind direction indicator consists of a low friction 360^{o} potentiometer which provides an electrical output calibrated directly with the wind direction. Zero reading was assigned to the line of the path of the microwave links.

3.3.5 The refractometer

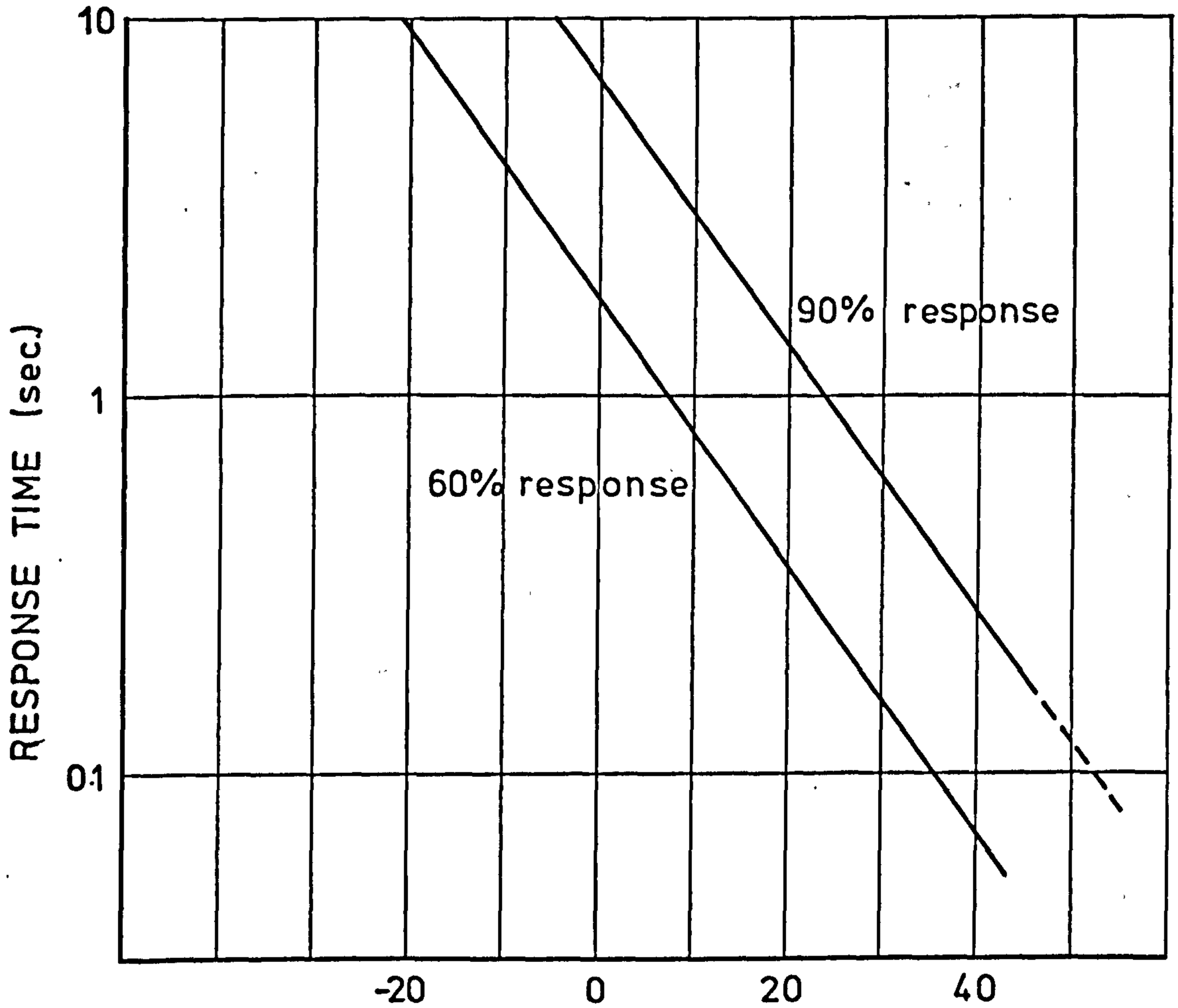

Fig. 3.16 Response time of humidity sensor as a function of temperature

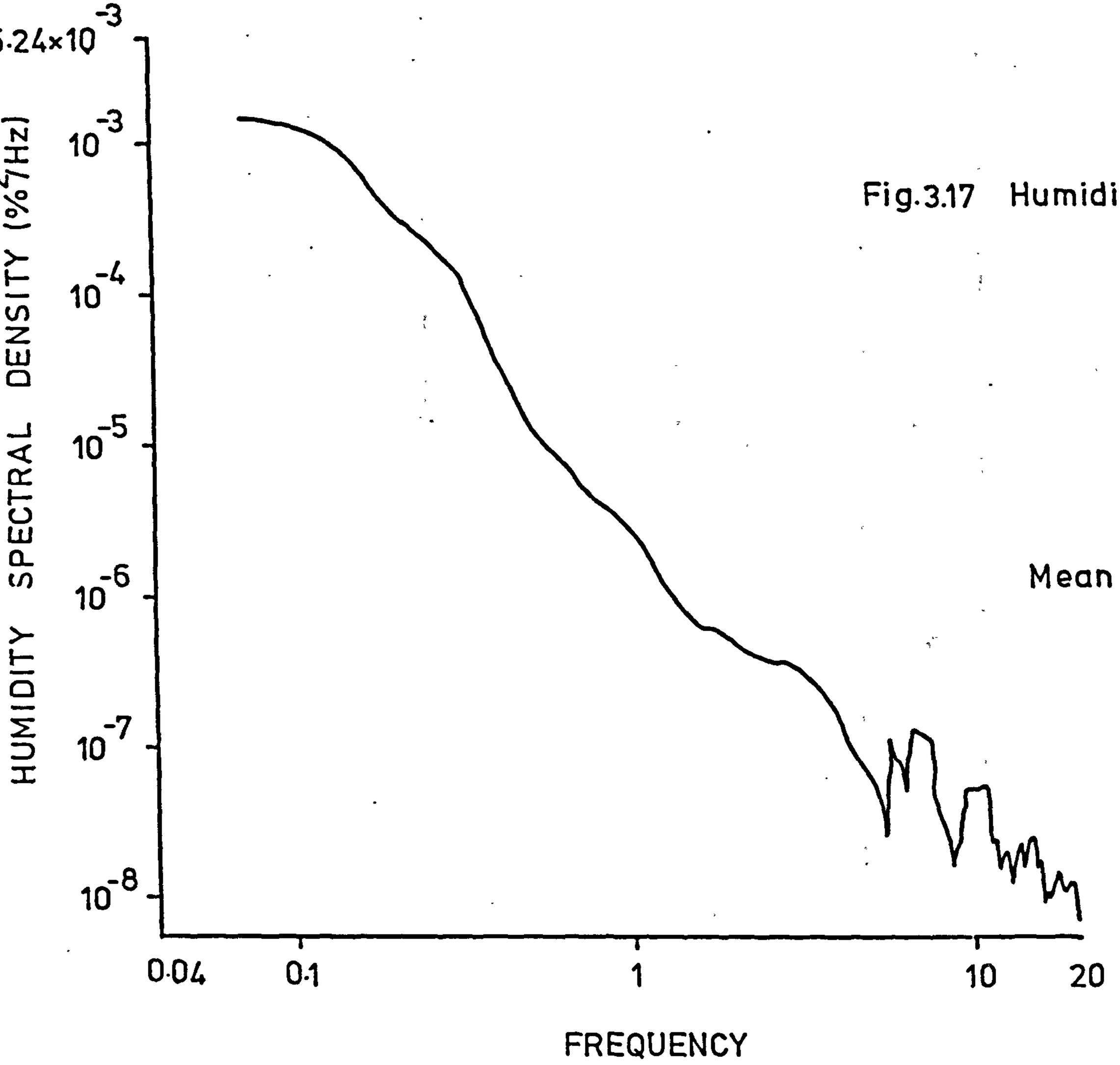

Fig.3.17 Humidity spectrum

All resistors in ohms

All capacitors in uF

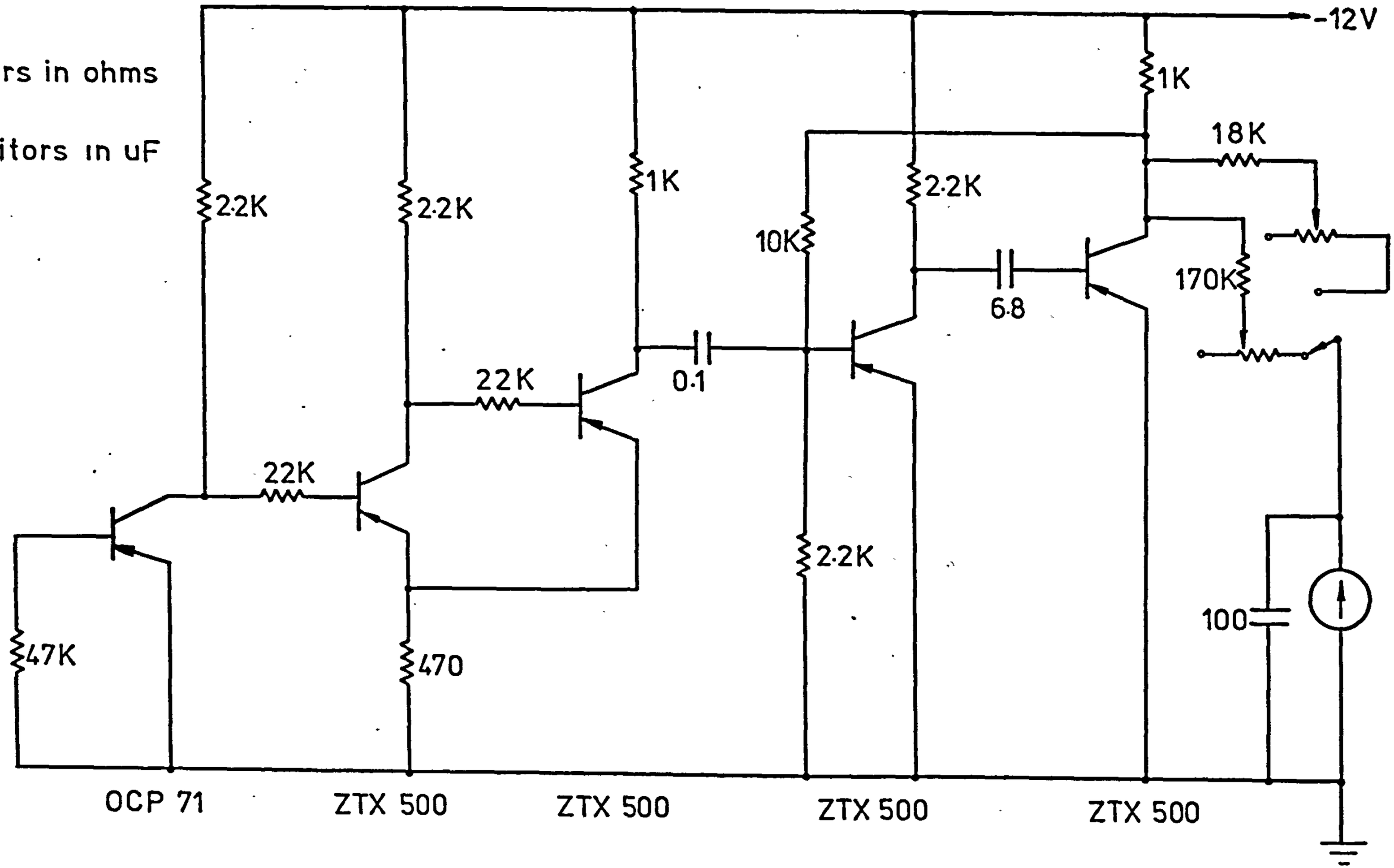

Fig. 3.18 The anemometer head amplifier.

The microwave radio refractometer used was designed and developed in this Department by Chan (1974). It uses the Crain system with the sampling cavity remote from the reference cavity which is at a receiver ground based. Oscillator stability is achieved by the use of modified Pound stabilizing system. The sampling cavity of the refractometer is TE_{011} resonator constructed from a section of metallized silica tube with perforated brass end plates. The choice of these two materials provides a very good thermal compensation for the sampling cavity. The microwave components are constructed in microwave integrated circuits (MIC). The block diagram for the frequency locking system is given in Appendix 3.3.

The receiver is of conventional design but with its local oscillator stabilized by a low temperature coefficient glass reference cavity through the modified Pound stabilizing system. The intermediate frequency is at 30 MHz.

The refractometer operates at a centre frequency of 10.588 GHz and transmits 10 mW of the power. The oscillator has a short term stability of 2.9×10^{-7} and a thermal stability of $6 \times 10^{-7}/^{\circ}C$ over a temperature range of $-15^{\circ}C$ to $30^{\circ}C$. The dynamic range of the refractometer is better than 4 MHz. The stability gives a resolution of about $\pm$ 0.06 N units.

A picture of the refractometer mounted on a freely rotation disc is shown in Figure 3.19.

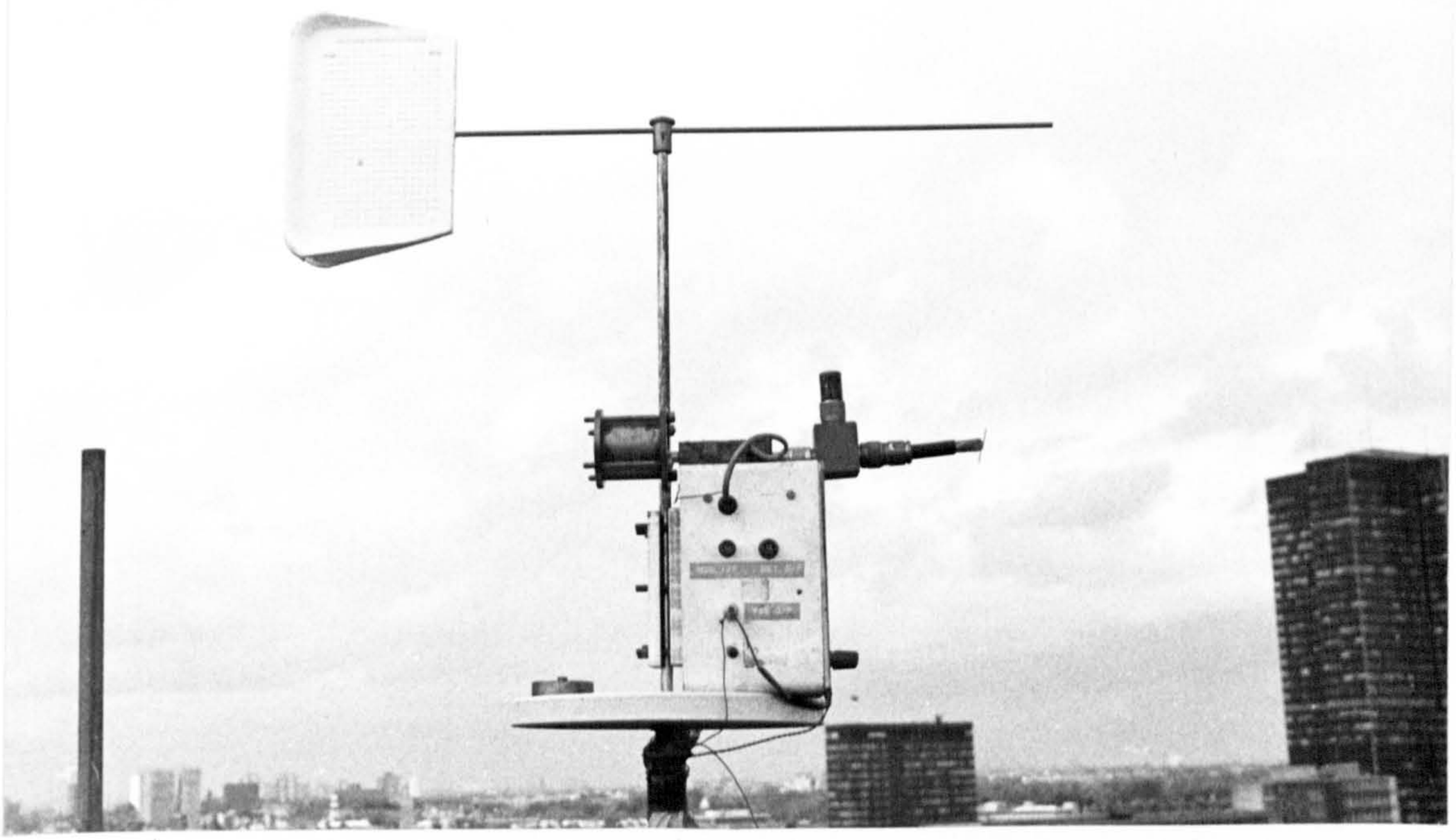

Figure 3.19 The refractometer on the freely rotating disc

The response time of the device relies on the flushing time of the volume of air through the sampling cavity which again depends on the wind speed. When in operation, the axis of the sampling cavity is always aligned in the same direction as the wind thus giving a flushing time T

$$T = \frac{l'}{\overline{V}} \qquad 3.2.4.1$$

where l' is the length of the cavity and $\overline{V}$ is the wind speed.

Figure 3.20 gives an estimated plot of the frequency response of the refractometer as a function of the wind speed. From this, it can be seen that the device gives a fairly high frequency response even under low wind condition. A typical spectrum of the refractivity showing response of the device under light wind condition (approx. 1m/s) is given in Figure 3.21.

3.3.6 The raingauge

This is an electronic raingauge for measuring rainfall over twenty second periods and uses the Met. Office Mk IV rain collector. The rain collected is channelled into a brass block which contains a filter, a reservoir and a stainless steel tube with a 2mm bore. The reservoir is maintained full and when water enters the collector, the reservoir overflows via the tube and drops of a standard size, dependent upon the bore of the tube, are formed. These drops are counted when they interrupt light from a light emitting diode shinning on a photo-transitor.

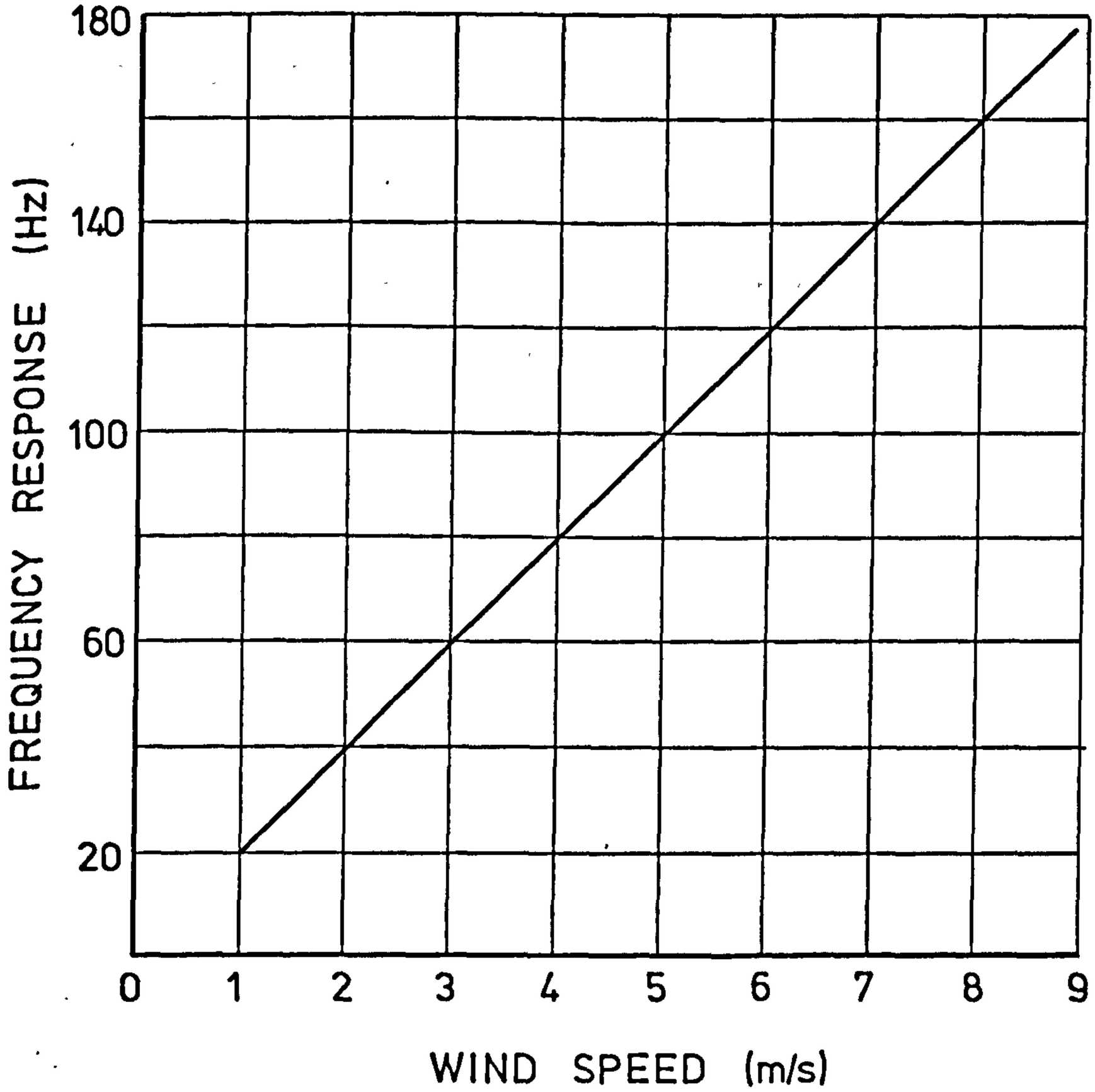

Fig. 3.20 Frequency response of the refractometer

The electronic circuit was originally designed by the Appleton Laboratory and was modified in this Department (Poskitt 1974). Further modification in the electronic circuit has been made for this experiment to increase the reliability of the raingauge. A block diagram of the system is shown in Appendix 3.4. The circuit contains a master clock which controls all the timing and logic of the system. The raingauge automatically prints out the time it starts raining and the number of drops in 20 second periods. In order to save paper tape and power, the gauge only operates when it rains. The number of drops are converted to rainfall rate in mm/hr. by means of a calibration curve.

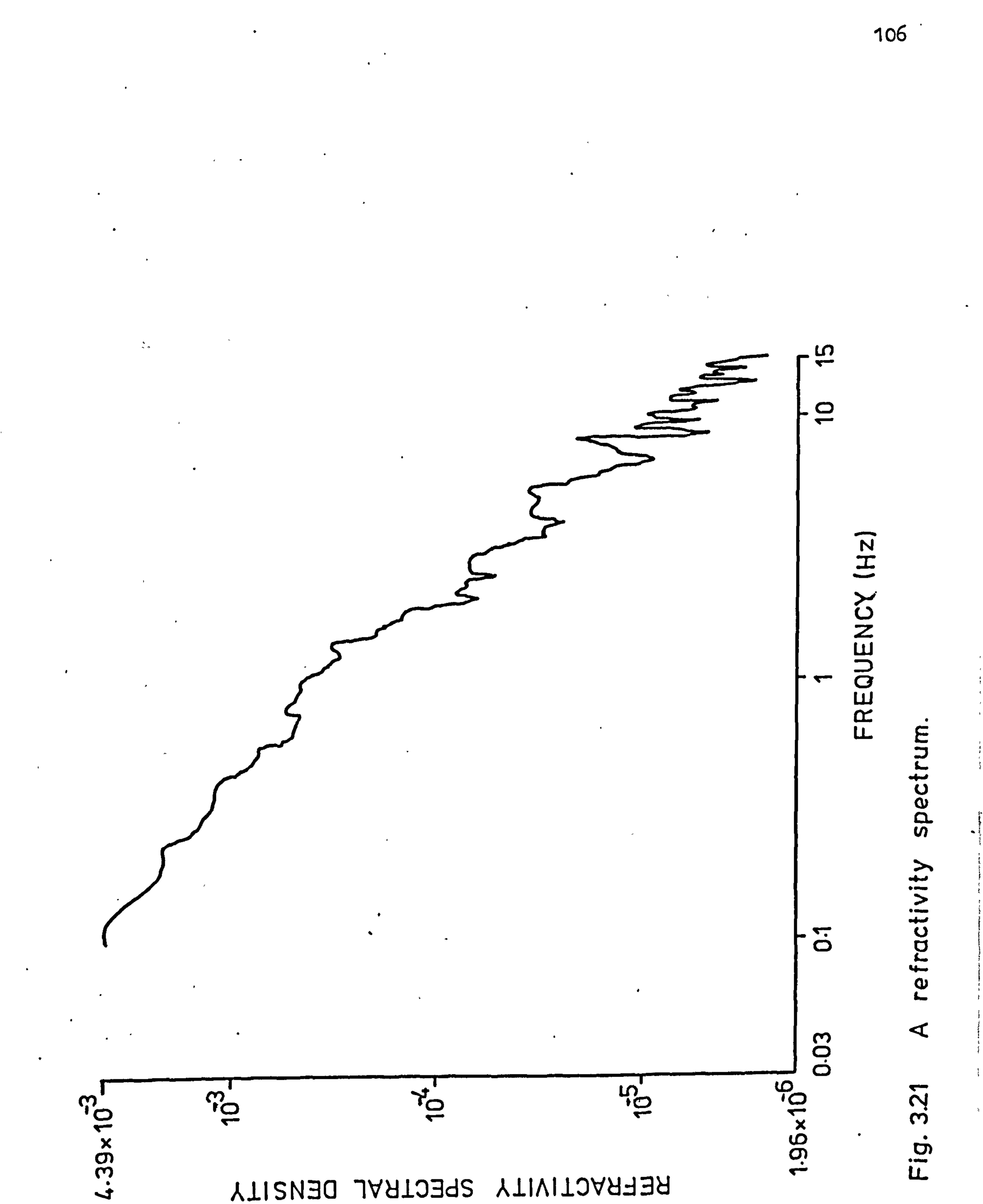

Fig. 3.21 A refractivity spectrum.

CHAPTER 4 DATA RECORDING AND PROCESSING

This chapter describes the method and the equipment used to record the data on magnetic tape; the problems due to noise introduced by the magnetic tape recorder, the method of overcoming this and the processing of the data. Some basic theory in sampling and digital filtering and some considerations on power spectral estimation are also described.

4.1 Equipment and analogue output

Pictures of the displaying and recording systems are shown in Figures 4.1a and 4.1b. The system provides visual displays of the amplitude fluctuations and the long term fading by means of the chart recorders 1 and 2. Chart recorder 1 displays the fluctuations of the signal whereas chart recorder 2 also shows the long term level of the fading. For the convenience of the long term statistics study, the signal level is also punched onto paper tape. Selected interesting phenomena in signal scintillations are recorded on magnetic tape for quantitive analysis.

The outputs from the temperature, humidity and wind speed sensors are also in analogue form. As well as being displayed directly on chart recorders, they can also be recorded directly on magnetic tape. The output of the refractometer is

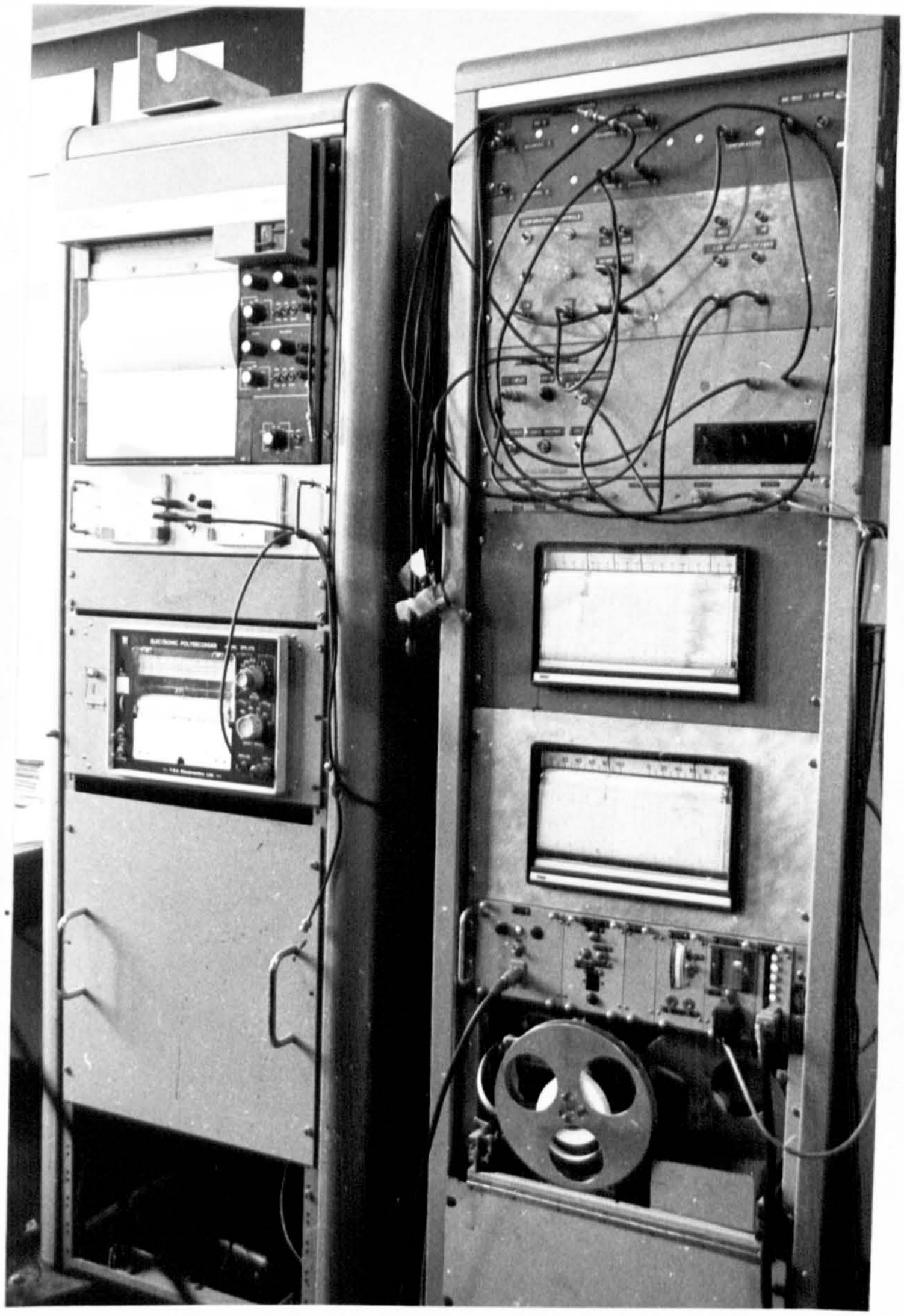

Figure 4.1a Display and amplifier system situated in the laboratory

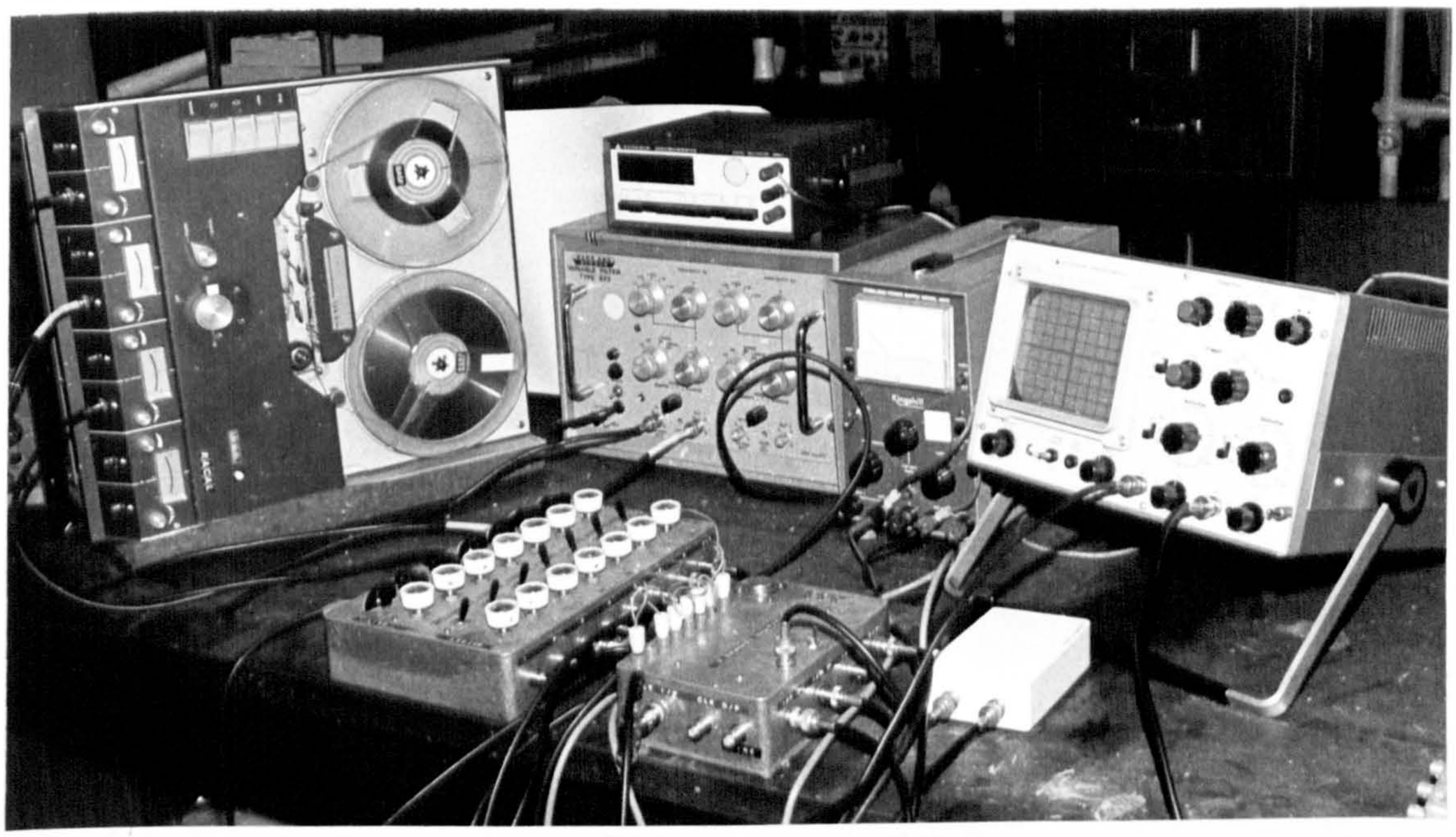

Figure 4.1b The recording system

in terms of frequency changes which need to be converted into an analogue signal voltage before being recorded on magnetic tape. Instead of using a traditional frequency discriminator which has limited linearity and accuracy for small frequency variations, the frequency is counted by a 50 MHz frequency counter and the BCD output of the counter is converted into analogue form by means of a digital to analogue converter which reads only the last three digits of the megahertz frequency, thus giving a quantized step corresponding to about 0.02 N unit (the conversion factor of the refractometer is 52.9 KHz/N unit). The circuit diagram for the device is shown in Figure 4.2 and was developed specifically for this project.

4.2 Recording of data

The tape recorder used is an Racal TDR 3 FM four-channel magnetic tape recorder having a bandwidth extending from d.c. to a frequency dependent upon the recording speed. With a speed of 3-3/4 inch/second, the cut-off frequency is 1250 Hz which is sufficient for the purpose of this experiment.

There are many quantities which need to be monitored, namely, the signals of the 110 and 36 GHz links, the temperature, the differential temperature, the humidity, the wind speed, the wind direction and the refractivity and it is desirable to record all of them in such a way that the time correspondence between

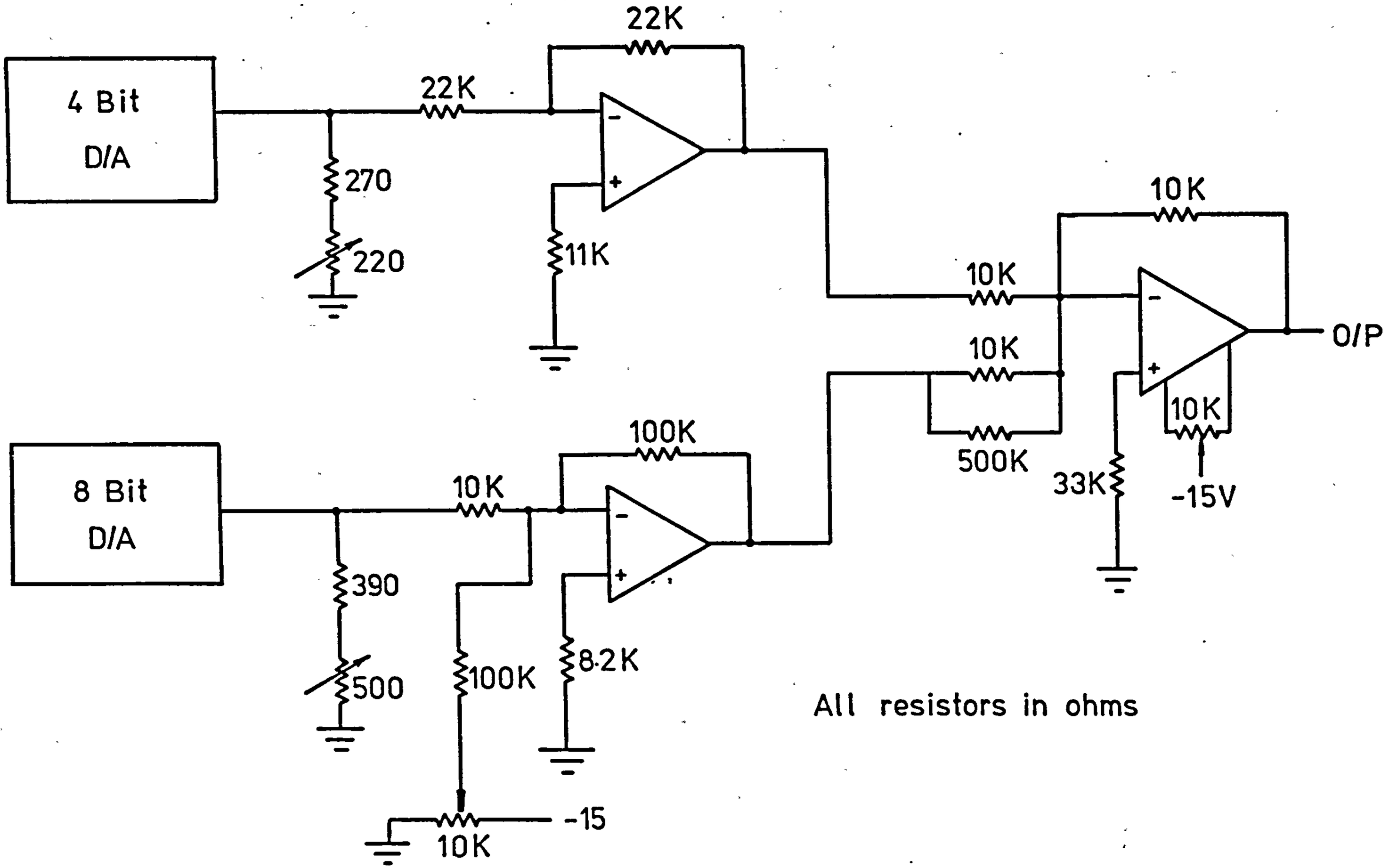

Fig. 4.2 Digital to analogue converter for the refractometer.

these quantities can always be maintained accurately. The simplest method of doing this is to use a tape recorder with sufficient channel inputs. However, the number of channels available in the available tape recorder is limited to four only, thus, the techniques of time multiplexing of the signals is used.

4.2.1 The multiplexing system

The block diagram of the multiplexing system is shown in Figure 4.3. The multiplexer employed is a 8 channel analogue gate the scanning of which is controlled by a logic circuit. The heart of the system is the control pulse which selects the channels. The frequency of the pulses depends on the sampling frequency required. For this experiment, the highest frequency fluctuations of any quantity can be quite safely assumed to be within 20 Hz thus a sampling frequency of 40 Hz for each channel was chosen. This means that the frequency of the train of pulses applied to the multiplexer is 8 x 40 Hz = 320 Hz. This frequency is first generated by a sine wave generator. The wave is passed to a squarer producing square pulses of the same frequency which are used to drive a counter. The logic output of the counter is applied to the multiplexer. The reason for first producing the sine wave is that it can easily be recorded on a track of the magnetic tape. Any change in the speed on replay effects this clock signal thus maintaining absolute sychronization. This wave also serves as the clocking pulse to the computer doing the analysis. A complete circuit diagram of the system is shown in

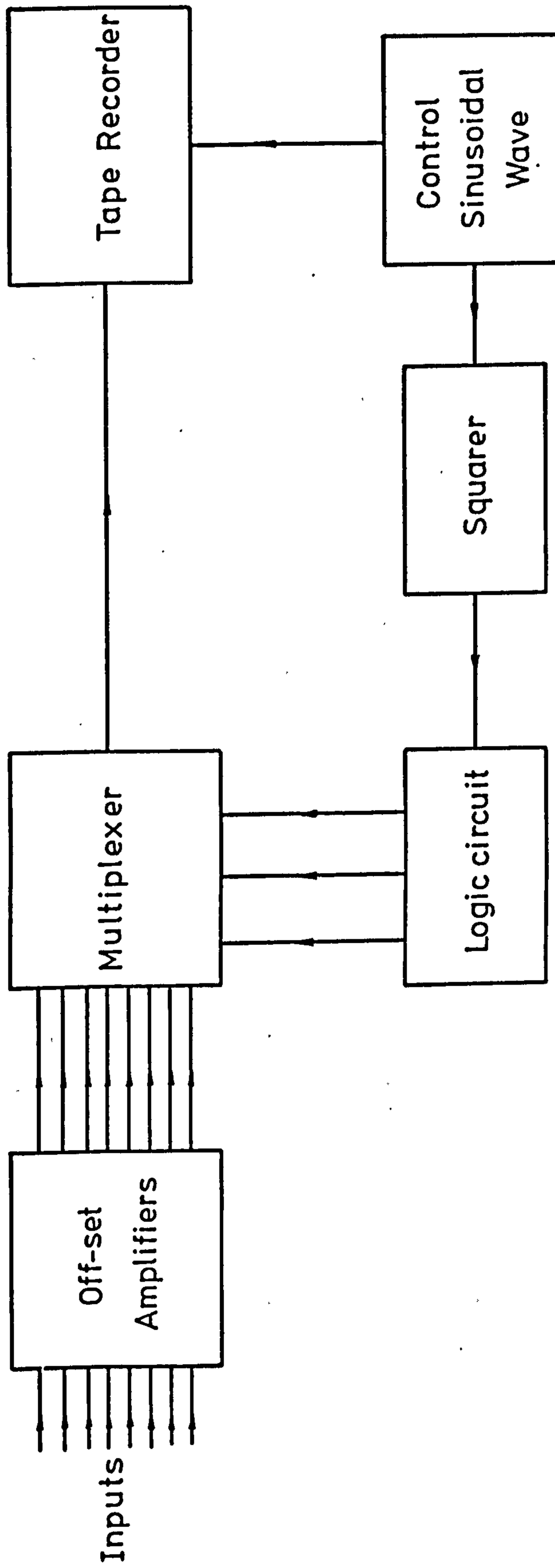

Fig. 4.3 Block diagram of multiplexing system

Figure 4.4a and a typical output from the system is also shown in Figure 4.4b.

Facility is also provided to reduce the sampling frequency on the replay process. This is achieved by using a logic circuit shown in Figure 4.5 which divides the train of control pulses into groups of 8. The separation of successive groups depends on the new sampling frequency.

Normally, the eighth channel output from the multiplexer is set to be a constant d.c. voltage (1.2 volts). This has two uses: it acts as a pilot signal to the computer to distinguish between individual channels and also it provides a means for the sychronization when the sampling frequency is reduced.

4.2.2 Recording procedure

The mean value of each quantity to be recorded is measured and this is substracted from the fluctuating signal by means of a set of off-set amplifiers as shown in Figure 4.6 before inputing to the multiplexing system. The purpose of doing this is to increase the dynamic range of the signal inputs to the tape recorder and thus improve the signal to noise ratio. The absolute values can easily be restored by simply adding a constant voltage to the fluctuating signals in the process of analysis.

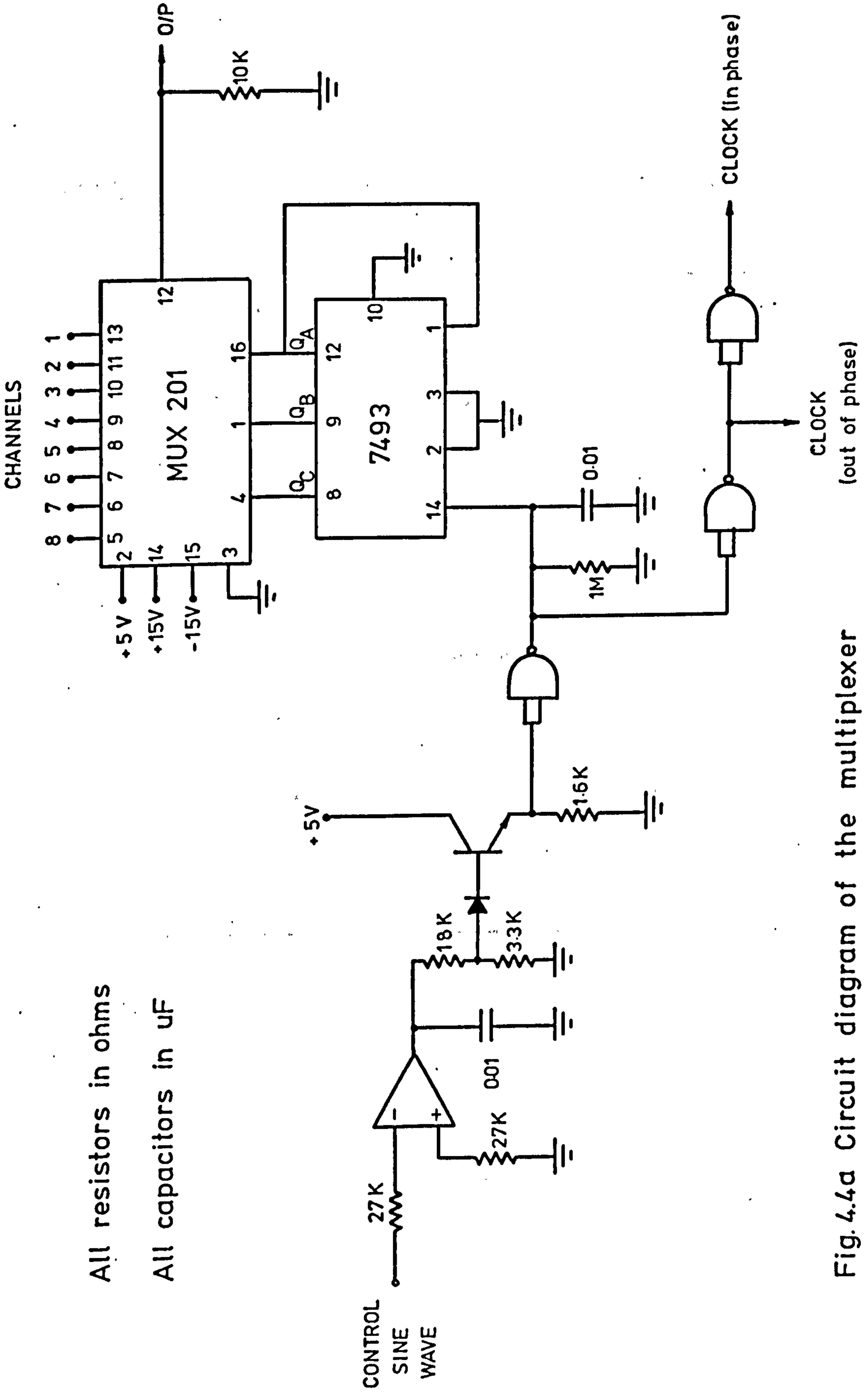

All resistors in ohms

All capacitors in uF

Fig. 4.4a Circuit diagram of the multiplexer

CHANNEL 1 2 3 4 5 6 7 8

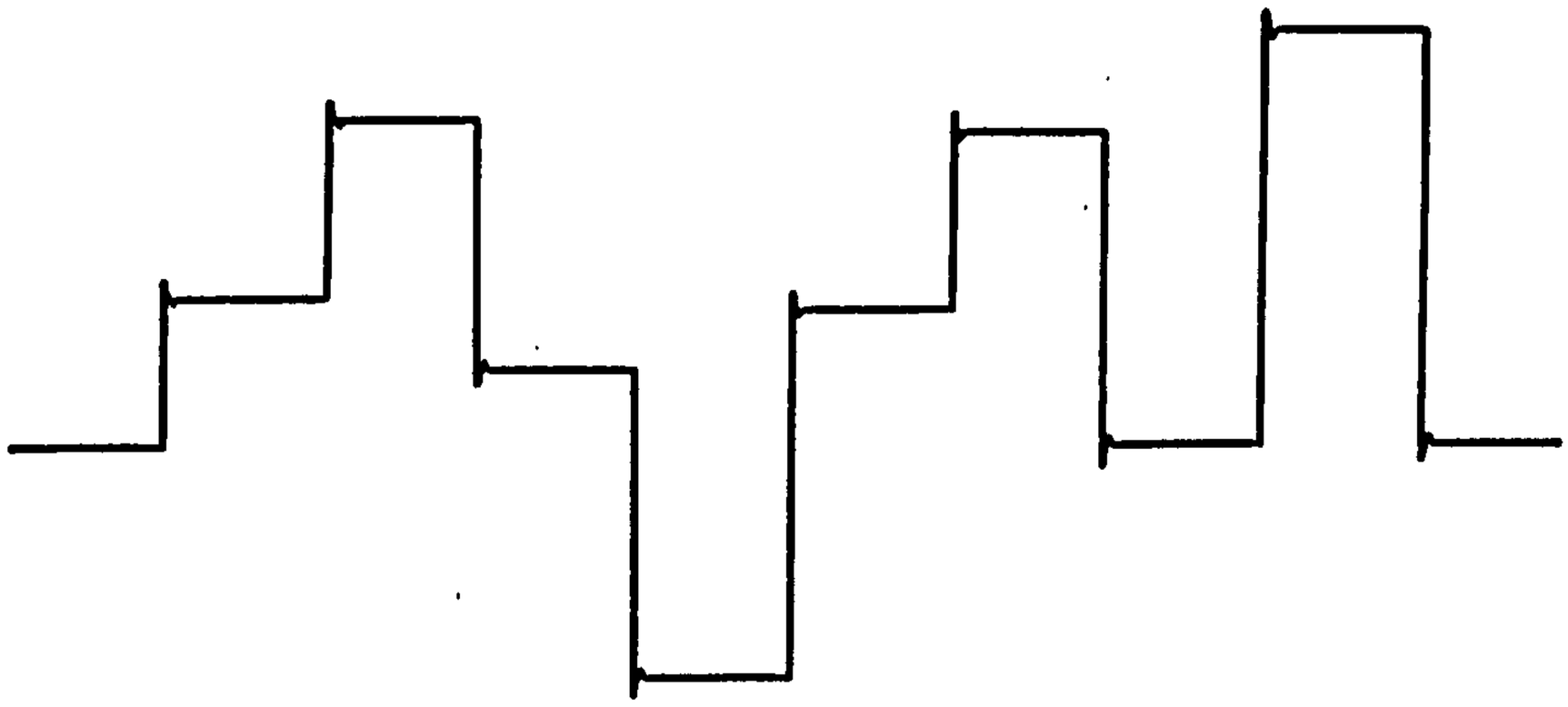

Typical multiplexed signal wave-form

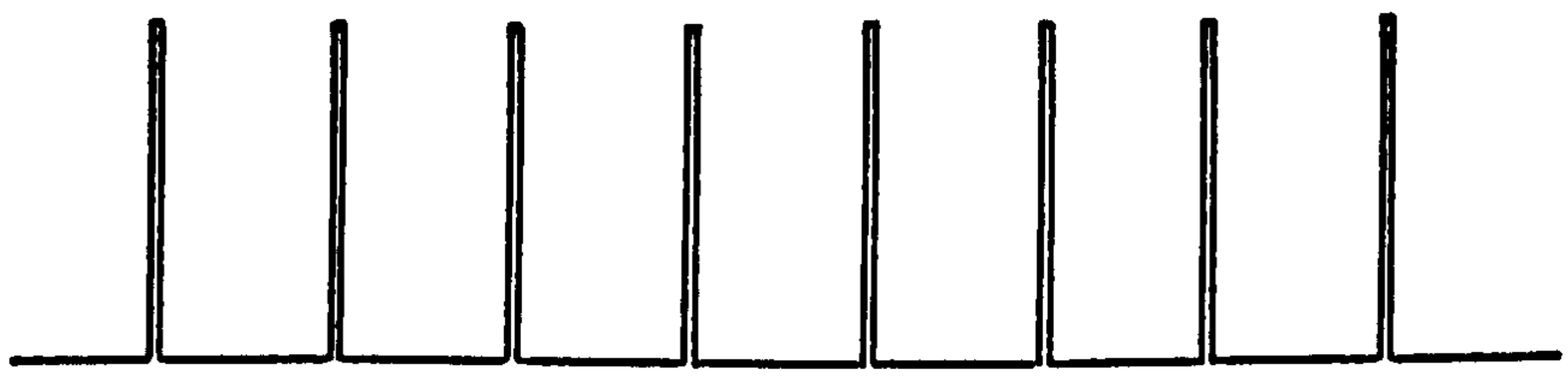

Sampling pulses

Fig. 4.4 b

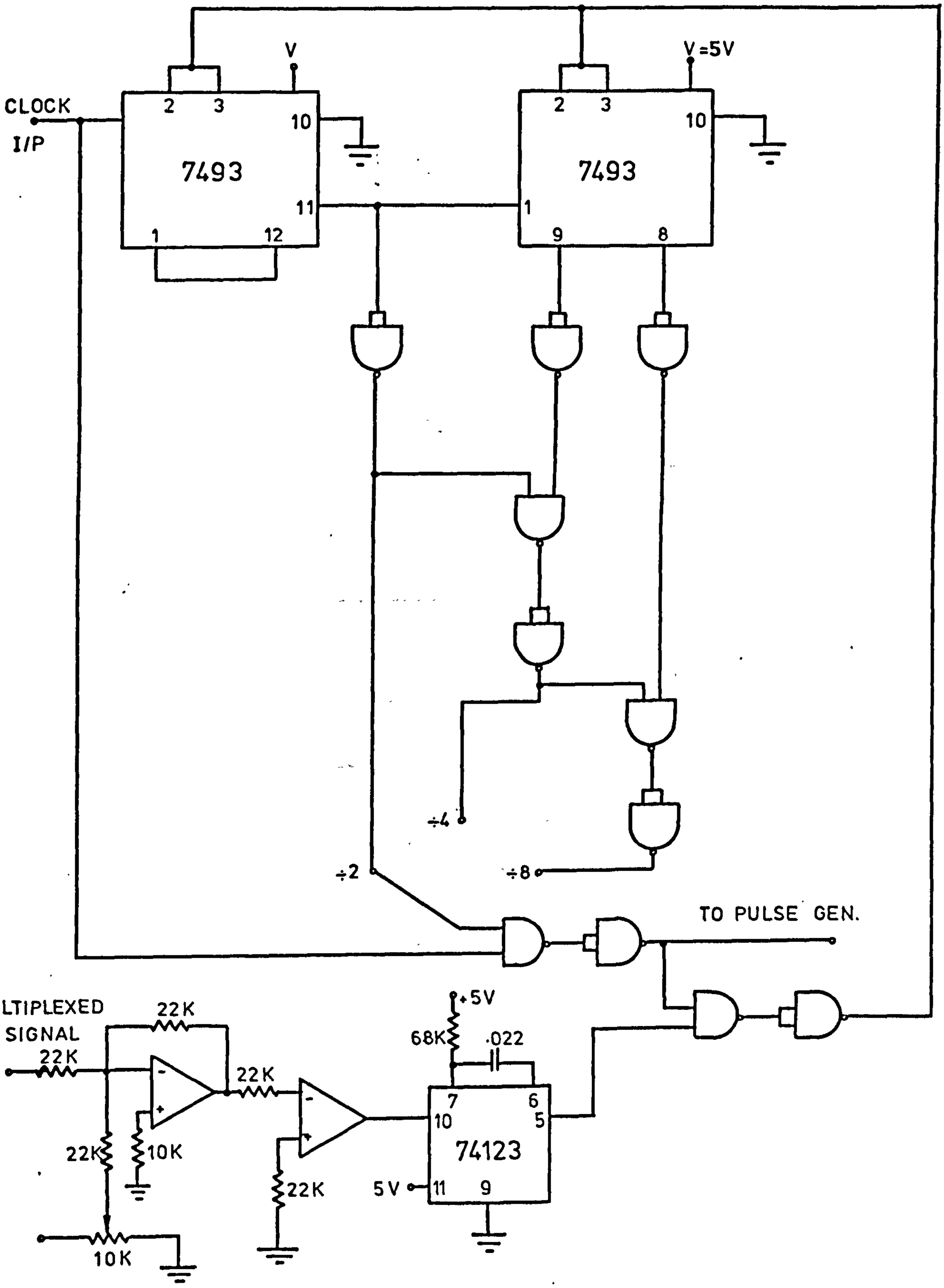

Fig. 4.5 Sampling frequency reduction system.

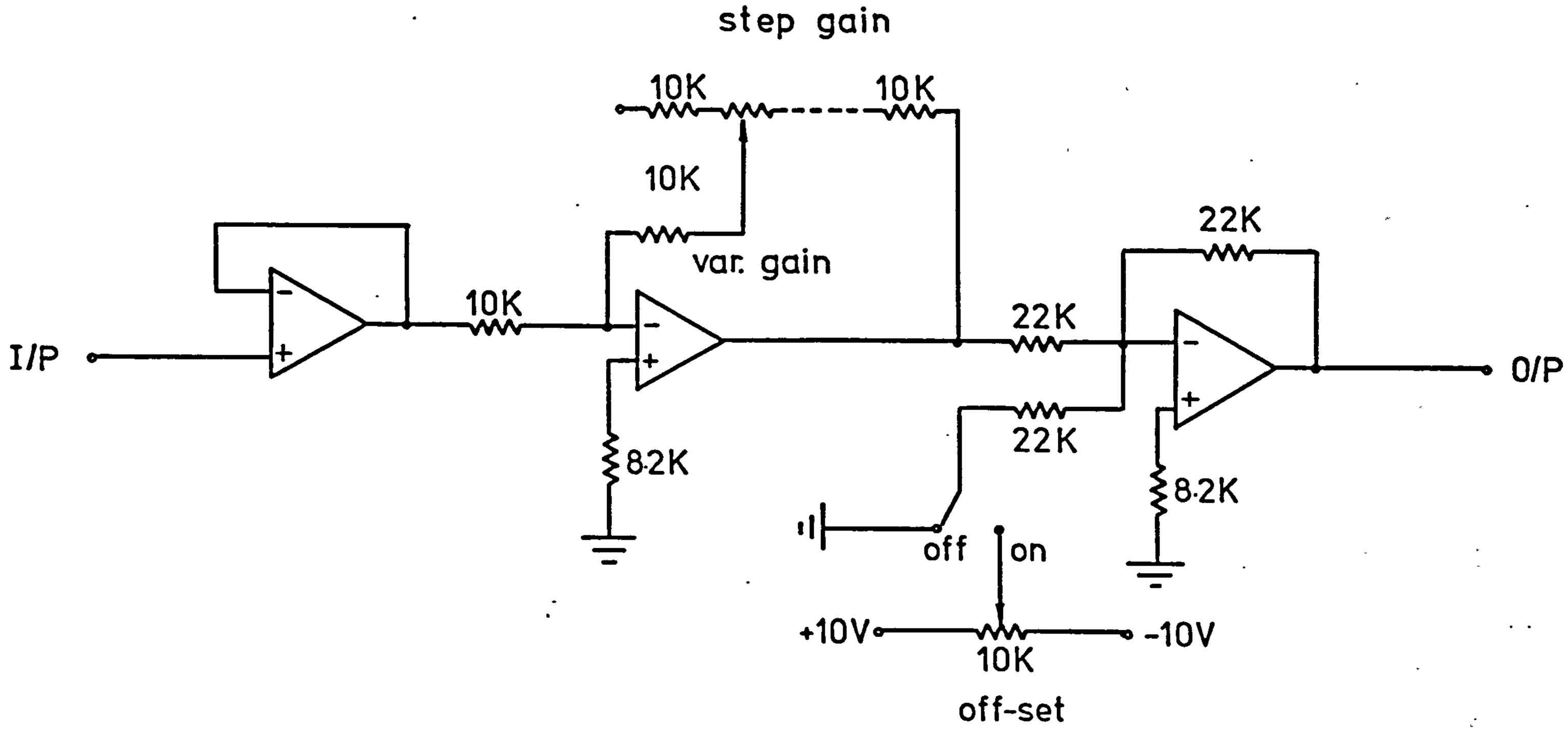

Fig. 4.6 Amplifier with variable gain and off-set

The possible ranges of the fluctuations of each quantity are noted from the chart recorder. The gains of the amplifiers for individual quantities are then adjusted so as to bring the maximum values of the amplified fluctuations to within $\pm$ 1 volt before inputing to the multiplexing system. The gain of each channel of the multiplexer is unity for all eight channels. The attenuator of the tape recorder is then adjusted so that 1 volt d.c. input gives a full recording level.

Each magnetic tape starts with two reference d.c. voltages. The first one is the zero reference voltage which is extremely useful in checking the zero reference of the signals recorded in the playback process. The other is the 1 volt d.c. voltage which is used to calibrate the magnetic tapes.

Channel 8 is a pilot signal for the computer and control pulse for sychronization (Section 4.2.1) and channel 7, when not being used for the refractometer data is used to monitor the zero reference during the recording and playback process.

The sine wave for synchronization and for clocking the computer is recorded simultaneously on another track of the magnetic tape.

4.3 Digitization of the data

To process the data, the first step is to obtain the

data in digital form on paper tape. This is done by using the analogue to digital converter of the Modular One computer available in the Department (Figure 4.7). The sampling sine wave is extracted from the magnetic tape and converted into a train of square pulses (Figure 4.8) of duration about 30 microseconds which is then used to clock the computer. The multiplexed signal read-out is sent to one channel of the analogue to digital converter (ADC). A program written in assembler language is used in sampling. The sampling is started by means of a d.c. voltage applied to another channel of the ADC. Particular care was taken to separate the channels of the multiplexed signal. Checking and testing of the sampled data are carried out to make sure that no mixing of the channels has occurred. (Mavrokoukoulakis 1977).

The ADC accepts signals within the range of $\pm$ 5 volts without saturation and has 2000 quantized steps for this maximum range. The print-out of the computer is thus between $\pm$ 1000 with each step corresponding to 5 mV. This implies that the maximum quantization error which may be encountered is less than or equal to 5 mV. Since, in the recording process, steps have already been taken to make the dynamic ranges of the fluctuations of each quantity as large as possible (Section 4.2.2), the digitization error is not significant. For example, if the short term nominal voltage of the fluctuation after amplification is 2 volts out of the maximum value of $\pm$ 5 volts. Then the quantization error is only 0.25%. In terms of the microwave signal fluct-uations, the 5 mV error is only 0.03 dB of the fluctuating signal.

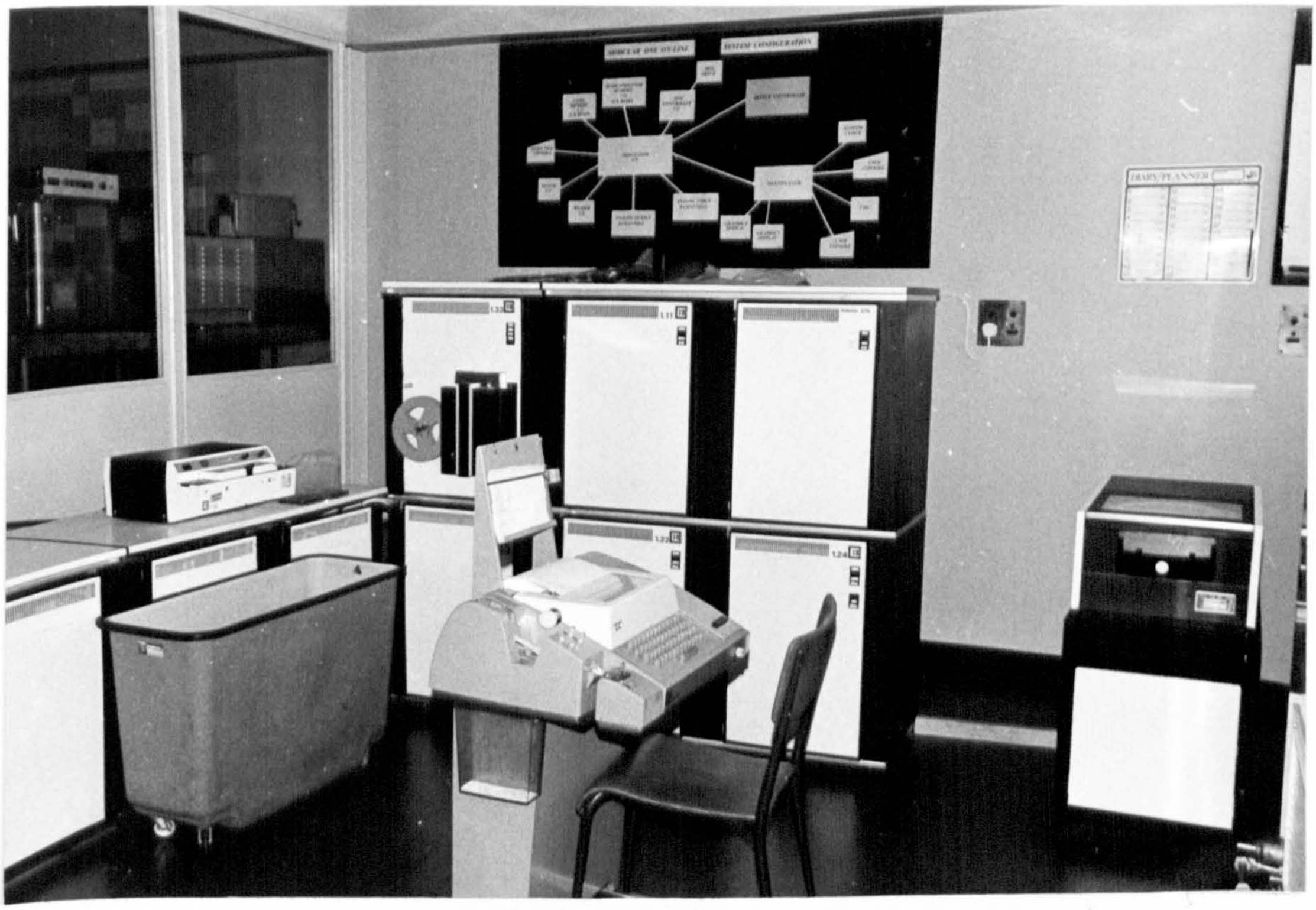

Figure 4.7 The Modular One computer in the Electronic and Electrical Engineering Department, U.C.L.

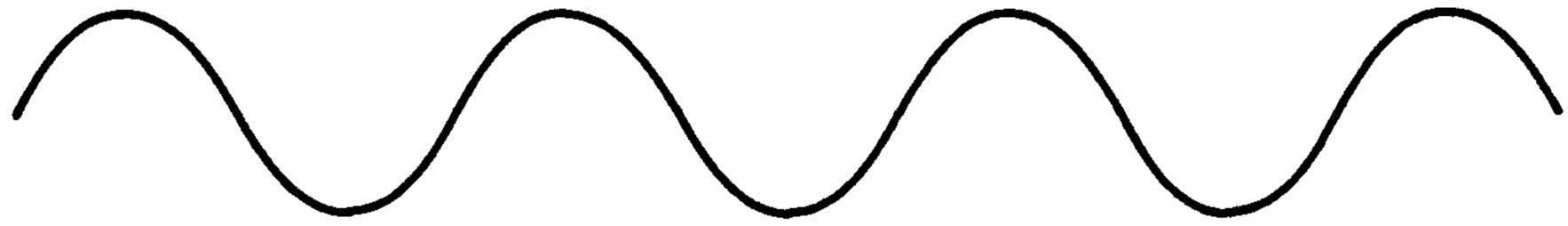

(a) sine wave

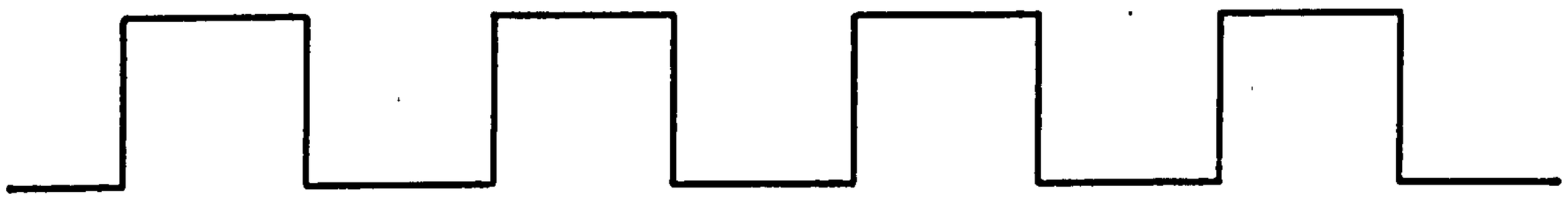

(b) square wave(after squarer)

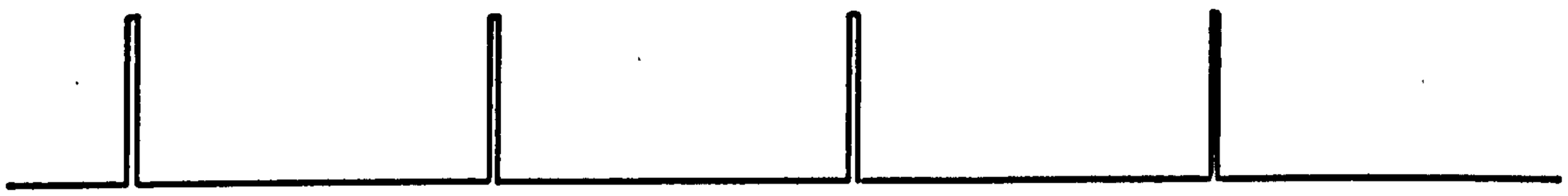

(c) pulses for computer clocking

Fig. 4.8 Conversion of sine clock wave into pulses for computer clocking.

The sampling process can be divided into two categories. The first one is to convert the continuous signals into digital form and to print them on paper tape. This kind of digitization was used mainly for spectral analysis. Normally, 1024 points are taken and pre-processing (Section 4.7) is carried out later in Fortran language.

The second type is for the study of some quantities involving statistical approaches, such as logarithmic amplitude variances, autocorrelations etc. In this case, instead of printing out the digital data of the continuous signals, pre-processing, filtering and all the necessary mathematical calculations are carried out immediately after the sampling using Assembler language and the computer prints out only the required quantities. The Mod. I computer can be programmed using both the Assembler or the Fortran IV languages. Assembler language was used for all digitizations at the beginning of the experiment, though it is a fairly low level computer language, because the problem of interference from other users of the computer when Fortran IV was used for digitization had not been overcome at that time. However, Fortran IV language was later used for both sampling and all analysis when this problem was solved.

4.4 The aliasing problem in sampling

In lumped, linear, continuous (i.e. not sampled) systems, time functions often taken the form of a sum of general

exponential components (Blackman 1975).

$$f(t) = \sum_{k=1}^{m} a_k e^{s_k t} \qquad \text{for } t > 0 \qquad 4.4.1$$

$$f(t) = 0 \qquad \text{for } t < 0$$

where s_k are the poles of the transformed signal which will be either real or in conjugate pair in the complex domain. The Laplace transform expression is

$$F(s) = \sum_{k=1}^{m} \frac{a_k}{(s - s_k)} \qquad 4.4.2$$

If impulse sampling of the function is considered, the sampled function will be given by

$$f^*(t) = \sum_{k=1}^{m} \sum_{n=0}^{\infty} a_k e^{s_k nT} \delta(t - nT) \qquad 4.4.3$$

which represents a series of delayed impulses in which the coefficients $a_k e^{s_k nT}$ are complex constants. Figure 4.9 shows the impulse sampling of a single exponential component. The Laplace transform of such a function may be written in closed form as

$$F^*(s) = \sum_{k=1}^{m} F_k^*(s) = \sum_{k=1}^{m} \frac{a_k}{1 - e^{(s_k - s)T}} \qquad 4.4.4$$

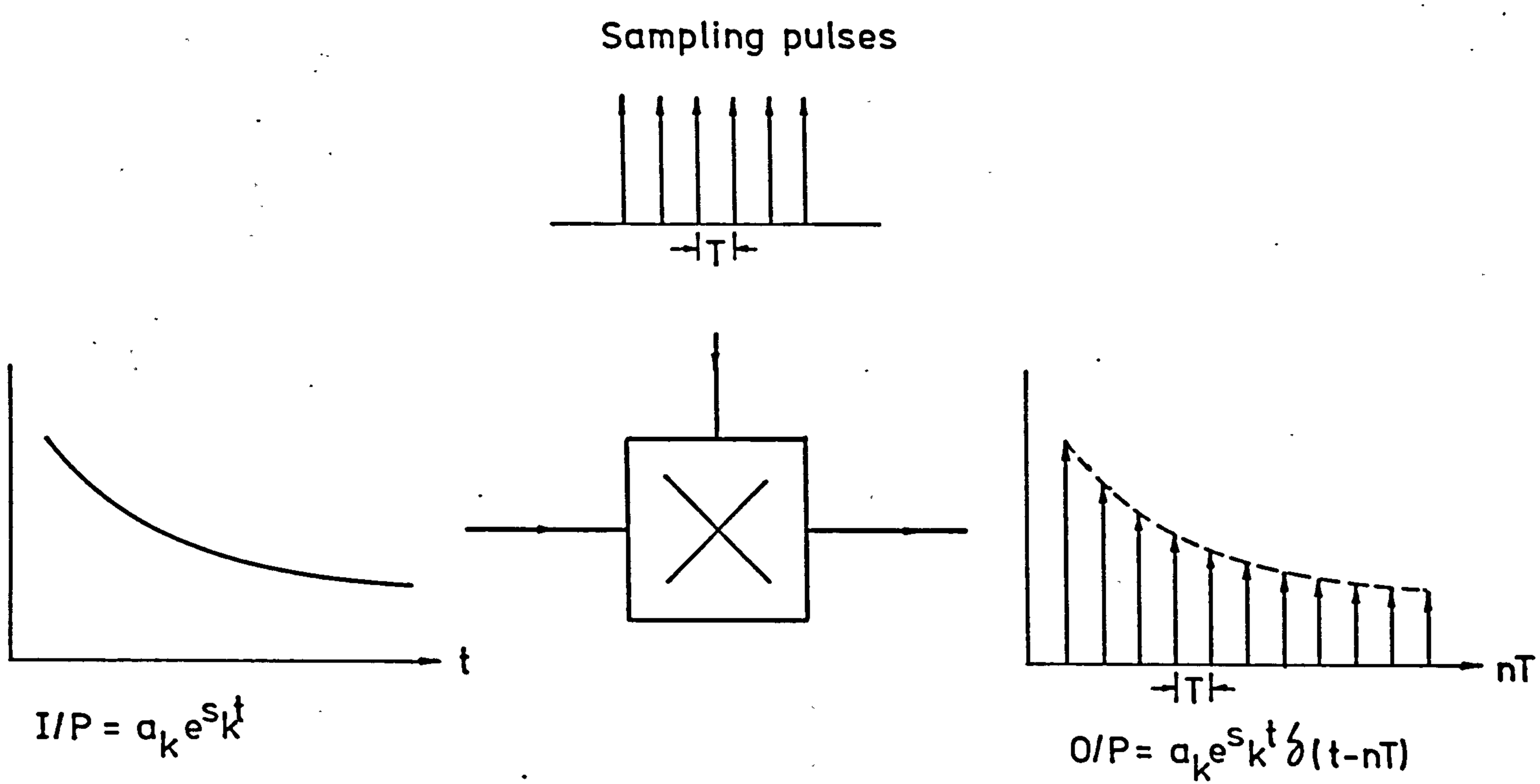

Fig. 4.9 Impulse sampling of a single exponential component.

From Equation 4.4.3, it can be seen that a general sampled exponential component

$$F_k^*(s) = \frac{a_k}{1 - e^{(s_k - s)T}}$$

has poles

$$s = s_k + \frac{j\,2\pi n}{T} \qquad -\infty < n < \infty \qquad 4.4.5$$

These results give a pole at s_k corresponding with the continuous signal, and a line of additional poles spaced at intervals $\frac{2\pi}{T}$ as illustrated in Figure 4.10. Since $F_k^*(s)$ has an infinite number of poles, it could be represented as a summation of individual poles with the general form

$$F_k^*(s) = \sum_{n=-\infty}^{\infty} \frac{b_n}{(s - s_n)} \qquad 4.4.6$$

where $s_n = s_k + \frac{j\,2\pi n}{T}$

The frequency spectrum $F(j\omega)$ of the continuous function can be obtained by evaluating $F(s)$ along the imaginary axis in the s plane. However, we have just seen that the effect of sampling is to repeat the pole-zero pattern of the original signal at intervals $j\Omega = \frac{j\,2\pi}{T}$ in the s plane, hence, the frequency spectrum must be the sum of the original frequency spacing $\Omega = \frac{2\pi}{T}$ apart. Figure 4.10b shows the frequency spectra for a continuous

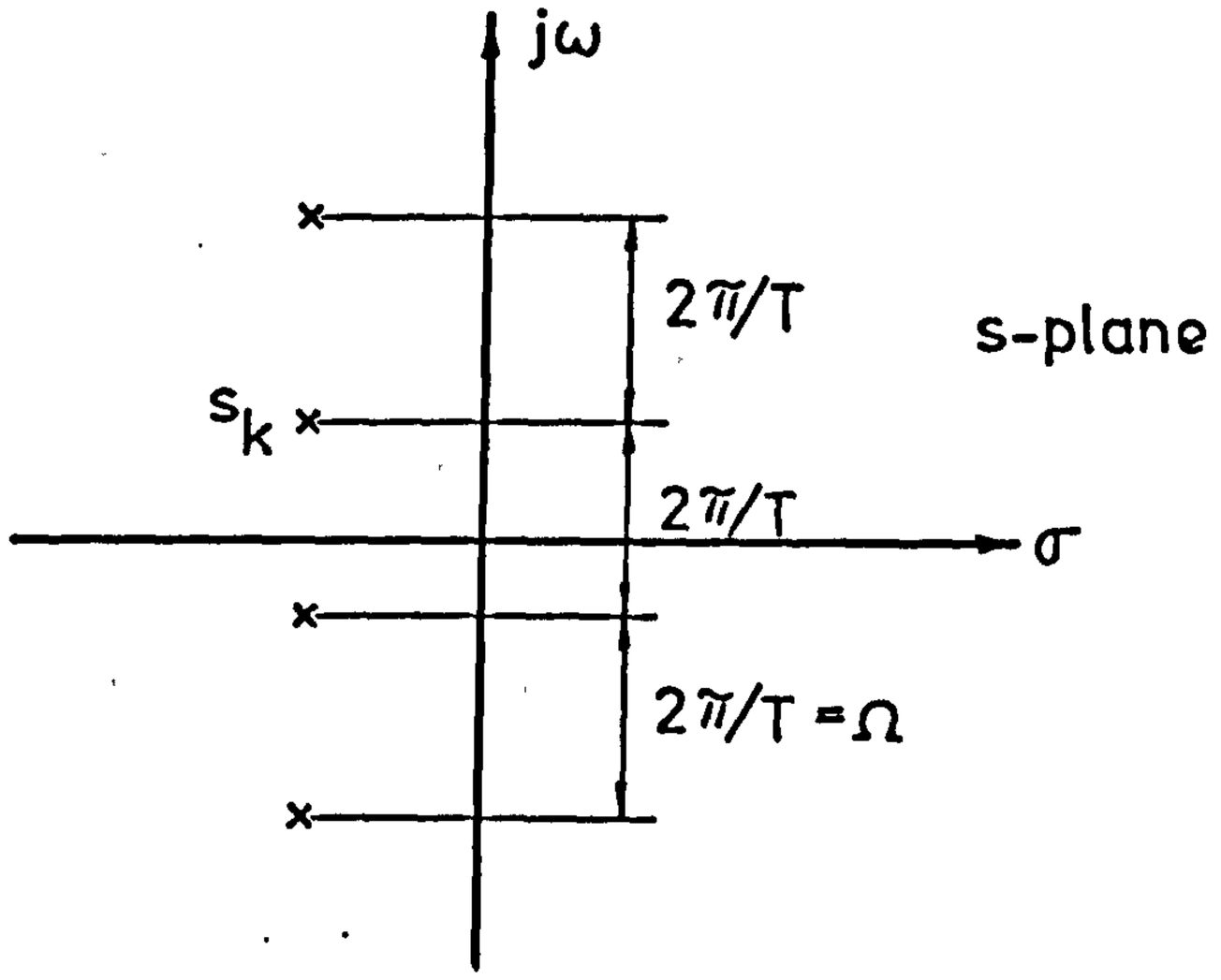

Fig. 4.10(a) Pole pattern for single sampled exponential

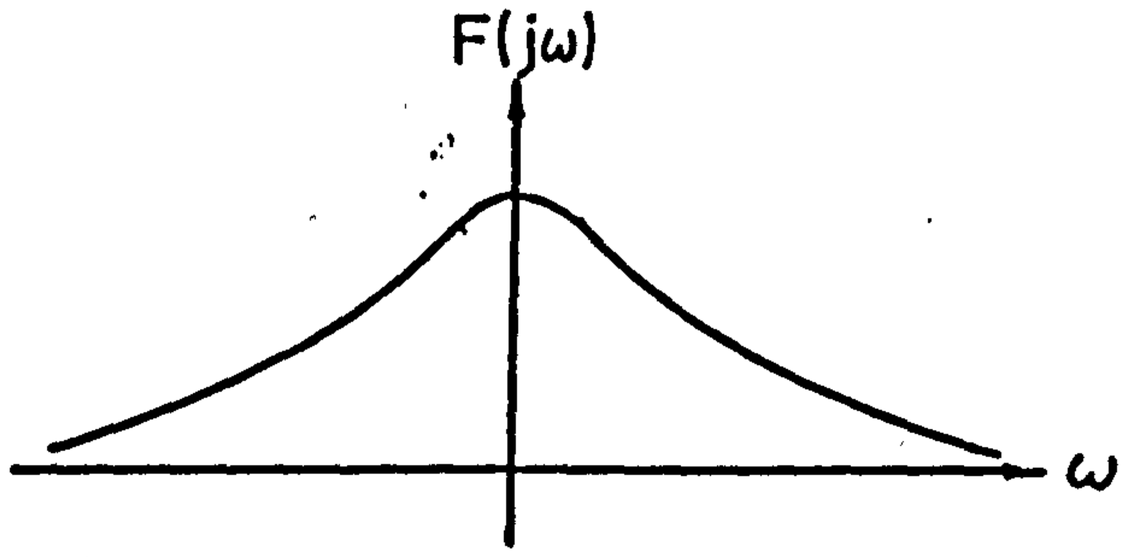

(i) spectrum for continuous signal

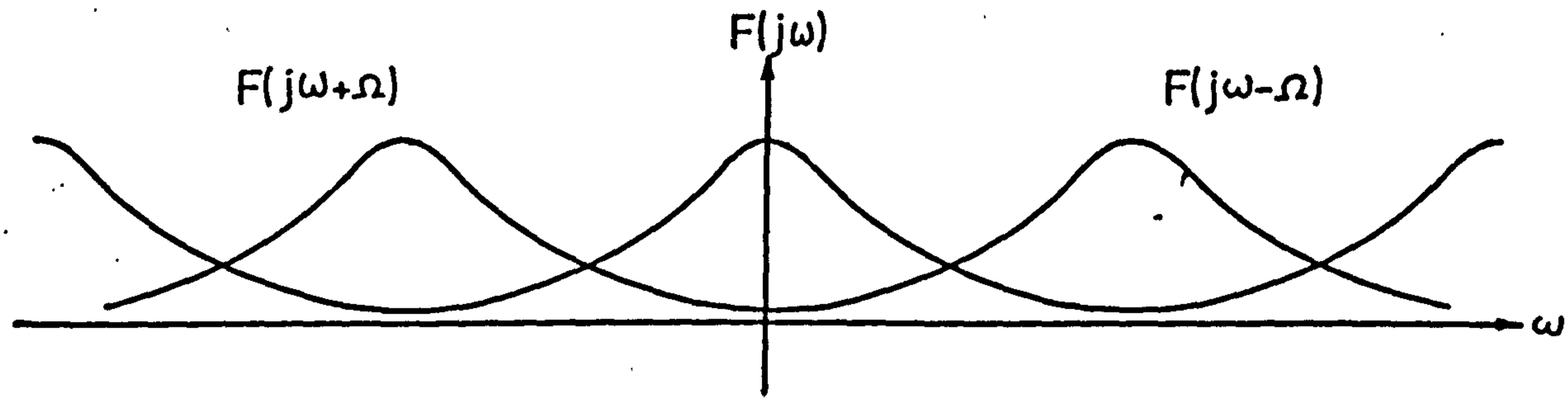

(ii) spectrum for sampled exponential

Fig. 4.10(b) Frequency spectra for (i) continuous (ii) sampled signal.

signal and the sampled signal.

Since, in general, for a sampled signal, the spectra overlap, the total signal present at any frequency depends on the addition of contributions from a number of spectra. The original can only be recovered if (a) $F(j\omega)$ has no components at frequencies exceeding $\frac{\Omega}{2}$ hence the spectra do not overlap. This is actually equivalent to the sampling theorem; (b) a filter is used which can pass $F(j\omega)$ perfectly and completely eliminate the other spectra.

In our case, the maximum frequency of any quantities can be regarded as within 20 Hz (Section 4.7.2), so a sampling frequency of 40 Hz was chosen. With this sampling frequency, it is clear that the mains 50 Hz give a component at 10 Hz. Of course, the higher the sampling frequency used the better is the recovery of the signal, however, this is limited by the frequency response of the FM tape recorder because of the multiplexing process and the resolution of the frequency in the spectral analysis.

4.5 Noise problem in the play-back process

The noise generated in the play-back process is mainly from the tape recorder. The recorder uses the frequency modulation technique which converts the fluctuating input signal into sinusoidal signal with varying frequency corresponding to the different levels of the input signal in the recording. Hence,

the signals actually recorded on magnetic tape are frequency modulated sinusoidal signals. In the playback process, recovery of the fluctuating signal is by the process of demodulation. So it can be seen that a slight instability in the speed of the tape recorder or any movement of the magnetic tapes both in recording and play-back process can produce spurious modulation to the signal and hence introduce noise. Mechanical vibration of the tape recorder used in this experiment produced instability and hence spurious modulation.

Inspection of the noise spectrum showed that the main frequency components are between 500 Hz and 2 KHz but there are also some other significant components around 3.5, 5, 7 and 10 Hz. At first sight, it would appear that the frequency components above 20 Hz, that is, above the region which we are interested in can be ignored. However, when aliasing is considered (Section 4.4) it can be seen that the problem is not so simple. Figure 4.11a shows the spectrum of the noise when aliasing effect is taken into account with a sampling frequency of 40 Hz. The component magnitudes are calibrated as temperature for comparison purpose. Figure 4.11b shows a spectrum of the temperature. The noise spectrum has a rather constant magnitude except at 3.5, 5, 7 and 10 Hz which can be seen clearly from the spectra. The effect of the noise on the signal is negligible at low frequency fluctuations, but as the frequency increases, the noise effect becomes significant.

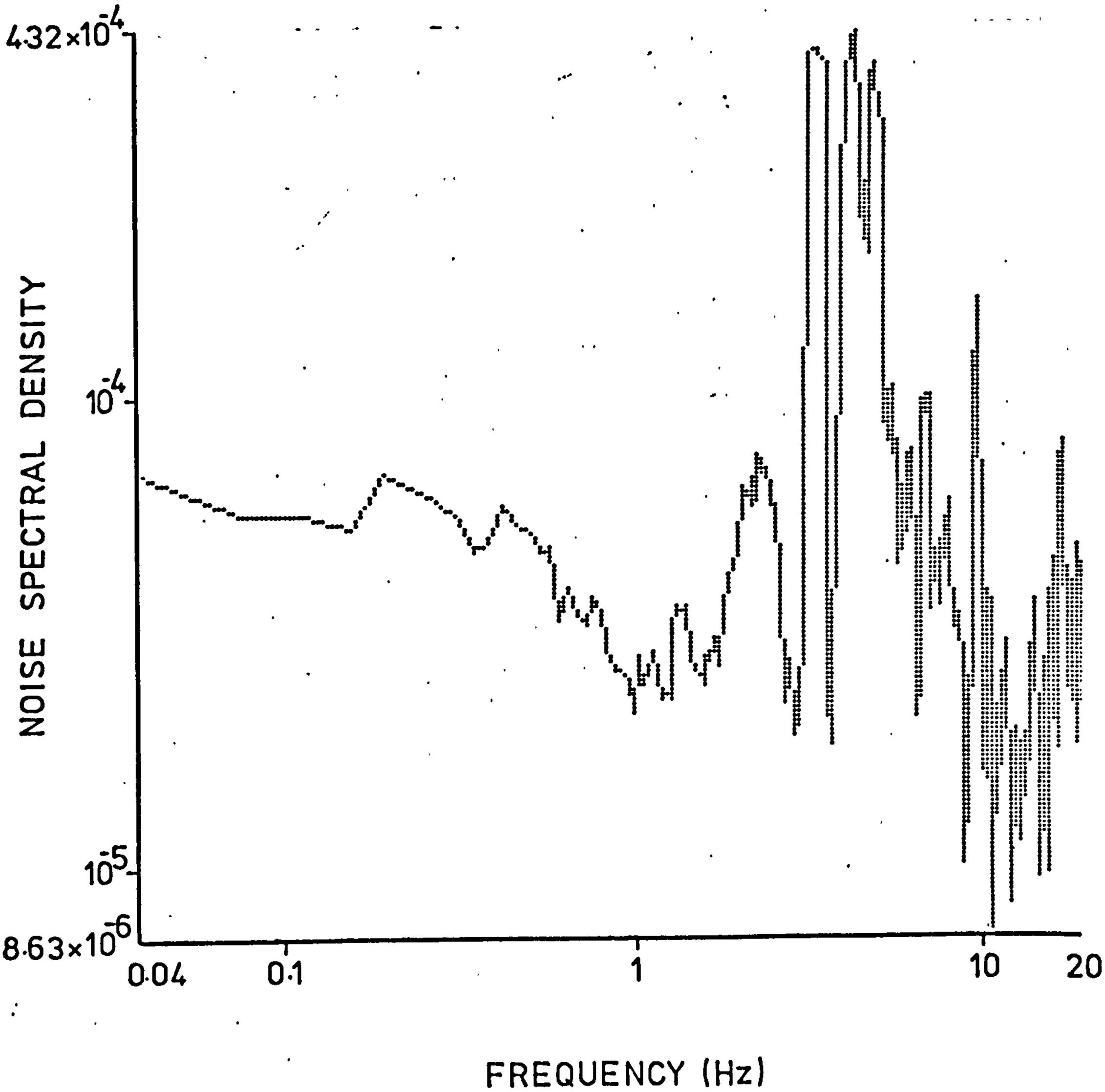

Fig. 4.11a Noise spectrum (with the same calibration as the temperature)

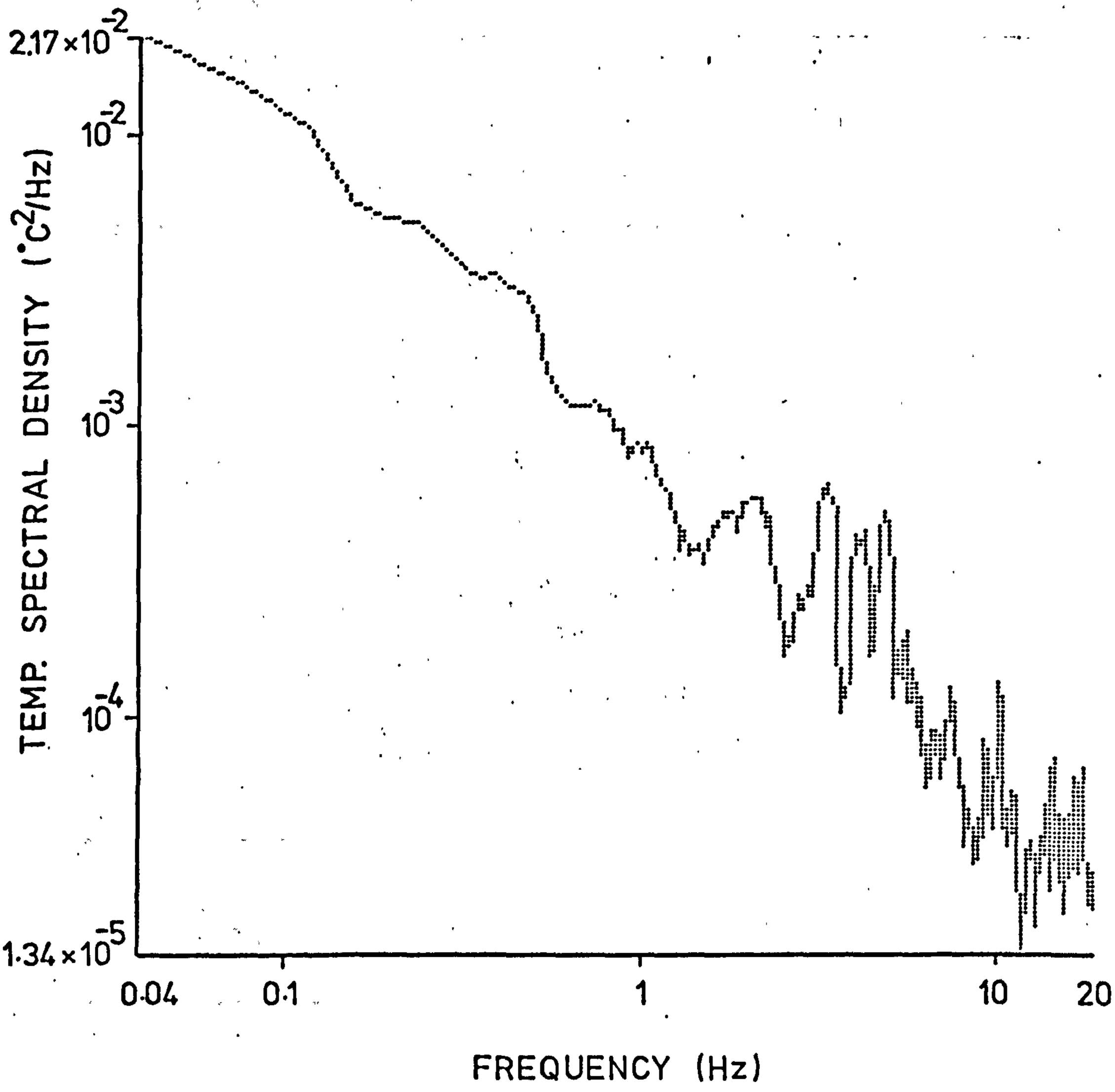

Fig. 4.11b A temperature spectrum.

Table 4.1 shows the typical percentages of error introduced by the noise to the variances of individual signal parameters. The error is about 4 to 5%. With the application of a 5 Hz low pass filter (Section 4.7.2), the error is improved by approximately a factor of 4 for individual cases.

In order to reduce the effect of the noise to a minimum, filtering of the sampled signal is required. However, since the signals are multiplexed with a frequency of 320 Hz, any real filtering with cut-off frequency at tens of hertz cannot be used. The only way is to separate the channels and then pass individual channels through low-pass filters. In view of this, the method of digital filtering is more simple and convenient.

Table 4.1 % error due to noise

Quantity / % error	36 GHz	110 GHz	Temp.	Hum.	Wind Speed
Without filter	4.25	4.13	2.65	3.97	8.5
With filter	1.05	1.02	0.71	1	2.4

4.6 Digital filtering

The principle of digital filtering is carried out by linearly combining past output samples with past and present input samples so as to form a linear difference equation describing the input-output behaviour of the system (Constantinides 1975) Thus if (n+1) input samples are used in the required linear combination process, along with m previous output samples, the kth sample value of the output signal will be given in the form:

$$y_k = a_o x_k + a_1 x_{k-1} + \ldots\ldots + a_n x_{k-n}$$

$$-(b_1 y_{k-1} + b_2 y_{k-2} + \ldots\ldots\ldots + b_m y_{k-m}) \qquad 4.6.1$$

where

$\{y_k\}$ is the set of output samples

$\{x_k\}$ is the set of input samples

$\{a\}$ and $\{b\}$ are sets of coefficients which are real and constant.

For the transfer function considerations, the discrete system transfer function is defined in terms of the z transform as the ratio of the z transform of the output signal to the z transform of the input signal. In general, the transfer function of Equation 4.6.1 is given by

$$G(z^{-1}) = \frac{Y(z)}{X(z)} = \frac{a_o + a_1 z^{-1} + \ldots\ldots\ldots + a_n z^{-n}}{1 + b_1 z^{-1} + \ldots\ldots + b_m z^{-m}} \qquad 4.6.2$$

where $Y(z)$ is the z transform of the output signal

$X(z)$ is the z transform of the input signal.

For a continuous filter, the stability of the filter is obtained if all the poles of the transfer function are in the left half s-plane. Transformation of the s-plane into z^{-1} plane by the equality $z^{-1} = e^{-sT}$ shows that the poles of the digital transfer function must have moduli which are greater than unity, that is $|z^{-1}| \geq 1$ for the purpose of stability.

Digital filters can be realized from the normalized transfer function of the continuous filter by the transformation of the s parameter into z^{-1} parameter. For low pass filter, the transformation is given by (Rader and Gold 1963)

$$s = \cot\left(\frac{\omega_c T}{2}\right) \frac{1 - z^{-1}}{1 + z^{-1}} \qquad 4.6.3$$

where ω_c is the cut-off frequency

T is the reciprocal of the sampling frequency.

Consider the Butterworth type low-pass filter which is convenient for the present purpose because of its sharp cut-off characteristic (Constantinides 1975). The general amplitude characteristic is given by

$$G(s^2) = \frac{A}{1 + s^{2n}} \qquad 4.6.4$$

where A is the amplitude constant and n is an integer.

If we consider the variable only on the imaginary axis of the s-plane, then $s=j\omega$ and z^{-1} becomes $e^{-j\omega T}$. Making use of Equation 4.6.3, we get

$$\left|G(\omega)\right|^2 = \frac{A^2}{1 + \left[\frac{\tan \frac{\omega T}{2}}{\tan \frac{\omega_c T}{2}}\right]^{2n}} \qquad 4.6.5$$

Solution of the poles on the z^{-1} plane can be obtained from Equations 4.6.3 and 4.6.4. Once the location of the poles are found, those lying outside the unit circle are chosen to form the digital transfer function. Comparison with the general transfer function (Equation 4.6.2) will immediately give the coefficients of the digital filter equation. Details and design of the Butterworth type low-pass filters are given in Appendix 4.1.

4.7 Pre-processing of the data

Before processing and analysing the data after digitization, it is advisable to pre-process the data, because of the finite length of the record and the discrete character of the values. To obtain results which are most accurate, we therefore pre-process the raw data and produce new sets of data.

Three main pre-processing operations are used.

4.7.1 The removal of the d.c. components

When analysing signal scintillations, it is the amplitude fluctuations of the parameters which is of interest. If the record is digitized for a very long period of time so that it contains at least one cycle of the lowest significant fluctuation frequency and assuming that the data is stationary, then the removal of the d.c. components can be carried out by subtracting the value of each data sample from its mean value, that is,

$$X'(n) = X(n) - \frac{1}{N} \sum_{j=1}^{N} X(j) \qquad 4.7.1$$

where $X'(n)$ is the new set of data with zero mean value

$X(n)$ is the set of raw data.

However, in an actual case, the mean value of any parameter is, generally, not stationary. In order to obtain the most accurate data samples of the fluctuations, the removal of the d.c. component is carried out by first obtaining the regression of the raw digitized data and a new set of data is generated by subtracting the individual data values from their corresponding value in the regression line. The method of regression, besides removing the d.c. components, also reduces the effects of very low frequency components which may contribute an error for the

finite period of digitization. Thus the new set of data is given by (Kreyszig 1962)

$$X'(n) = X(n) - Y(n) \qquad 4.7.2$$

where $Y(n) = a + nb$

and $$a = \frac{\sum n \sum nX(n) - \sum n^2 \sum X(n)}{(\sum n)^2 - N\sum n^2}$$

$$b = \frac{N\sum nX(n) - \sum n \sum X(n)}{N\sum n^2 - (\sum n)^2}$$

4.7.2 Filtering of the data

The filtering process eliminates the error due to the frequency components being folded back on low frequency components due to low sampling frequency. Filtering at a cut-off frequency of 5 Hz was used in the statistical analysis of the signal fluctuations. Based on the propagation theory in a turbulent medium (chapter 2 and 5), the dominant fluctuations of the microwave signal are at spatial wave number $K = \frac{2\pi f}{\bar{V}}$ (where $\bar{V}$ is the mean wind speed) with dimensions of the order of the first Fresnel zone $2\pi/(\lambda L)^{1/2}$ and $(\lambda L)^{1/2}$ is 5.7 metres and 3.3 metres for 8mm and 2.7mm wavelength respectively. Assuming that the mean wind speed normally varies from 1m/s to 10m/s, the dominant

frequencies of fluctuations may lie within the range of 0.2 Hz to 2 Hz. That is, the maximum dominant frequency will be at about 2 Hz. Thus, we can see that the use of a 5 Hz cut-off frequency is adequate and also eliminates greatly the error contributed by the spurious frequency components of the noise at 5 Hz and 7 Hz.

For the spectral analysis of the amplitude scintillation and the meteorological parameters, high pass filtering technique was used to remove the very low frequency fluctuations caused by instrumentation drift. It is impossible to use any filtering technique to eliminate the spurious frequency components at 5 Hz and 7 Hz if a wide-band spectrum is required. However, the cause of these components are known and since they can be easily distinguished, they can be ignored in any calculations.

4.7.3 Tapering of the data

The data used for spectral analysis is tapered because of the finite period of digitization. Details are given in Section 4.8.

4.8 Power spectrum estimation

The power spectrum is normally referred to the power (or energy) associated with each component of the complex line spectrum. The most important application of power spectral

analysis is in the investigation of continuous aperiodic waveforms. Unfortunately, merely segmenting and sampling a section of such a waveform may be quite inadequate in approximating the spectrum. The principal reason for this is that the segment may not be truly representative of the whole. Such a procedure leads to a "raw" or "unsmoothed" power spectrum.

In segmenting data from a long record, in order to perform the discrete Fourier transform required to establish the power spectral density, spurious spectral components are introduced (Coates 1975). The segmentation process is equivalent to multiplying the original time series (Figure 4.12a) by a rectangular data "window" (Figure 4.12b) passing N data points (Figure 4.12c). Consequently, the "true" spectrum of the time series is convolved with the Fourier transform of the rectangular function. This results in a derived spectrum which can only approximate to the "true" version (Figure 4.12d) because such convolution redistributes the Fourier amplitudes or equivalently mixes the frequency content. The effect can be better visualized by considering the signal X(t) as a single periodic component of amplitude A_o and frequency ω_o as shown in Figure 4.13a.

$$X(t) = A_o \cos \omega_o t \qquad 4.8.1$$

The Fourier transform of such a function is given by

$$X(\omega) = \frac{A_o}{2}[\delta(\omega + \omega_o) + \delta(\omega - \omega_o)] \qquad 4.8.2$$

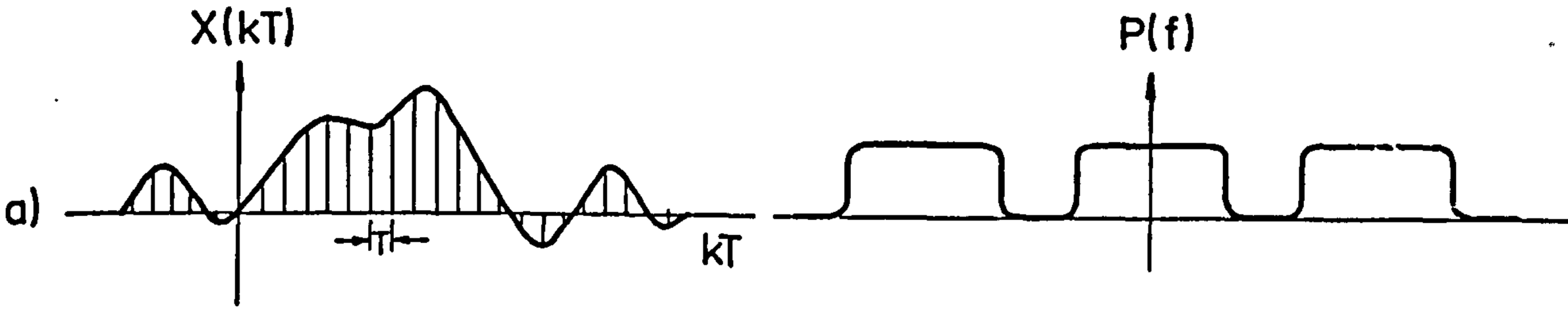

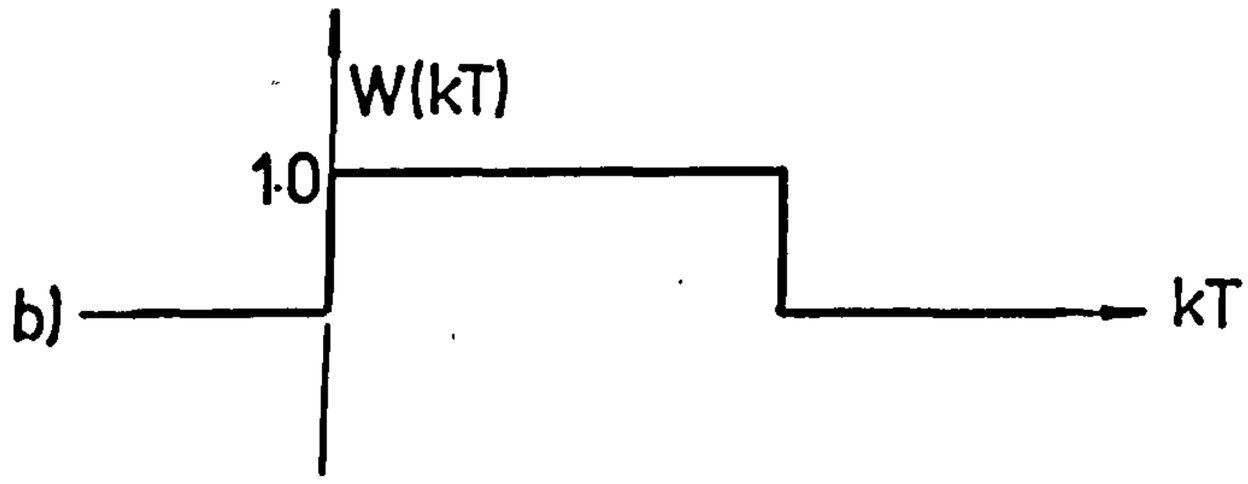

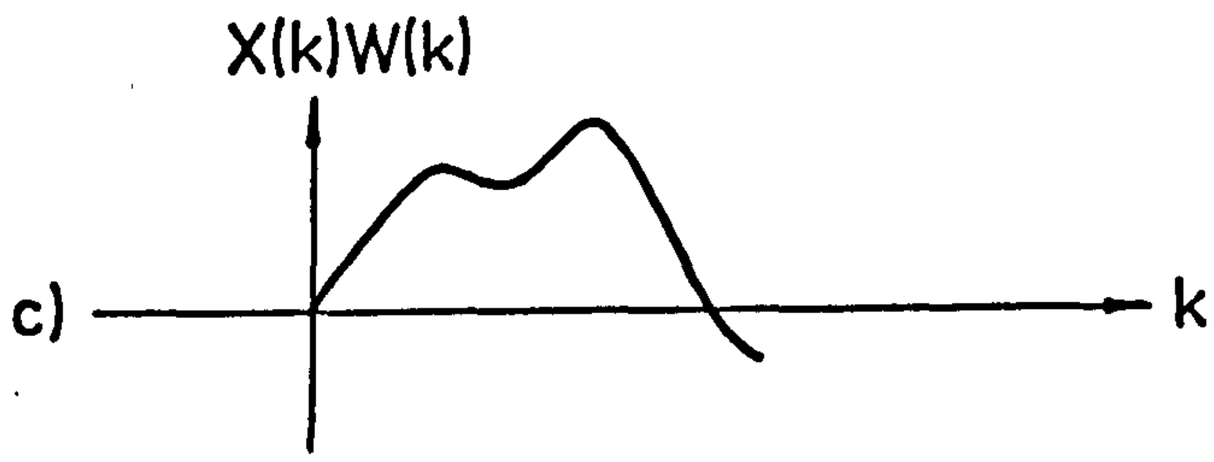

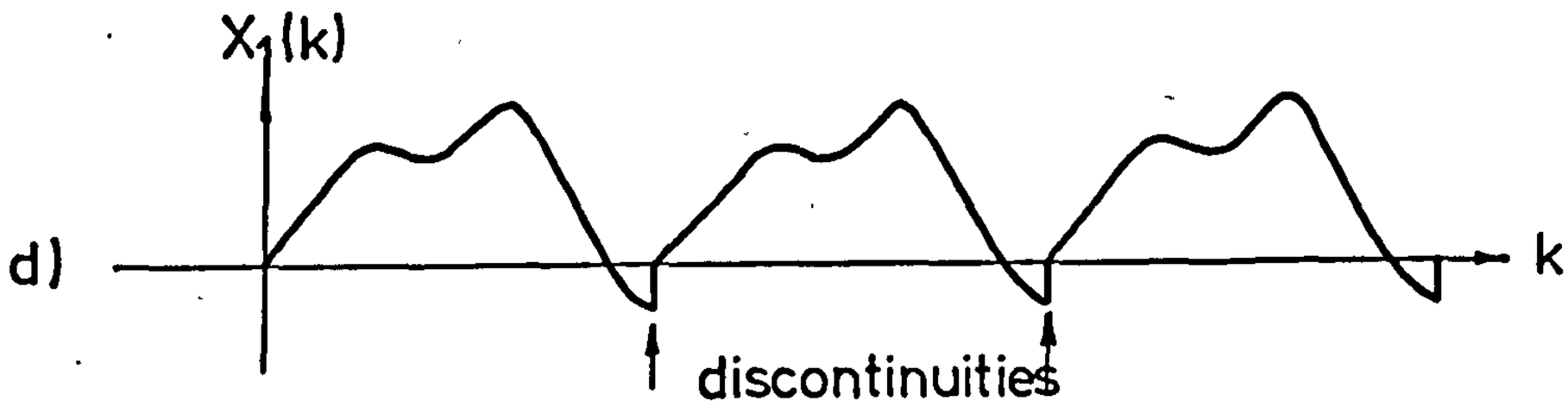

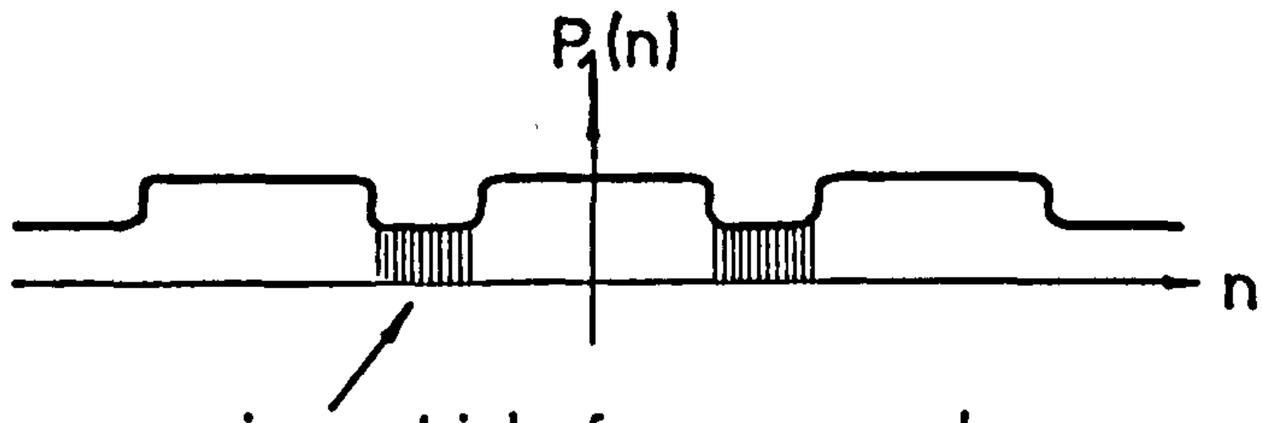

Fig. 4.12 Effect of segmentation on spectral density.

Consider the rectangular window in Figure 4.13b which is given by

$$W(t) = 1 \qquad \text{for } -\frac{T}{2} < t \leqslant \frac{T}{2} \qquad 4.8.3$$

$$W(t) = 0 \qquad \text{for } t = \text{otherwise},$$

the Fourier transform of this function is

$$W(\omega) = \frac{T}{2\pi}\left(\frac{\sin\frac{\omega T}{2}}{\frac{\omega T}{2}}\right) \qquad 4.8.4$$

The convolution of $X(\omega)$ and $W(\omega)$ leads to the two sided function

$$W(\omega + \omega_o) = \frac{A_o T}{4\pi}\,\frac{\sin(\omega \pm \omega_o)\frac{T}{2}}{(\omega \pm \omega_o)\frac{T}{2}} \qquad 4.8.5$$

centred at ω_o which shows the redistribution, spread or leakage of the energy content $\frac{A_o^2}{2}$ originally associated with the single Fourier component ω_o. The resultant spectrum is shown in Figure 4.13c.

This adverse effect of segmentation may be alleviated by the use of a data window which is other than rectangular. The basic requirement is that the window should cause the segmented time series to have no discontinuities at its end points. The window function which we adopt in our spectral analysis is the half-cosine bell expression applied to both data ends. This function is given by

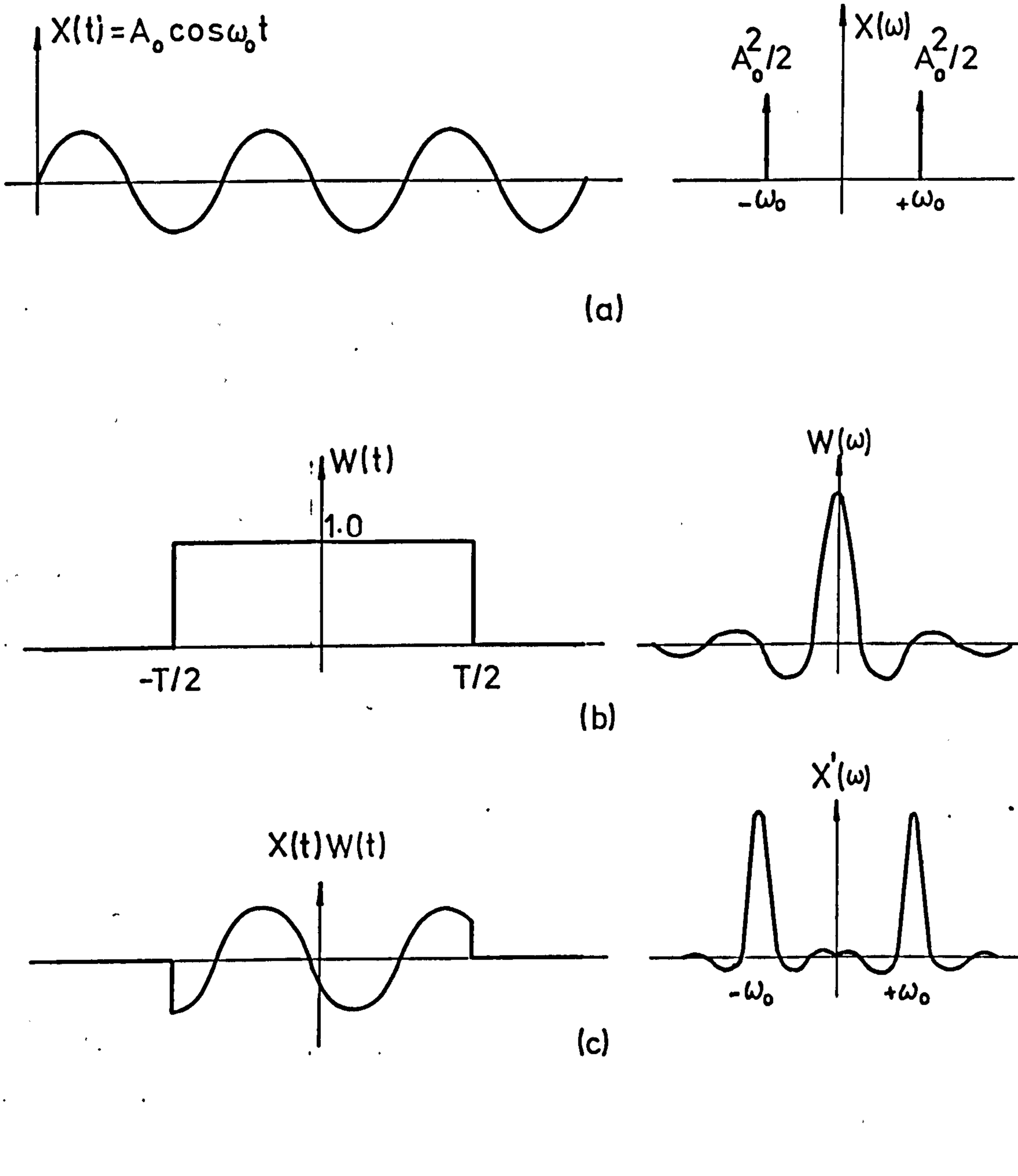

Fig. 4.13 Spread (convolution of frequency content) due to truncation (segmentation)

$$W(t) = 0.5\left[1 - \cos\pi\left(\frac{n}{L-1}\right)\right] \qquad n=0,1,2\ldots L-1$$

$$W(t) = 1 \qquad n=L,\ldots\ldots N-L-1 \qquad 4.8.6$$

$$W(t) = 0.5\left[1 - \cos\pi\left(\frac{N-1-n}{L-1}\right)\right] \qquad n=N-L,\ldots,N-1$$

The situation is shown in Figure 4.14.

In order to compromise between smoothing and resolution only a 10% cosine bell is used, that is, $L = \frac{N}{10}$.

The resolution of the spectrum is governed by the number of points and the sampling frequency and the relationship is given by

$$\Delta f = \frac{1}{N \cdot \frac{1}{f_{sampling}}} \qquad 4.8.7$$

Normally, 1024 points are chosen for the analysis with a sampling frequency of 40 Hz thus giving a resolution of 0.039 Hz which is adequate for most purposes.

In all the power spectral analyses, the Fast Fourier Transform (FFT) technique was used. The FFT is a computer algorithm, whereby, for appropriate length sequences, the finite discrete Fourier transform of the sequence may be computed much more rapidly than by other available algorithms.

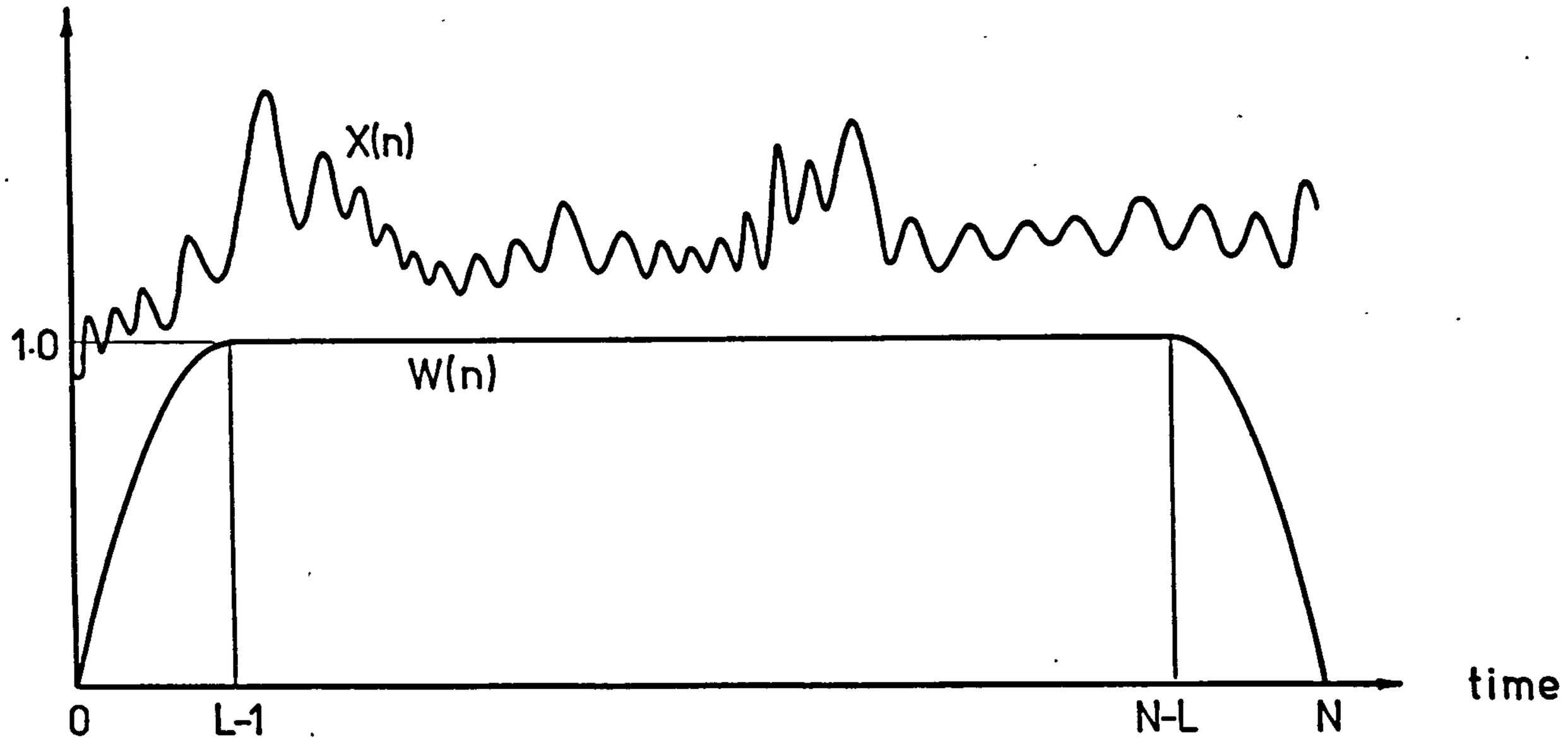

Fig. 4.14 Half cosine bell 'window' function

CHAPTER 5 WAVELENGTH DEPENDENCE OF MILLIMETRE WAVE FLUCTUATIONS

5.1 Introduction

The prupose of this experiment is to compare microwave scintillation measurements directly with theory. Ideally, a knowledge of the statistics of the turbulence along the entire path is desirable. However, the number of meteorological stations in practice, must be limited and usually measurements can only be made at a single or a few points. These few measurements must be used to characterize the turbulent state of the atmosphere along the entire path.

There are two main reasons for seeking a theory which predicts the effects of turbulence on millimetre wave propagation. In the first place, the efficient implementation of millimetre wave systems for communication purposes requires that the designer should be able to predict the amplitude of the millimetre wave carrier fluctuations induced by known (or assumed) turbulence. In the second place it would allow meteorologists, for example, to use millimetre wave scintillations to measure the state of the turbulence. Either approach requires the existence of an accurate theoretical treatment of the propagation problem.

As shown in Section 5.2, the millimetre wave fluctuations depend on the meteorological quantities C_n^2 (the refractive-index

structure parameter) or $\overline{n_1^2}$ (the mean square fluctuations of the refractive index), the wavelength of the transmitting signal and the path length. The wavelength and path length can be measured very accurately so that it is reasonable to measure the wavelength dependence of the microwave amplitude scintillations as a first step to verify the validity of the existing theory.

5.2 Theoretical background

Consider a refractive index structure function of the form

$$D_n(r) = \beta^2 r^p \qquad 5.2.1$$

where β^2 is an arbitrary constant and p is also a constant in the range $0 < p < 2$.

Using Tatarski's result (1961a) the one dimensional spatial spectrum corresponding to Equation 5.2.1 is

$$V(K) = \frac{\Gamma(1+p)}{2\pi} \sin\frac{\pi p}{2} \beta^2 K^{-(p+1)} \qquad 5.2.2$$

For isotropic random fields, the three dimensional spectrum $\Phi(K)$ is related to the one dimensional spectrum V(K) through

$$\Phi(K) = -\frac{1}{2\pi K}\frac{d\,V(K)}{dK} \qquad 1.1.8$$

Therefore

$$\Phi(K) = AK^{-(p+3)} \qquad 5.2.3$$

where $A = \frac{\Gamma(p+2)}{(2\pi)^2} \sin\frac{\pi p}{2}\ \beta^2$

For the case where the field quantities are homogeneous and isotropic in planes perpendicular to the direction of propagation, the correlation function (covariance) of the log-amplitude can be written as

$$B_A(\rho) = 2\pi \int_0^\infty J_o(K\rho)\ F_A(K,O)\ K\ dK \qquad 5.2.4$$

where $F_A(K,O)$ is the two dimensional amplitude spatial spectrum in the plane of the receiver.

For infinite plane wave propagation through homogeneous turbulence, $F_A(K,O)$ is given by (Equation 2.4.26)

$$F_A(K,O) = \pi k^2 L\ (1 - \frac{k}{K^2L} \sin\frac{K^2L}{k})\ \Phi_n(K) \qquad 5.2.5$$

Now, consider the two dimensional spectrum of the logarithmic amplitude fluctuations $F_A(K,O)$. It is clear that the spectrum can be considered to be the product of the spectrum of the refractive index $\Phi_n(K)$ and the appropriate filter factor

$$f(K) = (1 - \frac{k}{K^2L} \sin\frac{K^2L}{k}) \qquad 5.2.6$$

In the general case, $\Phi_n(K)$ has the form shown in Figure 5.1a. In the region of small scales, i.e. $K \gg 2\pi/l_o$, the function $\Phi_n(K)$

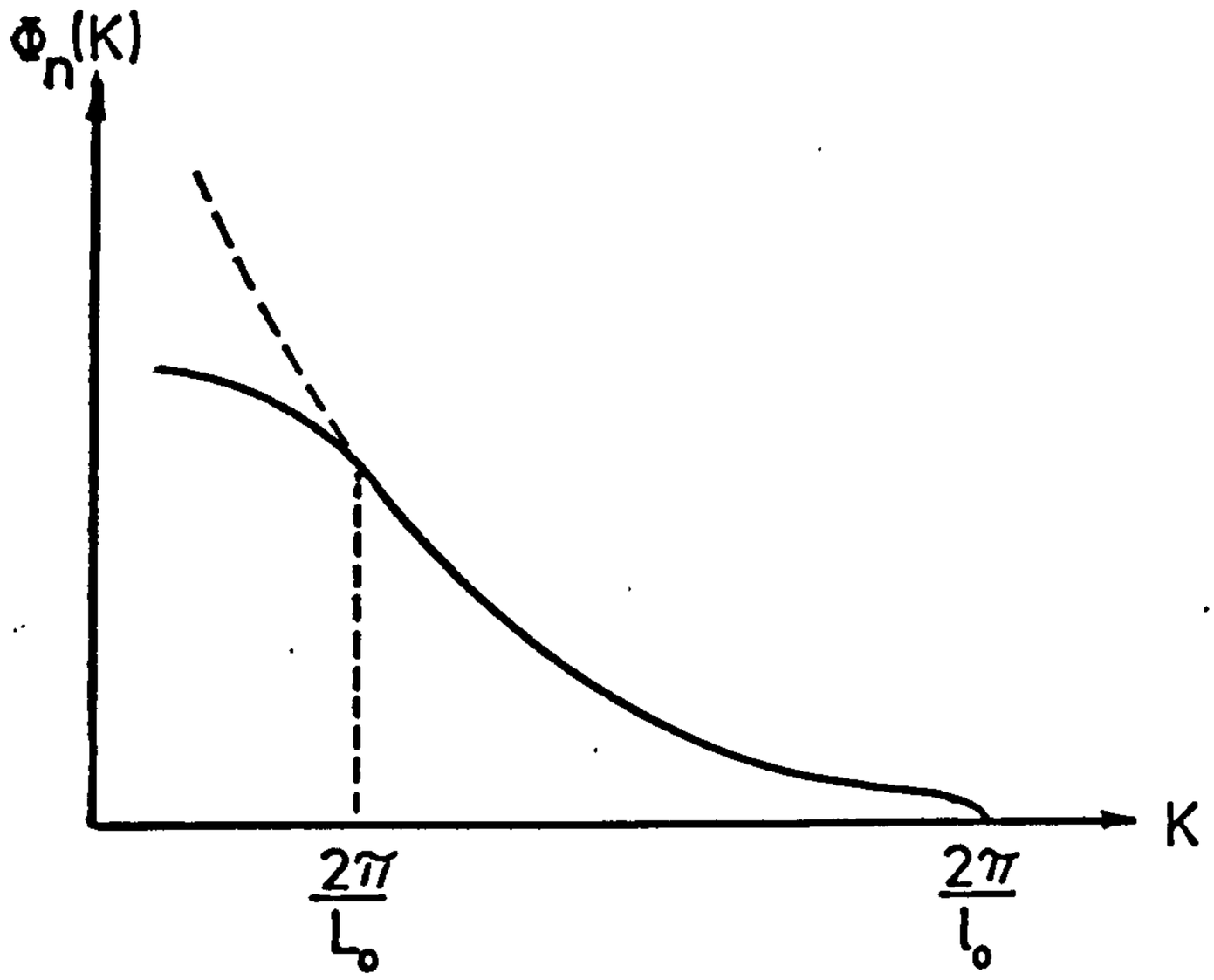

(a)

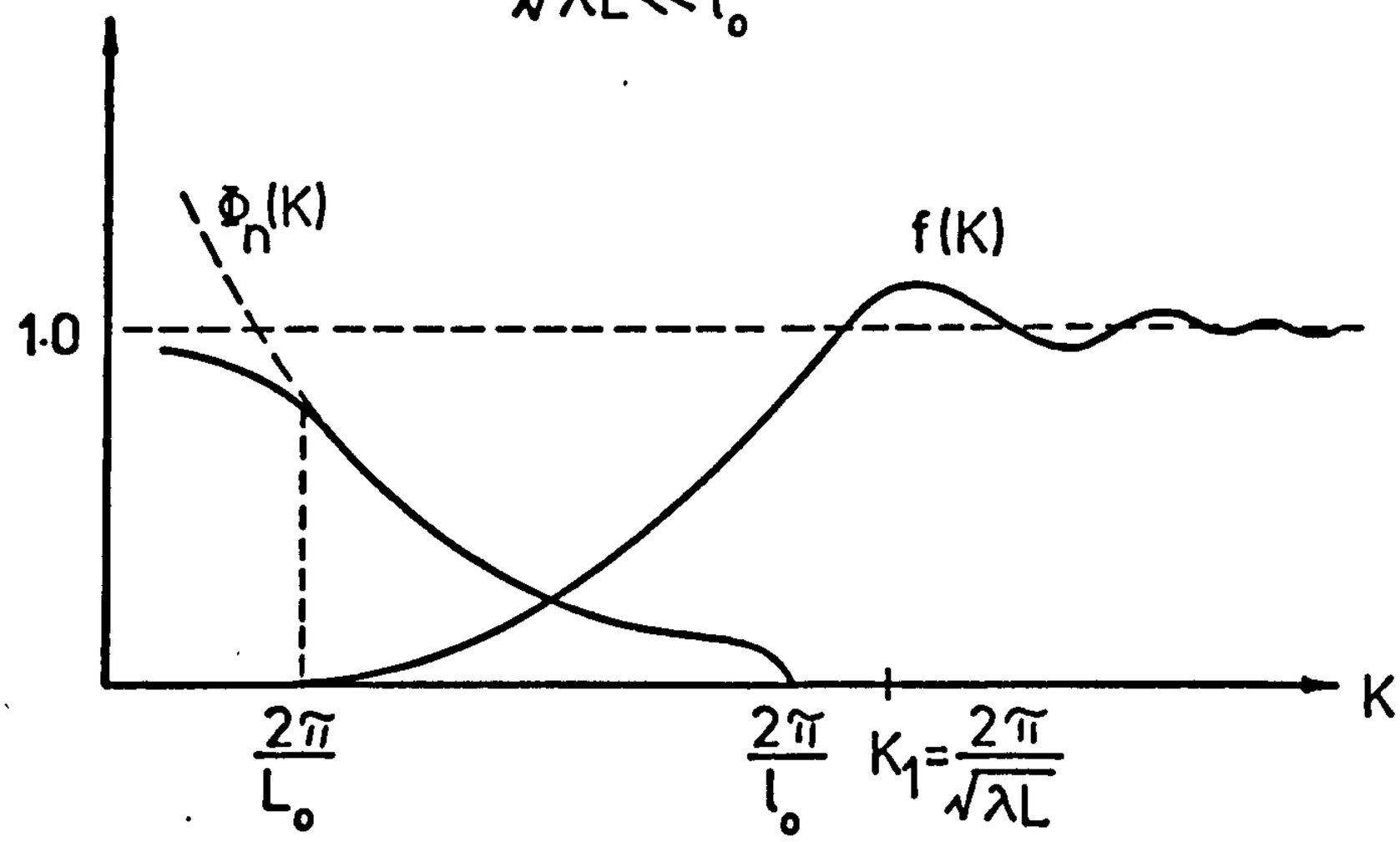

(b)

Fig. 5.1 a Refractive index spectrum

b,c,d Filter factor f(K)

is equal to zero or is negligibly small. For values of K lying between $2\pi/L_o$ and $2\pi/l_o$, $\Phi_n(K)$ grows as K decreases. In the case where the refractive index fluctuations obey the "two-thirds" law, $\Phi_n(K)$ is proportional to $K^{-11/3}$ in this region. For $K < 2\pi/L_o$, the growth of $\Phi_n(K)$ is reduced because the refractive index fluctuations are finite.

If the characteristic scale of the filtering function f(K) is defined as $K_1 = 2\pi/(\lambda L)^{1/2}$, then depending on the size of K_1, different approximation for f(K) can be made such that

$$f(K) \sim \frac{1}{6} \frac{K^4 L^2}{k^2} \qquad \text{for } K \ll K_1$$

5.2.7

$$\text{and} \qquad f(K) \sim 1 \qquad \text{for } K \gg K_1$$

and the following relative position of the points K_1, $2\pi/l_o$ and $2\pi/L_o$ are possible.

(i) $\sqrt{\lambda L} < l_o$

In this case (Figure 5.1b), the spectrum of the correlation function of the amplitude fluctuations $F_A(K,O)$ has a maximum value near the point $2\pi/l_o$ and the refractive index inhomogeneities with scales of order l_o have the greatest influence on the amplitude fluctuations. However, for millimetre wave propagation, $\sqrt{\lambda L}$ is of the order of metres whereas l_o is of the order of millimetres and no further consideration of this case will be given here.

(ii) $l_o \ll \sqrt{\lambda L} \ll L_o$

The situation for the amplitude fluctuations is shown in Figure 5.1c. The product $\Phi_n(K)$ and $f(K)$ has a maximum near the point $2\pi/(\lambda L)^{1/2}$ and goes to zero for $K \geq 2\pi/l_o$. The behaviour of the function $\Phi_n(K)$ for $K < 2\pi/L_o$ has almost no effect on the function $F_A(K,0)$, since in this region, the function $f(K)$ is near zero. Hence, the spectrum of the correlation function of the amplitude fluctuation has a maximum value near the point $2\pi/(\lambda L)^{1/2}$ and the refractive index inhomogeneities with scales of the order of $(\lambda L)^{1/2}$ make the largest contribution to the amplitude fluctuations of the wave. In this range, the complete expression for the spectral density must be used because no approximation for the function $f(K)$ can be made. Thus

$$F_A(K,0) = \pi k^2 L \left(1 - \frac{k}{K^2 L} \sin \frac{K^2 L}{k}\right) \Phi_n(K) \qquad 5.2.5$$

where k is the wave number of the millimetre wave and L is the path length through the turbulence.

If we let the refractive index spectrum function have the form of Equation 5.2.3 in this range, that is

$$\Phi_n(K) = AK^{-(p+3)}$$

Then

$$E_A(K,0) = \begin{cases} AK^{-(p+3)}\pi k^2 L \left(1 - \frac{k}{K^2 L} \sin \frac{K^2 L}{k}\right) & K < K_m' \\ 0 & K > K_m' \end{cases} \qquad 5.2.8$$

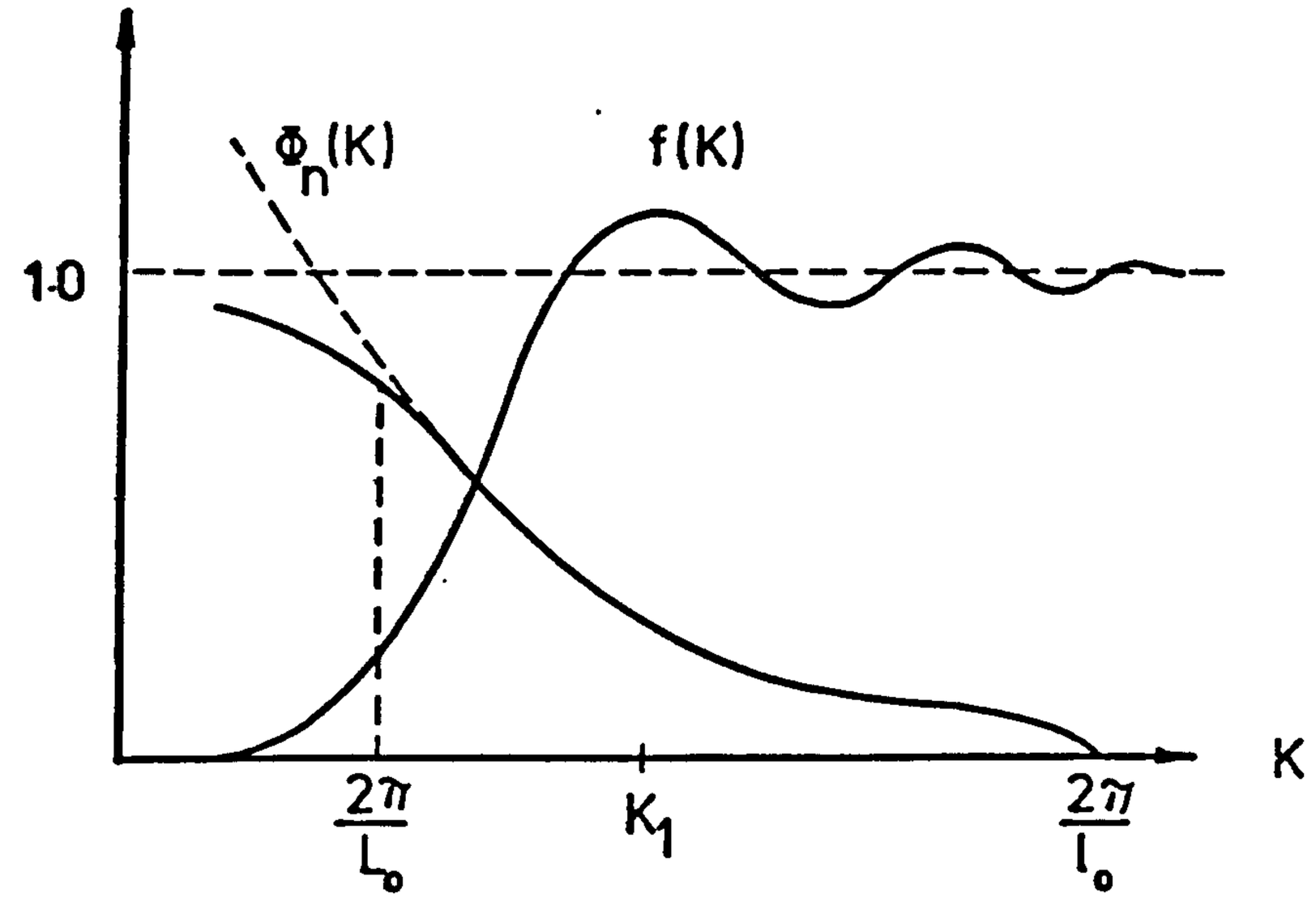

(c) $l_0 \ll \sqrt{\lambda L} \ll L_0$

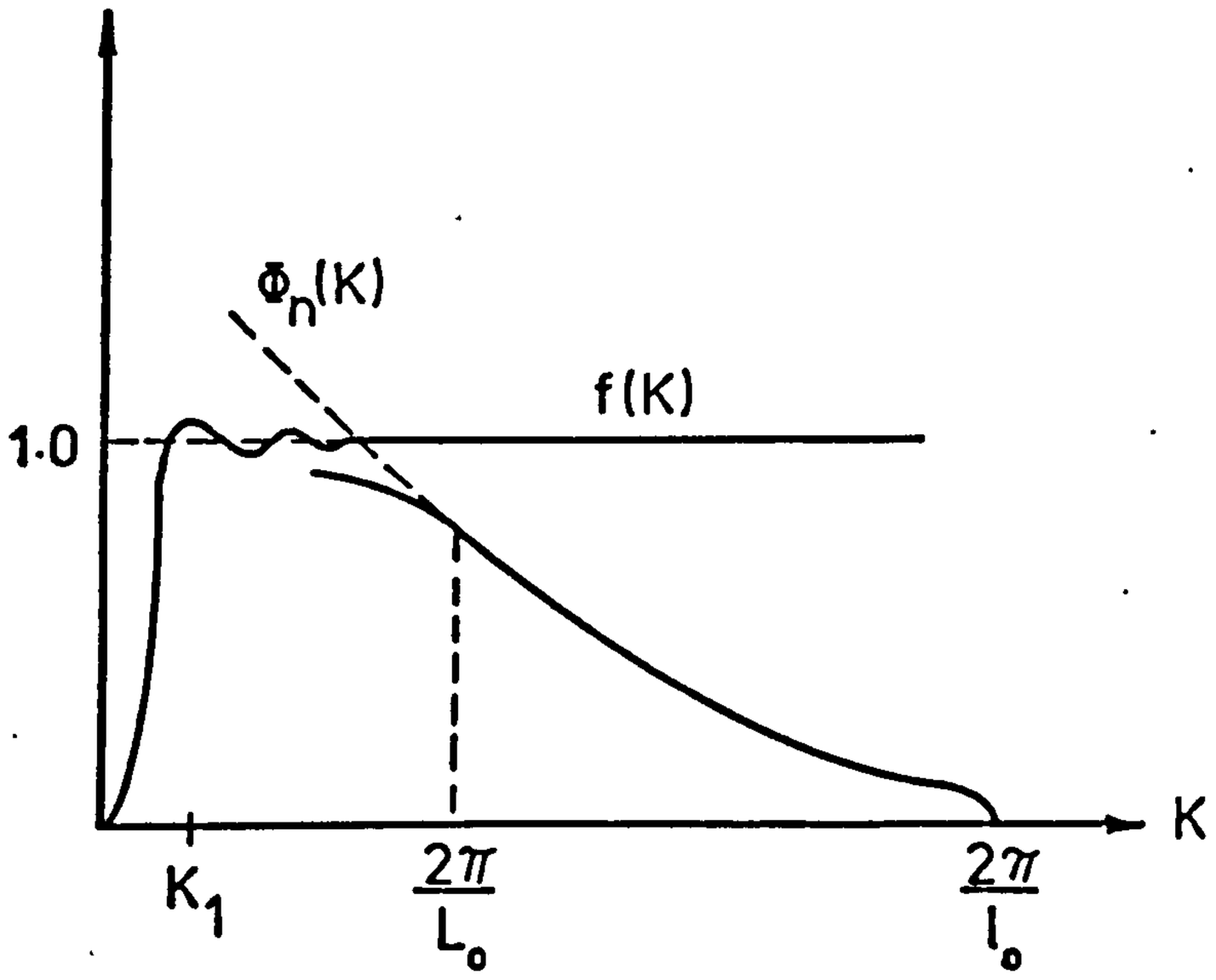

(d) $\sqrt{\lambda L} > L_0$

Fig. 5.1

The correlation function of the amplitude fluctuations is obtained by substituting Equation 5.2.8 into Equation 5.2.4

$$B_A(\rho) = 2\pi^2 A k^2 L \int_o^\infty J_o(K\rho)\ (1 - \frac{k}{K^2 L} \sin \frac{K^2 L}{k})\ K^{-(p+2)}\ dK \qquad 5.2.9$$

The variance of the logarithmic amplitude fluctuations thus becomes

$$\chi^2 = B_A(0) = 2\pi^2 A k^2 L \int_o^\infty (1 - \frac{k}{K^2 L} \sin \frac{K^2 L}{k})\ K^{-(p+2)}\ dK \qquad 5.2.10$$

Let $$\eta = \frac{K^2 L}{k} \qquad 5.2.11$$

and $$d\eta = \frac{2L}{k} K\ dK$$

then Equation 5.2.10 can be written as

$$\chi^2 = 2\pi^2 A k^2 L \int_o^\infty (1 - \frac{\sin\eta}{\eta})(\frac{k}{2L})(\frac{k\eta}{L})^{-(p+3)/2}\ d\eta$$

$$= 2\pi^3 A k^{(3/2 - p/2)} L^{(3/2 + p/2)} \left[\Gamma(5/2 + p/2) \cdot \sin \frac{(3/2 - p/2)}{2}\right]^{-1} \qquad 5.2.12$$

For infinite plane wave propagation, the logarithmic amplitude variance exhibits a $k^{(3/2 - p/2)}$ wave number dependence and a $L^{(3/2 + p/2)}$ range dependence.

In particular, if the refractive index of the atmosphere

obeys the two-thirds law, that is (Section 2.2)

$$\Phi_n(K) = \begin{cases} 0.033\ C_n^2\ K^{-11/3} & \text{for } K < K_m' \\ 0 & \text{for } K > K_m' \end{cases} \qquad 5.2.13$$

Equation 5.2.12 is reduced to (Tatarski 1961b)

$$\chi^2 = 0.31\ C_n^2\ k^{7/6}\ L^{11/6} \qquad 5.2.14$$

(iii) $\sqrt{\lambda L} \gtrsim L_o$

The situation is shown in Firure 5.1d. The chief contribution to the spectrum $F_A(K,O)$ is made by large inhomogeneities in the interval $(L_o, \sqrt{\lambda L})$. However in the range of scales exceeding L_o, the refractive index field is not locally homogeneous and istropic, so it is necessary to limit the amplitude fluctuation spectrum $F_A(K,O)$ for $K > 2\pi/L_o$.

In this region, the function f(K) is approximately equal to 1. Therefore,

$$F_A(K,O) = \pi k^2 L\ \Phi_n(K) \qquad \text{for } K \gtrsim \frac{2\pi}{L_o} \qquad 5.2.15$$

If it is assumed that the random refractive index field is statistically homogeneous and isotropic for all scales (as pointed out by Tatarski (1961b), such an assumption is made

because it considerably simplies the solution of the problem despite the fact that it is in fact not adequately justified in practice), then the field of the amplitude fluctuations of the wave in the plane x = L are also homogeneous and isotropic. Therefore, the correlation function is given by

$$B_A(\rho) = 2\pi^2 k^2 L \int_o^\infty J_o(K\rho)\, \Phi_n(K)\, K\, dK \qquad 5.2.16$$

The correlation function of the random refractive index field $B_n(r)$ and $\Phi_n(K)$ are related through Equation 2.1.7, that is

$$\Phi_n(K) = \frac{1}{2\pi^2 K} \int_o^\infty B_n(r) \sin(Kr)\, r\, dr \qquad 5.2.17$$

Tatarski (1961b) showed that for a wave propagating in the x direction, the correlation function is thus given by

$$B_A(\rho) = k^2 L \int_o^\infty B_n\left(\sqrt{\rho^2 + x^2}\right) dx \qquad 5.2.18$$

and the mean square amplitude fluctuations is

$$\chi^2 = B_A(0) = k^2 L \int_o^\infty B_n(x)\, dx \qquad 5.2.19$$

Let $L_n = \frac{1}{B_n(0)} \int_o^\infty B_n(x)\, dx = \frac{1}{\overline{(n_1^2)}} \int_o^\infty B_n(x)\, dx$, which is called the integral scale of the turbulence and agrees in order of magnitude with L_o (Tatarski 1961b), Equation 5.2.19 can be rewritten as

$$\chi^2 = \overline{(n_1^2)}\, k^2 L\, L_n \qquad 5.2.20$$

The logarithmic amplitude variance thus exhibits a k^2 wave number dependence.

5.3 The test of log-normality of millimetre wave fluctuations

The application of the central limit theorem in the derivation of the log-amplitude equations leads to a prediction of a log-normal distribution of the amplitude, that is χ has a normal distribution. Some workers, on either intuition or other grounds have argued for a Rayleigh or a Rice-Nakagami distribution for amplitude fluctuations (de Wolf 1967, 1968). Experimental results seem to support the claim for a log-normal distribution (Fried et al 1967).

From a physical point of view, in a line-of-sight case when the receiver is located in the turbulent medium, the received field is the result of mulitplicative effects. Consider the turbulent medium as composed of a large number of slabs (n) of the order of the outer scale size (Strohbehn 1968) orientated perpendicular to the direction of propagation. After passing through the first slab, the field can be represented as the original field A_o, multiplied by a random modulation $M_1(t)$, giving a field $A_1(t) = M_1(t)\ A_o$. As the field $A_1(t)$ passes through the second slab, it is further randomly modulated. As a result, the field at the receiver may be represented as

$$A_r(t) = M_n(t)\ M_{n-1}(t)\ \ldots\ldots\ M_2(t)\ M_1(t)\ A_o \qquad 5.3.1$$

Defining $\chi_r(t) = \log A_r(t) = \log A_o + \sum_{i=1}^{n} \log M_i(t)$, it can be seen that $\chi_r(t)$ is composed of the sum of a large number of independent components and therefore has a Gaussian distribution (by virtue of the Central Limit theorem). That is, the logarithmic of the amplitude has a Gaussian or normal distribution.

Figures 5.2 and 5.3 show the log-amplitude fluctuations of the 8.33mm and 2.73mm waves over a period of 25 seconds respectively and Figures 5.4 and 5.5 show the typical cumulative probability plots of the log-amplitudes on Gaussian probability paper. The ordinate is the log-amplitude (in dB) and the abscisss is P(w); where

$$P(w) = \int_{-\infty}^{w} Q(u)\, du \qquad 5.3.2$$

and Q(u) is the probability density function for log-amplitude. The abscissa scale is constructed such that a normal random variable would give a straight line plot. It is clear that the probability distributions of both wavelengths (8.33mm and 2.73mm) are almost linear when plotted on log-normal probability paper and therefore satisfy the test for log-normality.

5.4 The ratio $\sigma^2_{110} / \sigma^2_{36}$ experiment

5.4.1 Experimental details

The aim of this experiment is to verify the wave-length

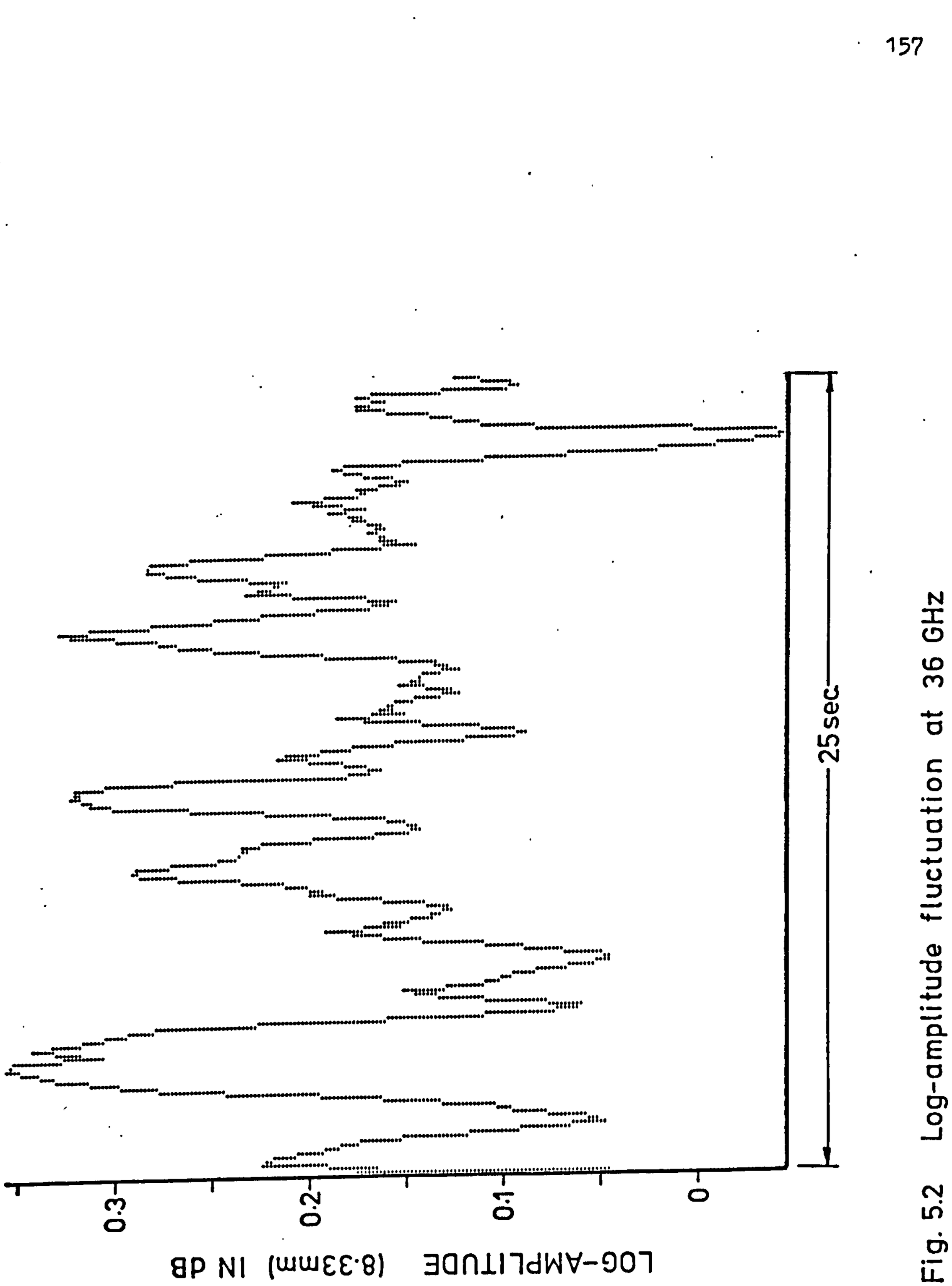

Fig. 5.2 Log-amplitude fluctuation at 36 GHz

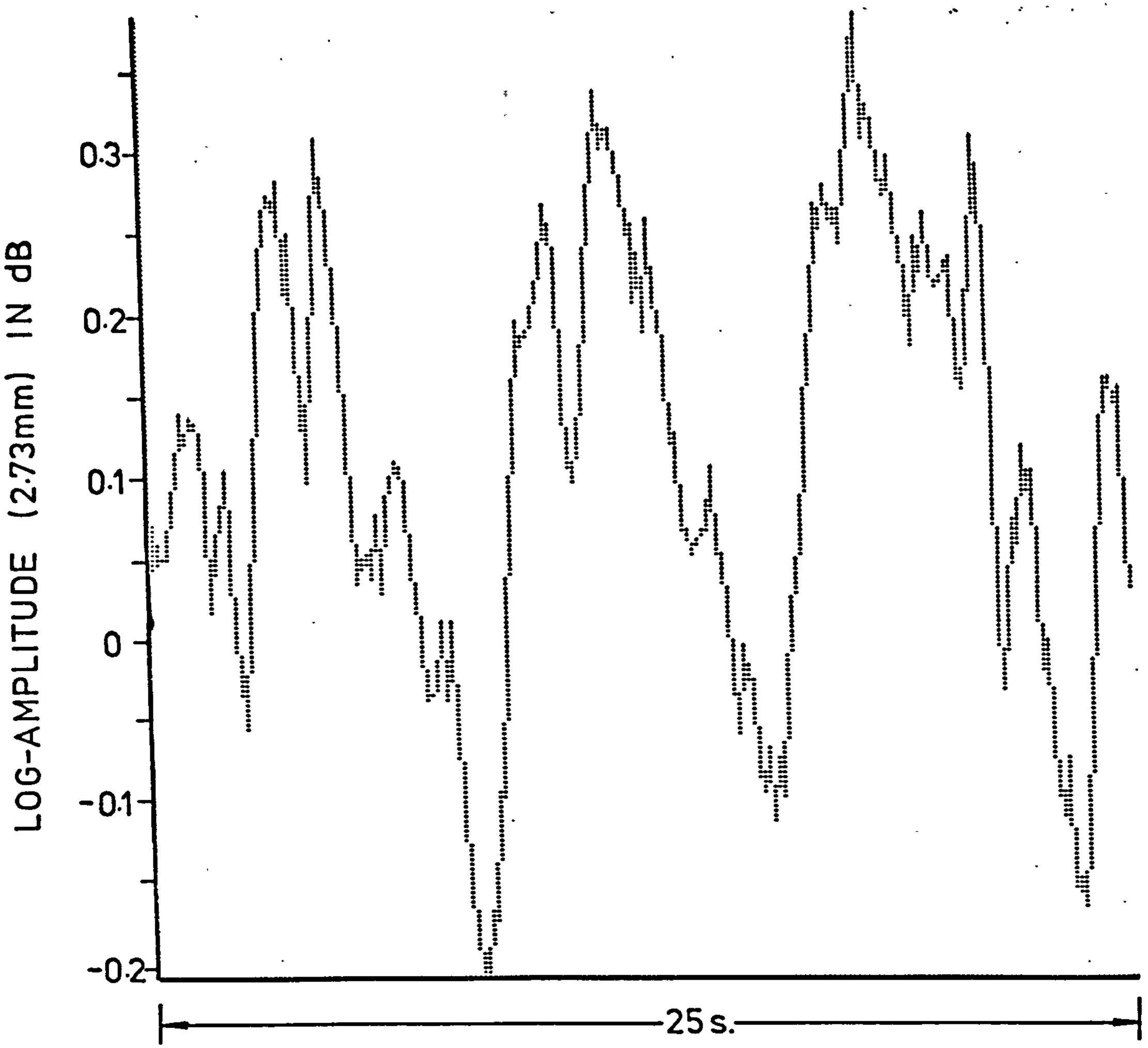

Fig. 5.3 Log-amplitude fluctuations at 110 GHz

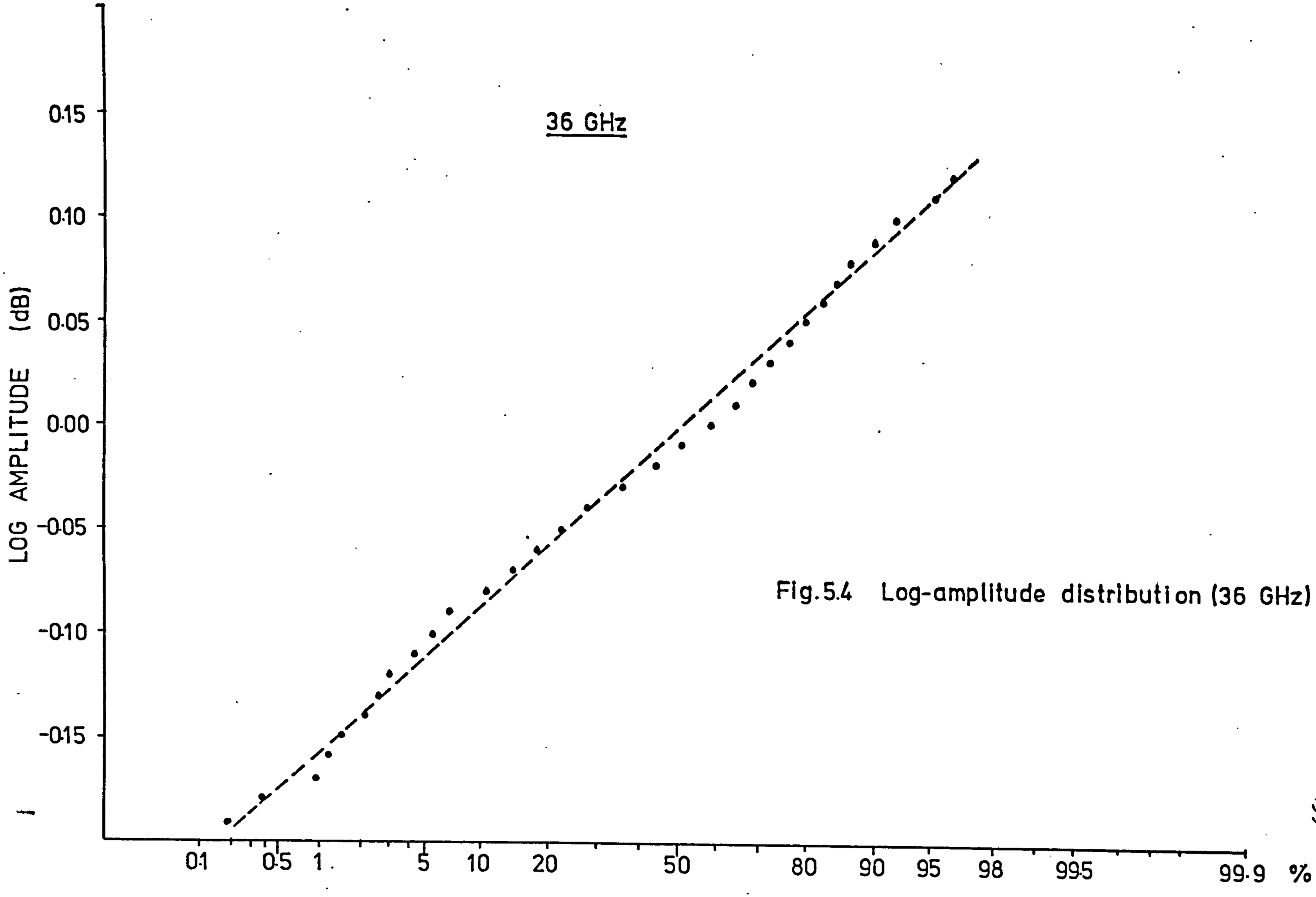

Fig.5.4 Log-amplitude distribution (36 GHz)

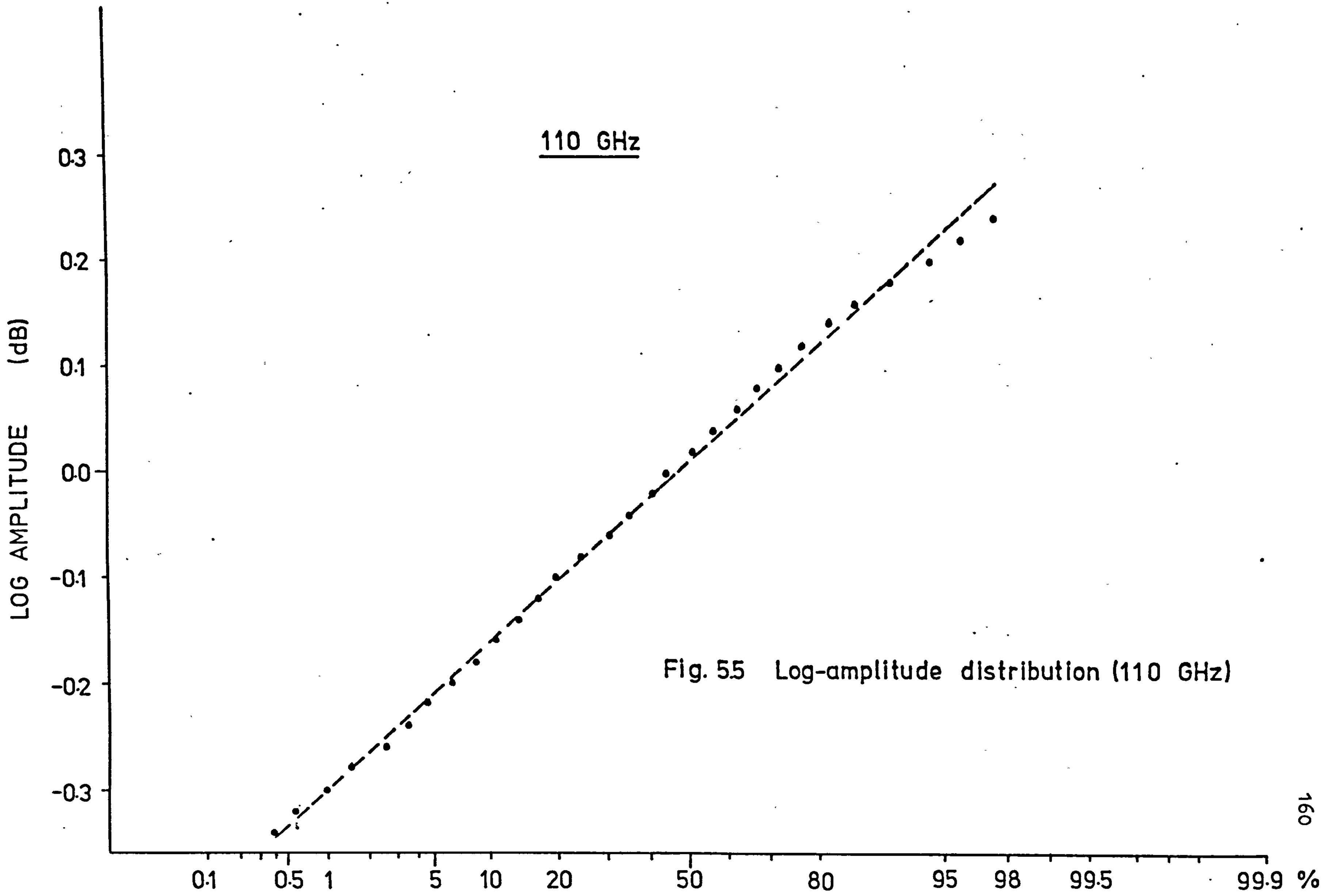

Fig. 5.5 Log-amplitude distribution (110 GHz)

dependence of the amplitude fluctuations. The two frequencies used in this experiment were 36 GHz (λ = 8.33mm) and 110 GHz (λ = 2.73mm). The two links which share exactly the same path, is 4.1 Km in length. The meteorological station is located at the receiving end of the links (U.C.L.) where records of the amplitude fluctuations, temperature, humidity and wind speed were made.

Since the formulae derived in Section 5.2 are for amplitude fluctuations $\chi^2 = (\ln A/A_o)^2$ and the measured signal fluctuations are calibrated in dB, so Equations 5.2.14 and 5.2.20 are converted to (Appendix 5.1)

$$\sigma^2_{signal} = 23.39\ C_n^2\ k^{7/6}\ L^{11/6} \quad (dB^2) \qquad 5.4.1$$

for $l_o < \sqrt{\lambda L} < L_o$

and $$\sigma^2_{signal} = 75.45\ n_1^2\ k^2\ L\ L_n \quad (dB^2) \qquad 5.4.2$$

for $\sqrt{\lambda L} > L_o$

The variances of the amplitude fluctuations of the two links were computed from groups of 600 samples over 15 seconds (sampling frequency is 40 Hz) in the time series. Normally, the duration of each experiment lasted at least for one and a half hours. The results are presented as the ratio of the amplitude variance of the 110 GHz to the amplitude variance of the 36 GHz, that is $\sigma^2_{110}/\sigma^2_{36}$ versus the variance of the 36 GHz.

The results presented in this chapter are from experiments carried on Saturdays and Sundays. Experimental results obtained during weekdays are not suitable for the purpose of this experiment because of the artifical fluctuations produced by the hot air coming from an air-conditioning plant below the propagation path (Section 8.2). Figure 5.6 shows the typical amplitude fluctuations of the two frequencies recorded on charts.

Spectra of the temperature were produced (Section 5.4.2) every 15 minutes. Theoretically, the spectra of the refractive index should be used, but, unfortunately, the refractometer was not in operation during this period of the experiment. However, Gjessing et al (1972) have plotted the slopes of measured humidity and refractive index spectra against temperature spectrum slopes for frequencies in the range 0.1 to 1 Hz (when reduced to scale size using the mean wind speed, the 1 Hz points varies over 1 to 10 metres) and found that although the slopes vary over a wide range, the plotted points tend to lie along a 45 degree line indicating that on many occasions the spectrum slopes and hence the outer scale size are well represented by the corresponding temperature spectrum alone. Figures 5.7 shows this result. Moreover, Tatarski (1961a) has showed mathematically that the forms of the meteorological parameter spectrum are the same, differing only by a constant (Section 2.2). Thus the use of the temperature spectra in this experiment appears to be justified.

The scale sizes were calculated from the one-dimensional

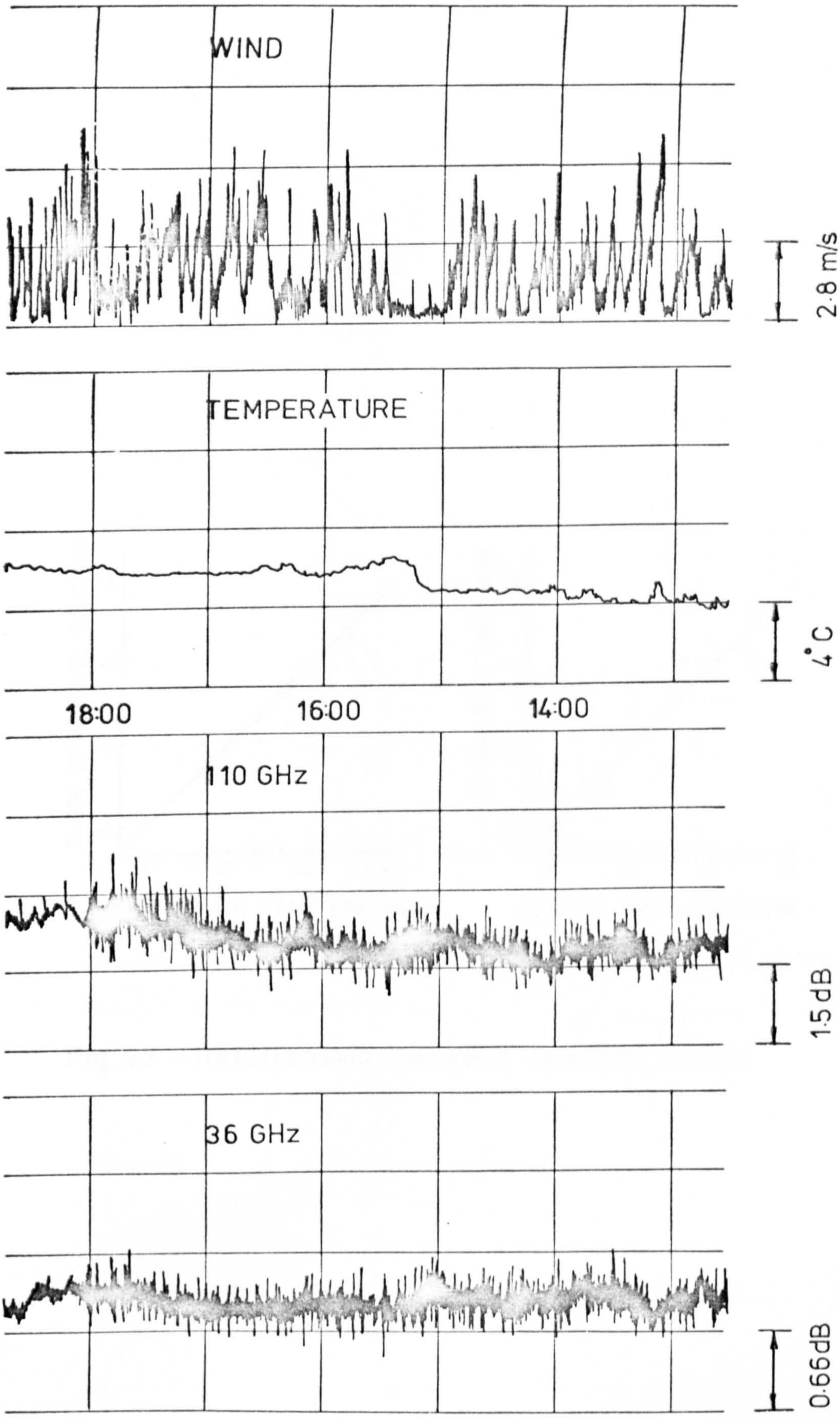

Fig. 5.6 A chart record of signals, temp. and wind

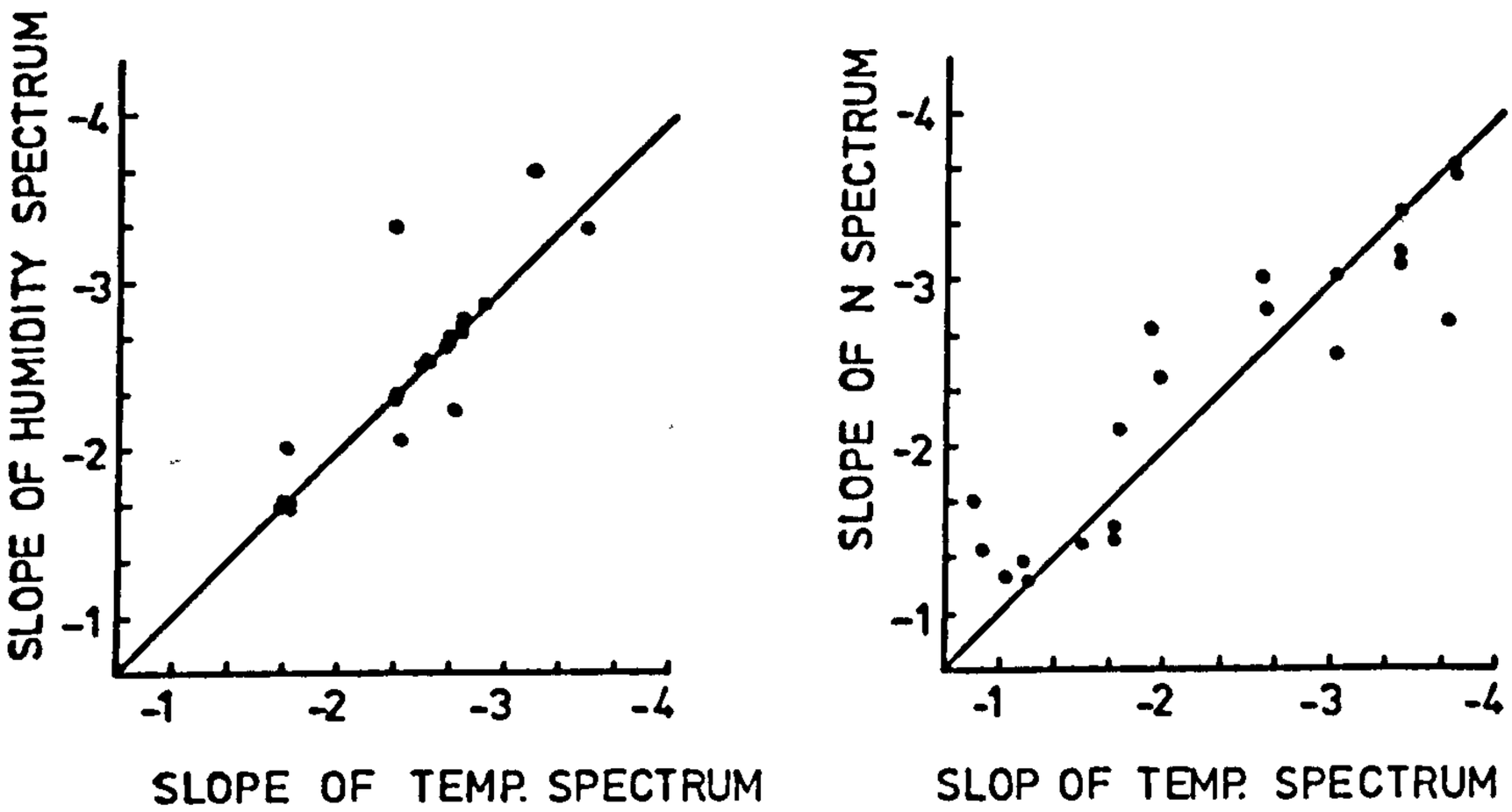

Fig. 5.7 Relationship between spectral slopes

frequency spectra of the temperature by using the relation

$$l = \frac{\overline{V}}{f}$$

where l is the scale size

$\overline{V}$ is the mean wind speed at the location of the temperature sensor during the measurement.

f is the frequency obtained from the temperature frequency spectra.

Based on Equations 5.4.1 and 5.4.2, the theoretical values of the ratio of the log-amplitude variances at 110 GHz and 36 GHz should be

$$\sigma^2_{110} / \sigma^2_{36} = \left(\frac{8.33}{2.73}\right)^{7/6} = 3.68 \qquad \text{for } \sqrt{\lambda L} < L_o$$

and

$$\sigma^2_{110} / \sigma^2_{36} = \left(\frac{8.33}{2.73}\right)^{2} = 9.33 \qquad \text{for } \sqrt{\lambda L} \gtrsim L_o$$

In order to show the correlation between the amplitude fluctuations at the two frequencies, plots of the variances are also presented.

5.4.2 Results

5.4.2.1 Condition: $\sqrt{\lambda L} < L_o$; temperature spectrum slope $\sim -5/3$

Figure 5.8 shows results of measurements taken over

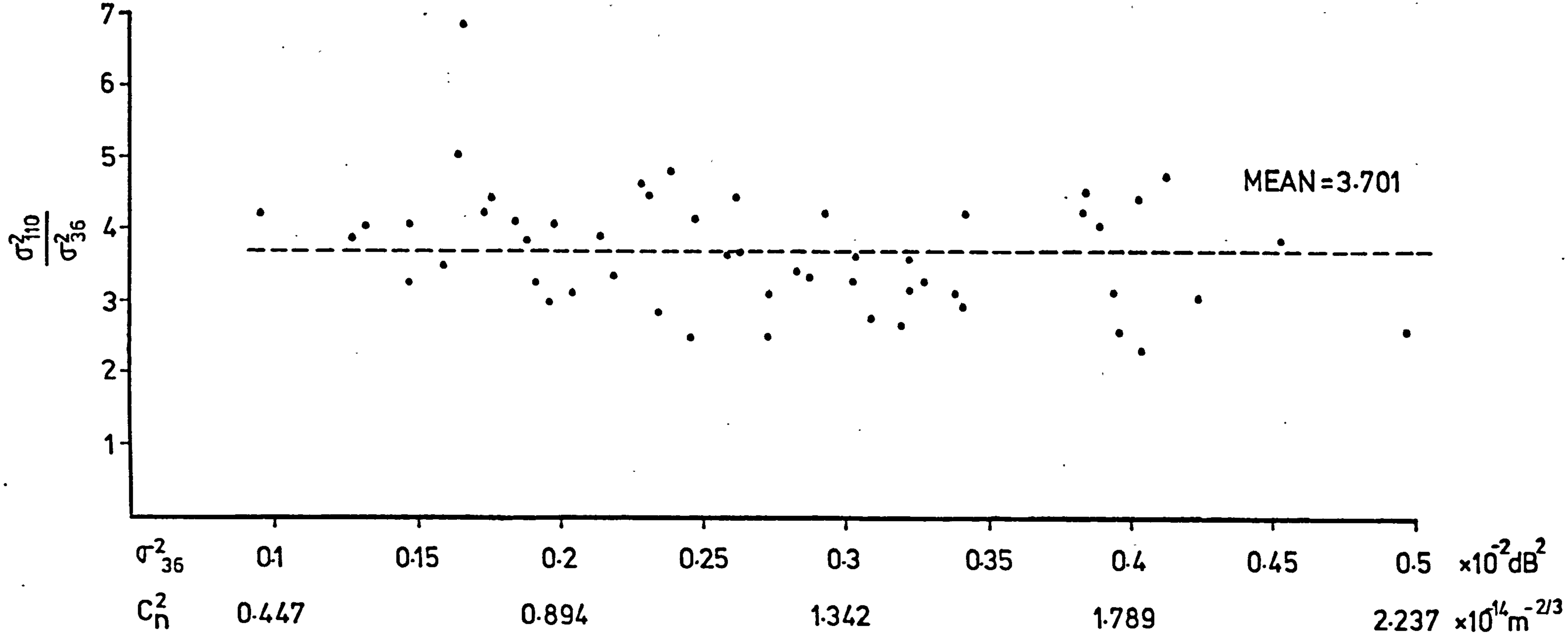

Fig. 5.8 Ratio of variances of amplitude fluctuations $\sigma^2_{110}/\sigma^2_{36}$ against σ^2_{36} and C_n^2.

a one and half hour period (from 8:40 to 10:10 GMT) on 11th July 1976. Plotted along the ordinate is the ratio $\sigma^2_{110} / \sigma^2_{36}$ defined as the ratio of the log-amplitude variances at 110 GHz and 36 GHz. The absicssa is the log-amplitude variances for the 36 GHz and the calculated values of C_n^2 (Equation 5.2.14). The mean value obtained is 3.701. The log-amplitude variance of the 36 GHz was seen to be within the range 0.09 x 10^{-2} dB^2 to 0.55 x 10^{-2} dB^2. It can be seen that the data points are distributed fairly uniformly about the mean value line. The highest ratio obtained in this set of data is 6.81 and the lowest 2.3.

Figure 5.9 shows the plots of the log-amplitude variance of both frequencies against time. It can be seen that they are very well correlated.

Figure 5.10 shows one of the temperature spectra taken during the same period of time. The slope of this spectrum is estimated to be very close to -5/3 (i.e. it satisfies the two-thirds law) and the inertial subrange starts at a frequency of about 0.154 Hz which corresponds to a scale size of about 23 m (the mean wind speed during this period was 3.68 m/s). Analysis of six temperature spectra at different times during the period of measurements shows that the spectrum slopes have a fairly constant value and deviate only slightly from the mean value of -5/3. The mean value of the outer scale size from all the spectra was estimated to be of the order of 25 metres.

5.4.2.2 Condition: $L \gtrsim L_o$; temperature spectrum slope $\sim$ -5/3

Fig. 5.9 Variances of amplitude fluctuations at 36 GHz and 110 GHz against time

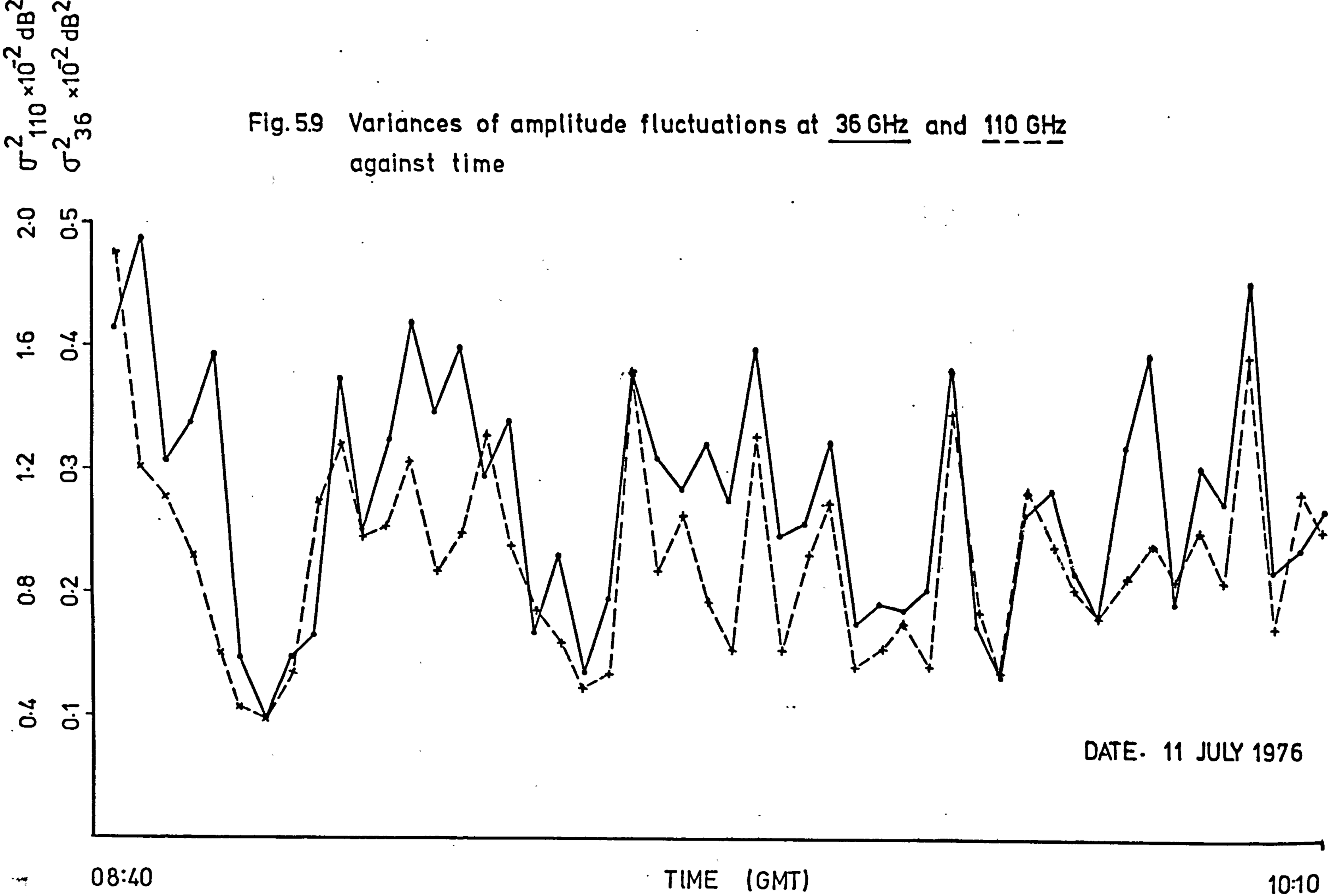

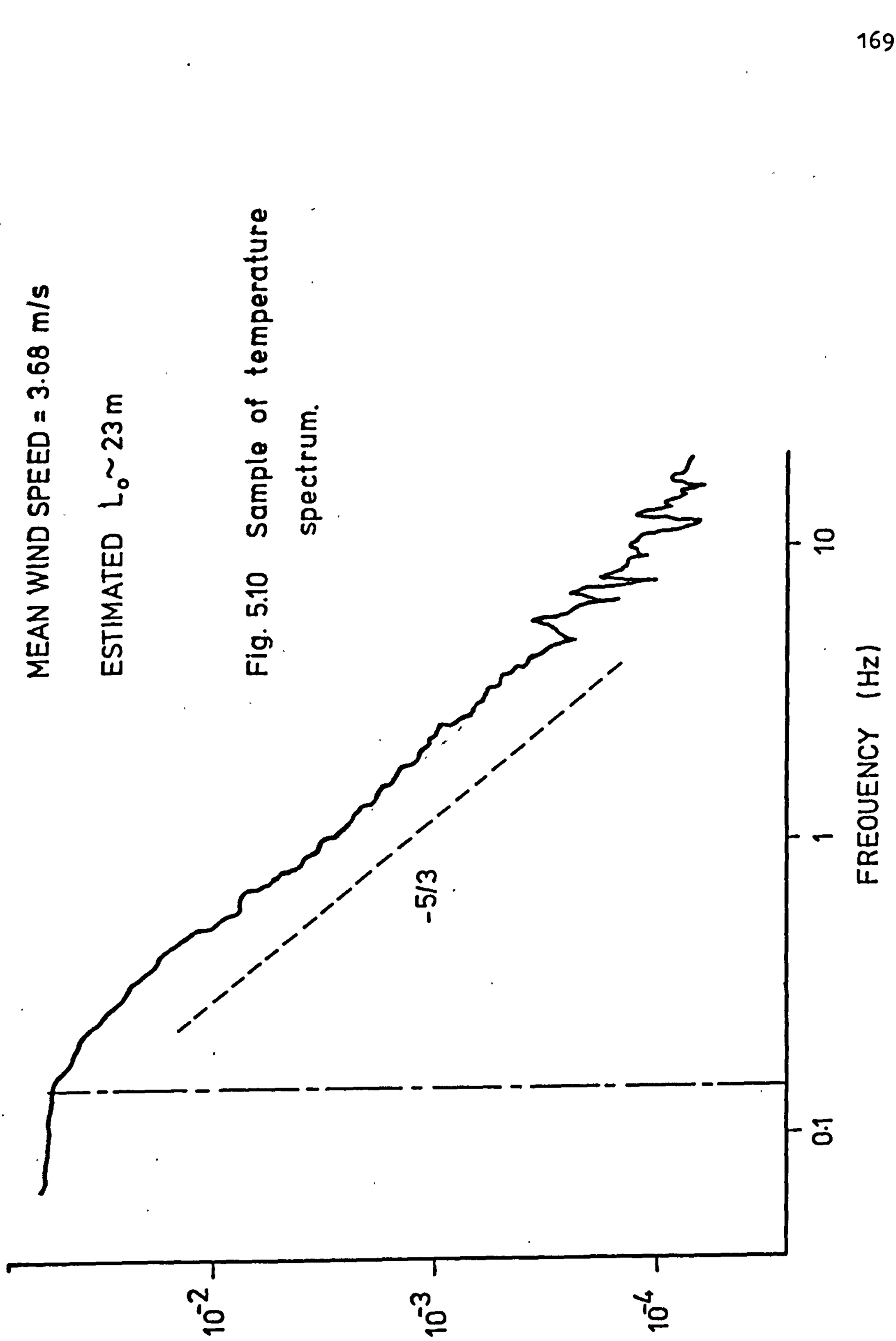

Fig. 5.10 Sample of temperature spectrum.

This set of data was taken on the 24th July 1976 from 15:00 to 16:30 GMT (Figure 5.11). It gives a completely different mean ratio value of 9.81 with the highest ratio of 13.5 and the lowest of 4.3. The log-amplitude variance for the 36 GHz was found to be confined to the range 0.05×10^{-2} dB^2 to 0.7×10^{-2} dB^2.

Figure 5.12 shows the individual plots of the log-amplitude variances against time. The correlation between the two plots is again reasonably good.

Figure 5.13 shows a typical temperature spectrum during this period. The slope is very close to -5/3 but the outer scale size is only 1.9 metres. Analysis of other temperature spectra shows that the mean spectrum slope is about -5/3 and the outer scale size is of the order of 1.5 metres.

5.4.2.3 Condition: L_o undetermined; temperature spectrum slope ~-5/3

Figure 5.14 presents the set of measurements taken on 11th July 1976 from 13:00 to 14:30 BST. The mean ratio value is 5.40. The highest ratio value is 8.75 and the lowest is 3.04. The log-amplitude variance for 36 GHz is within 0.15×10^{-2} dB^2 and 0.7×10^{-2} dB^2.

The two log-amplitude variance plots for the two frequencies are shown in Figure 5.15. It can be seen that the correlation is very good.

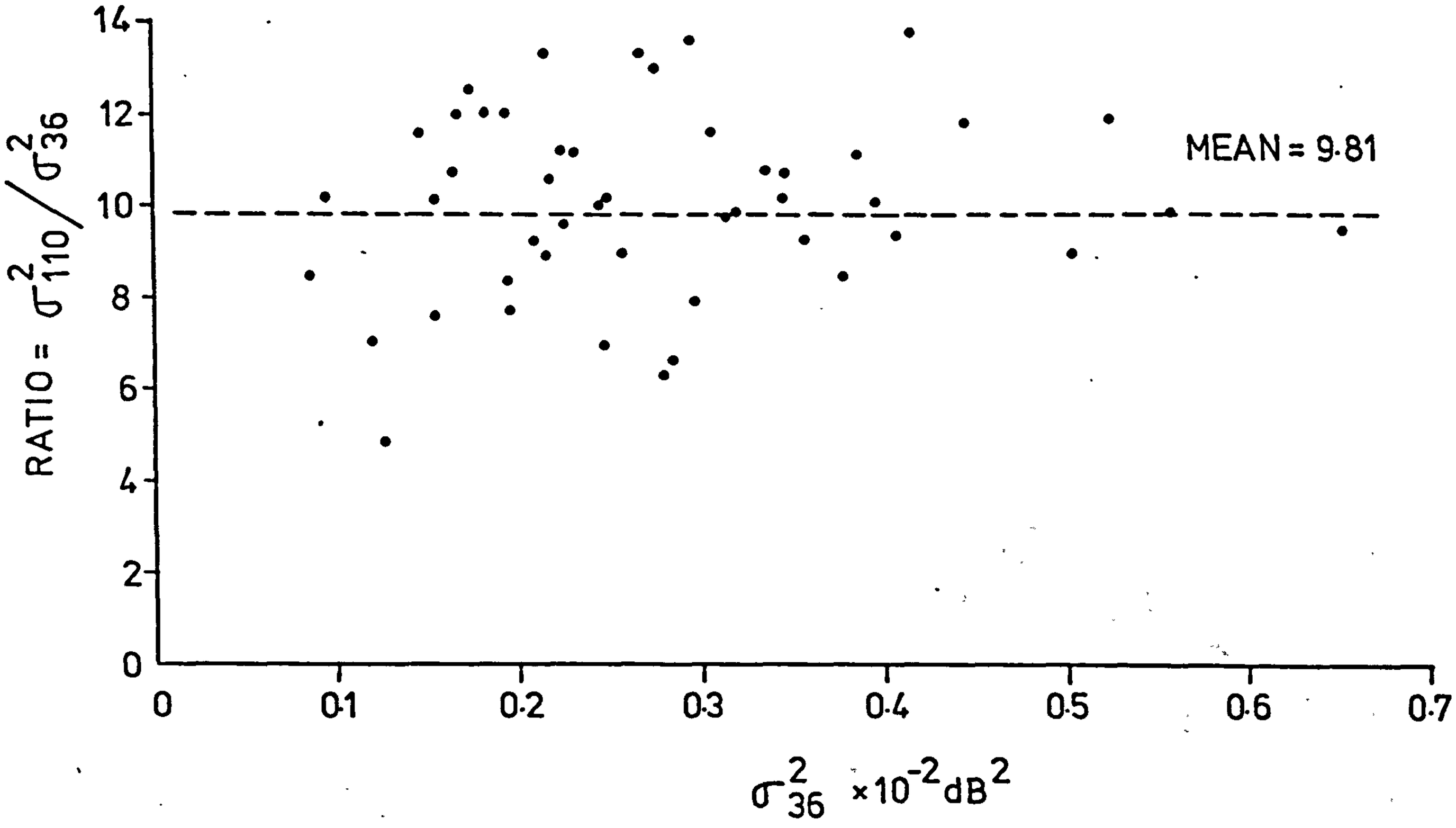

Fig. 5.11 Ratio of variances $\sigma^2_{110}/\sigma^2_{36}$ against σ^2_{36}

Fig. 5.12 Variances of amplitude fluctuations against time

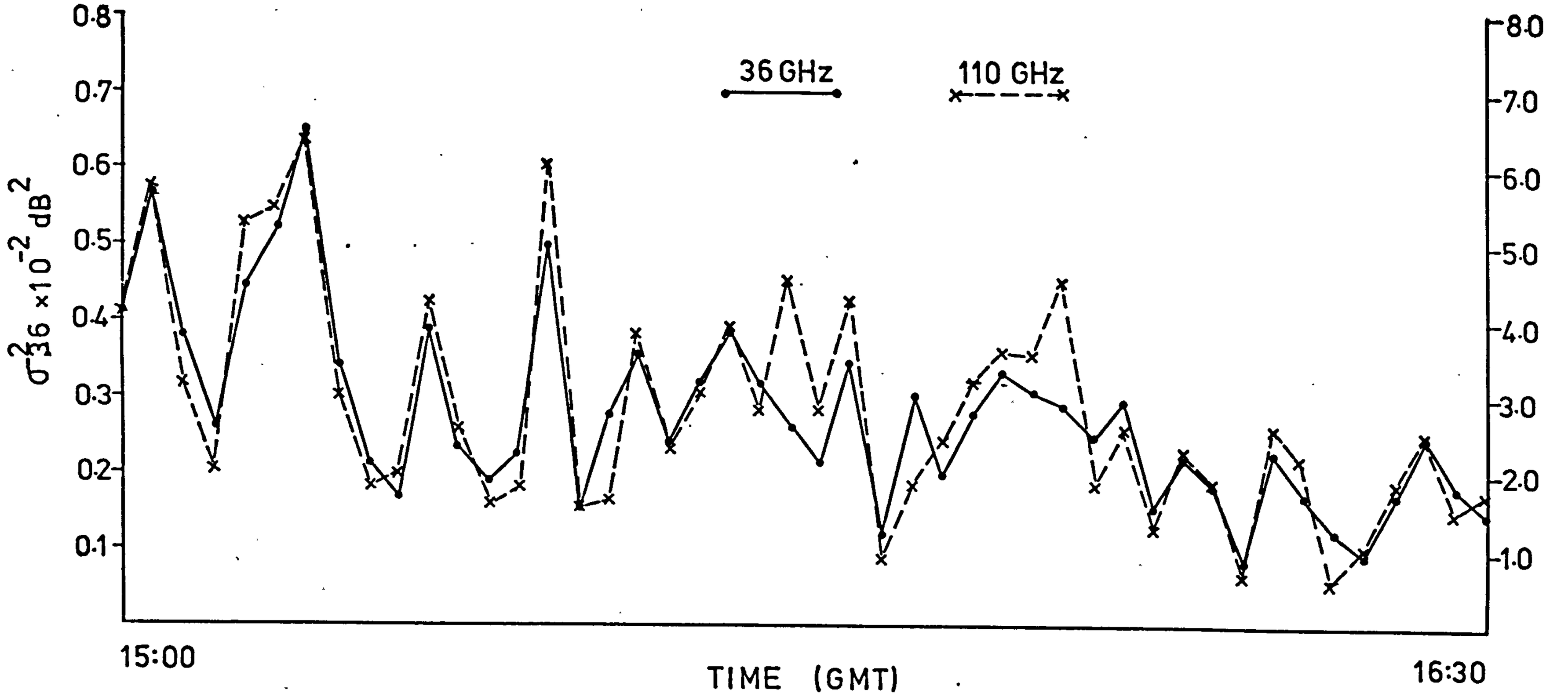

MEAN WIND SPEED = 0.86 m/s

ESTIMATED $L_o \sim 1.9$ m

Fig. 5.13 Sample of temperature spectrum.

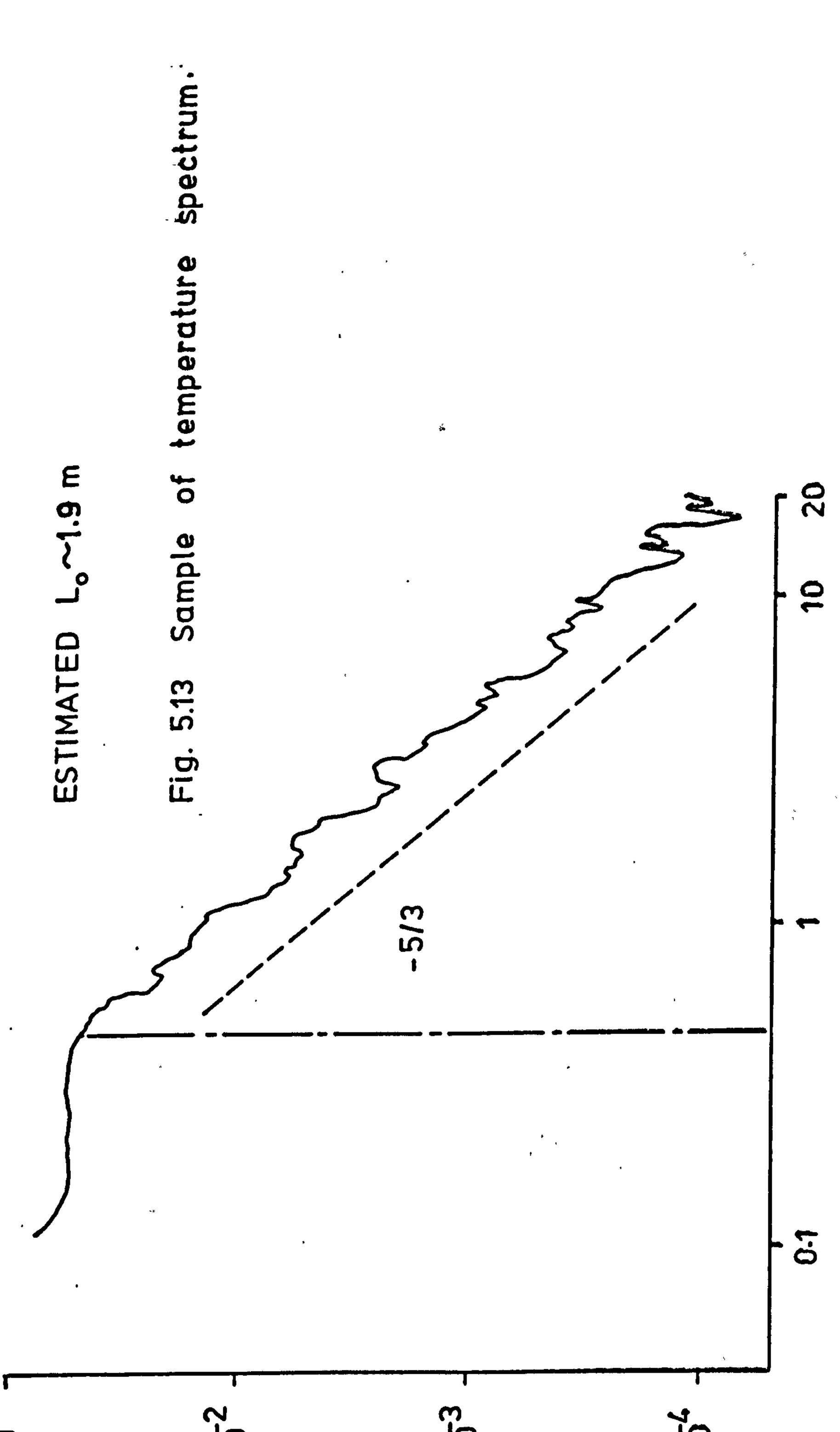

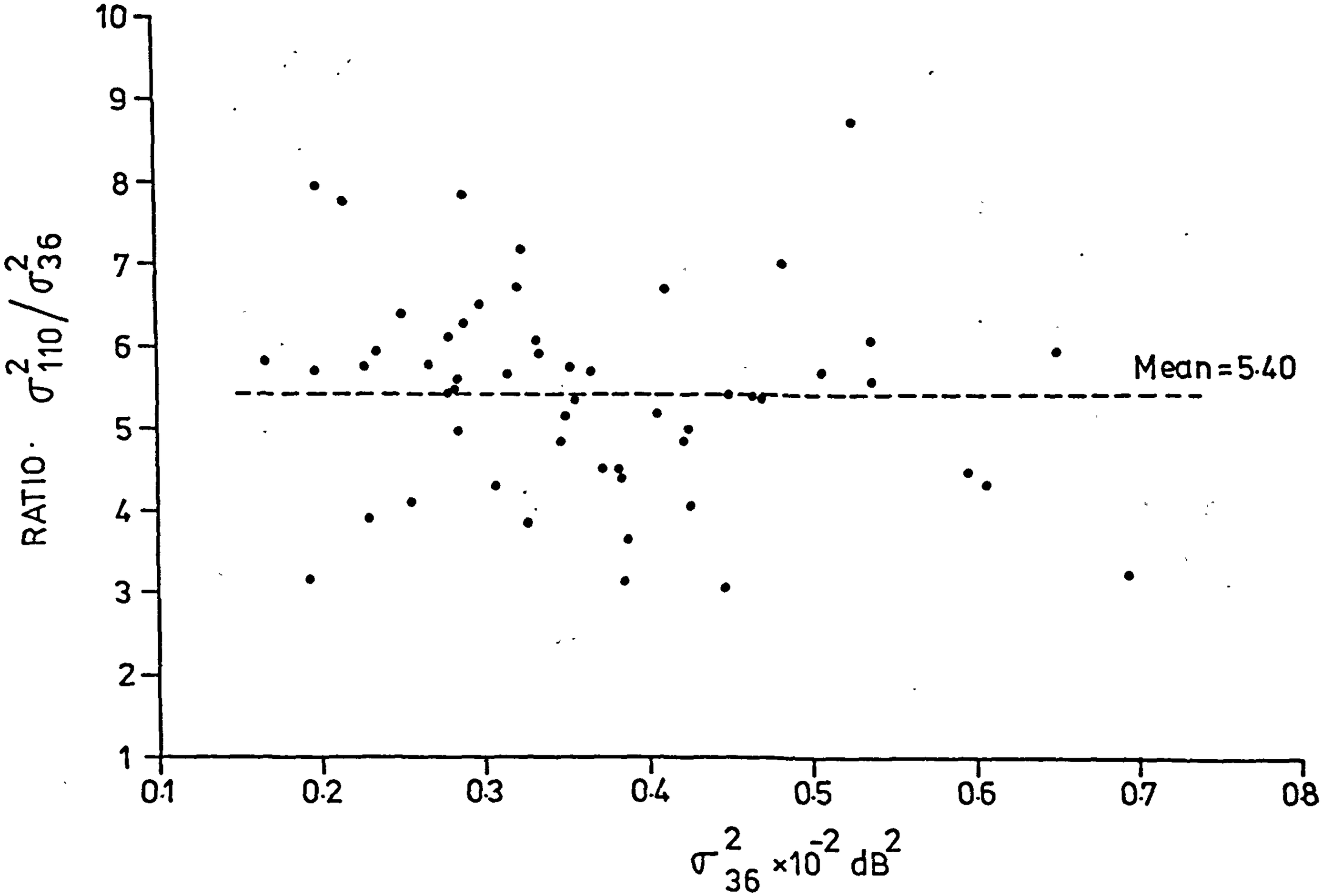

Fig. 5.14 Ratio of variances at 110 and 36 GHz against variance at 36 GHz.

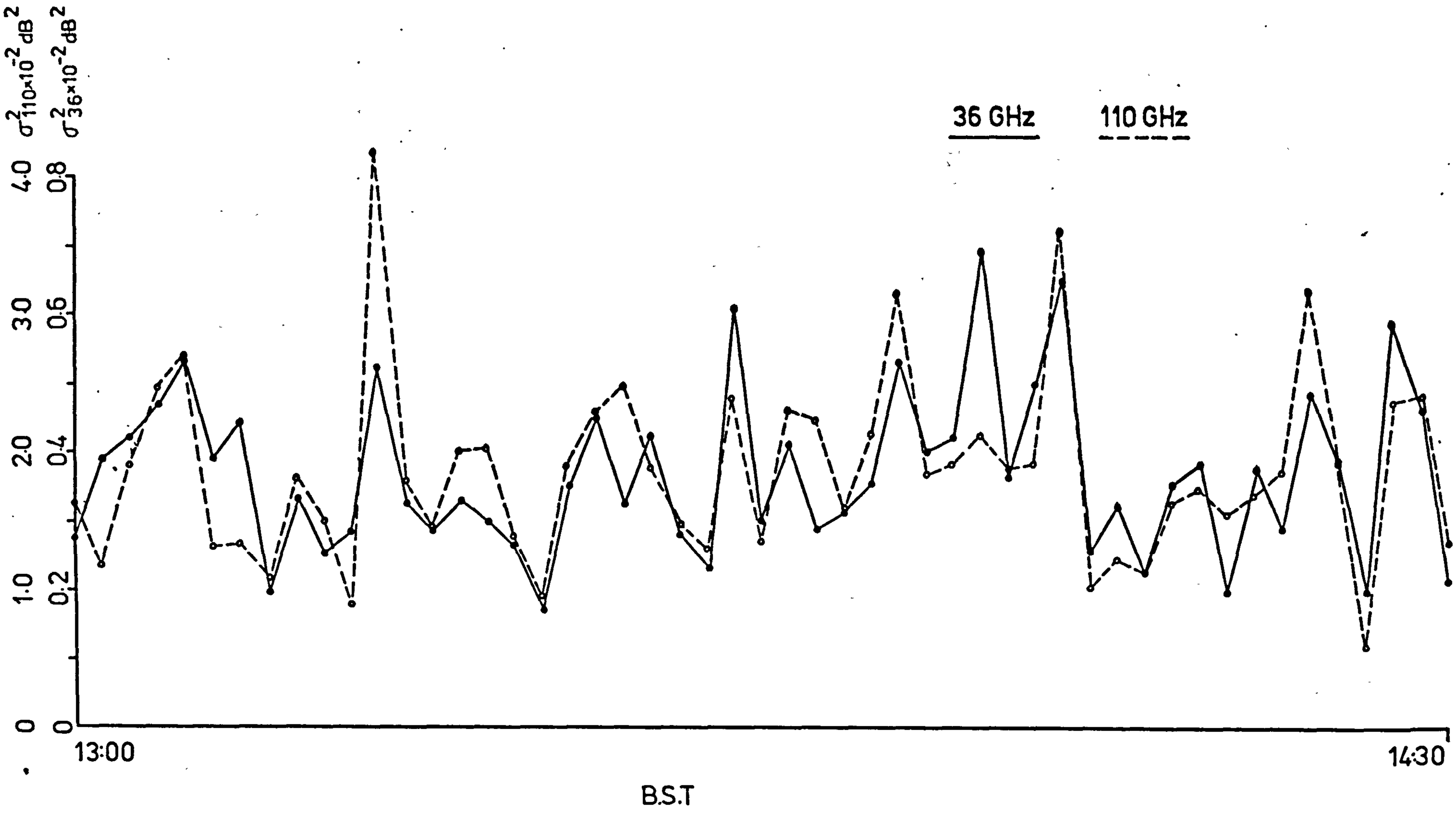

Fig. 5.15 Variances of amplitude fluctuations at 110 and 36 GHz against time.

Figure 5.16 is a typical temperature spectrum taken during the same period. The slope is approximately -5/3 and the outer scale size is about 5 metres in this particular spectrum (the wind speed is about 4m/s). The investigation into other temperature spectra taken during this period shows that the spectral slopes are fairly constant at approximately -5/3 and the outer scale size varies from 2.3 metres to over 50 metres.

5.4.3 Summary

The main points of the results given in the previous section and some other typical results together with calculated values of C_n^2 are summarized in Table 5.1. Other sets of results not presented here show the same trend.

5.4.4 Discussion

It is clear that the wavelength dependence of the amplitude fluctuations of millimetre waves depends very much on the structure of the atmospheric turbulence. The size of the outer scale of the turbulence is of particular importance. Theoretical analysis based on local homogeneity and isotropy shows that the log amplitude fluctuations for plane wave propagation exhibits a $k^{(3/2 - p/2)}$ wave number dependence when $\sqrt{\lambda L}$, the dimension of the first Fresnel zone, is within the range of the dimensions of the inhomogeneities in the inertial subrange that is, $l_o \ll \sqrt{\lambda L} \ll L_o$ and exhibits a k^2 wave number dependence when

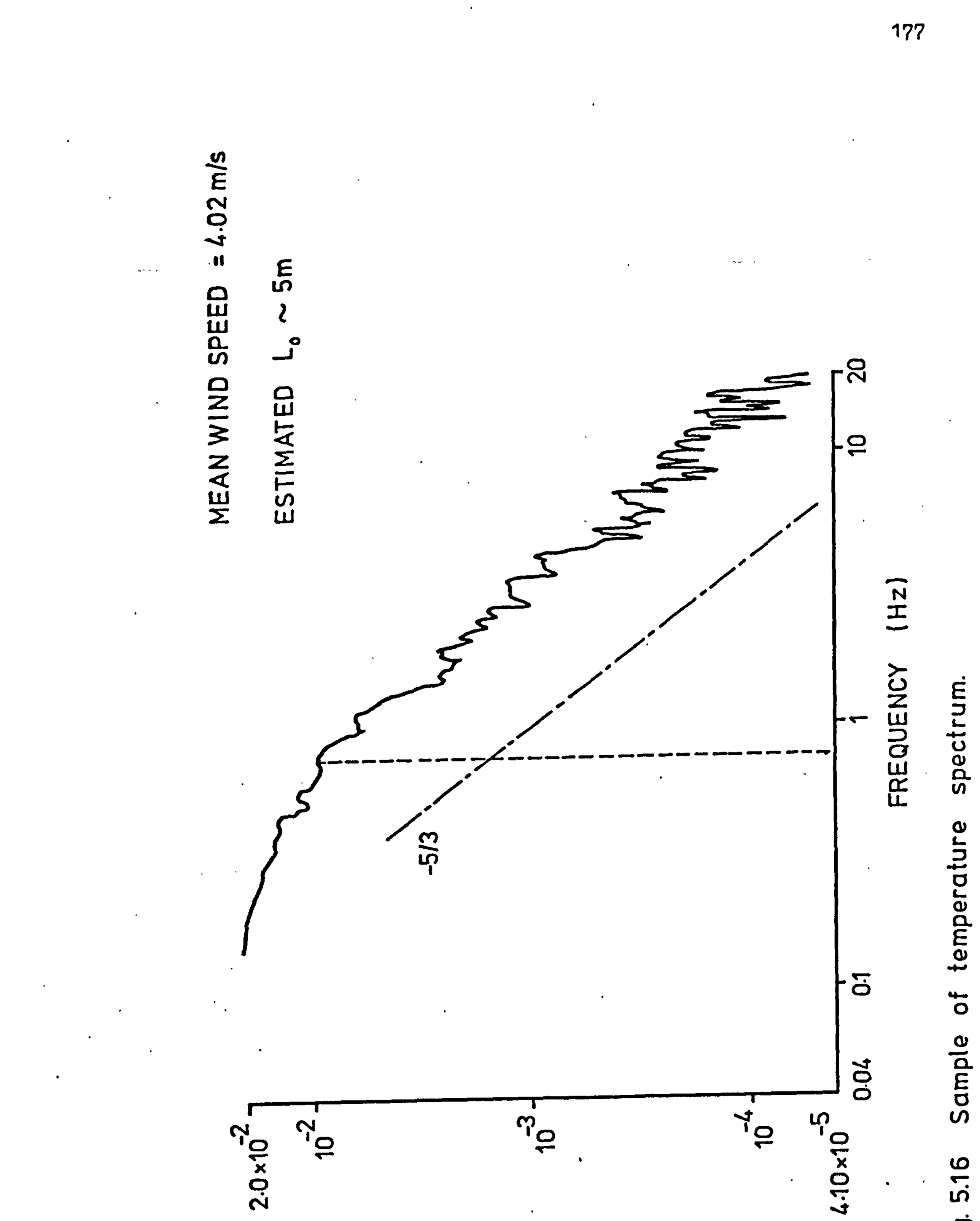

Fig. 5.16 Sample of temperature spectrum.

Table 5.1 Summary of results

No.	$\frac{\sigma^2_{110}}{\sigma^2_{36}}$	Range of ratio	Temp.spectal slope	Order of L_o (metre)	Predicted C_n^2 ($m^{-2/3}$)
1	3.701	2.3 - 6.81	~ -5/3	25	1.2×10^{-14}
2	3.879	2.1 - 10.4	~ -5/3	20	3.1×10^{-14}
3	3.83	1.95 - 7.05	~ -5/3	over 50	2.2×10^{-14}
4	3.889	2.4 - 5.57	~-5/3	15	1.2×10^{-14}
5	9.309	4.3 - 18.1	~-5/3	1	*
6	9.81	6.3 - 13.5	~-5/3	1.5	*
7	5.403	3.08 - 8.75	~-5/3	2.3-- 50	*
8	6.962	4.05 - 11.8	~-5/3	3-- 20	*

* No value of C_n^2 is given here because the equation for calculating C_n^2 is not applicable under this condition

$\sqrt{\lambda L} \gtrsim L_o$. The results of this experiment clearly verify this point.

For the wavelengths used in this experiment (that is, 8.33mm and 2.73mm) and assuming the two-thirds law for the meteorological parameters, the theoretical ratio value should be 3.68 for $\sqrt{\lambda L} < L_o$ and 9.33 for $\sqrt{\lambda L} > L_o$. It is not necessary to consider the lower limit, that is $\sqrt{\lambda L} \gg l_o$ because the inner scale is only of the order of 1 millimetre and $\sqrt{\lambda L}$ has values of 5.77 metres and 3.3 metres respectively for the 8.33mm and 2.73mm wavelengths. Concerning the size of the outer scale, it is reported that it may vary from the order of metres to hundred of metres depending on the height above the ground. (Strohbehn 1968)

Under the conditions of $\sqrt{\lambda L} < L_o$ and the -5/3 law for the temperature spectrum, a mean ratio value of 3.701 which is very close to the theoretical value of 3.68 was obtained experimentally. The physical size of the outer scale of the turbulence was estimated to be of the order of 25 metres from the temperature spectra and the slopes of the spectra are approximately -5/3 which corresponds to the "two-thirds" law. So it is expected that a good agreement should be obtained. (Section 5.4.2.1)

Under a different condition that $\sqrt{\lambda L} > L_o$, a completely different result was obtained even though the -5/3 power law of the temperature spectrum was still obeyed. The physical size of the outer scale was estimated to be of the order of 1.5 metres and the spectrum slope is very close to -5/3. The mean ratio

value is found to be 9.81 (Section 5.4.2.2) which agrees with the theoretically predicted value of 9.33 when the condition $\sqrt{\lambda L} \gtrsim L_o$ is met. It can be seen from Figure 5.11 that the individual ratio values scatter about the mean value, however, this is expected in any experimental measurements and the results described gives a very good indication of the dependence of the amplitude fluctuations on the outer scale size.

Section 5.4.2.3 presents the result which gives a mean value of 5.40 and the spectrum slope of the temperature has a value very close to -5/3. This result cannot be related to any theoretical values because there was a large variation in the physical size of the outer scale. Because of the variation in the outer scale size which sometimes was greater than $\sqrt{\lambda L}$ and sometimes small than or comparable to $\sqrt{\lambda L}$, a ratio which is neither close to 3.68 nor 9.33 would be expected.

5.5 Conclusions

The log-amplitude fluctuations at 8.33 millimetre and 2.73 millimetre wavelengths were found to have a log-normal distribution.

The results obtained from the ratio experiment show very good agreement between experimental and theoretical values. Such a good agreement is remarkable considering measurements of temperature were taken only at one point. Based on these results

it can be concluded that the log-amplitude variances at frequencies 36 GHz and 110 GHz have a $k^{(3/2 - p/2)}$ wave number dependence which is $k^{7/6}$ when p is 2/3 (that is, the two-thirds law is operative) when $\sqrt{\lambda L} < L_o$ and a k^2 wave number dependence when the condition $\sqrt{\lambda L} \gtrsim L_o$ is met. Hence particular attention should be paid to the physical size of the outer scale of the turbulence when one decides to apply theoretical equations to estimate the amplitude fluctuations in the millimetre wavelength range.

CHAPTER 6 EFFECT OF WIND VELOCITY ON THE AMPLITUDE SCINTILLATIONS OF MILLIMETRE RADIO WAVES.

6.1 Introduction

Amplitude scintillations of millimetre radio waves depend on the fluctuations of the atmospheric refractive index which in turn has a time dependence which is a function of the wind speed. Hence it can be envisaged that information about the wind velocity along a propagation path can be deduced from millimetre wave scintillation measurements. This chapter gives experimental evidence which confirms the relationship between millimetre wave amplitude scintillations and the transverse wind speed along the propagation path. The theoretical basis of the experiment is that the normalized spectral density of a particular component of the scintillation fading spectrum is related to the wind speed transverse to the propagation path (Section 6.3.3). The normalized spectral density can be measured and hence the averaged value of the transverse wind speed over the whole path can be determined. Comparison of the theoretically calculated wind speed and that measured by a conventional anemometer at the receiving end of the link is also presented.

The idea of using electromagnetic waves for remote probing of the atmosphere has received a considerable amount

of interest (Special Issue IEEE, 1969; Lee and Waterman 1968). The advantages of remote probing are that it is possible to measure quantities which are very difficult or impractical to measure by conventional devices and it gives the averaged values of these quantities over a path or a region, which is the true spatial average. This cannot be found by averaging widely separated point measurements. The successful construction of an optical wind sensor which uses the motion of the scintillation pattern to measure the transverse component of wind blowing across a laser beam has been reported by Lawrence et al (1972) and Ochs et al (1976). Shen (1970) has developed a numerical method, using the correlation and the slope at zero lag of the correlation function, to deduce the refractive index structure parameter C_n^2 and wind profiles from scintillations observed over a 28 km microwave link.

Optical frequencies exhibit much larger amplitude scintillations than millimetre waves which can be an advantage when used for measurement pruposes. However, saturation of the amplitude scintillations which is unlikely in a millimetre wave system can easily occur in the optical case as the strength of refractive-index turbulence increases. Furthermore, light sources in the field of view, particularly those near the receiver, may contribute to the error in an optical remote-probing system. No such problem exists for a microwave system.

6.2 Preliminary observations

The temporal nature of the amplitude fluctuations has been examined by determining the correlation time or time lag, τ, from the correlation function of the scintillations. The correlation time is the time required for the correlation to fall to 0.5. The reciprocal of the correlation time multiplied by 2π is defined as the "spectral width" of the fluctuations, that is, $\Delta f = \frac{1}{2\pi\tau}$. Figure 6.1 shows the spectral width of the amplitude fluctuations at 36 GHz obtained from an experiment carried out between 14:30 and 16:00 BST on the 24th July, 1976. The auto-correlation function of the fluctuations was computed at one minute intervals and the spectral width was deduced ($\Delta f = \frac{1}{2\pi\tau}$). A typical example of the correlation function is shown in Fig. 6.2. It can be seen that the spectral width of the variations ranges from 0.15 to 1.2 Hz with a prominent peak occurring at about 15:45 BST.

The transverse wind speed measured at the receiving end of the link for the same period of time is also shown in Fig. 6.1. This was obtained by taking the average of the instantaneous wind speed over one minute intervals. Some points of similarity between wind speed and the spectral width of the amplitude fluctuations can be observed. Both share the prominent peak around 15:45 BST and the trend of the variations shows some significant detailed similarity.

The correlation between the spectral width and the wind

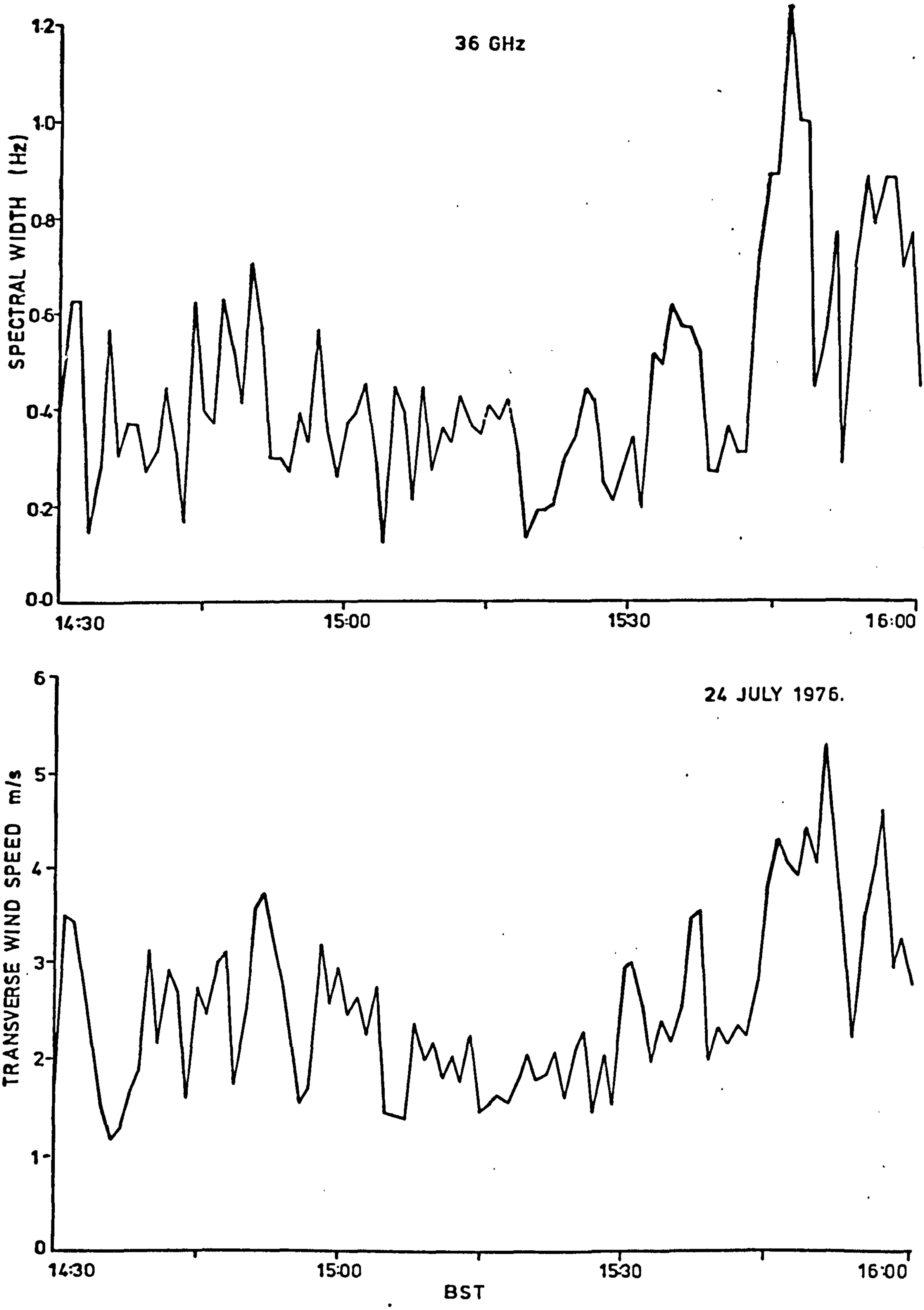

Fig. 6.1 Correlation of spectral width wind speed

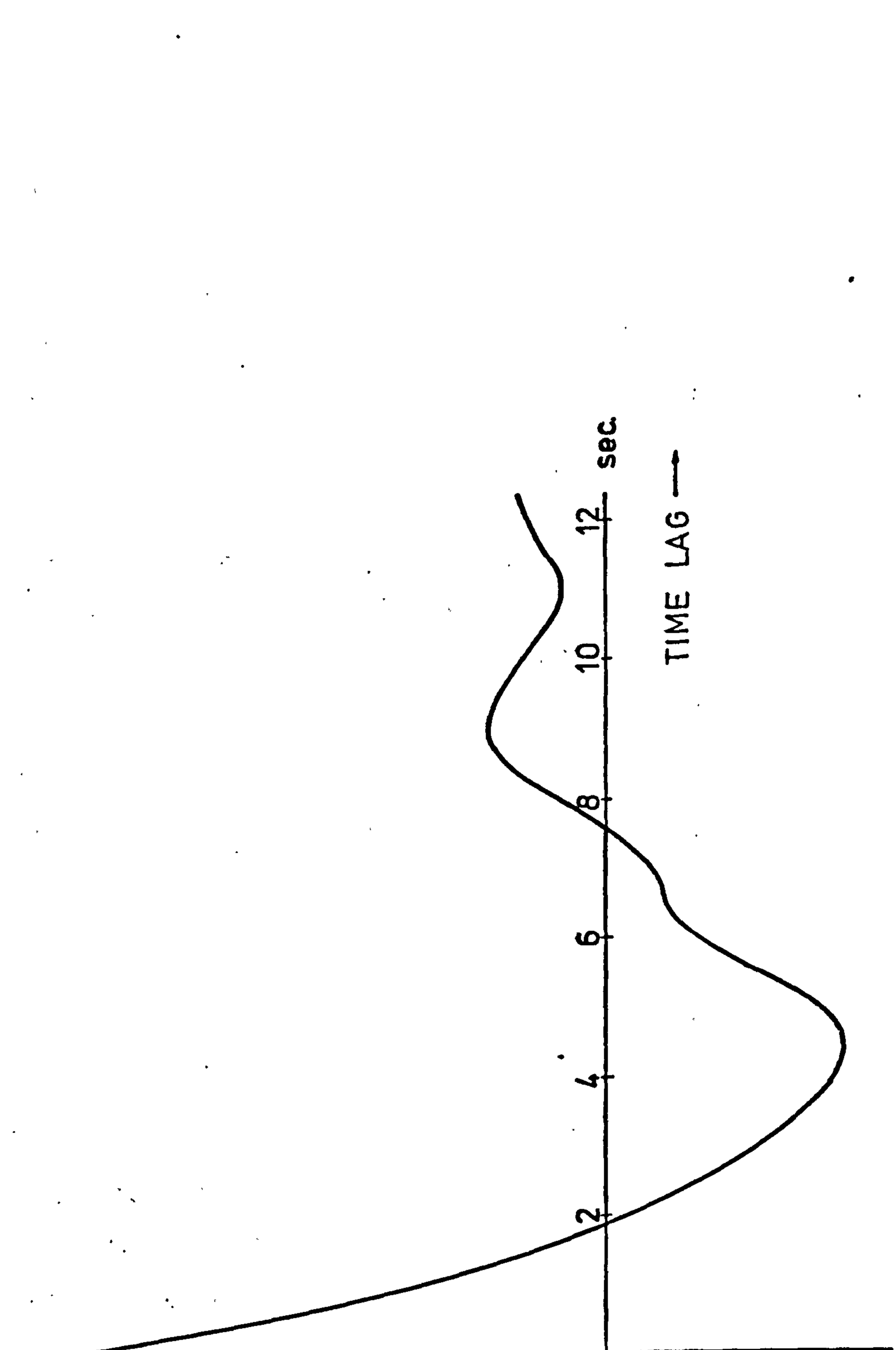

Fig. 6.2 Auto-correlation function of the 36 GHz signal fluctuations.

velocity can be simply understood. In Section 5.2, it is mentioned that amplitude fluctuations are mainly contributed by a scale size L' of the order of the first Fresnel zone size $(\lambda L)^{1/2}$ (where λ is the wavelength and L is the path length). Hence this scale size L' characterizes the spatial pattern of the scintillations. The correlation time or the time lag, τ , for the scintillation pattern to fall to 0.5 will be dependent on the time that this characteristic scale is blown across the path by the wind, and the value of this time is simply given by $\frac{L'}{V}$, where V is the transverse wind velocity across the path. In other words, the correlation time or the time lag is proportional to $\frac{L'}{V}$ and is of the same order as $\frac{L'}{V}$. From the definition of the spectral width, the spectral width is related to the wind velocity by

$$\Delta f = \frac{1}{2\pi\tau} = \frac{V}{2\pi L'}, \qquad 6.2.1$$

Hence from Equation 6.2.1, it can be seen that the spectral width is directly proportional to the transverse wind velocity.

The above is only a very simple derivation, since, in practice, the amplitude fluctuations are contributed to by scales of all sizes, the amount of the contribution being a function of the scale size. However, from the results shown in Figure 6.1 it can be concluded that the temporal characteristics of the received signal are largely the result of the horizontal component of drift of a "frozen" spatial distribution of scale sizes, rather than of temporal changes in this distribution.

6.3 Theoretical background

6.3.1 Taylor's Hypothesis

In practical measurements, only the temporal power spectrum of scintillations can be conveniently obtained. The relation between the spatial power spectrum and the temporal power spectrum can easily be established by making the approximation involving the use of Taylor's hypothesis of "frozen" turbulence (Lumley and Panosky 1964) which assumes that the temporal variations of some quantity measured at a point are caused by the uniform motion of the atmosphere past the point and the internal motions of the atmosphere may be neglected.

Assuming Taylor's hypothesis, the field at a point (y_o, z_o) on a plane transverse to the direction of propagation (i.e. x direction) at time t is the same as the field at the point $(y_o + V_\perp \tau', z_o + V_\perp \tau')$ on the same plane at time $(t+\tau')$, where $V_\perp$ is the average velocity component perpendicular to the path. Hence the time autocorrelation function $R_A(\tau')$ of the log-amplitude fluctuations at the point (y_o, z_o) can be expressed in terms of the space correlation function $B_A(\rho)$ as

$$R_A(\tau') = B_A(V_\perp \tau') \qquad 6.3.1$$

The condition under which Taylor's hypothesis is applicable to propagation work was studied by Tatarski (1961a). He considered the fact that the chief contribution to the amplitude

fluctuations is produced by the inhomogeneities of order $(\lambda L)^{1/2}$ (Section 5.2) contained inside a paraboloid $y^2 + z^2 = \lambda x$ with its vertex at the point of observation. The field can only be appreciably affected as a result of displacement of an inhomogeneity along the axis of the paraboloid when the ratio between the size of the inhomogeneity and the diameter of the paraboloid changes appreciably. Such a displacement is of order L. At the same time a displacement of the inhomogeneity perpendicular to the axis of the paraboloid by an amount of $(\lambda L)^{1/2}$ will change the field considerably. The time required for this displacement to take place is given by $\tau'' = \frac{(\lambda L)^{1/2}}{V_\perp}$. The longitudinal displacement in the same time period τ'' is equal to

$$\Delta x = \tau'' V_{\parallel}$$

$$= \left(\frac{V_{\parallel}}{V_\perp}\right) (\lambda L)^{1/2} \qquad 6.3.2$$

where $V_{\parallel}$ is the wind component along the axis of propagation . If Δx is very much smaller than L ($\Delta x \ll L$), i.e.

$$\frac{V_\perp}{V_{\parallel}} \gg (\lambda/L)^{1/2} \qquad 6.3.3$$

then the effect of the parallel wind component on the amplitude scintillation can be neglected.

Taking λ to be 8.33 mm and L = 4.1 Km, $(\lambda/L)^{1/2}$ is 2.03×10^{-6}. This corresponds to an angle of 1.16×10^{-4} degree between the direction of the wind and the propagation path. Hence it can be seen that Taylor's hypothesis is applicable

under nearly all conditions except in the case when the wind velocity is exactly along the propagation path.

6.3.2. Temporal power spectrum of the amplitude scintillaions

The two-dimensional spectral density of the logarithmic amplitude scintillations under the condition that the Kolmogorov spectrum of turbulence is assumed and that the outer scale size L_o is greater than the dimension of the first Fresnel zone $(\lambda L)^{1/2}$ is given in Section 5.2 by

$$F_A(K,0) = 0.033\pi C_n^2 k^2 L \left(1 - \frac{k}{K^2 L} \sin \frac{K^2 L}{k}\right) K^{-11/3} \qquad 6.3.4$$

The corresponding correlation function giving a spectral density of Equation 6.3.4 is (Tatarski 1961b)

$$B_A(\rho) = 2\pi^2(0.033)\, C_n^2 k^2 L \cdot \left[\int_o^\infty J_o(K\rho) \cdot \left(1 - \frac{k}{K^2 L} \sin \frac{K^2 L}{k}\right) K^{-8/3}\, dK \right] \qquad 6.3.5$$

Making use of Taylor's hypothesis, the general relation between the spatial correlation function $B_A(\rho)$ and the frequency spectrum W(f) under the assumption of "frozen" turbulence is given by the definition of the frequency spectrum.

$$W(f) = 4 \int_o^\infty \cos(2\pi f \tau')\, R_A(\tau')\, d\tau'$$
$$= 4 \int_o^\infty \cos(2\pi f \tau')\, B_A(V_\perp \tau')\, d\tau' \qquad 6.3.6$$

Tatarski (1961) has evaluated the frequency spectrum for a plane wave propagating through a medium with a refractive index spectrum given by (Section 2.2)

$$\Phi_n(K) = 0.033\, C_n^2\, K^{-11/3} \qquad 2.2.9$$

The frequency spectrum is approximately equal to (Lawrence and Strohbehn 1970)

$$W(f) = \frac{0.15}{f_o}\chi^2 \left[1 + 0.48\,\Omega^{4/3} + ...\right], \Omega \ll 1 \qquad 6.3.7$$

or
$$W(f) = 1.14\,\chi^2 \frac{\Omega^{-8/3}}{f_o}, \Omega \gg 1 \qquad 6.3.8$$

where χ^2 is the log-amplitude variance of the fluctuations,

$f_o = V_\perp / (2\pi\lambda L)^{1/2}$ is called the characteristic frequency,

$\Omega = f/f_o$

and f is the frequency of the log-amplitude fluctuations.

6.3.3 Relationship between normalized spectral density, frequency and wind velocity

Taking the values in this experiment where $\lambda = 8.33$ mm and L = 4.1 Km and assuming the transverse wind speed ranges from 0.5 m/s to 5 m/s, then the characteristic frequency f_o will be within the range 3.4×10^{-2} to 3.4×10^{-1}. If a particular frequency f is chosen such that $\Omega = f/f_o \gg 1$, then Equation 6.3.8 must be used.

Based on Equation 6.3.8 where

$$W(f) = 1.14 \chi^2 \frac{\Omega^{-8/3}}{f_o} \qquad \Omega \gg 1 \qquad 6.3.8$$

and substituting the values of Ω, the normalized spectral density will be given by

$$\frac{W(f)}{\chi^2} = 1.14\ f^{-8/3} \frac{V_\perp^{5/3}}{(2\pi\lambda L)^{5/6}} \qquad 6.3.9$$

that is, the normalized spectral density is proportional to the 5/3 power of the transverse wind speed and bears a $f^{-8/3}$ relation with the frequency.

6.4 Experimental details

The purpose of this experiment is to show experimentally the 5/3 power dependence of the normalized spectral density on the transverse wind velocity and to deduce the average wind speed from the scintillation measurements. The amplitude fluctuations of the 36 GHz singal were recorded on magnetic tape for subsequent digitization and analysis. Also the wind speed and wind direction were recorded at the receiver. The data was sampled at a rate of 40 Hz and spectra of the scintillations were obtained for every 1024 samples. Averaged values of the wind speed and wind direction for the same period of time were evaluted. The normalized magnitude of the spectral density at 0.99 Hz were obtained from the evaluated spectra by drawing the best straight lines through the spectral slope and taking the values at 0.99 Hz. The choice of this frequency is not important as long as it is in the linear region of the log-log plot of the frequency

spectrum (see Equation 6.3.9). In this experiment, 0.99 Hz was well within the linear region of the frequency spectrum and the magnitude of the power spectral density was far above the noise level, thus increasing the reliability of the data.

At the frequency chosen (0.99 Hz), the values of Ω for the scintillation fading spectrum were within the range 2.9 to 29 for the range of transverse wind speed, $V_\perp$, from 5 m/s to 0.5 m/s, i.e. $\Omega > 1$. Therefore Equation 6.3.9 can be used to evaluate the theoretical value of the mean wind velocity.

6.5 Experimental results

A typical frequency power spectrum of the 36 GHz scintillation is shown in Figure 6.3. This spectrum was taken on the 24th July, 1976. It has a slope which is very close to -8/3 thus showing that the "two-thirds" law of the Kolmogorov spectrum of turbulence was operative. This slope is not always -8/3 but depends on whether the "two-thirds" of the turbulence is operative or not. However, from the slope of the scintillation fading spectrum, the law governing the turbulence can be obtained (i.e. a -8/3 slope of the scintillation fading spectrum indicates that the 2/3 law is operative). The slope of the scintillation spectrum was found to be very close to -8/3 for all the data taken in this experiment, thus making the application of Equation 6.3.9 valid.

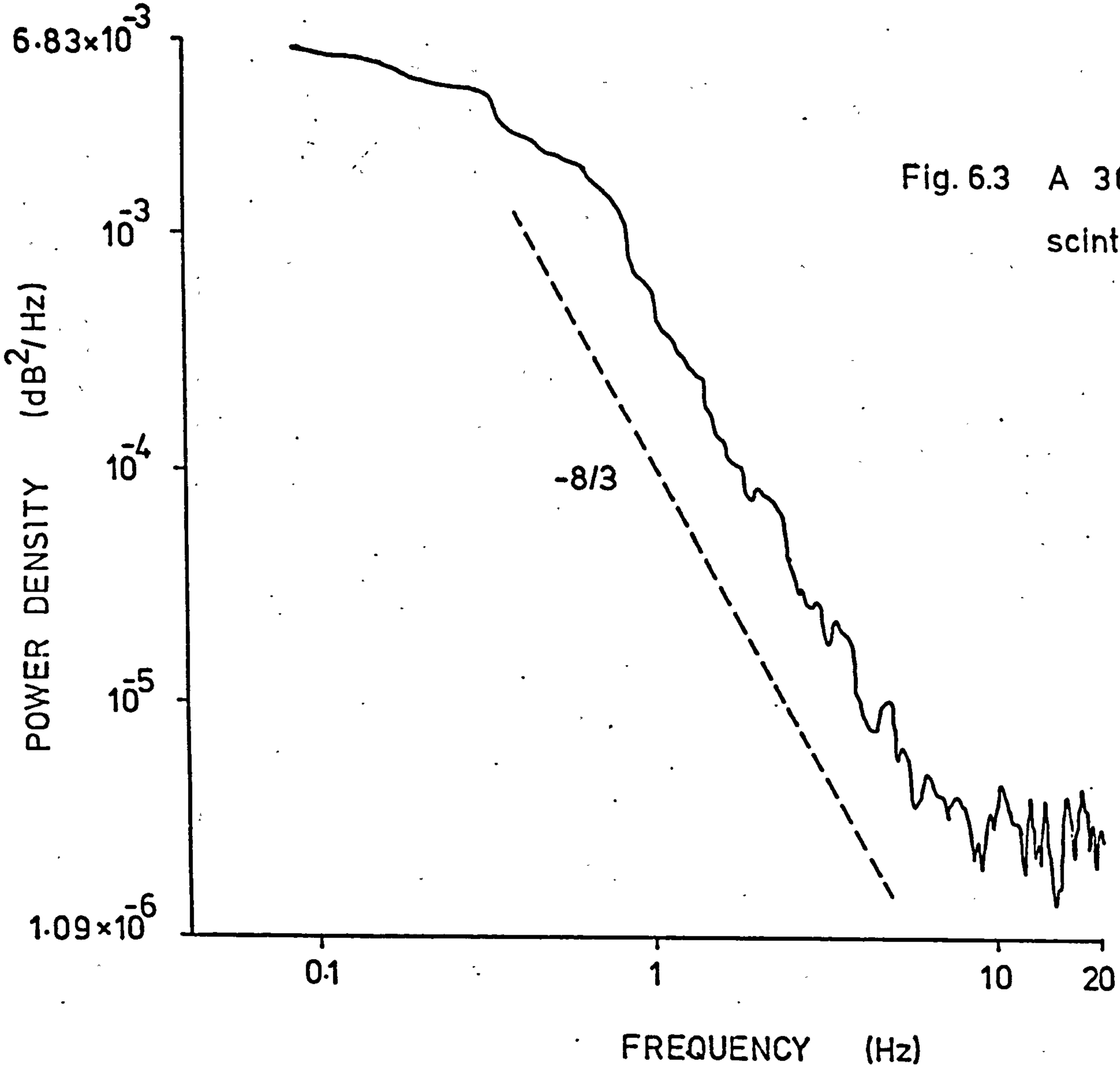

Fig. 6.3 A 36 GHz amplitude scintillation spectrun.

The plot of the measured transverse wind speed versus the normalized spectral density at 0.99 Hz is shown in Fig. 6.4. The range of the transverse wind speed covered was between 0.8 m/s to 6 m/s whereas the nromalized spectral density ranges from 0.009 to 0.2. This data was obtained from 80 scintillation fading spectra from experiments performed in July, 1976. All the experiments were carried out under sunny conditions. The dashed line represents the theoretical relation (Equation 6.3.9) between the transverse wind speed and the normalized spectral density at the frequency 0.99 Hz. The regression line is also shown in the figure. It can be seen that the slope of the regression line is only slightly greater than 5/3, the theoretical value, while only a small difference between the experimental and theoretical values was found.

Figure 6.5 shows the directly measured and the theoretically calculated transverse wind speed between 13:30 and 15:00 GMT on the 24th July, 1976. Very good correlation between the two values is apparent. Both showed peak values around 14:00 and 15:00 and dips around 13:45 and 14:30 and the detailed correlation is good.

The relation between the directly measured and theoretically calculated values is shown in Figure 6.6. It is clear that the theoretical values are greater than the directly measured values. The ratio of the measured wind speed to the calculated wind speed was found to be 0.85.

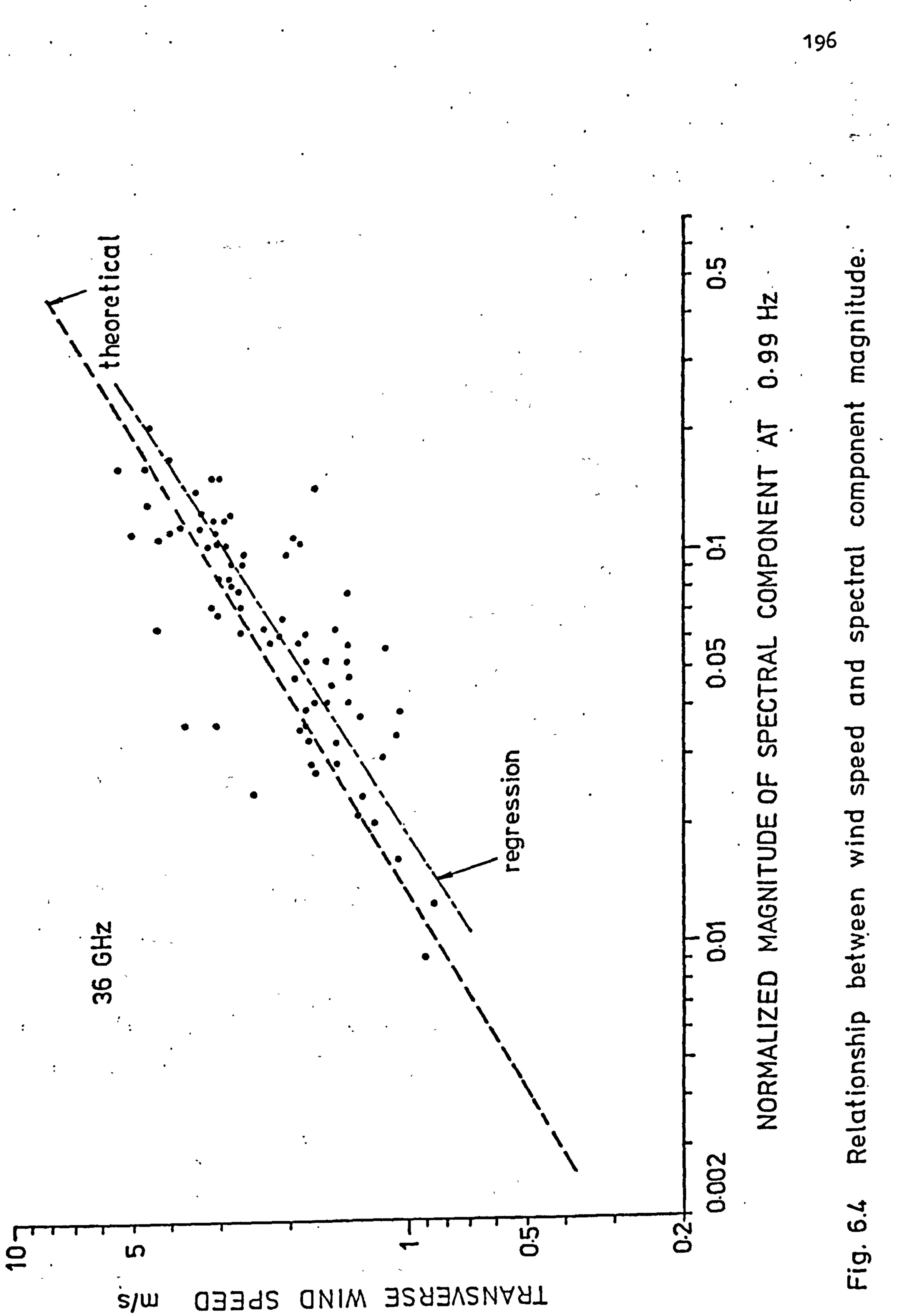

Fig. 6.4 Relationship between wind speed and spectral component magnitude.

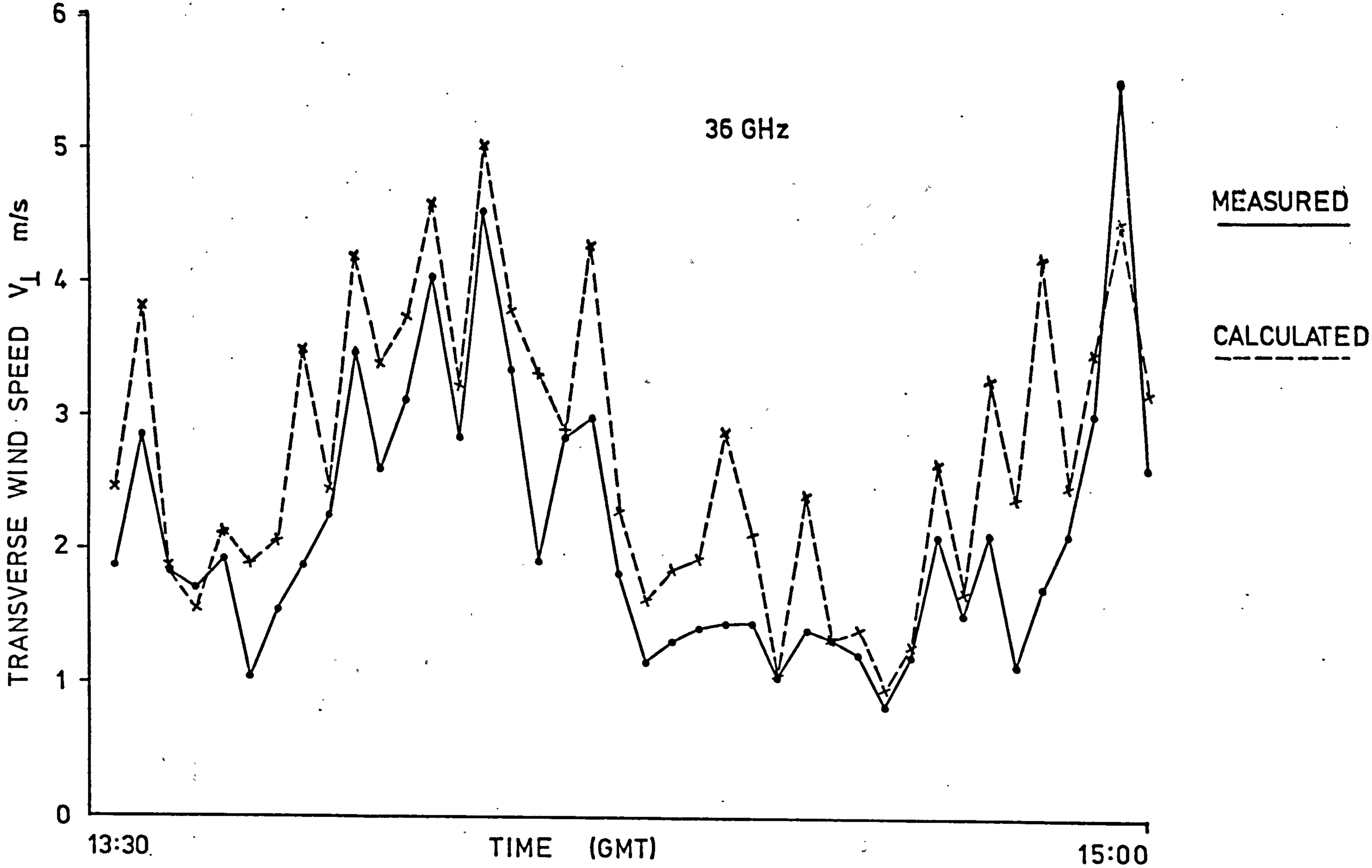

Fig. 6.5 Comparison of measured and calculated wind speed.

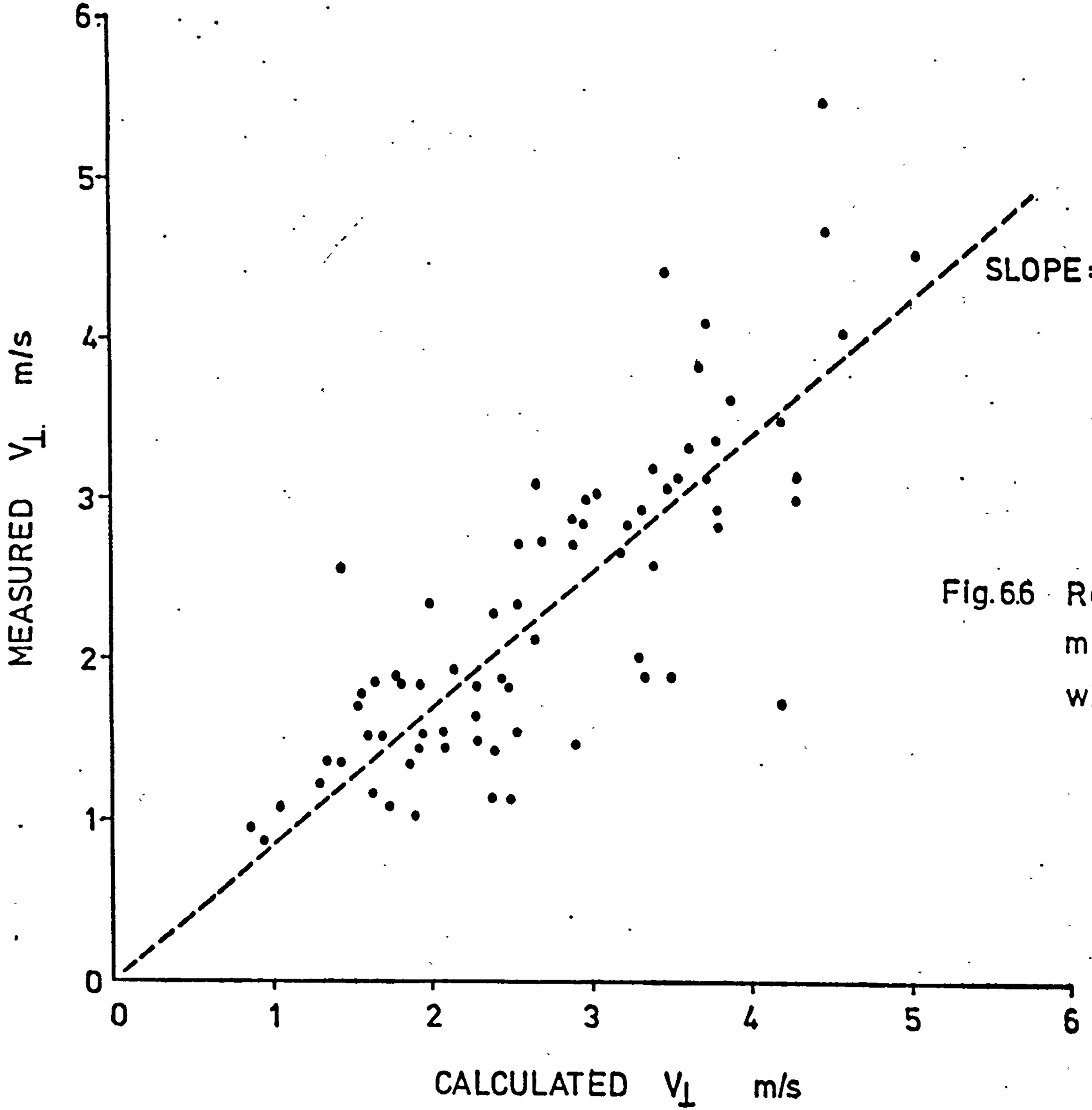

Fig.6.6 Relationship between measured and calculated wind speed.

6.6 Conclusions

The slope of the frequency power spectrum of the scintillation fading at 36 GHz tends to follow a value of -8/3. This provides a very simple means to check the structure of the atmosphere, i.e. whether or not the "two-thirds" law is operative.

The result obtained from the wind experiment shows good agreement between the experimental and theoretical values. It was found that the normalized power spectral density at a particular frequency of the scintillation fading is directly proportional to the 5/3 power of the transverse wind speed which indirectly implies that Taylor's hypothesis of "frozen" turbulence is a good approximation. Comparison of the directly measured and theoretically calculated transverse wind speed show good correlation though the theoretically calculated values tend to be higher than the actual values. The ratio of the measured wind speed to the calculated wind speed was found to be 0.85. This agreement is considered to be very good in view of the fact that the direct measurements were only made at the receiving end of the link whereas the calculated values were the averaged effect over the whole propagation path. Since half of the link passes over a park and the majority of the rest of the path is above buildings and only two buildings which are near to and stand higher than the path of the link are likely to locally distort the wind speed and its direction, the disturbance introduced to the wind velocity along the path is expected to be

minimal. The results of this experiment thus clearly demonstrate the feasility of using millimetre wave propagation for the remote probing of wind speed.

CHAPTER 7 REFRACTIVITY AND MILLIMETRE WAVE PROPAGATION.

7.1 Introduction

Random variations in the refractive index of the atmosphere are produced by random variations in pressure, humidity and temperature (Bean and Dutton 1968). The intensity of the refractive index variations associated with scales in the range l_o (inner scale of turbulence) to L_o (outer scale of turbulence) is expressed by the refractive index structure function which represents the variance of the difference in refractive index at two points separated by a distance r, where $l_o < r < L_o$. Experimental measurement of the spectrum of the atmospheric refractive index fluctuations in the free troposphere shows good agreement with the "two-thirds law (Gjessing et al 1972). The amount of scintillation fading is proportional to the magnitude of the refractive index structure parameter C_n^2 or the variance of the refractive index fluctuations depending on the size of the outer scale of turbulence (Section 5.2).

In this chapter, some of the experimental results on the atmospheric refractive index fluctuations are presented. Comparison is made between the magnitudes of the signal scintillations and the refractive index fluctuations and the C_n^2 value obtained from the refractivity frequency spectrum and from the scintillation formula (Equation 7.2.8). Long term statistics of the variation of atmospheric refractive index in London area

are also evaluated. This was found to be useful in the transit-time variation studies which are closely related to a digital transmission network. (Pierce 1969)

7.2 Refractive index frequency spectrum

7.2.1. Theory

Assuming that the refractive index has structure function of the form

$$D_n(r) = C_n^2 r^p \qquad (0 < p < 2) \qquad 7.2.1$$

this corresponds to an one-dimensional spatial spectral function

$$V_n(K) = \frac{\Gamma(1+p)}{2\pi} \sin\frac{\pi p}{2} C_n^2 |K|^{-(p+1)} \qquad 7.2.2$$

If the two-thirds law holds, i.e. p = 2/3, then

$$V_n(K) = 0.1244 C_n^2 K^{-5/3} \qquad 7.2.3$$

In practice, frequency spectra are measured, not wave-number spectra and conversion from one to the other can be made through Taylor's hypothesis. Let $S_n(f)$ denote the frequency spectral function; then the frequency and wave number spectra are related by (Kaimal 1973)

$$\int_0^\infty S_n(f)\, df = \sigma_n^2 = \int_0^\infty V_n(K)\, dK \qquad 7.2.4$$

where σ_n^2 is the variance of the refractive index fluctuations.

Since $K = \frac{2\pi f}{\overline{V}}$ or $dK = \frac{2\pi}{\overline{V}} df$, then

$$\int_0^\infty S_n(f)\, df = \int_0^\infty V_n(K)\, \frac{2\pi}{\overline{V}}\, df \qquad 7.2.5$$

that is

$$f\, S_n(f) = \frac{2\pi f}{\overline{V}}\, V_n(K)$$

or $$f\, S_n(f) = K\, V_n(K) \qquad 7.2.6$$

Therefore the frequency spectral function of the refractive index fluctuations is given by

$$S_n(f) = \frac{K}{f}\, V_n(K)$$

$$= 0.0365\, C_n^2\, f^{-5/3}\, \overline{V}^{2/3} \qquad 7.2.7$$

From Equation 7.2.7, it can be seen that the refractive index frequency spectrum has a slope of -5/3 if the "two-thirds" law is obeyed. Furthermore, the refractive index structure function parameter C_n^2 can be deduced directly from the refractive index frequency spectrum if the mean windspeed is known and is given by

$$C_n^2 = 27.37\, S_n(f)\, f^{5/3}\, (\overline{V})^{-2/3} \qquad 7.2.8$$

7.2.2 Experimental measurement of refractive index spectrum.

Figure 7.1 shows part of a chart record of the refractive index obtained in a refractivity measurement experiment between 17:08 and 18:12 BST on the 5th September, 1976. The weather was a little bit cloudy and the temperature was around 20°C. The

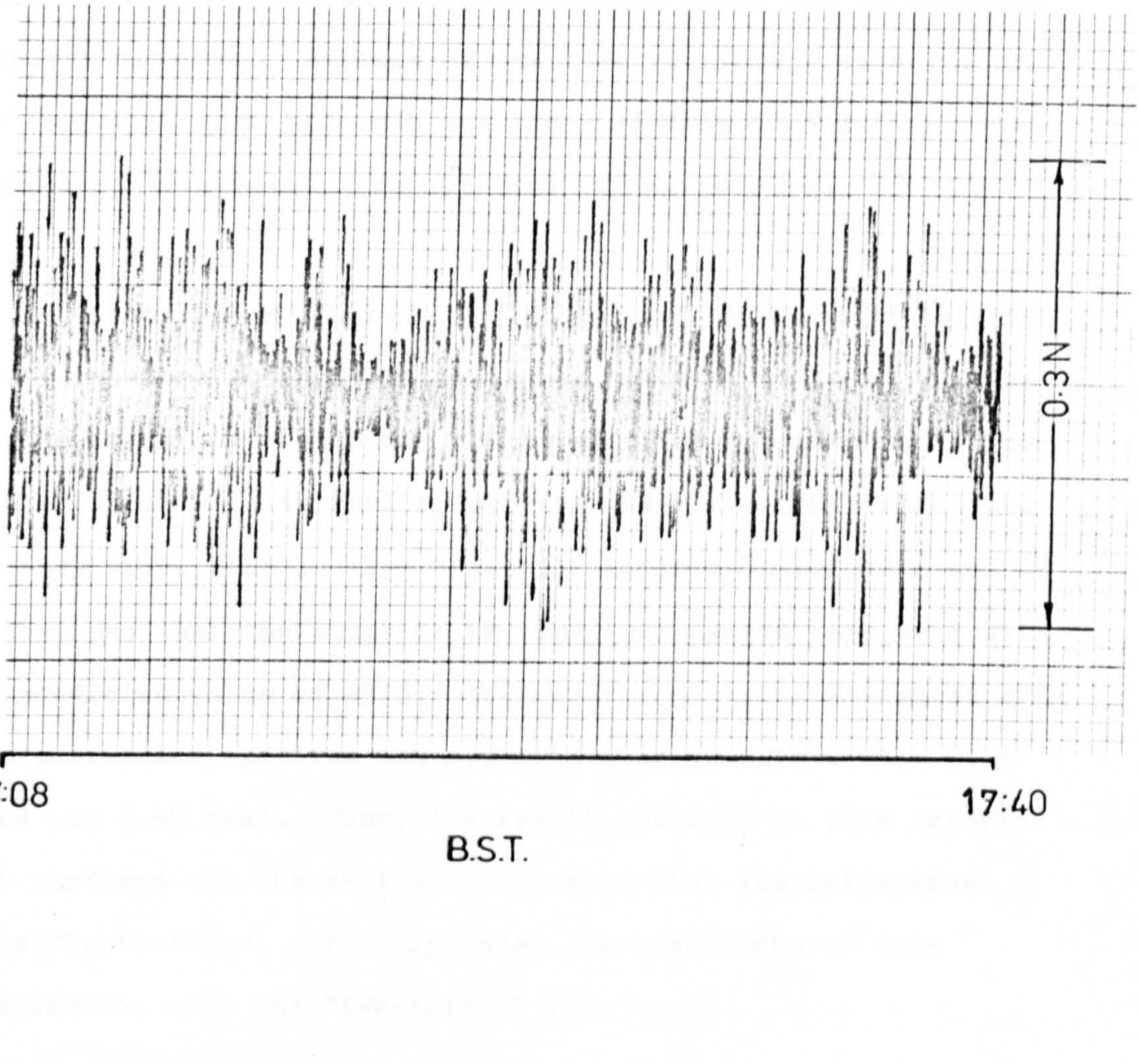

Fig. 7.1 Chart record of refractive index fluctuations.

measurement was carried out by means of the radio refractometer described in Chapter 3. Data from the magnetic tape recording was digitized at a sampling frequency of 40 Hz. Power spectra were obtained using a Fast Fourier Transform Program (Mavrokoukoulakis 1977). Low and high pass filtering of the data was carried out in order to remove very low frequency fluctuations which might have been due to instrumental drift and to minimize spectral aliasing. Because of the limited storage capacity of the computer, each spectrum was computed from 1024 data points. A total of 46 spectra were obtained during this run.

The slope of most of the spectra, obtained in this run, were very close to -5/3, being in the range -1.55 to -1.7. The average outer scale size was estimated to be the order of 10 m. Figure 7.2 shows a typical refractive index frequency spectrum. The -5/3 slope line is also drawn for comparison purposes and it can be seen that the slope of the spectrum agrees very well with the predicted value of -5/3. The outer scale size estimated from this particular spectrum was approximately 10 metres (the wind speed was 2.47 m/s). Thus, the result obtained in this experiment confirms the theoretical prediction that the refractive index fluctuations, certainly under the conditions of this experiments, obey the "two-thirds" law.

7.3 Refractive index fluctuations and scintillation fading.

The scintillation fading on the 36 GHz link was also

Fig. 7.2 Sample of refractivity spectrum.

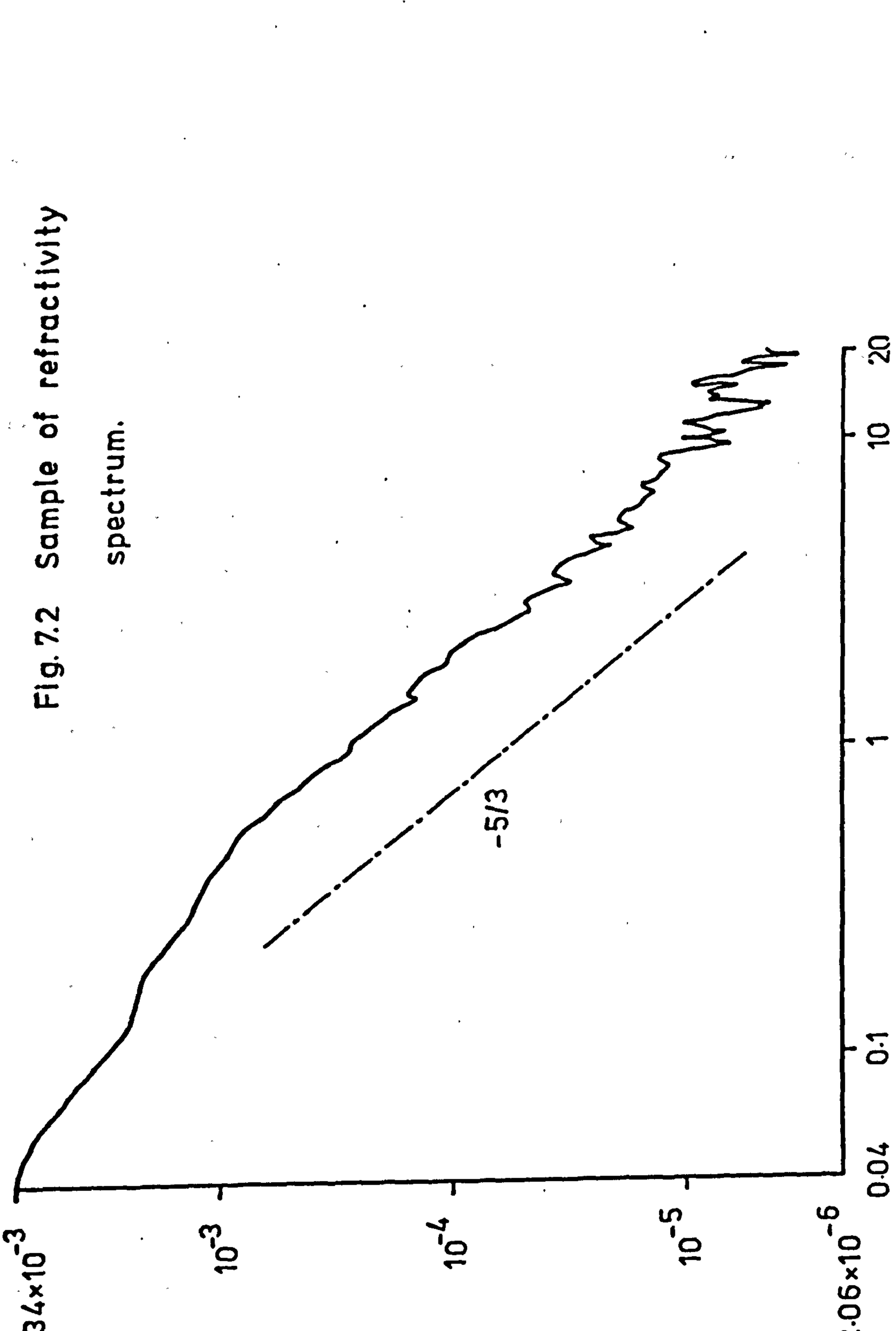

recorded over the same period as the refractive index measurements. Only very weak scintillations were observed during the course of the experiment. The first quantities to be compared are the variances of the refractivity fluctuations and the log-amplitude scintillations. The variances were computed from every 1024 data samples. Figure 7.3 gives the plots of the variances of the 36 GHz signal fluctuations and the refractivity fluctuations from 17:08 to 18:12 BST on the 5th September, 1976. The refractivity was measured at only one point at the receiving end and the link scintillations are due to the integrated effect along the whole propagation path. Therefore point by point comparisons might not be expected to show much correlation. However the correlation is surprisingly good and it can be seen that marked similarities, particularly the values around 17:25 and 17:40 exist.

A comparison of the scintillation fading spectrum and the refractivity frequency spectrum is given in figures 7.4(a), (b) and figures 7.5(a),(b). These represent two sets of spectra which show some similarities. Figure 7.4(a) is a refractivity frequency spectrum which has a spectrum slope very close to -5/3. The outer scale was estimated to be about 10 metres (the wind speed was 2.6 m/s). Figure 7.4(b) is the corresponding scintillation spectrum, the slope was found to be very close to -8/3. One noticeable feature in this spectrum is the step-wise characteristic at some frequencies along the spectrum slope. The same characteristic is observed at approximately the same frequencies in the refractivity frequency spectrum though not so prominent. Both spectra have a cut-off frequency at about 5 Hz.

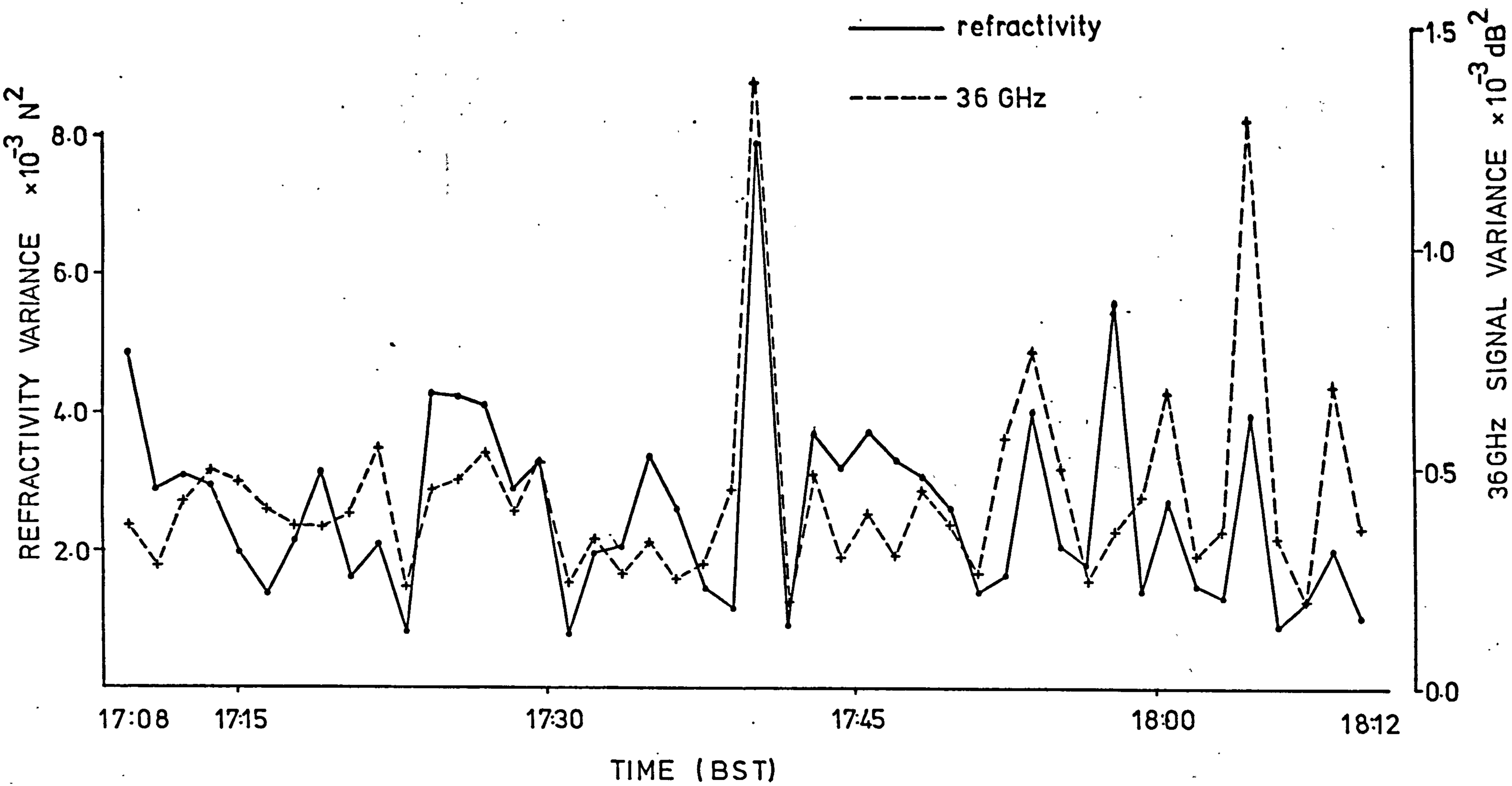

Fig. 7.3 Variances of refractivity and 36 GHz signal.

Fig. 7.4 (a),(b) Comparison of refractivity & signal spectra.

(a) Refractivity spectrum

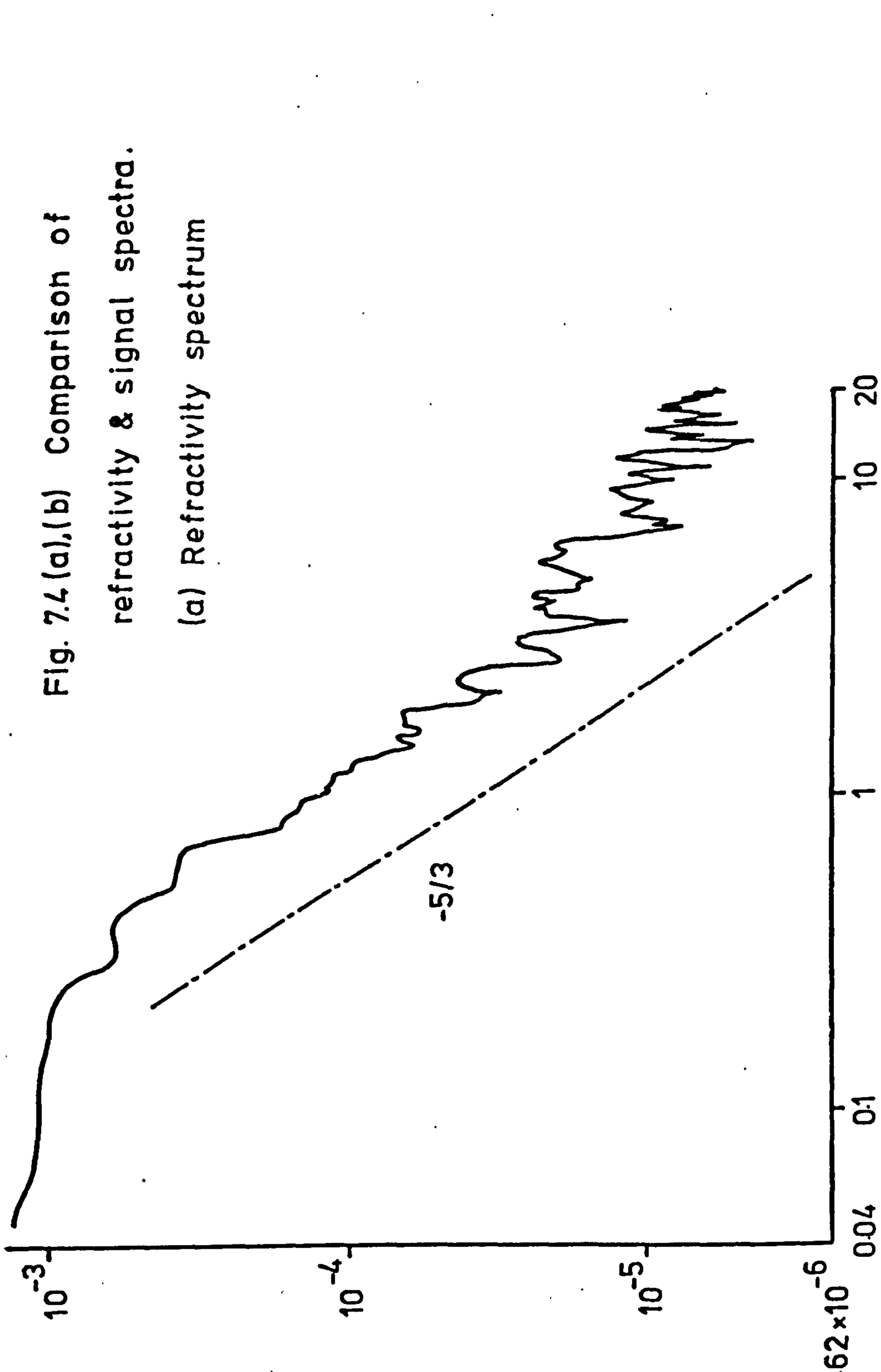

Fig 7.4b 36 GHz signal spectrum.

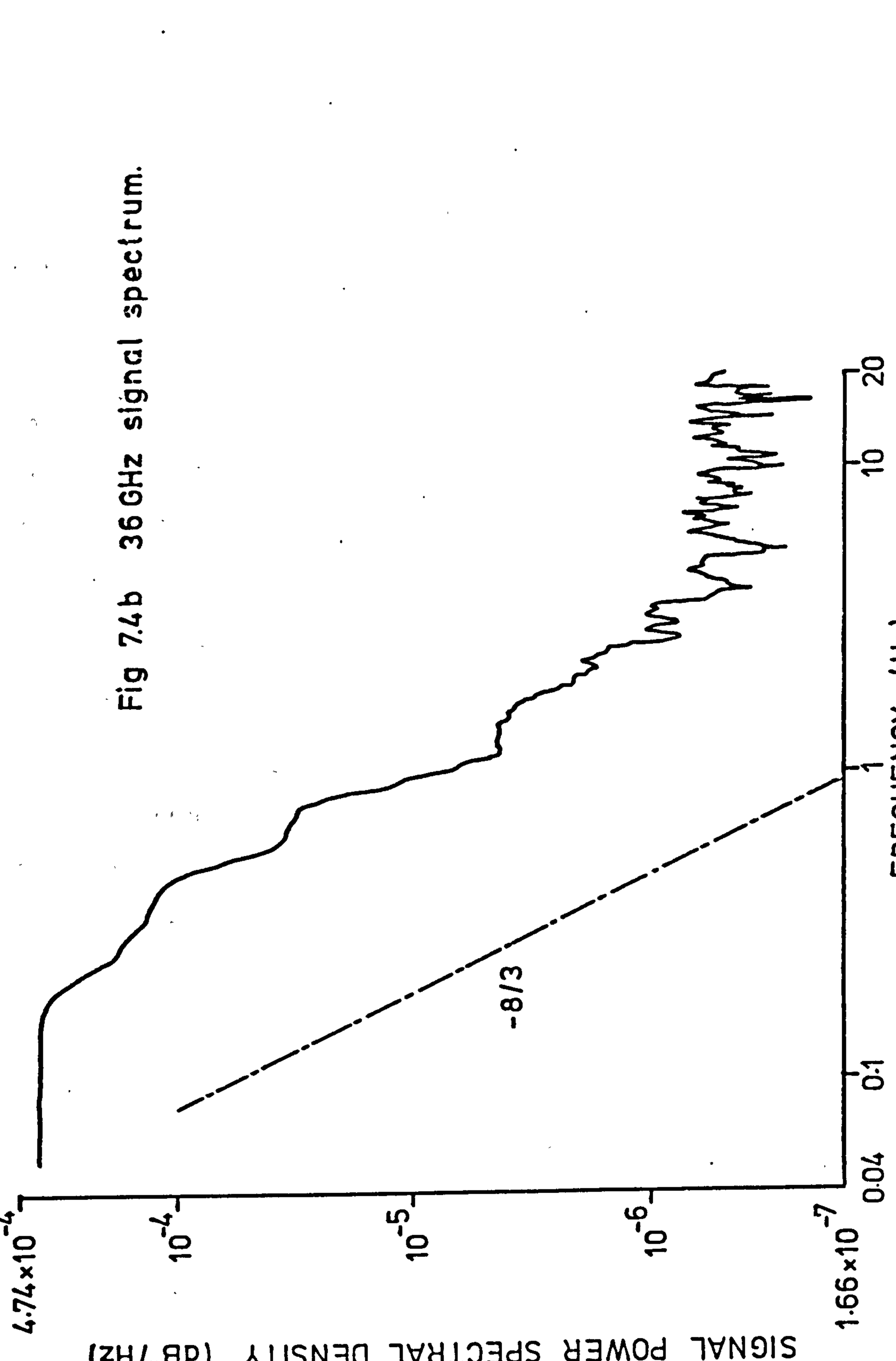

Figures 7.5(a) and (b) show the same sort of characteristic. The spectrum slopes are very close to -5/3 and -8/3 for the refractivity and scintillations respectively and the outer scale size is again around 10 metres. The step-wise characteristic is very prominent in this case but there is a shift of frequency the cause of which may be due to the fact that the average wind speed along the entire path differed from the mean wind speed measured at the receiving end.

7.4 Comparison of C_n^2 obtained from refractive index frequency spectra and from the scintillation formula.

From Equation 7.2.8 in Section 7.2.1, the value of C_n^2 from the spectral function is given by

$$C_n^2 = 27.37\ S_n(f)\ f^{5/3}\ (\bar{V})^{-2/3} \qquad 7.2.8$$

At the same time, the variance of the log-amplitude fluctuations, under the condition that $L_o > (\lambda L)^{1/2}$, is related to C_n^2 through Equation 5.4.1

$$\sigma^2 = 23.39\ C_n^2\ k^{7/6}\ L^{11/6} \quad (dB^2) \qquad 5.4.1$$

Therefore the relationship between log-amplitude variance and C_n^2 can be verified statistically by comparing the C_n^2 obtained from both equations.

In this experiment, the frequency of 1 Hz was chosen in the evaluation of C_n^2 from the spectral function. The mean wind velocity was the average of the instantaneous wind speed

Fig.7.5 Comparison of refractivity and signal spectra.
(a) Refractivity spectrum.

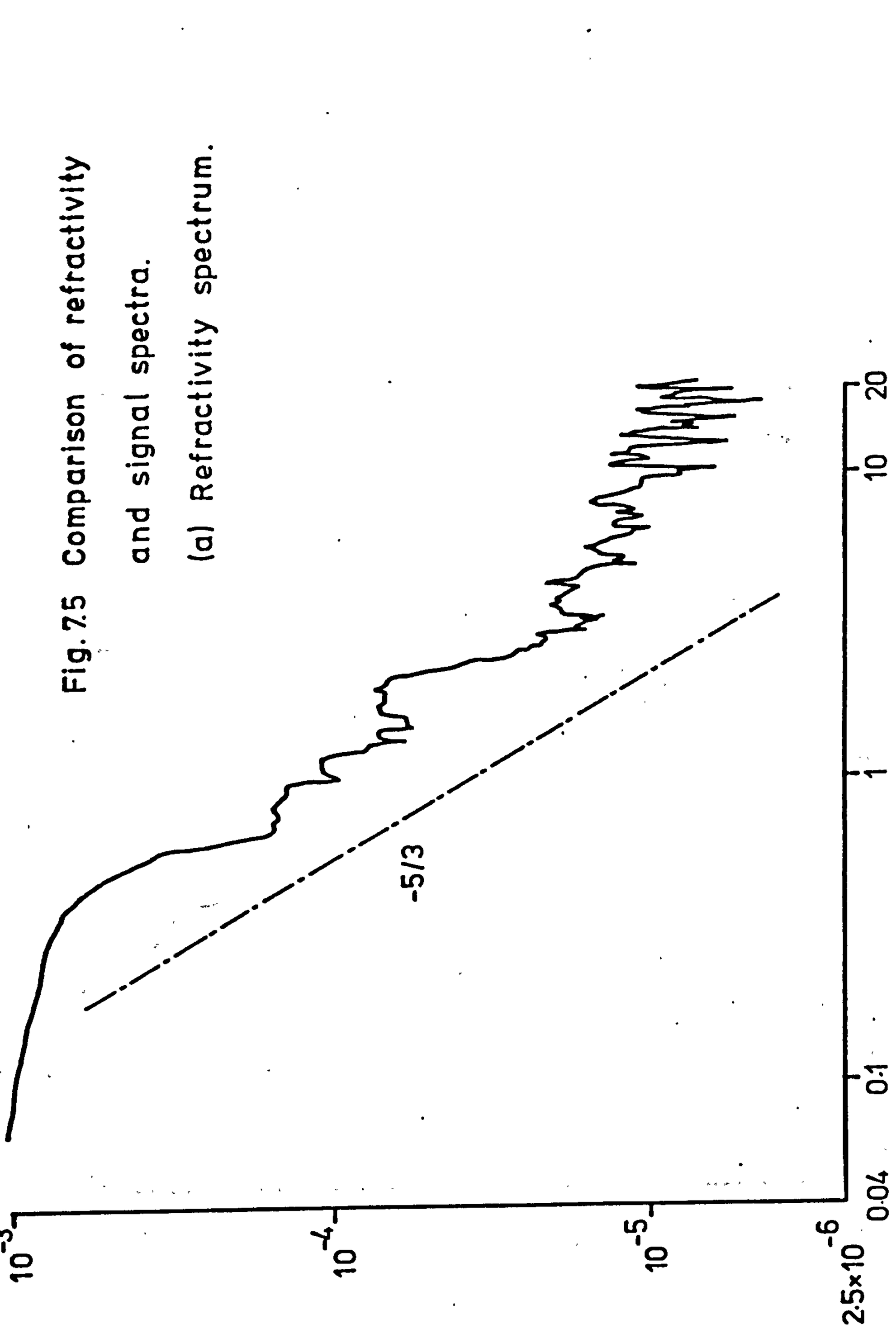

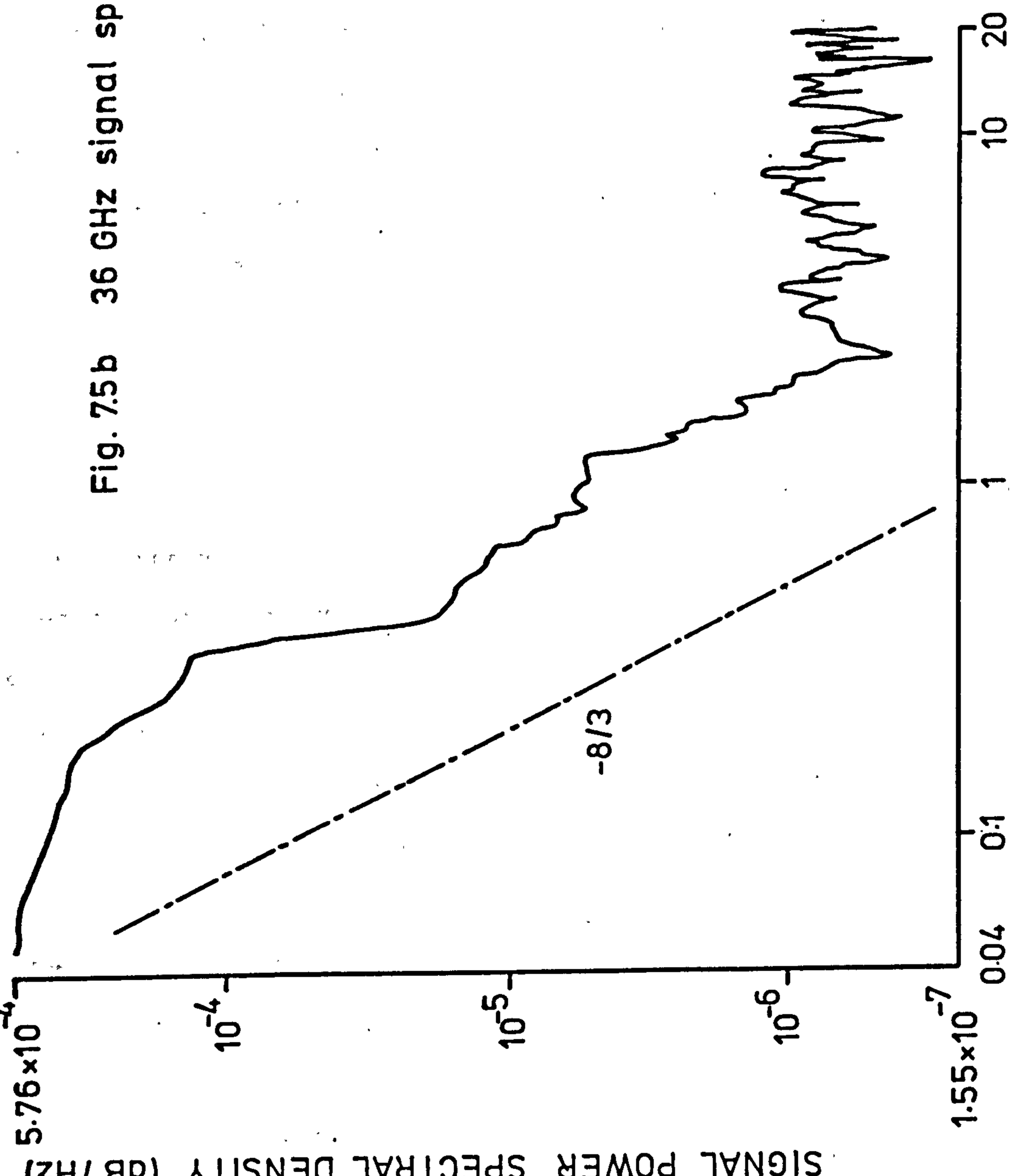

Fig. 7.5b 36 GHz signal spectrum.

over the same time period covered by the spectrum. The variance of the log-amplitude fluctuations over the same time period was also computed. Figure 7.6 shows the plot of the C_n^2 from the spectral function against the variance of the log-amplitude fluctuations. The data points are scattered but this is to be expected since the comparison was made between measurement at one point and the integrated effect of the whole path. However, it can be seen that the data points are scattered very well along the straight regression line.

Figure 7.7 gives the values of C_n^2 deduced from the refractivity spectral functions and the log-amplitude variances respectively. The two plots show some surprisingly good point to point correlation. The average value of C_n^2 obtained from the spectral functions was found to be $0.32 \times 10^{-14} m^{-2/3}$ whereas that obtained from the log-amplitude variances was $0.25 \times 10^{-14} m^{-2/3}$. The deviation is about 21% from the value obtained by refractivity measurement. However, this deviation should be considered to be tolerable in view of the fact that point measurement and path averaged measurement are being compared. This result does give experimental support to the theoretical relationship proposed by Tatarski (Equation 5.4.1) between the log-amplitude variance of wave fluctuations and C_n^2 and also indicates the feasibility of using millimetre wave propagation measurement to determine C_n^2.

7.5 Transit time variations in line-of-sight tropospheric propagation paths in central London area.

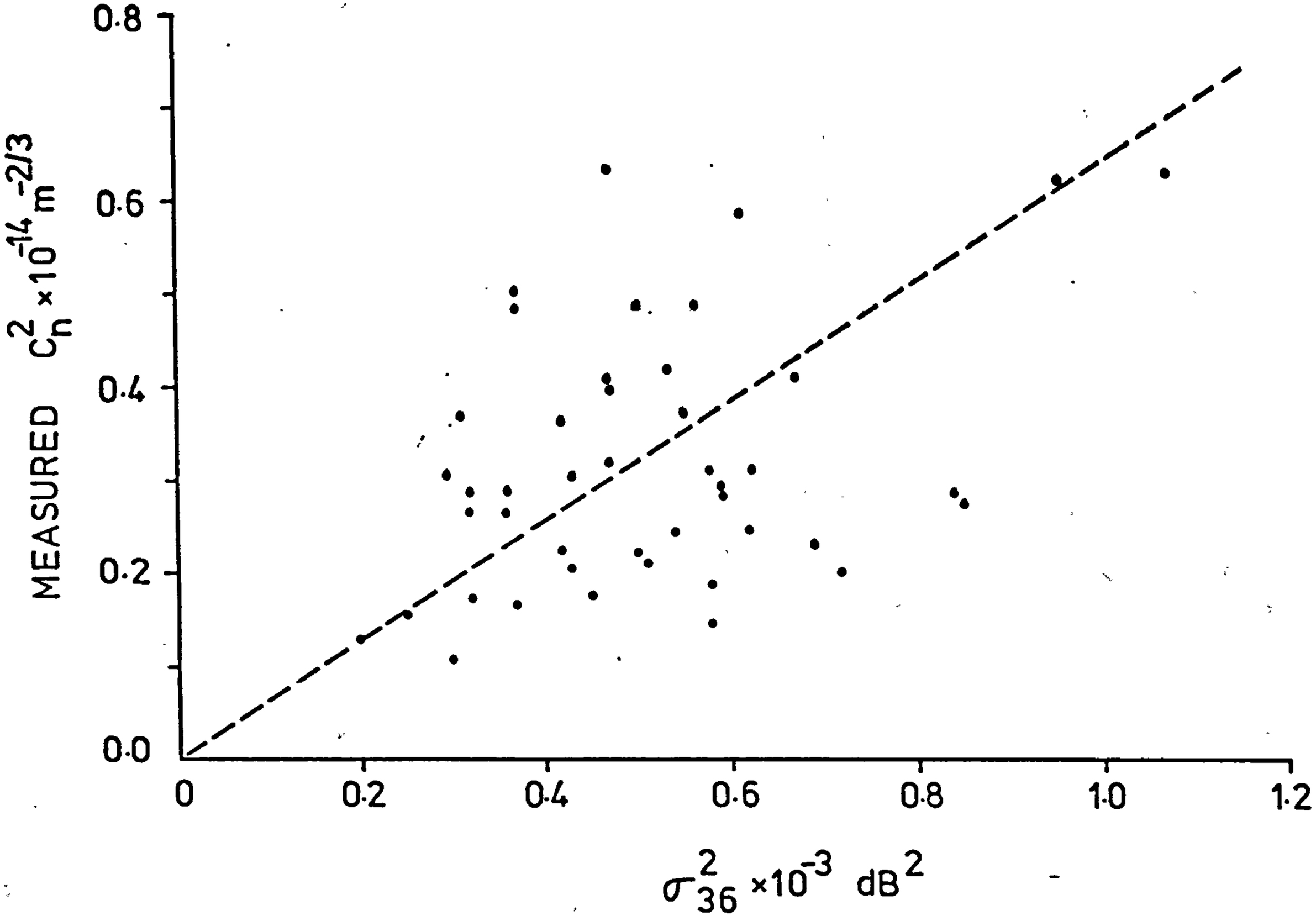

Fig 7.6 Measured C_n^2 against 36 GHz signal variance.

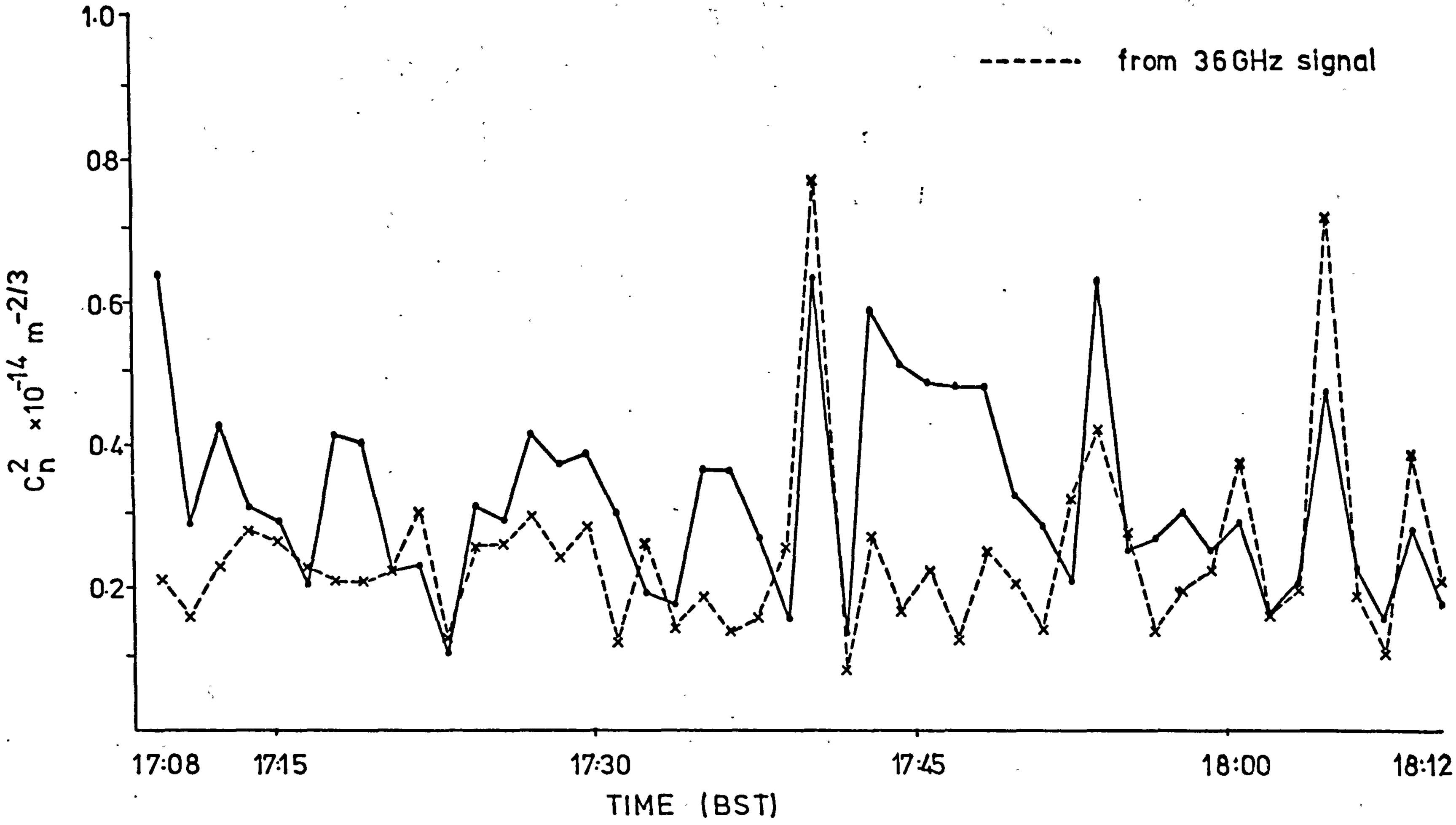

Fig. 7.7 C_n^2 from N spectra and 36 GHz amplitude scintillations.

7.5.1 Long term statistics of atmospheric radio refractive index.

Because of the wide bandwidth availability at millimetre wavelengths, it is very likely that digital transmission systems will be used at these frequencies. However, the transit-time variations in line-of-sight tropospheric propagation paths can cause problems on the synchronization of a digital transmission network (Pierce 1969), so it is desirable to have a knowledge of the extreme values for these transit-time variations under practical conditions.

Figure 7.8 gives the annual variation of the refractive index in the central London area in the year 1976. The values of the refractivity were computed from Equation (1.2.1) and the data for pressure, humidity and temperature were obtained from London weather centre in Holborn. The upper curve gives the weekly maximum values and the lower gives the minimum values. The maximum value of the refractive index in the year was 355 N units and the minimum 283 N units, i.e. a maximum difference of 72 N units. The largest differences between the maximum and minimum values were obtained during summer time (June to August) and the higher values of the maximum value occured during hot weather.

Figure 7.9 shows the diurnal variation of the refractivity on 30th June, 1976. This was the day on which the maximum variation in the refractive index for the whole year occurred, a variation between 329 N units and 276 N units.

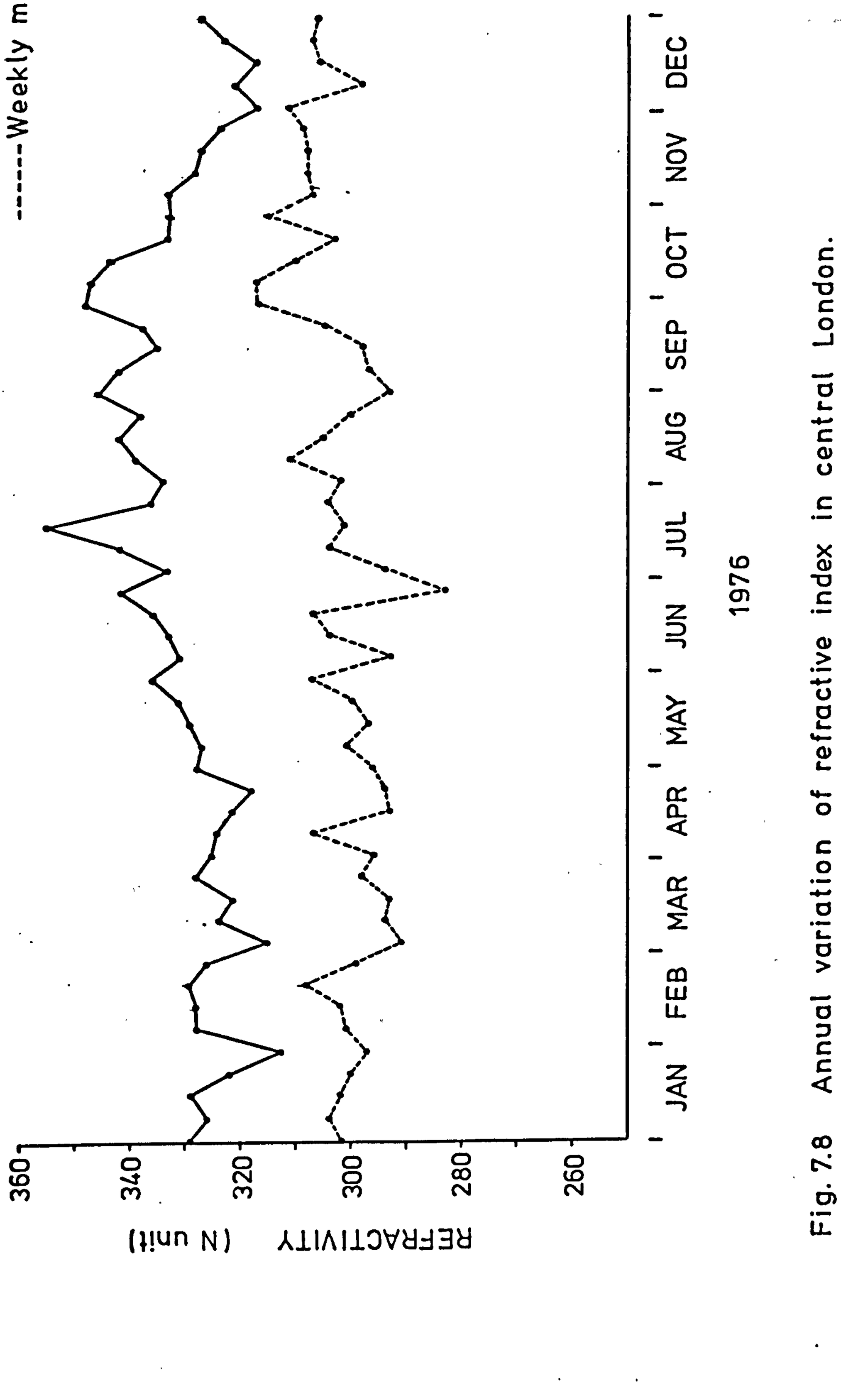

Fig. 7.8 Annual variation of refractive index in central London.

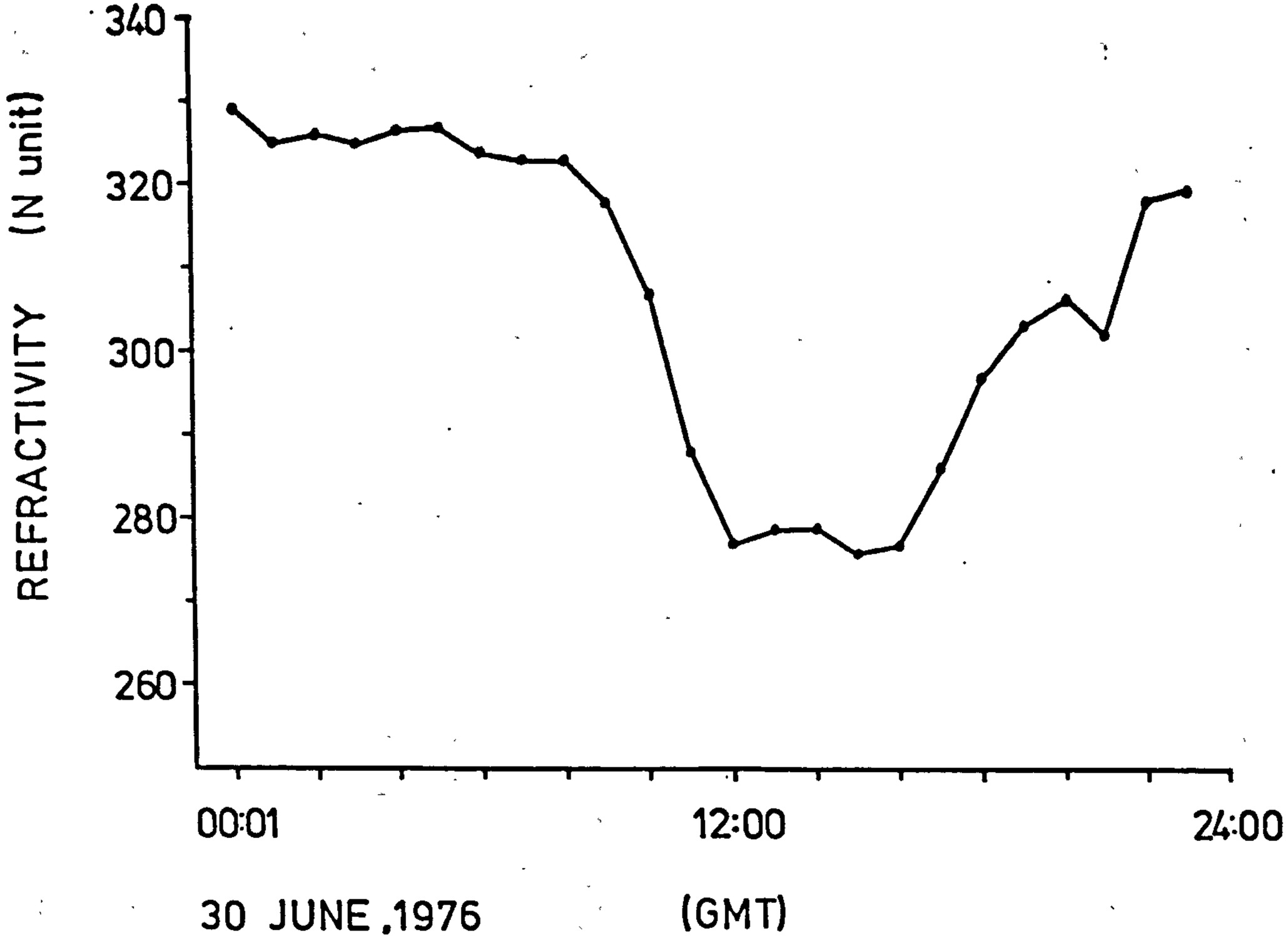

Fig. 7.9 Diurnal variation of refractive index.

From 08:00 to 12:00 GMT, the refractive index fell by 46 N units.

7.5.2 Magnitude of transit-time variations in the atmosphere.

The transit-time τ is given by the simple expression

$$\tau = \frac{1}{c} \int_{P_1}^{P_2} n \, ds \qquad 7.5.1$$

where c is the velocity of light = 3×10^8 m/s

n is the medium refractive index

ds is the differential path length

and P_1 and P_2 are the limits representing the end points of the path.

For the sake of simplicity, we shall assume Δn_{max} to be the maximum refractive index change which is expected over a given period of time (in our case, a period of one year is chosen) and that the changes in refractive index over the whole path L (metre) are prefectly correlated and equal to Δn_{max}, then, the corresponding maximum transit-time variation $\Delta\tau_{max}$ is given by

$$\Delta\tau_{max} = \frac{1}{c} (\Delta n_{max}) \cdot L \qquad 7.5.2$$

Assuming the value of the maximum refractive index change in the central London area in the year 1976, that is, $\Delta n_{max}=72 \times 10^{-6}$ (Section 7.5.1), the maximum transit-time variation is given by

$$\Delta\tau_{max} = 2.4 \times 10^{-13} \, L \quad \text{(seconds)} \qquad 7.5.3$$

Figure 7.10 plots the maximum transit-time variation against propagation path length.

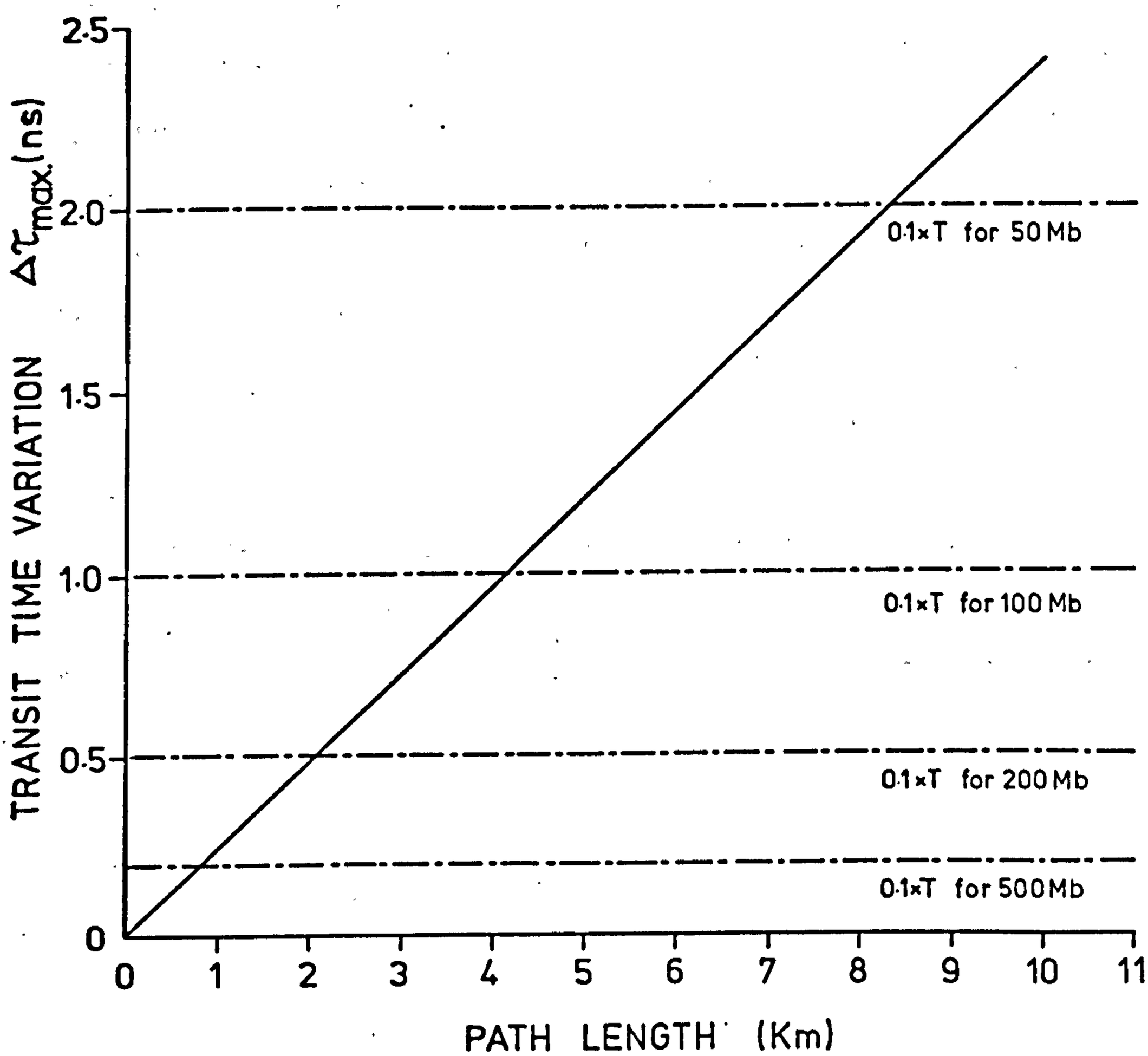

Fig. 7.10 Transit-time variation against path length.

To investigate the effect of this transit-time variation on the synchronization of a digital transmission system, consider the problem of synchronizing two clocks separated by a distance L metres. For a digital system with a pulse spacing T, two clocks may be considered synchronized if they are in phase to within a factor α of a pulse spacing. Normally, a factor $\alpha = 0.1$ is chosen. In Figure 7.10, lines of $\alpha \cdot T$ for pulse rates of 50, 100, 200 and 500 Mb are drawn. The intersections of these lines with the curve $\Delta\tau_{max}$ determine the maximum path lengths for which the transit-time variations may be neglected. For the synchronization criterion that $\alpha = 0.1$, the maximum path lengths are approximately 8.3, 4.2, 2.1 and 0.8 kilometres for pulse rates of 50, 100, 200 and 500 Mb in the central London area. In other words, for a certain path length, say, 4 Km, the maximum pulse rate that can be used without any problem arising from the transit-time variations is about 100Mb. Hence it is evident that if a high pulse rate and a long propagation path are to be used, some compensation for refractive index changes must be incorporated in a digital system running on a universal clock.

7.5.3 Estimation of rate of compensation for transit-time variation.

The above section does not provide any information on how rapidly the refractive index should be compensated. To do this, the time derivative of the transit-time variation must be considered.

Based on Equation 7.5.1, the time derivative of the transit-time variations is given by

$$\frac{d\tau}{dt} = \frac{1}{c} \int_{P_1}^{P_2} \frac{dn}{dt}\, ds \qquad 7.5.4$$

If, again, we assume for simplicity that $\frac{dn}{dt}$ is constant over a certain period of time and is the same along the whole propagation path, then

$$\frac{d\tau}{dt} = \frac{1}{c} \left(\frac{dn}{dt} \right) \cdot L \qquad 7.5.5$$

Assuming the extreme case on the 30th June, 1976 where the greatest rate of change of refractive index was 19 N units in one hour (between 10:00 to 11:00) then

$$\left(\frac{d\tau}{dt}\right)_{max} = 1.056 \times 10^{-6} L \quad \text{(nsec/min)} \qquad 7.5.6$$

Figure 7.11 gives the plot of this transit-time derivative against path length. From this curve, it can be seen that for a path length of 4 Km, the rate of change of transit-time variations is only 0.0042 nsec. in a minute which corresponds to 0.0021 bit in a 500 Mb system or 0.00084 bit in a 200 Mb system. If the same criterion of synchronization is adopted (i.e. $\alpha = 0.1$), the time required to have the two clock pulses differing by 0.1 of the pulse spacing for a 500 Mb system is approximately 47 minutes and for a 200 Mb system 120 minutes. That is, compensation for atmospheric transit-time variation has to be made for the order of one hour for short propagation links of several kilometres. However, all the data used in this evaluation assumes extreme values and the results provide upper bound limits for a digital transmission system design only.

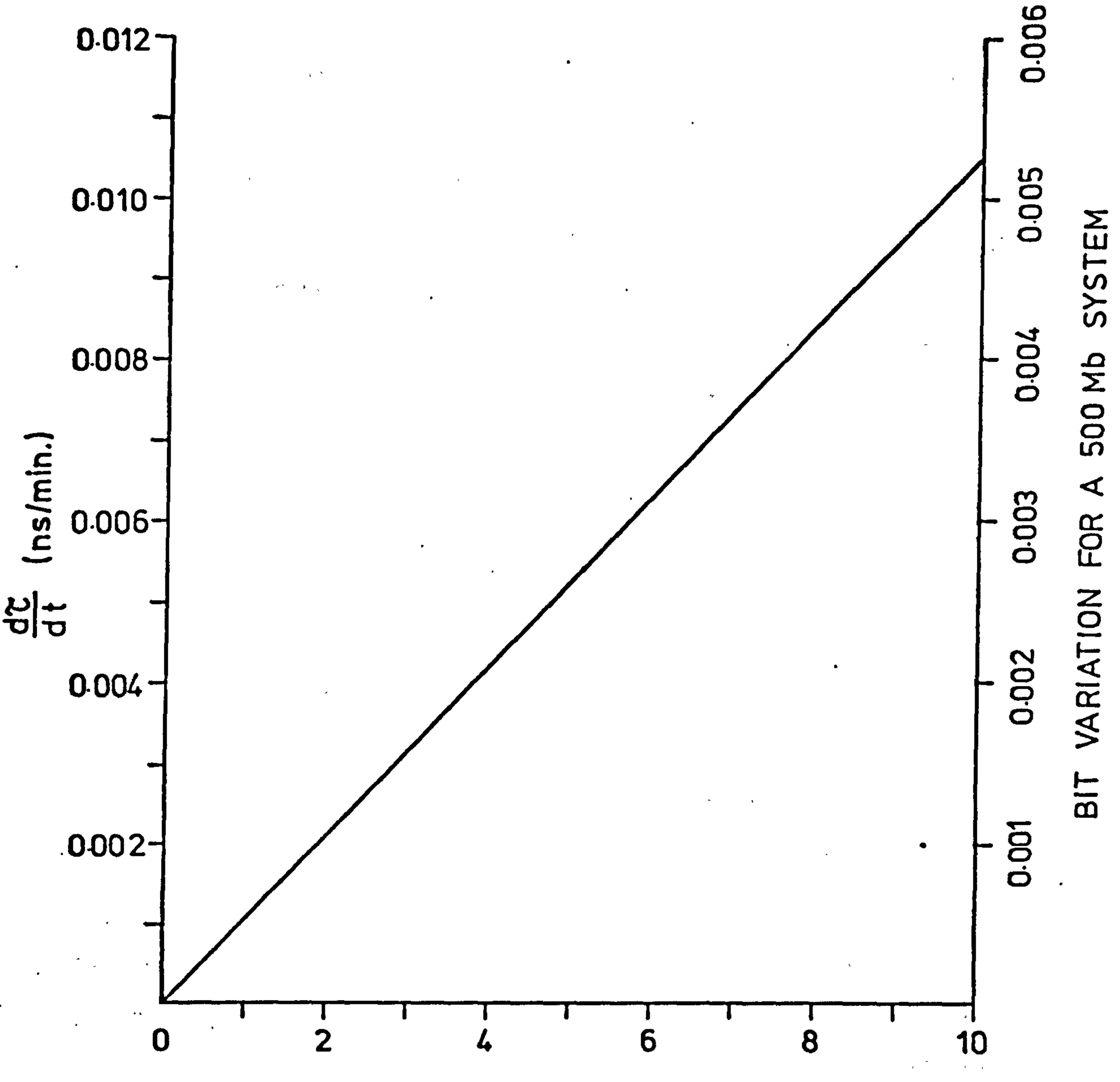

Fig. 7.11 Rate of transit-time variation against path length.

CHAPTER 8 SOME INTERESTING ANOMALOUS PHENOMENA OBSERVED AT 36 GHz

In this chapter, some interesting phenomena of the 36 GHz signal variations observed on this link are described. These include anomalous large amplitude fluctuations due to the environmental conditions in a town area, attenuation due to fog and some other scintillation effects which were suspected to be due to multipath propagation. Because of limited knowledge of the atmospheric structure causing these anomalous scintillation effects, no attempt is made to explain them quantitatively.

8.1 Daily variation of signal amplitude

Continuous recordings of the signal mean amplitude have shown a 24 hour periodicity of maxima and minima of the signal. In the absence of precipitation, the maximum value normally occurs around noon and the minima between midnight and the early hours of the morning. Under normal conditions, the level of the fluctuations also correspond with these maxima and minima signal values. There are virtually no fluctuations during night time but after dawn, both the signal level and the fluctuations increase. Figures 8.1(a) and 8.1(b) give an example of a 24 hour period chart recording of the signal level on a summers day (27-28th August, 1975) together with the temperature record. In this particular record, a difference of about 1 dB in levels within 24 hours was observed. The peak

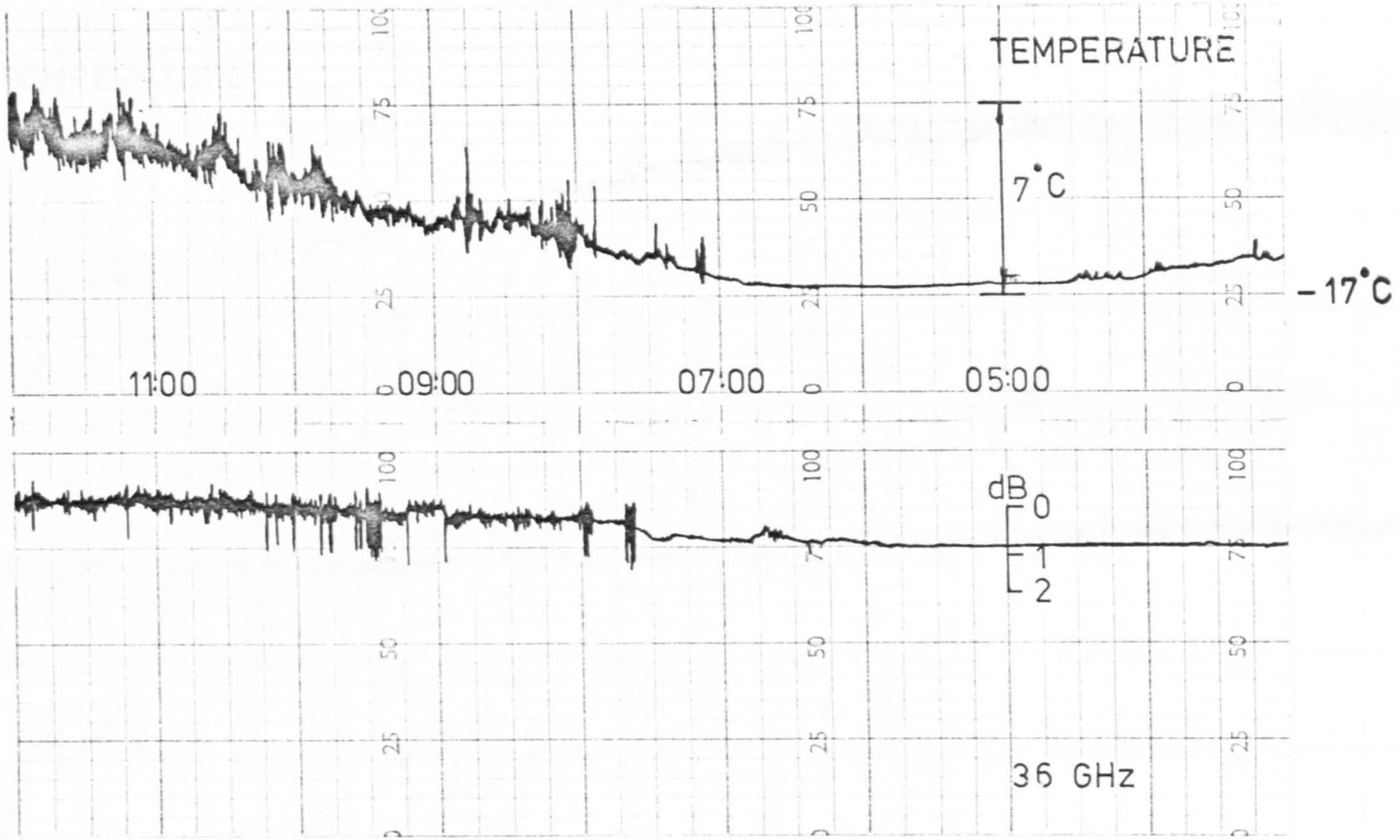

Fig. 8.1 Daily variation of 36 GHz signal.

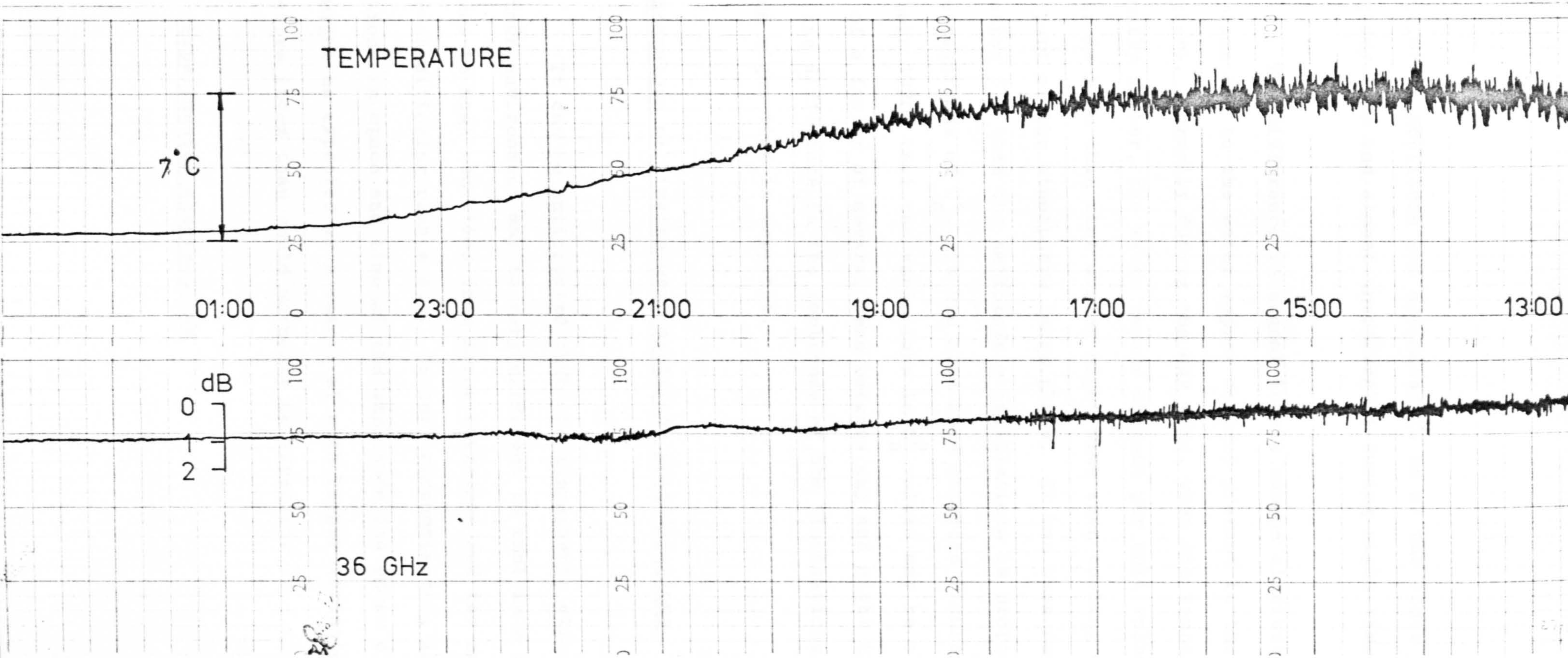

(b)

27-28 AUG. 75

Fig. 8.1

scintillation amplitude was estimated to be of the order of 0.4 dB during day time and almost unnoticeable during night time.

The difference in signal levels can be attributed to absorption due to the water vapour content present in the atmosphere. Normally during the day time, when the temperature is usually higher, the water vapour content per unit volume of the air is less than that during night time when cooling of the lower part of the atmosphere takes place. It has been established in Section 5.2 that the amplitude scintillations is proportional to the magnitude of C_n^2. It has also been reported (Lawrence and Strohbehn 1970) that the variations in C_n^2 values may be of the order of a factor of several tens between day and night time, hence the difference in the amplitude of the fluctuations between day and night time is expected.

8.2 Anomalous millimetre wave amplitude scintillations

It can be anticipated that the atmospheric structure in a town environment may be very different to that in a rural area due to heat radiation from large buildings and the output of air conditioning plants etc. In such circumstances, large variations in space and time of the amplitude and phase of a radio wave might be expected as a result of much larger variations in refractive index than would normally be expected.

8.2.1 Experimental observations

According to Tatarski's theory, the mean square value of the log-amplitude fluctuation, χ^2, is given by Equation 5.4.1

$$\chi^2 = 23.39\ C_n^2\ (\frac{2\pi}{\lambda})^{7/6}\ L^{11/6} \qquad (dB^2) \qquad 5.4.1$$

Assuming a typical value of C_n^2 for a warm summers day of $4 \times 10^{-14}\ m^{-2/3}$ and a value L of 4.1 Km, the corresponding mean square log-amplitude fluctuations is $8.94 \times 10^{-3}\ dB^2$ for the 36 GHz signal. This figure corresponds to an approximate peak to peak fluctuation of 0.27 dB, a value which has been obtained on this link under normal conditions. However, actual observation showed that values as high as 1.5 dB can occur under some circumstances.

Figures 8.2 and 8.3 show the chart records of examples of large scintillations on Thursday 8th July, 1976 and Wednesday 7th July, 1976. The wind speed was moderate at about 3 m/s and the mean temperature about 29°C. The largest peak to peak fluctuations were more than 1.5 dB. It can be seen that the amplitude of the fluctuations fell sharply at about 20:00 BST and 17:30 BST respectively. This reduction in amplitude of fluctuations also occurred in other recorded examples at approximately 8:00 p.m. on Thursdays, at 5:30 p.m. on other weekdays and 1 p.m. on Saturdays. These large fluctuations were caused by the output of an air-conditioning plant of a departmental store not far away from the propagation path at about 1.5 Km from the receiving end. The reduction in the amplitude fluctuations occurred when the plant was switched off at closing time. The amplitude of the scintillations was also

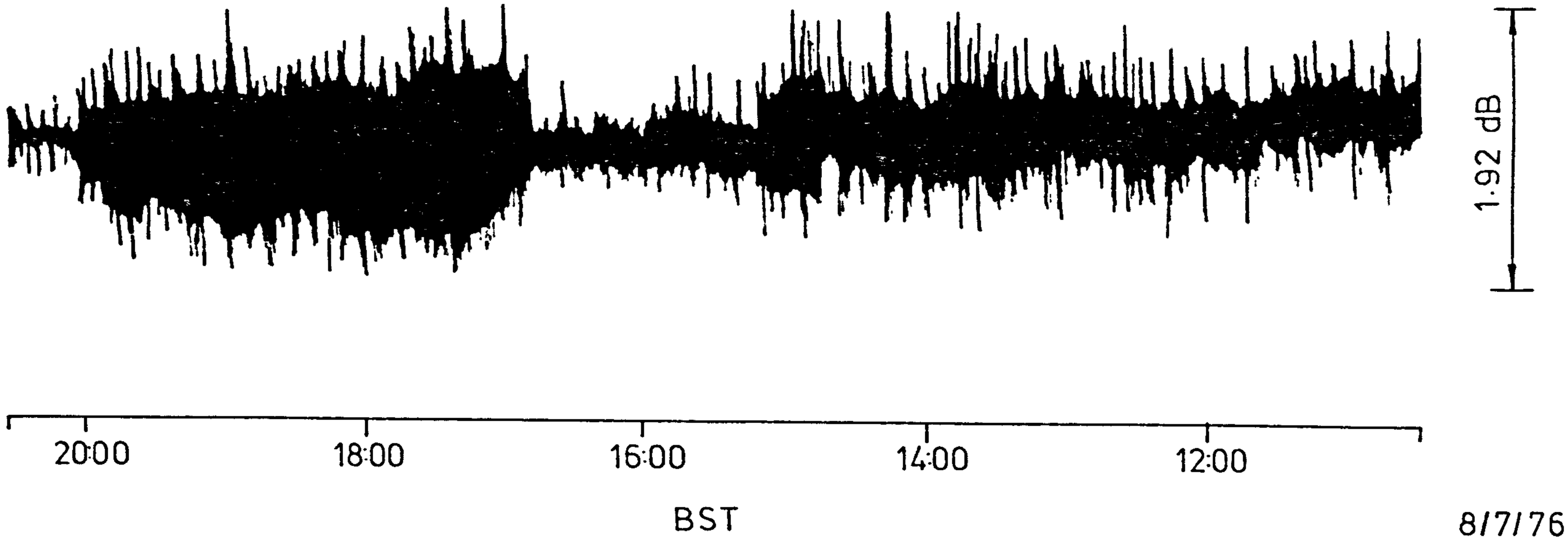

Fig. 8.2 Chart record of amplitude fluctuations at 36 GHz on 8 July 1976

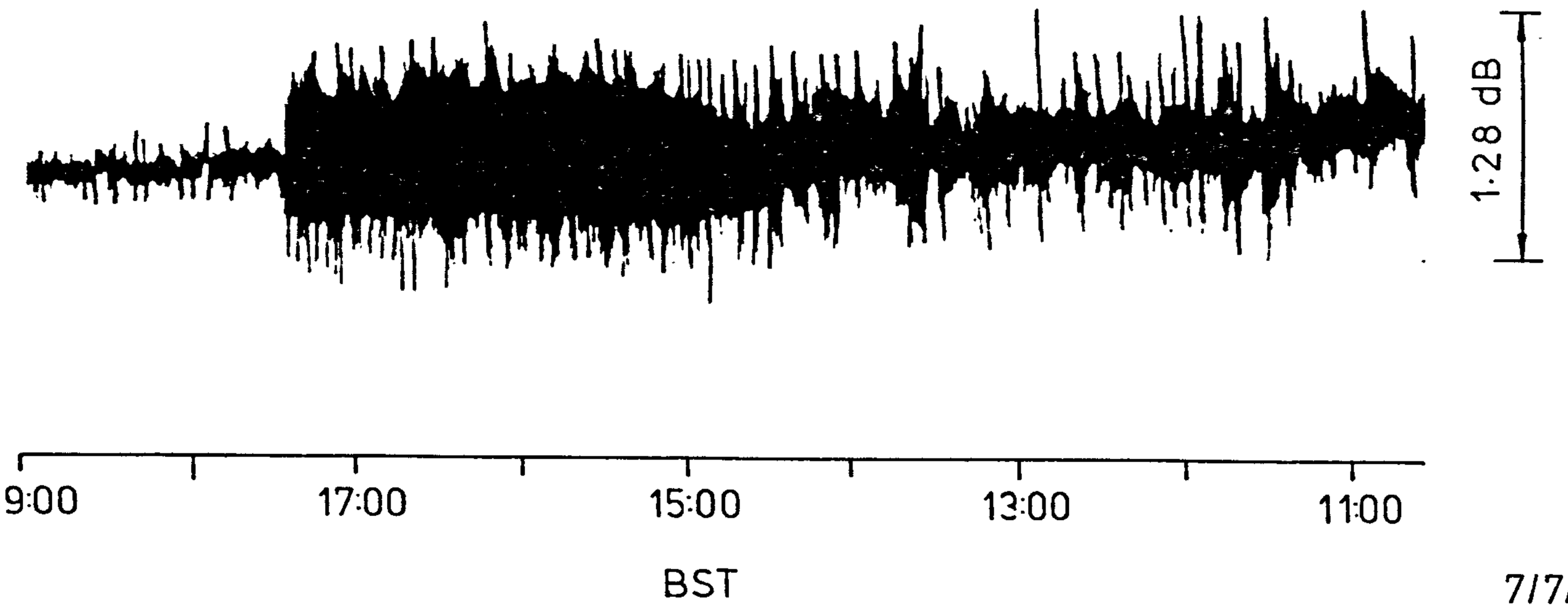

Fig. 8.3 Chart record of amplitude fluctuations at 36 GHz on 7 July 1976.

dependent on the wind direction. The output of the air-condition plant is not immediately below the propagation path but on its eastern side. This is clearly demonstrated in Figure 8.2 where the fluctuations between 15:00 to 16:40 BST decreased and increased again due to a change in wind direction which in the corresponding time veered from south-east (almost perpendicular to the path) to approximately south-south-east and back to south-east.

Figure 8.4 gives an example of the frequency scintillation spectrum of these large fluctuations. It has a spectrum slope very close to -8/3 and does not seem to differ from other fading spectra obtained under normal conditions except that it has larger amplitudes and a fairly flat response at the very low frequency end. Examination of the autocorrelation of these fluctuations reveals some periodicities of approximately 16 seconds and 1.8 seconds (Figure 8.5). Assuming the average wind speed of 3.5 m/s, these periodicities were estimated to be caused by scale sizes of approximately 56 metres and 6.3 metres respectively. In comparison with Figure 6.2 in Chapter 6 where an autocorrelation under normal condition of the atmospheric structure is shown, it is clear that the smaller size might be contributed by the hot air from the chimney of the air-conditioning plant.

Figure 8.6 shows the cumulative plot of the fades (or enhancement) of the signal in 25 milliseconds intervals. The data was sampled at a rate of 40 Hz and the absolute magnitude of the difference in signal levels between two consecutive points was calculated. This set of data was taken on the 8th July, 1976

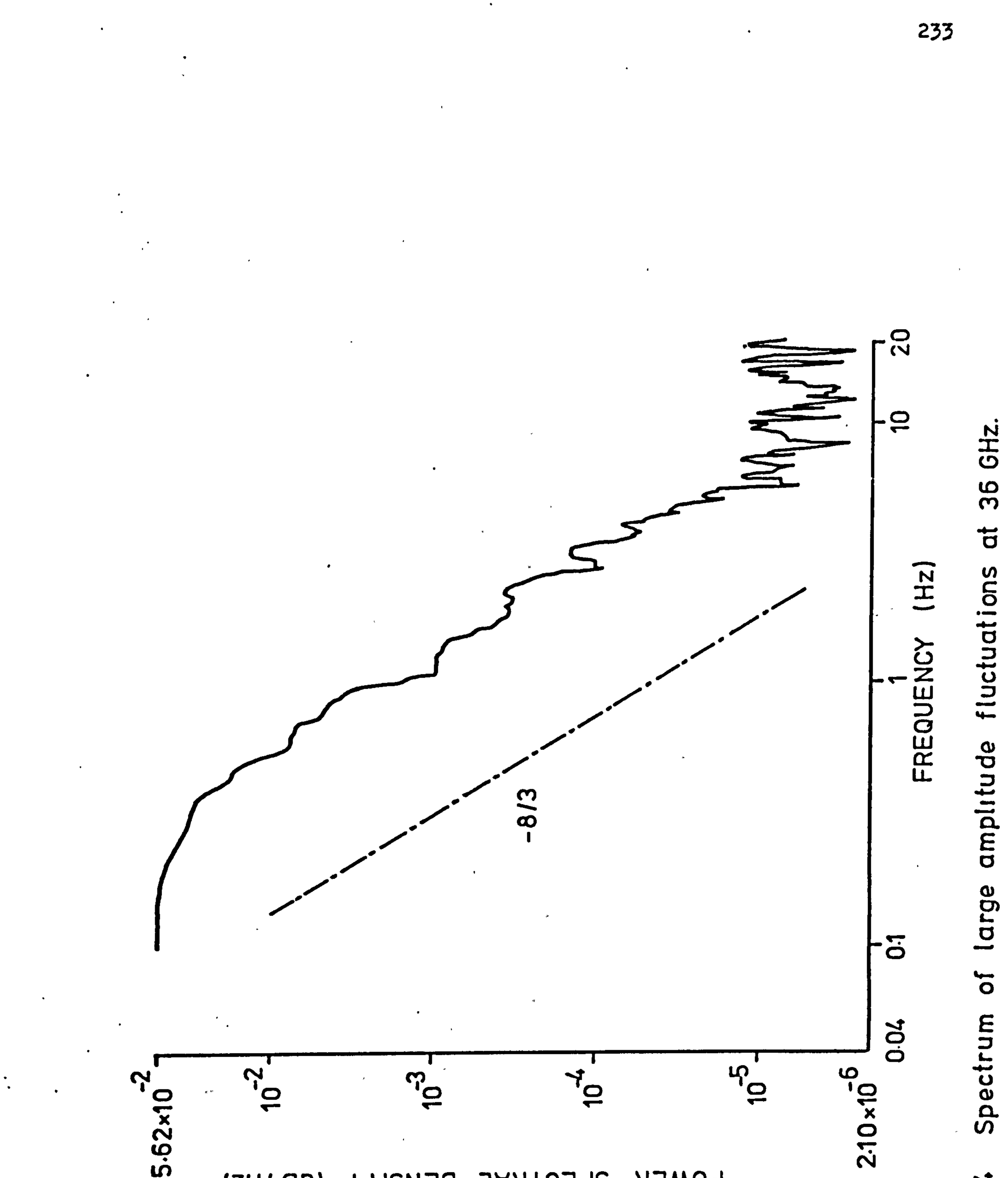
Spectrum of large amplitude fluctuations at 36 GHz.
FREQUENCY (Hz)
2.1
0.04
0.1
1
10
20
-8/3
10^{-2}
10^{-3}
10^{-4}
10^{-5}
10^{-6}
2×10^{-2}
5.6×10^{-6}
POWER SPECTRAL DENSITY (dB^2/Hz)

Fig. 8.4

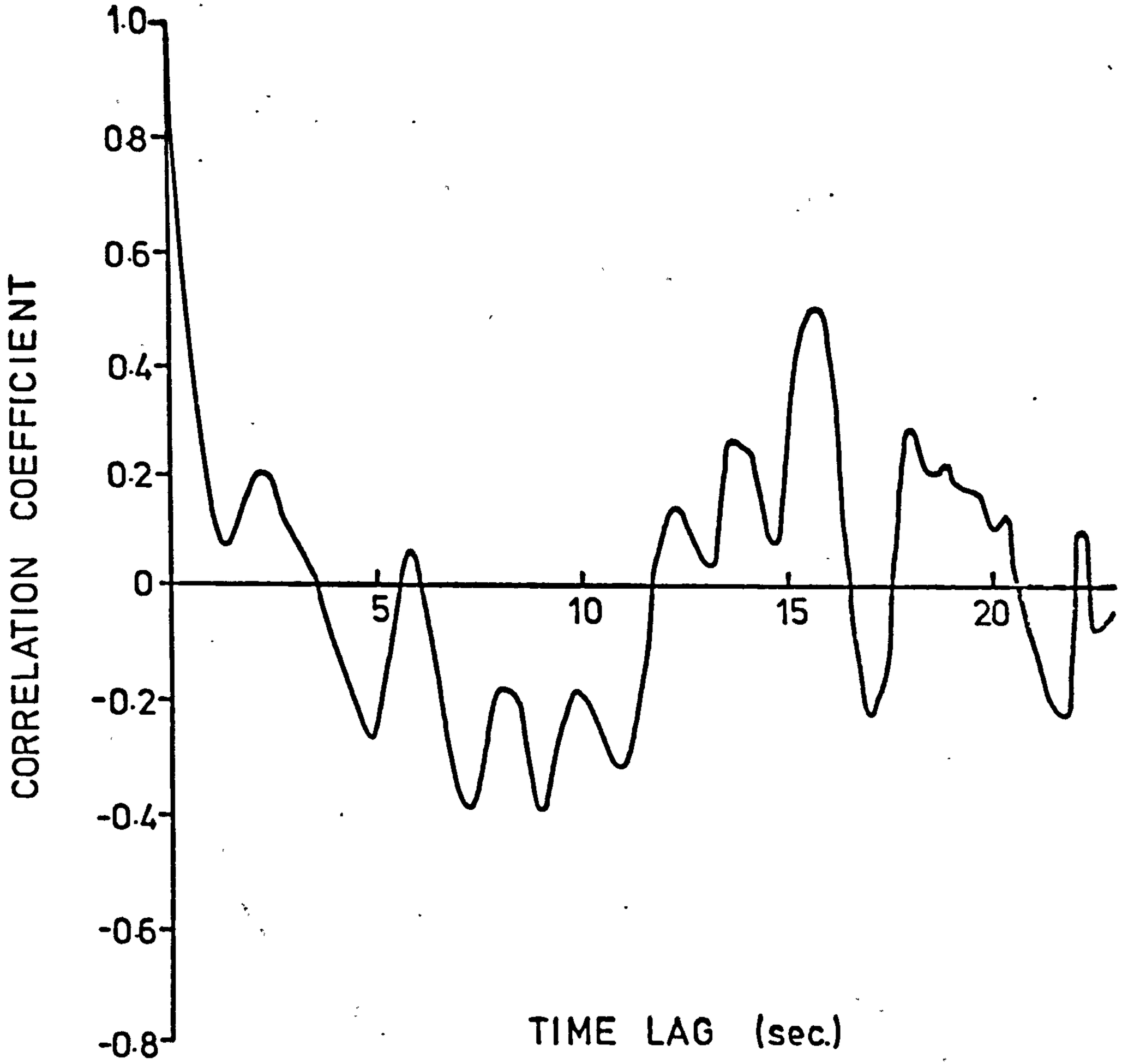

Fig. 8.5 Correlation function of the anomalous large fluctuations at 36 GHz

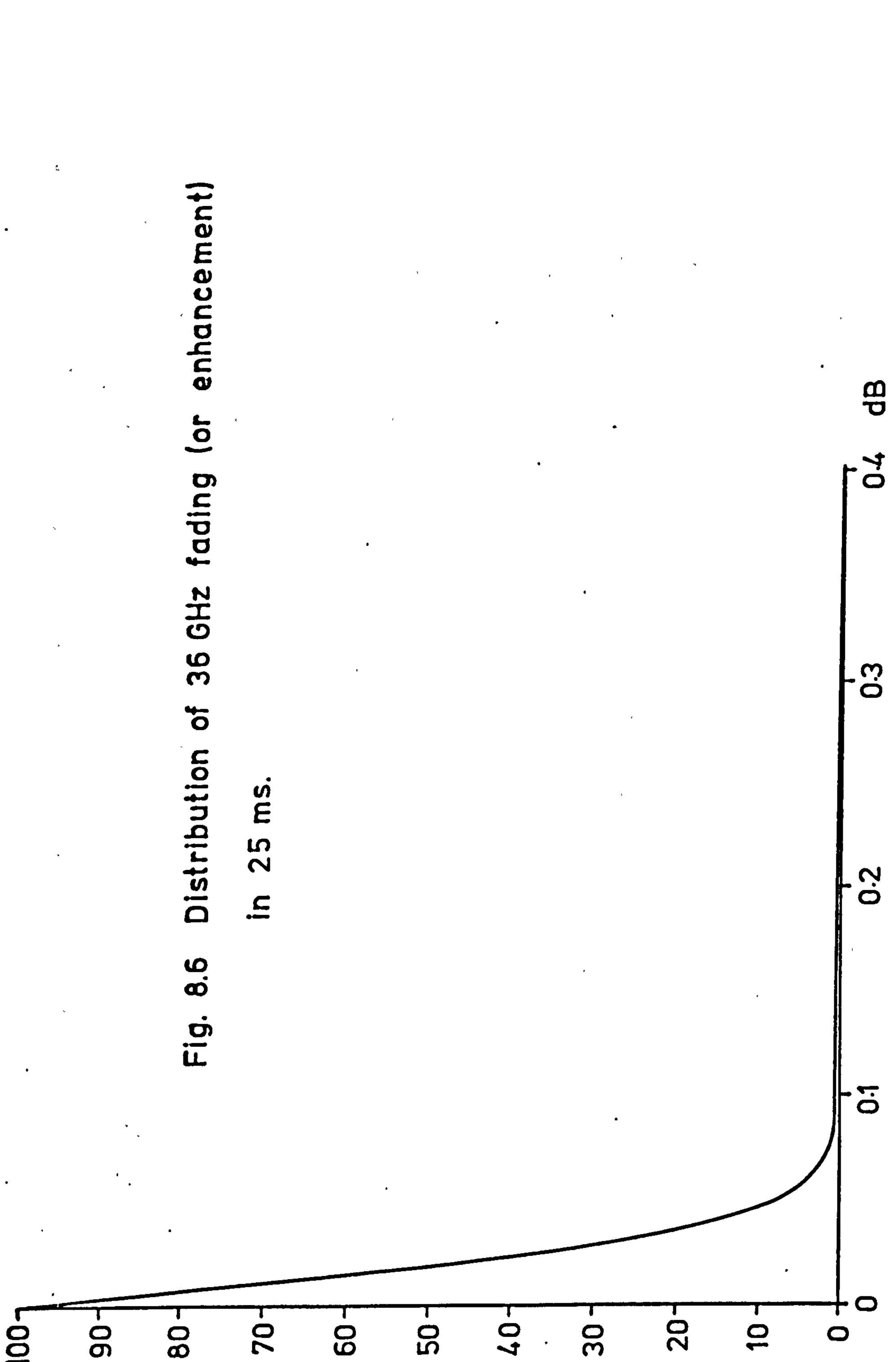

Fig. 8.6 Distribution of 36 GHz fading (or enhancement) in 25 ms.

between 17:00 and 18:30 BST. The ordinate is the percentage of time that a certain value of the fade in a 25 millisecond period in the abscissa is exceeded. The abscissa is the fade (or enhancement) in dB in a 25 millisecond interval. It can be seen that the maximum change in signal levels in 25 milliseconds is 0.4 dB. For one percent of the time during the period of the experiment (i.e. 54 seconds in 1.5 hours), the rate of change of amplitude of the fluctuations is 0.08 dB in 25 milliseconds.

8.2.2 Discussion

Assuming that the atmospheric turbulent medium can be considered to be composed of a large number (n) of slabs of the order of the outer scale size oriented perpendicular to the direction of propagation and that the original field A_o is amplitude modulated by random modulations $M_i(t)$ when passing through individual slabs, the log-amplitude at the receiver will be given as the sum of these independent modulated components (Section 5.3), that is

$$\log A_r(t) = \log A_o + \sum_{i=1}^{n} \log M_i(t) \qquad 8.2.1$$

Therefore it can be seen that if there are a number of such air-conditioning plants near the path the effect on the signal fluctuations will be additive. For example, if there are five such plants near the path, the maximum fluctuation would be about 7.5 dB. Correspondingly, the rate of change of amplitude would be considerably increased. Since it is very likely that a millimetre wave system would use digital modulation, it might be

expected that these fluctuations in carrier amplitude may not only be a contributory cause of the background error rate of the coded signal but may even produce a short burst of high error rate which can upset the synchronization of a system. However, little is known about the effect of carrier amplitude fluctuations on the performance of a digital communication system and it thus warrants further studies along an appropriate path in a town environment to investigate whether or not the performance would be significantly degraded by these large amplitude fluctuations.

8.3 Attenuation due to fog

Ryde (1946) has shown that as long as the ratio between the droplet diameter D and the wavelength λ is less than 0.015 (i.e. $D/\lambda < 0.015$), attenuation by fog, at a given temperature and wavelength in the centimetre band, is proportional to the total mass of water present in unit volume of air. Although the visibility depends upon both drop size and number of drops and not entirely on the liquid water content, in practice, however, visibility is an approximation of the liquid water content. Furthermore, Radford (1938) has shown that a log-log plot of the mass concentration of the droplets and the visibility is a straight line. Therefore, the attenuation of radio waves, to a good approximation, may be related to the range of visibility in a fog.

Based on Ryde's work, Saxton and Hopkins (1951) have

evaluated the attenuation to be expected in fogs at a temperature of $0^{o}C$ for wavelengths λ= 1.25 cm, 2.25 cm, 3.2 cm and 10 cm for various ranges of visibility. Their results are represented in Figure 8.7. The attenuation will vary with temperature because the dielectric constant of water changes with temperature; therefore at $15^{o}C$ and $25^{o}C$, the attenuation in Figure 8.7 should be multiplied by 0.6 and 0.4 respectively. In Figure 8.8, the attenuation due to fog at a wavelength of 8.33 millimetres for given visual ranges is plotted by means of an extrapolation of Figure 8.7 for a temperature of about $0^{o}C$. This curve will be used for comparison purpose with the measured attenuation on the 36 GHz link.

Figure 8.9 reproduces the chart record showing the attenuation due to fog on the 29th November, 1975. The maximum attenuation was more than 0.5 dB and occurred between 20:00 and 21:00 GMT. The visibility during that period was of the order of 300 metres.

A collection of the values of attenuation associated with fog on the U.C.L. 36 GHz link is presented in Table 8.1 together with the ranges of visibility obtained from the London Meteorological Office. The estimated attenuation was obtained from the curve in Figure 8.8 and forms a column of the table. The temperature on almost all of these occasions was close to $0^{o}C$ and therefore no temperature corrections for the attenuation have been introduced.

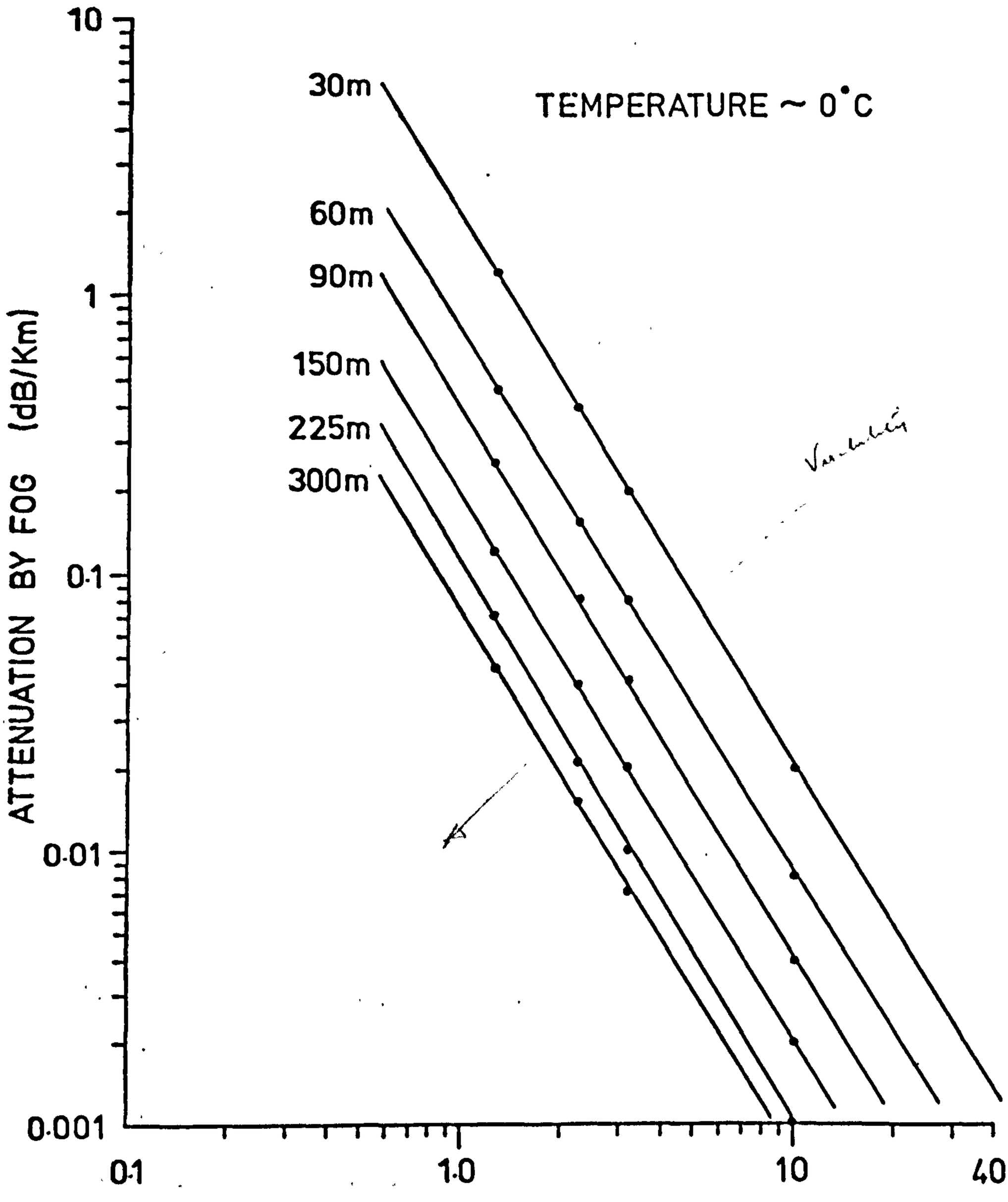

Fig. 8.7 Variation of attenuation by fog with wavelength and visibility.

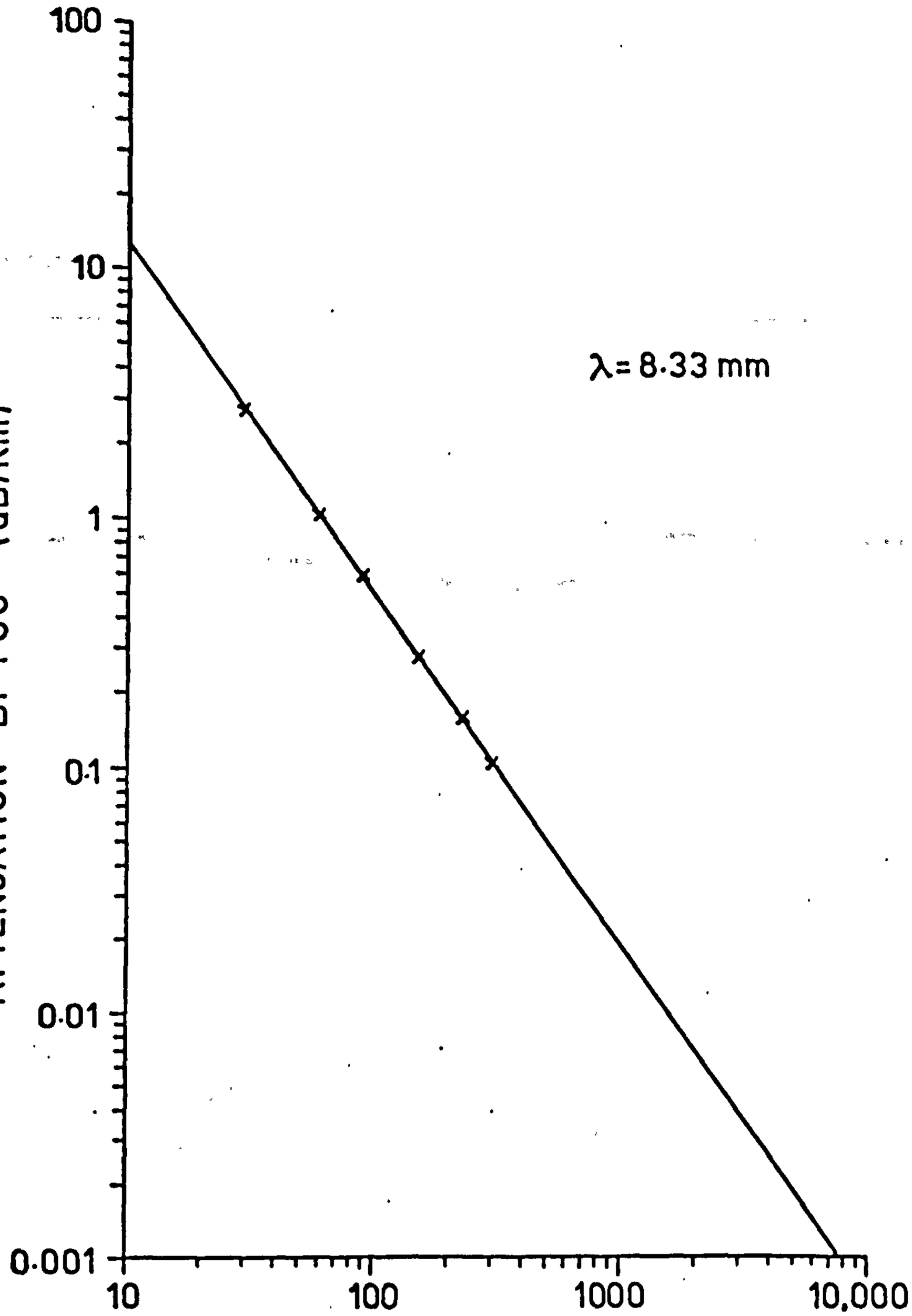

Fig. 8.8 Variation of attenuation due to fog with visibility at λ=8·33 mm.

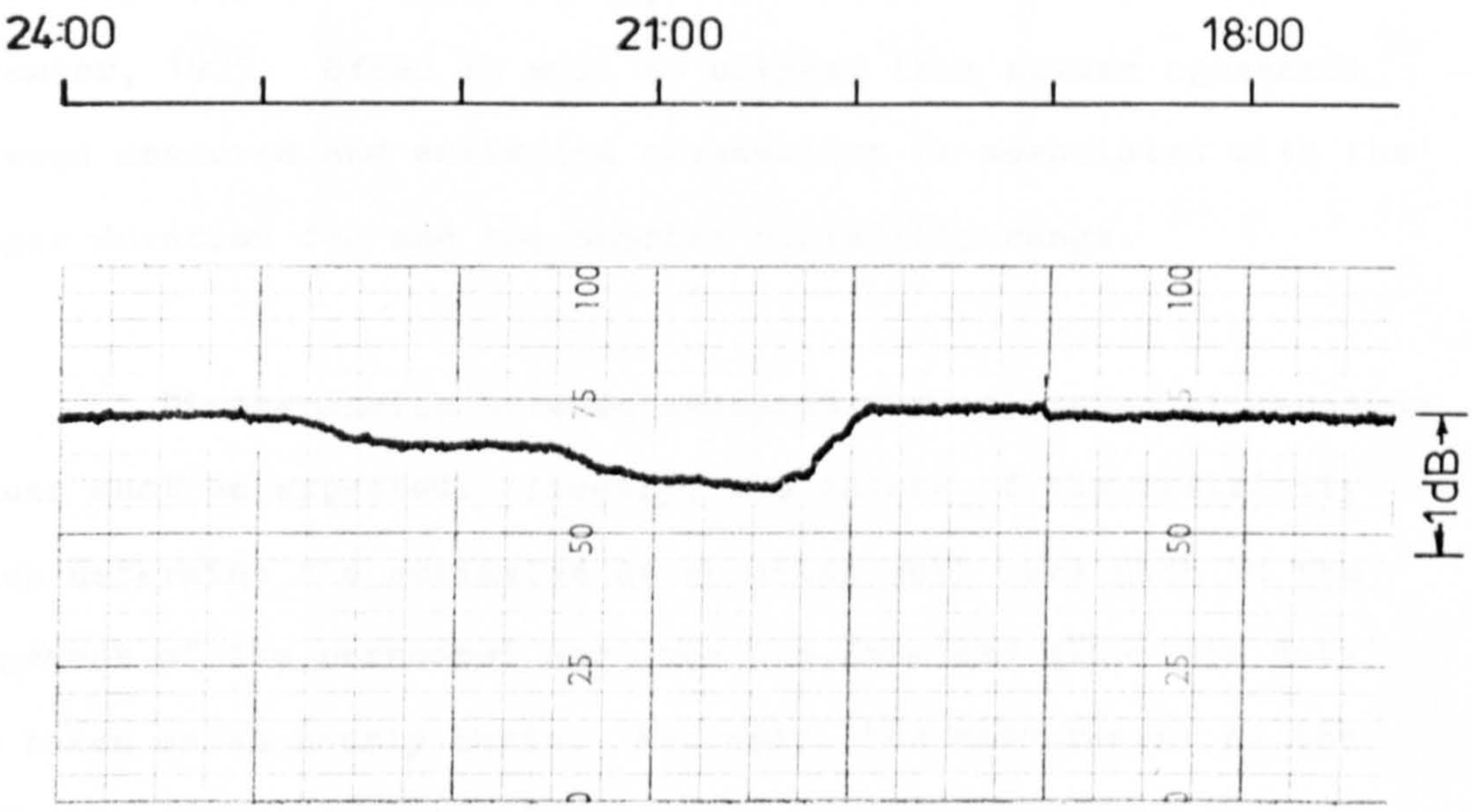

Fig. 8.9 Chart record of attenuation due to fog at 36 GHz.

It can be seen from Table 8.1 that sometimes the measured attenuation agrees very well with the estimated values whereas at other times, discrepancies are apparent. For example, on the 28th of October 1975, the measured and estimated values agreed very well between 06:00 and 08:00 GMT but at 09:00, they differ considerably. Good agreement was obtained on the 29th-30th November, 1975 but large discrepancies occurred on the 20th December, 1975. Often it will be noticed that better agreement between measured and estimated attenuation is associated with the longer duration fog and the shorter visibility range.

Discrepancies between measured and estimated attenuation values must be expected. Firstly, the values of the visibility which determine the estimated attenuation rely very much on the judgement of the personnel who take the data and also this data was taken on an hourly basis. Secondly, the measurement of the visibility was made only at one point, that is, very local weather conditions may have a great influence on the data. The attenuation on the link is due to the integrated effect along the entire propagation path along which the fog might be patchy. From the data obtained, the estimated attenuation on many occasions (11 out of 18), gives the same order of magnitude as the measured attenuation.

Tabel 8.1 Link attenuation due to fog.

Date	Hour GMT	Temp. °C	V.P. mb	Visibility metres	Est.Att. dB	Mea.Att. dB
28.10.75	06:00	6.3	9.2	230	0.64	0.56
	07:00	4.7	8.4	230	0.64	0.60
	08:00	5.0	8.6	500	0.22	0.25
	09:00	5.0	8.6	1200	0.06	0.16
29.11.75	21:00	3.4	7.6	300	0.44	0.44
	22:00	3.5	7.6	500	0.22	0.26
	23:00	3.5	7.7	300	0.44	0.12
30.11.75	00:01	3.8	7.8	800	0.11	0.07
	01:00	3.9	7.9	3000	0.02	0.12
	02:00	3.5	7.7	1200	0.07	0.07
	03:00	2.9	7.6	1000	0.08	0.11
	04:00	2.9	7.5	1000	0.08	0.11
15.12.75	19:00	1.2	5.8	500	0.22	0.29
	20:00	1.7	5.9	800	0.11	0.40
	21:00	0.8	5.7	1000	0.08	0.26
20.12.75	21:00	4.8	8.4	1500	0.05	0.15
	22:00	4.4	7.8	1500	0.05	0.23
	23:00	4.4	7.8	1500	0.05	0.07

8.4 Multipath fading and some other anomalous scintillations

Multipath propagation is the dominant cause of fading on a long hop lower frequency system. However since only short path lengths can be used at millimetre wavelengths, this effect may not be so severe. Ruthroff (1971) has theoretically estimated the length of a link below which the fading due to multipath propagation is less than 3 dB and found that at a frequency of 30 GHz, the path length limit is about 4.8 Km. However, this depends very much on the actual meteorological conditions which may vary considerably from place to place.

The primary cause of multipath propagation is the existence of a layered structure in the troposphere where the refractive index no longer varies continuously with height but has discontinuities which change rapidly with height. Such layering has been observed and studied by Lane (1968) and a gradient of about 1 N unit/ metre within layers of an average thickness of 10 metres was suggested.

During the continuous running of the 36 GHz link over the past two and half years, only one occasion was observed in which the fading was suspected to be due to multipath effects. The chart recording is shown in Figure 8.10. It occurred between 21:00 and 06:00 GMT on the 6th-7th November, 1975. The maximum fading was about 2 dB. The sky was very clear; the day time temperature was about 14°C while at night the temperature fell to about 5°C. The water vapour pressure was approximately 8.5 mb.

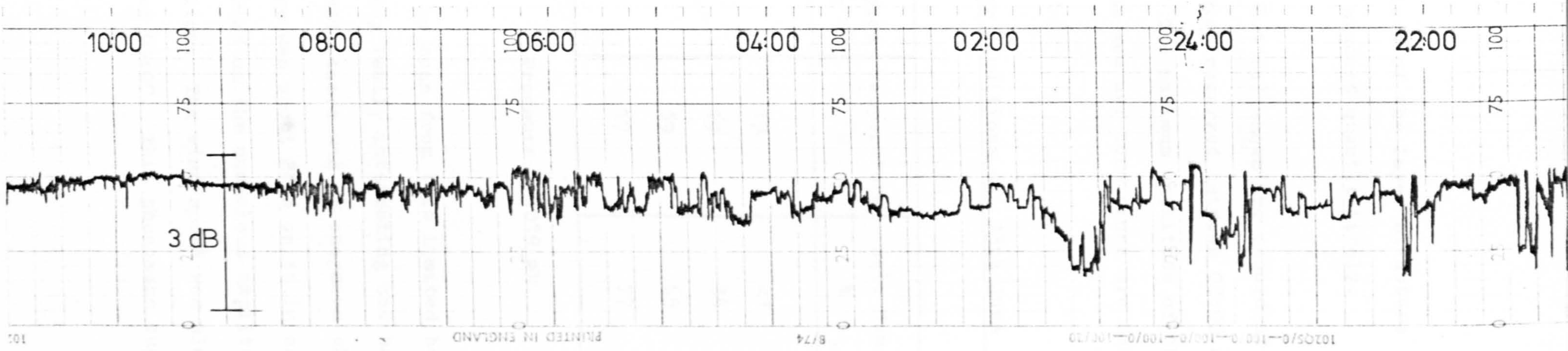

6–7/11/75

Fig. 8.10 Suspected multipath fading at 36 GHz.

However, due to lack of the layer structure information, this effect cannot be studied quantitatively.

Figure 8.11(a) shows the record of some anomalous scintillations which occurred between 02:00 and 03:00 BST on the 13th June, 1975. The maximum amplitude of the fluctuations was about 1.5 dB. The weather conditions are shown in Table 8.2.

Table 8.2 Weather conditions on 13th June ,1975

Time BST	Wind speed m/s	Temperature °C	Rel. Hum. %	V.P. mb	Refractivity N units
01:00	0	19	21	4.7	291.4
02:00	0	19	34	7.6	304.1
03:00	2	19	65	14.2	332.9
04:00	2	17	77	15.2	340.1

Pressure = 1019 mb

It can be seen from this limited hourly meteorological data that something really interesting had happened. Between 02:00 and 03:00 BST, there was an enormous change in the refractive index. The change was about 28 N units in an hour and occurred in the same time period as the anomalous amplitude scintillations occurred on the link. The wind speed was almost zero at 02:00 and about 2 m/s at 03:00. This phenomena suggested that a layer

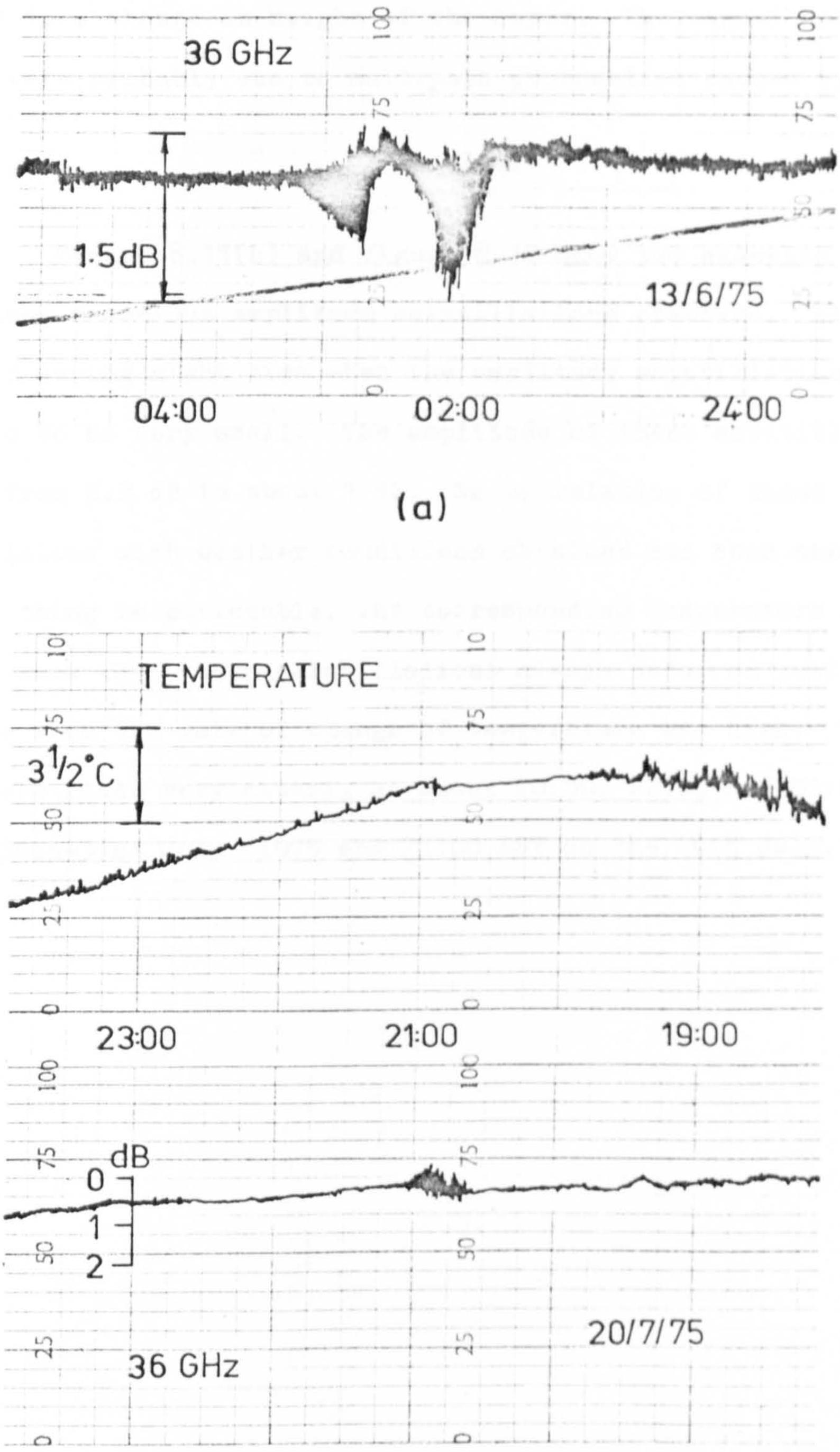

Fig. 8.11 Anomalous scintillations on the 36 GHz link.

might have been present and the enormous refractive index change was due to a change in height of the layer. The signal scintillations were probably due to multipath propagation caused by the layer.

Figure 8.11(b) and Figure 8.12 show two examples of some other anomalous amplitude scintillations observed. All these occurred during night time when the amplitude scintillations were expected to be very small. The amplitude of these scintillations ranged from 0.2 dB to about 1 dB. No correlation of these scintillaions with weather conditions obtained has been observed but one thing is noticeable, the corresponding temperature chart records show that these scintillations always occurred just at the time when the rate of change of temperature was high. These are demonstrated very clearly at about 20:00, 22:00 and 01:00 BST on the 30th-31st July, 1975 and 21:00 BST on the 20th July, 1975.

Fig. 8.12 Anomalous scintillations on the 36 GHz link.

CHAPTER 9 ATTENUATION BY PRECIPITATION AND RELIABILITY OF SYSTEM.

9.1 General introduction

At frequencies above 30 GHz, the wavelength of radio signals become comparable to raindrop diameters. As a result, a significant amount of attenuation is experienced when a microwave signal propagates through precipitation and this can impose a severe limitation on system performance. Prediction of the effects of rainfall in a location in which it is proposed to install a radio link is therefore important. It is particularly useful to establish relationships between attenuation experienced over a link and point rainfall rate measurements.

Classical electromagnetic theory allows, to some extent, the calculation of the attenuation by rain if the raindrops are considered as being dielectric spheres. A theoretical approach to this problem was developed by Ryde and Ryde (1944) and has formed the basis of much subsequent work. However, their theoretical results are for uniform rainfall along the path between transmitting and receiving antennas. In order to obtain a quantitative picture of the relationship between attenuation and rainfall rate experienced in practice, a great deal of systematic measurement of instantaneous rainfall intensity and rain-induced attenuation needs to be made. Numerous experiments have been carried out to verify the validity of the Ryde theory

(Medhurst 1965) and agreement between theory and experiment is not completely satisfactory. Indeed it is still not clear whether it is the experimental limitations or the theoretical assumptions which are the cause of this disagreement.

This chapter gives a review of the theory on rain-induced attenuation and some experimental results on the 36 GHz and 110 GHz links. Since the two links share a common path and are attenuated by the same volume of rain and therefore fade together, thus dual frequency study can indicate the validity of the theory which predicts a strong dependence on raindrop size distribution.

9.2 Theoretical evaluation of attenuation by rain

The analysis given here is mainly based on a review paper by Fedi (1975) (Tahim 1975).

When a radio wave is propagated through regions containing water droplets, the microwave power will be attenuated by two mechanisms. Some of the energy will be absorbed and converted into heat, and some of the energy will be scattered from the direct ray path. In the case of a plane monchromatic wave incident upon a spherical raindrop embedded in a non-dissipative medium, the total energy W removed per unit time by the drop is given by

$$W = S \cdot Q\left[D, \lambda, \eta(\lambda, T)\right] \qquad 9.2.1$$

where S is the magnitude of the incident Poynting vector and Q is the extinction cross-section of the drop, which may be interpreted as the sum of a scattering cross section and an absorption cross-section. The extinction cross-section is a rather complicated function of the drop diameter D, the wavelength λ and the complex refractive index of water, η, which in turn is a function of the temperature T and wavelength λ. It can be assumed that the total energy removed by N identical particles is proportional to N. The necessary conditions for this to hold, in practical cases, appear to be that (1) the drops are randomly scattered, with uniform average intensity, throughout the space between the transmitting and receiving antennas; (2) the assumption of a plane wavefront at each drop position is adequate and (3) the interaction between drops is negligible. The last condition implies that the distance between drops is sufficiently large to allow each particle to form its own scattering pattern undisturbed by the presence of the others. These are allowable assumptions when the distance between the drops is greater than five times their diameter (Ryde and Ryde 1944) as will normally be the case.

Therefore, in passing through a layer dx in thickness, the decrease in the magnitude of the incident Poynting vector is given by

$$-\frac{d\,S(x)}{dx} = S(x)\cdot\gamma(x) \qquad 9.2.2$$

where $\gamma(x) = \int_0^\infty n(D,x)\cdot Q\ dD$ and is commonly defined as the extinction coefficient.

and $n(D,x)\ dD$ is the average number of drops per unit volume with diameter lying between D and D+dD

For a propagation path L, the magnitude of the Poynting vector at the receiving end is obtained by integrating Equation 9.2.2 giving

$$\ln \frac{S(L)}{S(0)} = -\int_0^L \gamma(x)\ dx \qquad 9.2.3$$

If it is assumed that n(D,x) does not depend on x, i.e.

$$n(D,x) = n(D)$$

the attenuation in dB/unit length can be expressed by

$$A = 10 \log_{10} \frac{S(L)}{S(0)} = 4.34\gamma$$

$$= 4.34 \int_0^\infty n(D)\cdot Q\ dD \qquad 9.2.4$$

It is general practice to associate the attenuation with the rainfall rate R, defined as the volume of water reaching the ground per unit time and given by

$$R = \int_0^\infty \frac{4}{3}\pi \left(\frac{D}{2}\right)^3 \cdot n(D)\cdot V(D)\ dD \qquad 9.2.5$$

where V(D) is the terminal velocity of the raindrops of diameter D in still air. However in Equation 9.2.5 n(D) is not a conveniently measurable parameter and it is more convenient to make experimental measurements of the distribution m(D), defined as the fraction of the total volume of water reaching the ground due to drops of diameter D. This distribution can be related to

n(D) and R by means of the expression:

$$m(D) = \frac{\frac{4}{3}\pi\left(\frac{D}{2}\right)^3 \cdot n(D) \cdot V(D)}{R} \qquad 9.2.6$$

From Equations 9.2.4, 9.2.5 and 9.2.6, the attenuation per unit length can therefore be represented by

$$A = \frac{6 \times 4.34}{\pi} R \cdot \int_0^\infty \frac{Q\left[D, \lambda, \eta(\lambda, T)\right]}{V(D) \cdot D^3} m(D)\, dD \qquad 9.2.7$$

Numerical results for rain-induced attenuation computed from Ryde's formula have been given by several authors (Medhurst 1965) (Setzer 1970). It has been suggested that the approximate theoretical variation of A with R is given by the simple exponential relation (Gunn and East 1954)

$$A = c \cdot R^{\alpha} \qquad 9.2.8$$

or for R greater than some appropriate values (being dependent on the frequency) by (Bodtmann and Ruthroff 1974)

$$A = a + bR \qquad 9.2.9$$

where c, α, a and b are constants dependent on frequency.

9.3 Measured rainfall attenuation

Numerous experiments have been carried out to verify the validity of the theoretical relationship between attenuation

and rainfall rate at various frequencies. The usual procedure for measurement of rainfall attenuation has been the straight forward one of setting up transmitting and receiving antennas at the ends of a line-of-sight path and locating a number of raingauges along the path.

In general, as concluded by Medhurst (1965), the agreement between measured and predicted values is not completely satisfactory. A wide scatter of points is almost always reported. In many cases, a substantial portion of the points lies within the extreme limits of theoretically predicted attenuation, but there is a marked tendency for observed attenuation to fall well above predicted values. On the other hand, measurements made recently, seem to confirm the data predicted by the theory (Norbury and White 1972) (Sander 1975) (Llewellyn Jones and Závody 1973). Moreover, a dual frequency measurement experiment by Semplak (1971) also shows good agreement with the theoretical computations.

Discrepancies between experimental and theoretical values may be due to a considerable number of causes. Besides the shortcomings in the experimental techniques and errors in the meteorological instruments used in the experiments, the experimental values assumed for m(D), $\eta(\lambda, T)$ and V(D) in the calculation of attenuation-rainfall rate relationship; the variation in $\eta(\lambda, T)$ and V(D) due to temperature and wind velocity respectively, may vary the predicted values considerably.

9.4 Variations in theoretical calculations

9.4.1 Drop size distribution effect

Three drop size distributions are generally adopted, namely those proposed by Laws and Parsons (1943), Marshall and Palmer (1948) and Joss et al (1968), of which the Laws-Parsons distribution is most commonly used (Figure 9.1). Marshall-Palmer and Joss et al proposed exponential distributions that give n(D) directly. The distribution is represented by the general expression

$$n(D) = n_o e^{-bD} \qquad 9.4.1$$

where n_o is a constant and b is a parameter related to the terminal velocity V(D) and the rainfall rate. Joss et al, in addition, proposed three different distributions of the same form depending on the characteristics of the rainfall, that is, drizzle; widespread and thunderstorm.

The effect of the drop size distribution on attenuation values at 35 GHz due to rainfall was studied by Norbury and White (1973) who concluded that over the range 5 to 150 mm/h the attenuation values vary by about 10% between distributions and that the dependence of the attenuation on drop size distribution is at a minimum in the region 20 to 40 GHz.

9.4.2 Temperature effects

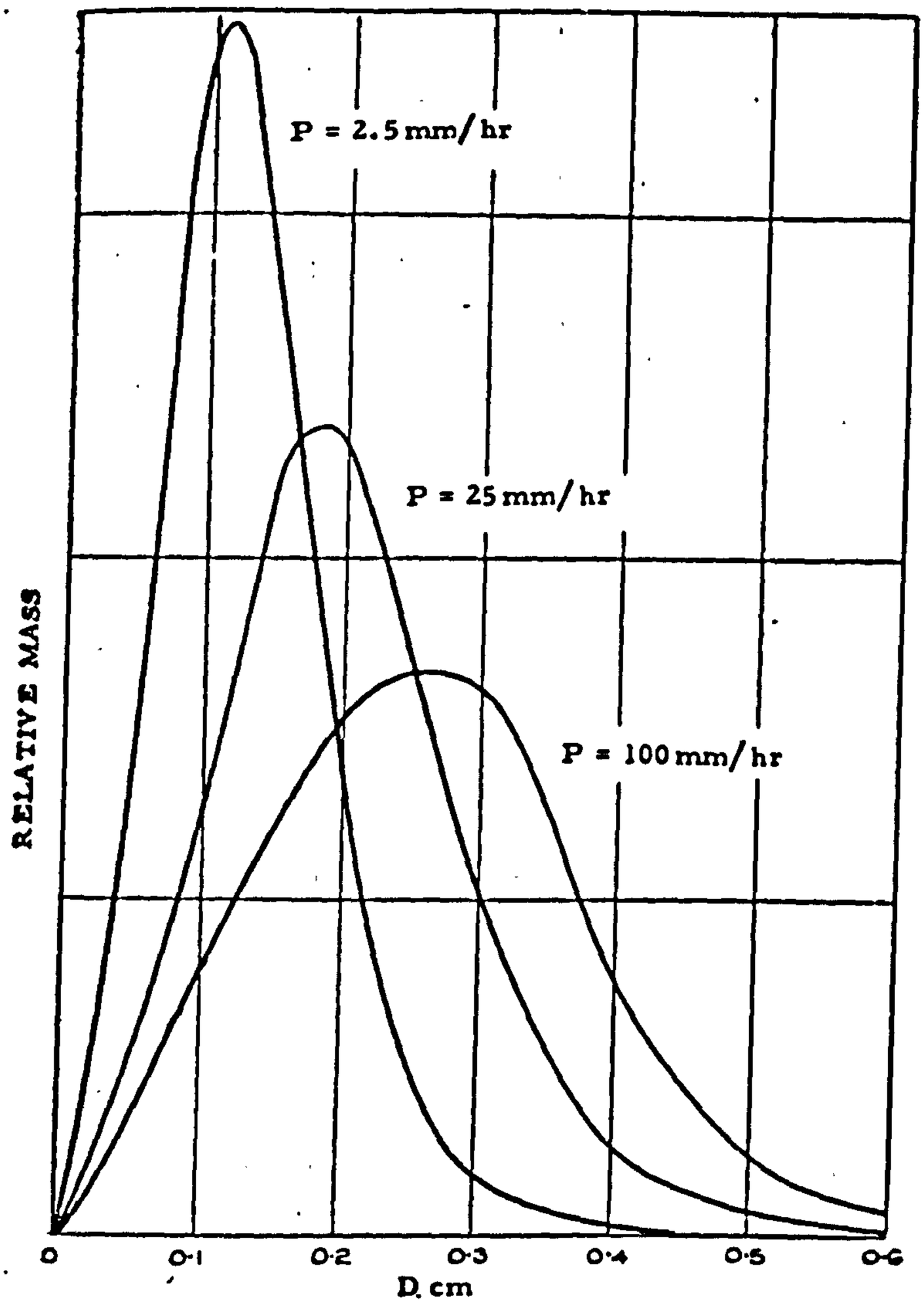

FIGURE 9.1. *Relative total mass of liquid water in the air contributed by rain drops of diameter* D *for various precipitation rates.*
(Derived from Laws and Parsons' distributions for a horizontal surface by dividing by the appropriate terminal velocities.)

Temperature variations cause changes in the complex dielectric constant of water, thus altering the values of attenuation coefficient. Percentage change in attenuation with respect to the value at 18°C was computed by Ryde et al (1944). In the temperature range 0 to 40°C and for wavelengths of 10 mm or less, the percentage change does not exceed ± 20 percent and are generally much less. The largest percentage change is found to be at low precipitation rates.

9.4.3 Effect of the vertical component of wind velocity

In the theoretical calculation of rain-induced attenuation it is always assumed that raindrops fall through still air and the terminal velocity of raindrops in still air proposed by Gunn-Kinzer (1949) is assumed (Figure 9.2). However considerable turbulence does occur during some rainfall and a vertical wind component may be present. Although the raindrops density in the microwave beam is independent of the vertical wind velocity, assuming homogeneous mixing, the rainfall rate measured at the ground is not. Even at some quite moderate vertical wind velocities, the observed rainfall rate is altered considerably. Norbury and White (1973) computed the effect of vertical wind velocities on the ground measured rainfall rate and found that a change of about 40% of the measured rainfall rate is possible at low precipitation rates for a vertical wind velocity of about 1 m/s. Hcwever, unlike the effects due to drop size distribution and temperature, the uncertainties arising from the vertical

Table removed due to third party copyright

Fig.9.2 Dependence of terminal velocity on drop diameter (Gunn-Kinzer)

motion of drops are much more difficult to access.

9.4.4 Effect due to non-spherical shape of raindrops

In practice, raindrops are not truly spherical (as assumed in Ryde's theory) but tend to be flattened at the base, the amount of flattening increasing with the size of the drops. It is due to this oblateness of the raindrops that the attenuation would be sensitive to polarization. It is reported (Tahim 1975) that at frequencies below 50 GHz, attenuation for horizontal polarization might be slightly higher and attenuation for vertical polarization some percent lower than the theoretical value assuming spherical drops.

9.5 Rainfall attenuation measurements at 36 and 110 GHz

9.5.1 Experimental details

Fading measurements were made on the two links at 36 GHz and 110 GHz and the rainfall rate was measured by an electronic raingauge situated at the receiving end. The signal levels were recorded on charts and were also punched on paper tape. Thirty levels of the signal amplitude covered the range from 0 to 20 dB and 0 to 35 dB for the 36 GHz and 110 GHz respectively. The sampling frequency was 3 samples per channel per minute. The raingauge gave readings of the rainfall rate

up to 35 mm/h in steps of 0.56 mm/h. The integration time was 20 seconds.

Care was taken in the selection of data. Normally, data was taken only during prolonged, widespread rainfall at a moderate precipitation rate so as to ensure a greater degree of uniformity of rainfall over the whole propagation path, since rain cells are more localized for rain with a high precipitation rate and short duration (Weible and Dressel 1967). Evaluation of the attenuation-rainfall rate relationship was based on data punched on paper tape. The first step in the data processing was to plot the sampled attenuation levels and the sampled rainfall rate. Only data on those occasions which showed a marked correlation was used for analysis. This selection of data greatly improved the reliability of the result.

It was also the purpose of this experiment to test the validity of Laws-Parsons raindrop distribution. Since rain-induced attenuation at centimetric and millimetric wavelengths is a function of drop size; conversely, a measure of drop size can be obtained from multi-frequency measurements over a common propagation path. The ratio of the attenuations measured simultaneously at the two wavelengths (36 GHz and 110 GHz) was plotted against the attenuation at either wavelength and the result was compared with that theoretically obtained by assuming Laws-Parsons drop size distribution.

9.5.2 Experimental results

Figure 9.3 shows the chart records of the rain-induced attenuation at 110 GHz and 36 GHz on the 31st May, 1976. The maximum attenuation was about 17 db for the 110 GHz signal and approximately 7 dB for the 36 GHz signal. One point clearly shown is the close correlation between the two records. Another chart record of a large fade of long duration at 36 GHz is shown in Figure 9.4. In this prolonged shower, an attenuation higher than 20 dB was observed.

Figure 9.5 shows the attenuation-rainfall rate relation at 36 GHz obtained from data taken during six showers in the year 1976 under the condition that the rainfall was expected to be uniform along the entire propagation path. The ordinate is the attenuation in db/Km and the abscissa is the rainfall rate. The range of rainfall rate considered is up to about 18 mm/h. The line representing the theoretical attenuation-rainfall rate relationship assuming the Laws-Parsons drop size distribution is also shown. Scattering of data points can be observed, particularly at low precipitation rates. The trend is that the measured attenuation seems to be higher than that theoretically predicted. The attenuation coefficient was found to be 0.286 dB/Km-mm/h which is about 12% higher than the theoretical value.

The attenuation-rainfall characteristic obtained from four showers for 110 GHz is shown in Figure 9.6. Again, scattering of data points can be observed. The line derived from Ryde's theory assuming the Laws-Parsons drop size distribution together with the regression line (drawn by eye) are presented for

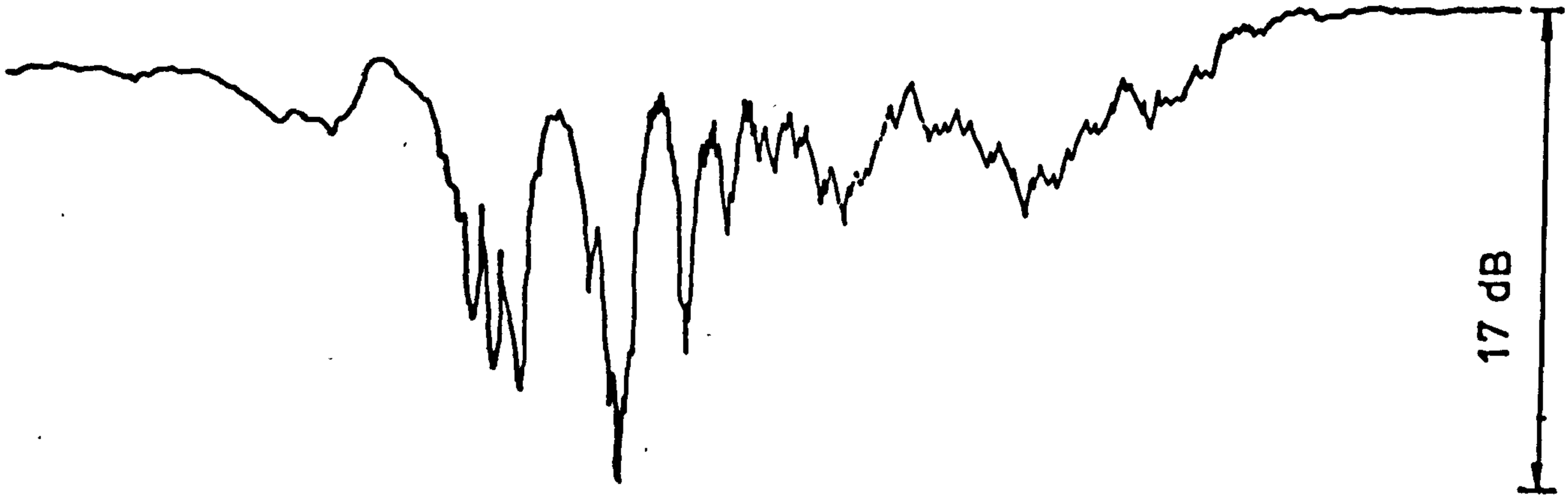

110 GHz

DATE: 31/5/76

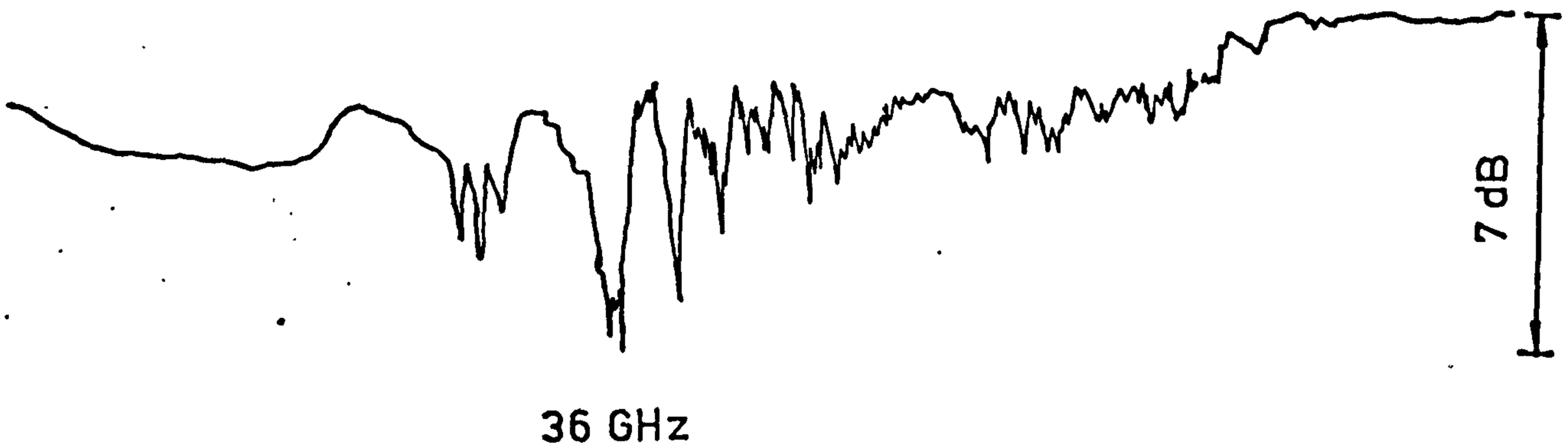

36 GHz

Time ?

Fig. 9.3 Chart records of rainfall attenuations

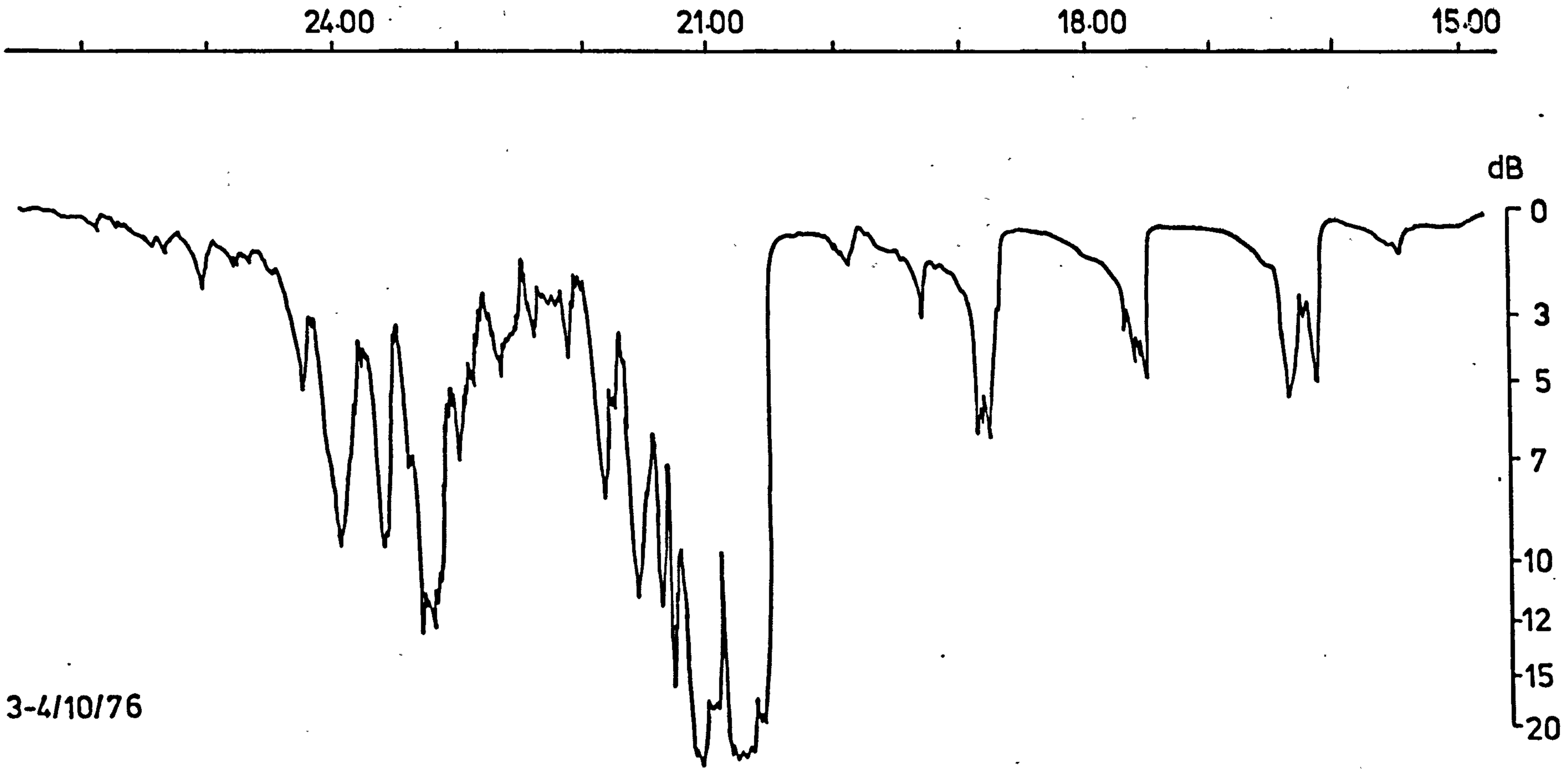

Fig. 9.4 Chart record of large rainfall attenuation at 36 GHz

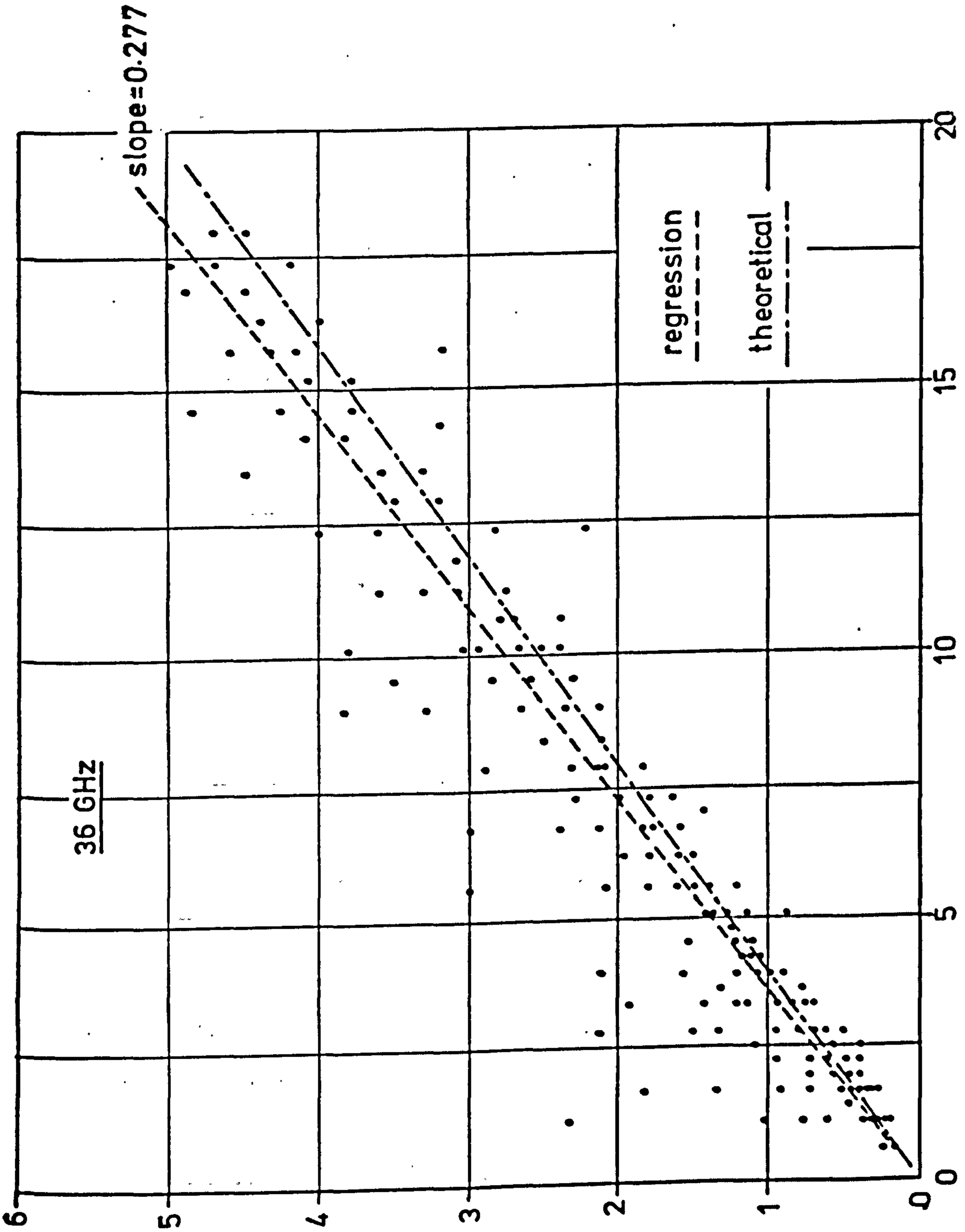

Fig. 9.5 Rainfall attenuation characteristics at 36 GHz.

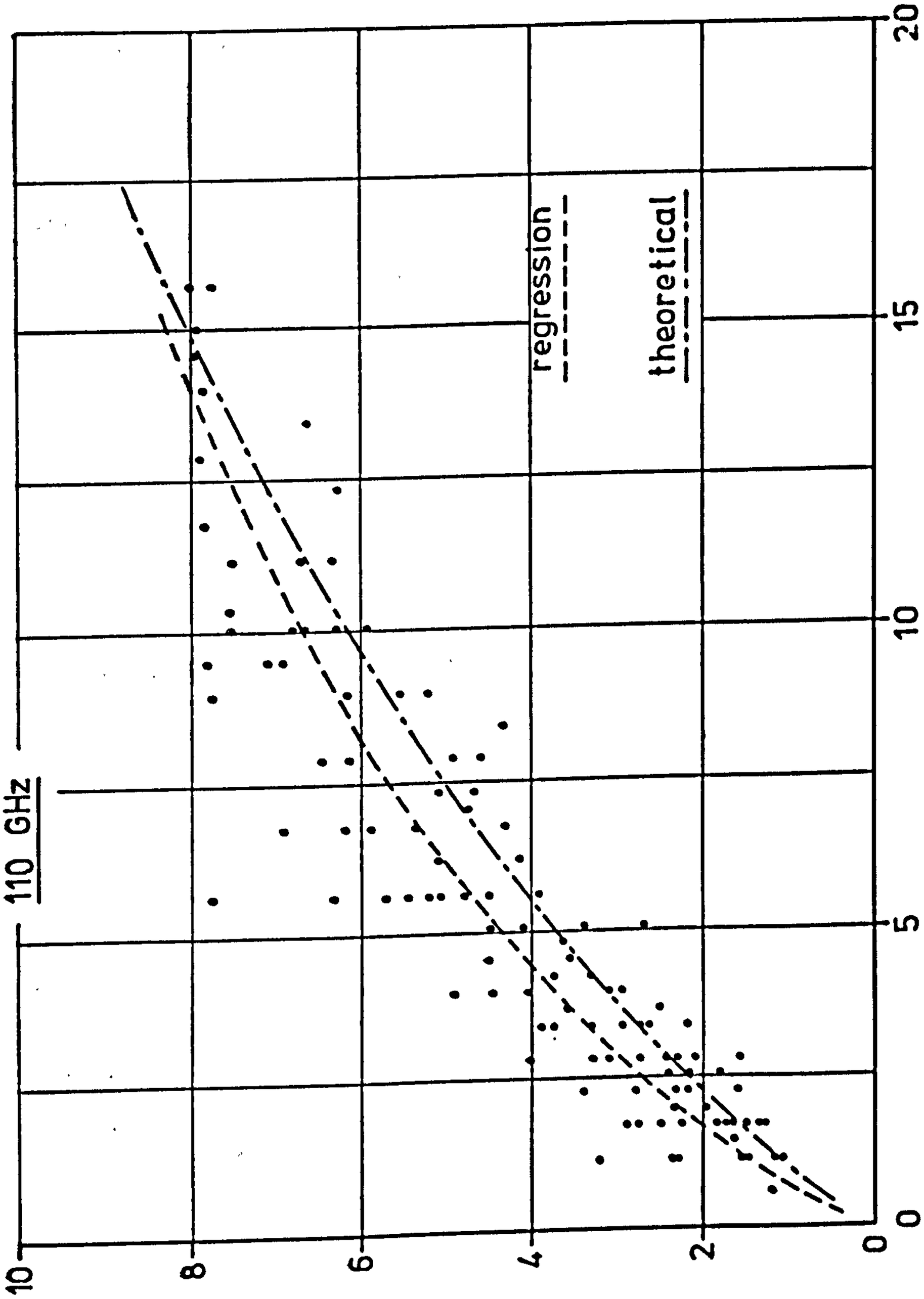

Fig. 9.6 Rainfall attenuation characteristics at 110 GHz.

comparison. It can be seen that the measured attenuation tends to be higher than the predicted value. The deviation is about 17% at about 3 mm/h and approximately 4% at 14 mm/h.

Ratio of attenuation measured simultaneously at the two frequencies (att_{110}/att_{36}) was plotted against the attenuation at either frequency (att_{36} or att_{110}) in Figures 9.7 and 9.8. The dashed lines represent the theoretical ratio of 110/36 GHz attenuation obtained using the Laws-Parsons drop size distribution assuming a uniform rainfall rate over the path. Although the data points are scattered, it is apparent that the theoretical ratio derived from the Laws-Parsons fits the data well particularly for attenuation exceeding 4 dB/Km at 110 GHz and 1.5 db/Km at 36 GHz.

9.5.3 Conclusions

No definite conclusion on the experimental values of the attenuation coefficient for the two frequencies (36 GHz and 110 GHz) can be derived from the attenuation-rainfall rate measurements presented in Figures 9.5 and 9.6 because the effects of different parameters on attenuation-rainfall measurements and the lack of homogeneity in rainfall intensity along the propagation path may contribute to a considerable discrepancy between experimentally measured and theoretically predicted values. It is very difficult (or impractical) to take into account effects due to all these parameters and a discrepancy of less than 20%

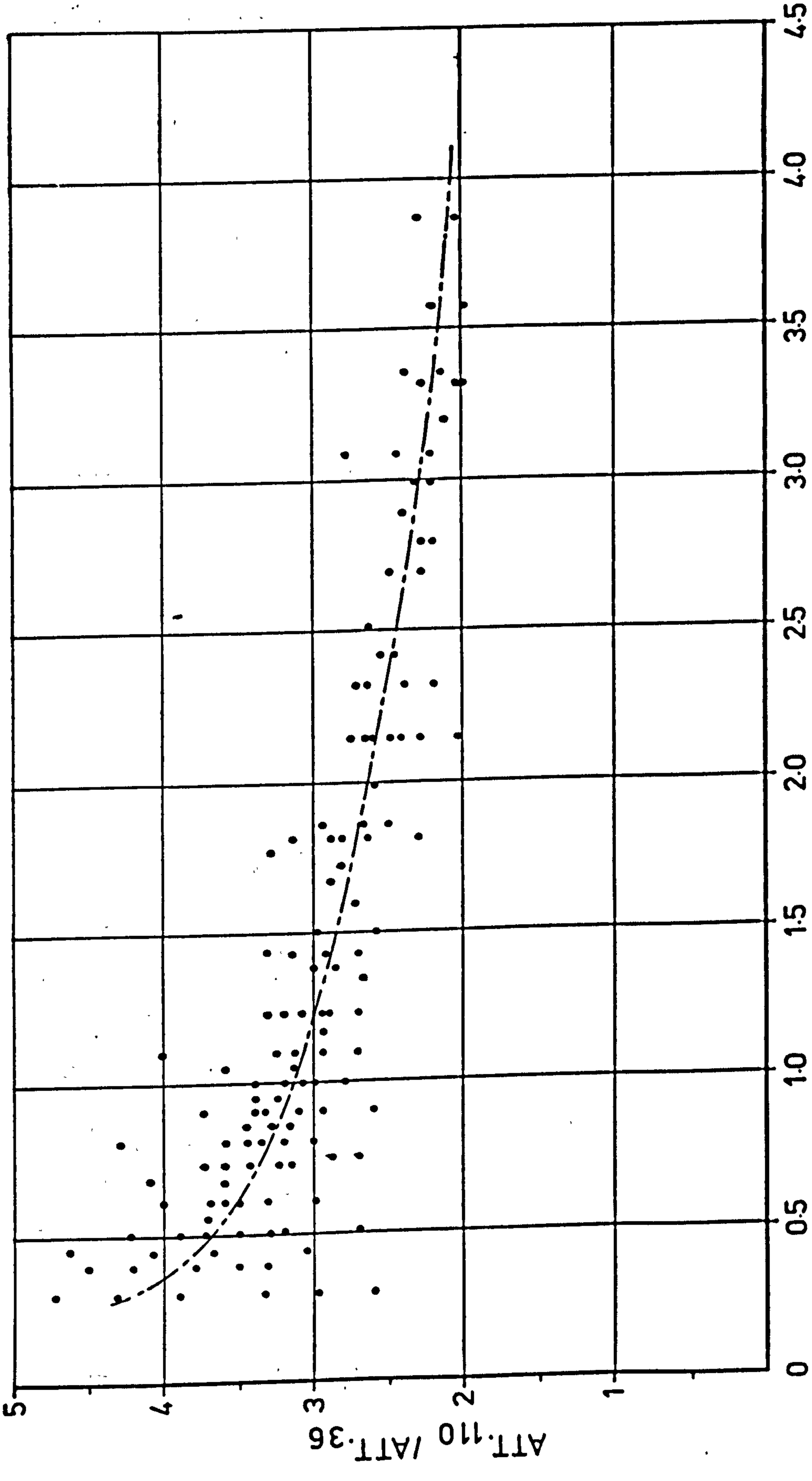

Fig. 9.7 Ratio of 110/36 GHz attenuations against attenuation at 36 GHz.

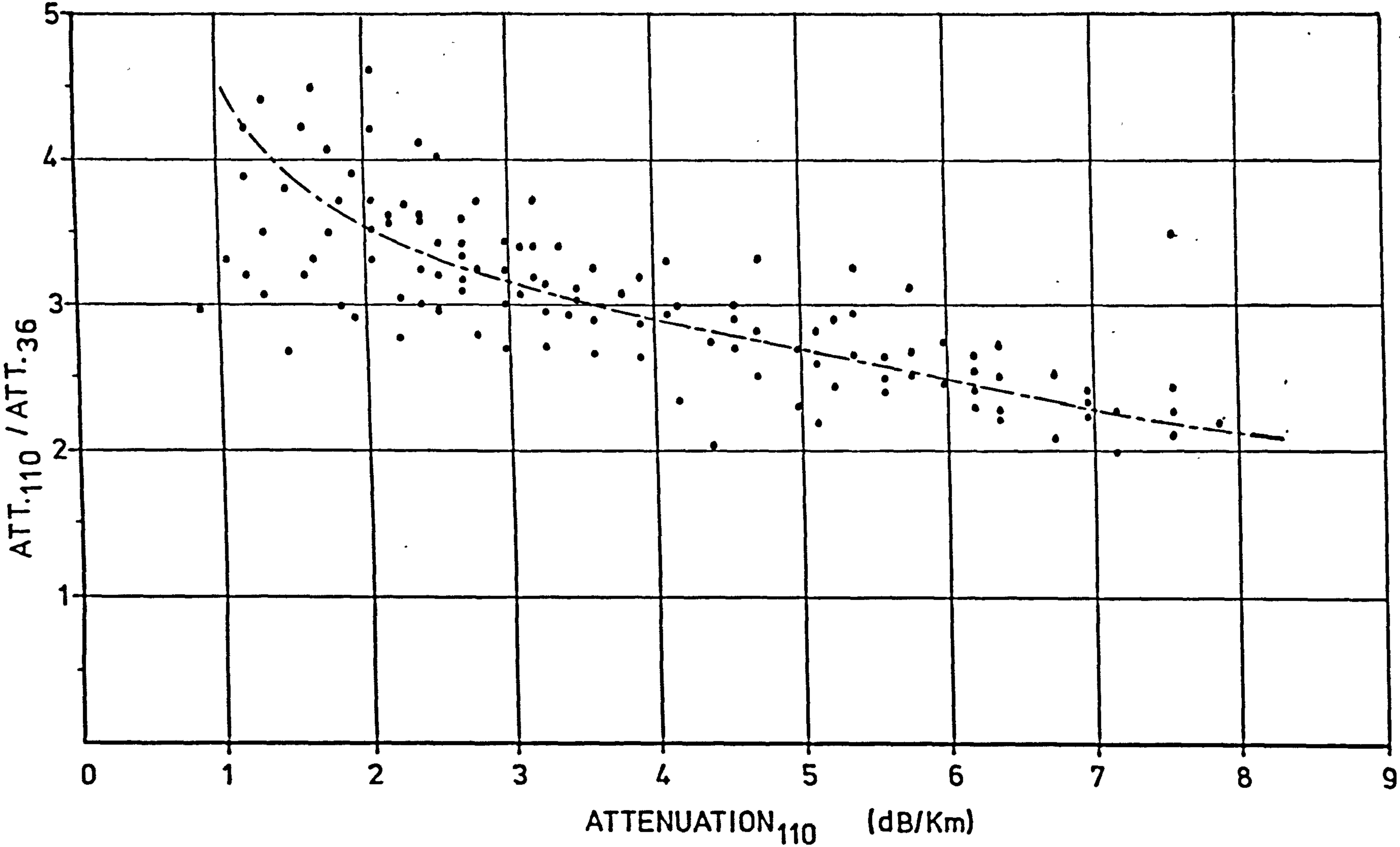

Fig. 9.8 Ratio of 110/36 GHz attenuations against attenuation at 110 GHz.

is tolerable. Hence, it can be concluded that the theoretical prediction gives quite a good estimate of rain-induced attenuation and can be useful in system design.

The measurements of the ratio of the attenuations at 110 GHz and 36 GHz appear to be consistent with computations based on the Laws-Parsons raindrop size distribution and hence it is reasonable to assume that the Laws-Parsons drop size distribution adequately represents the rain on terrestrial microwave communications paths.

9.6 Attenuation due to snowfall

Little is known about the attenuation caused by ice-crystals and snow. Ice crystals are not spherical and the theory obtained from spherical drops no longer applied. It is only known that the attenuation depends on the mass of the crystals and varies inversely with the wavelength (Matthews 1965). Snow can vary from minute individual crystals--powder snow--of mass from 0.1 to 10 mg, to large flakes which may have a diameter of the order of a centimetre or more (Best 1957). Under normal conditions, attenuation by snow is much less than attenuation by rain of the same precipitation rate (Weibel and Dressel 1967), but, in snow-storms, the ice-crystals may grow in size up to 3 mm or more and may aggregate to form snowflakes, the attenuation would then be quite considerable. Figure 9.9 shows the record of the signal attenuation at 36 GHz due to a snowstorm which

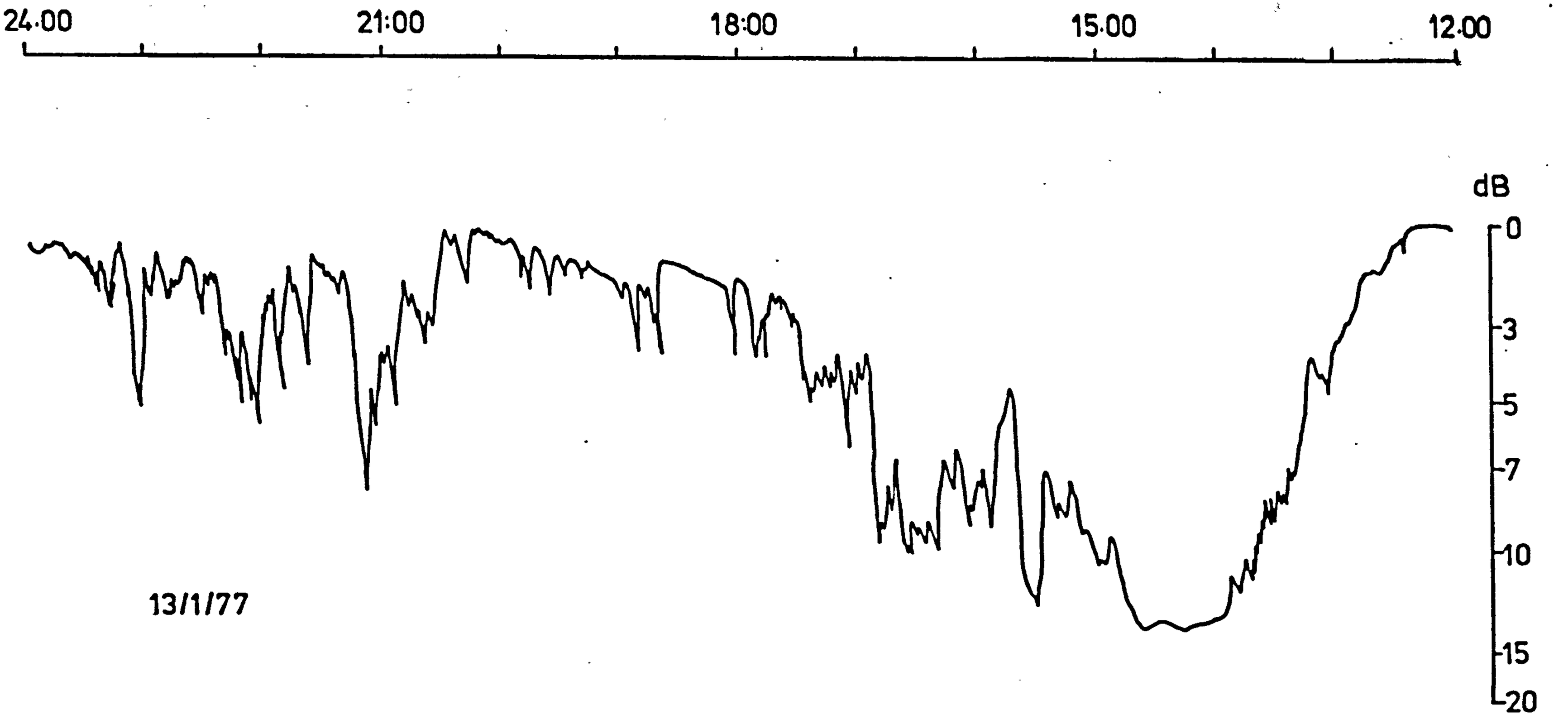

Fig. 9.9 Chart record of attenuation at 36 GHz due to snowfall.

occurred on January, 1st, 1977. Attenuation as high as 14 dB was observed on this link.

9.7 System reliability at 36 GHz

Although attenuation due to rainfall inevitably imposes very severe limitations on the reliability obtainable in line-of-sight telecommunications links for frequencies above 15 GHz, increasing demand for frequency space, combined with the development of reliable solid state devices, has stimulated widespread interest in the use of these frequencies for short communication links. From communication design engineer's point of view, the reliability of the system is most important. This section presents the fading measurements on the 4.1 Km line-of-sight propagation link at 36 GHz which has been operated continuously for a period of more than one and half years in central London area.

Figure 9.10 shows the attenuation, up to 20 dB, versus the percentage of time a given value of attenuation is exceeded. The period of time covered is from 1st of February,1976 to the 25th of May 1977. It can be seen that the 20 dB fading margin was exceeded for about 0.0047% of the period of time covered (i.e. about 31 minutes in 455 days). Figures 9.11 and 9.12 show the performance obtained during two "worst" calender months (October 1976 and December 1976) in which the attenuation and the duration of the deep fades were highest and longest respectively. During the course of 16 months of observations the attenuation due to

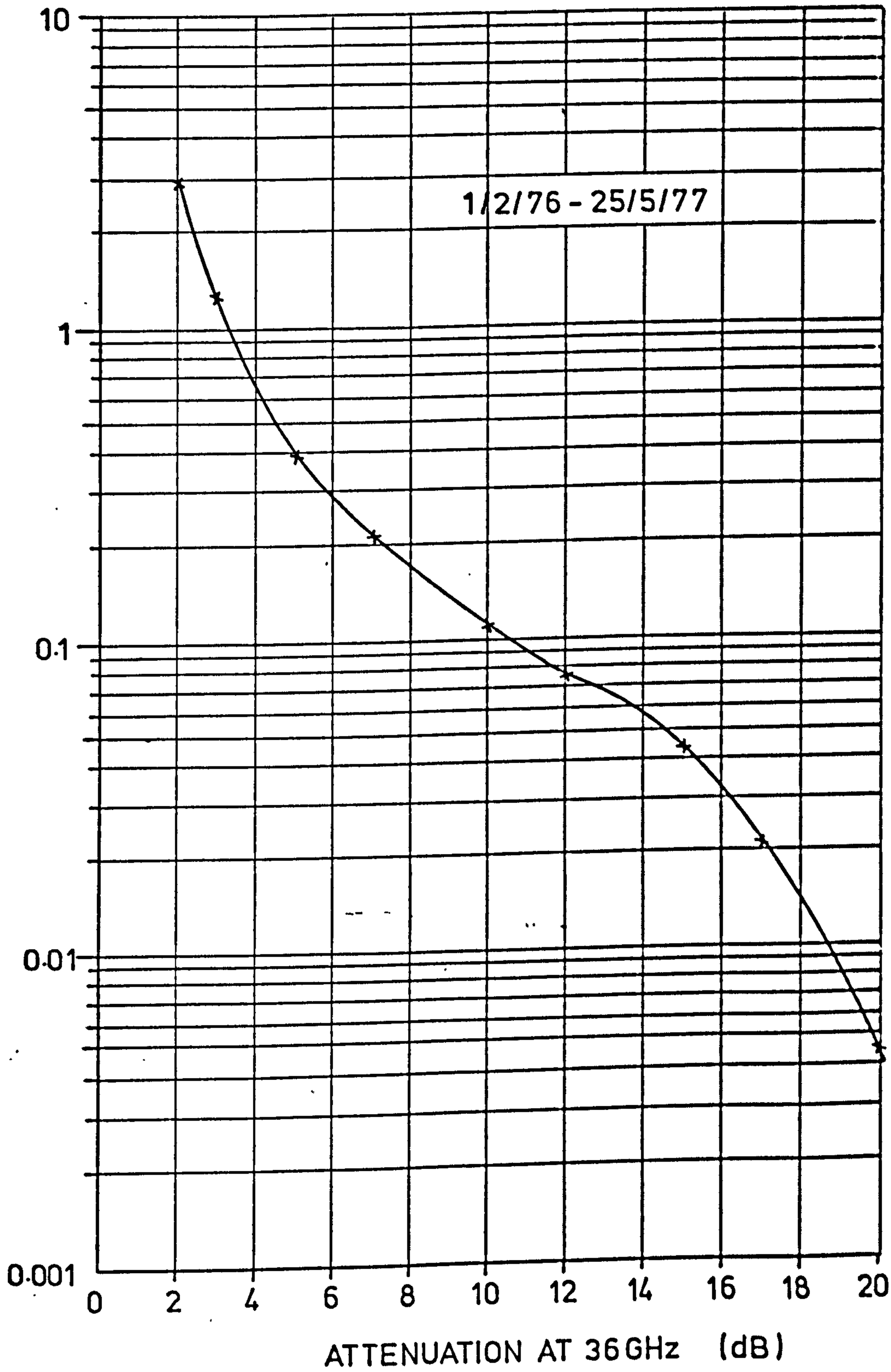

Fig. 9.10 Distribution of 36 GHz attenuation.

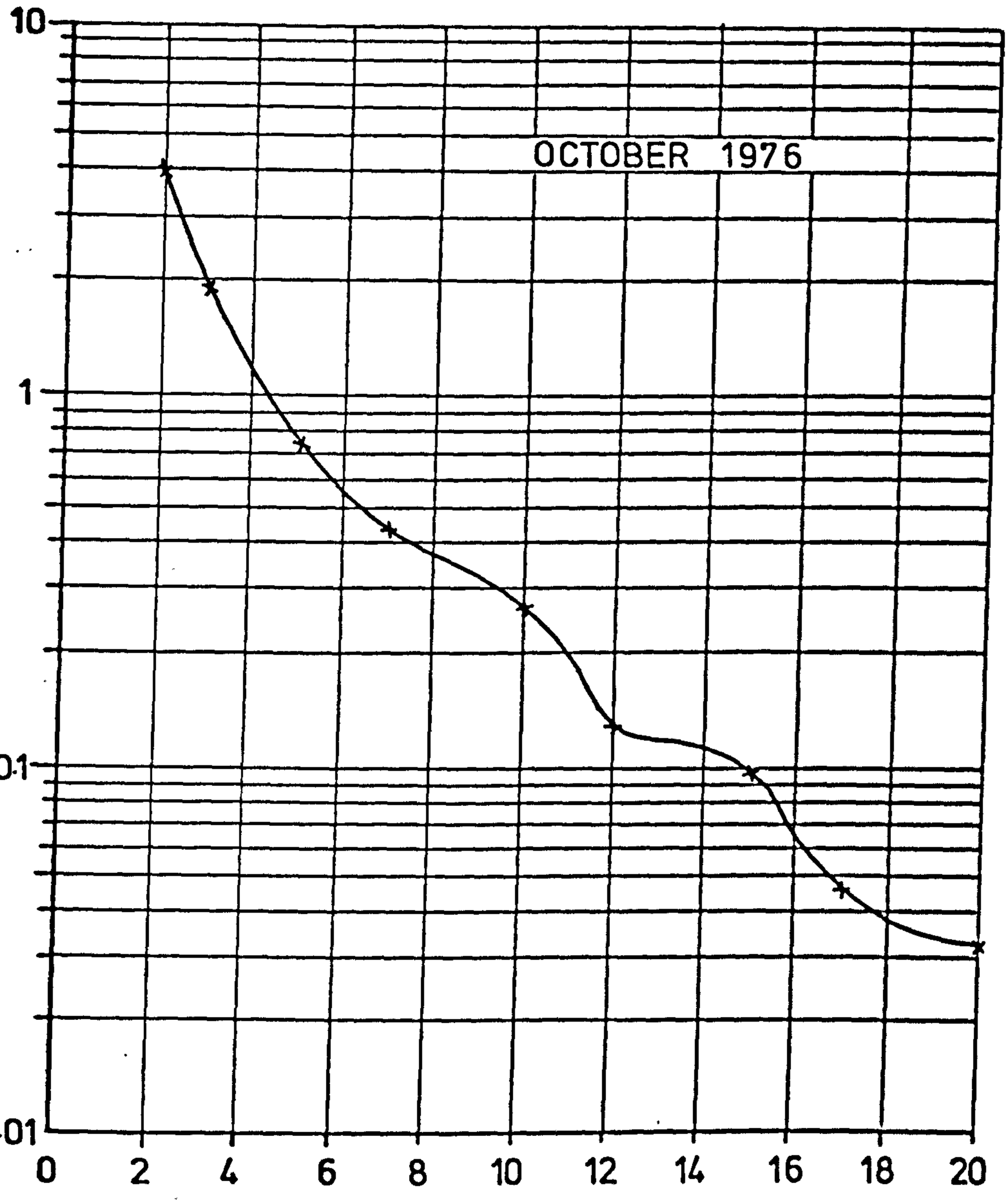

Fig. 9.11 Distribution of 36 GHz attenuation in October 1976.

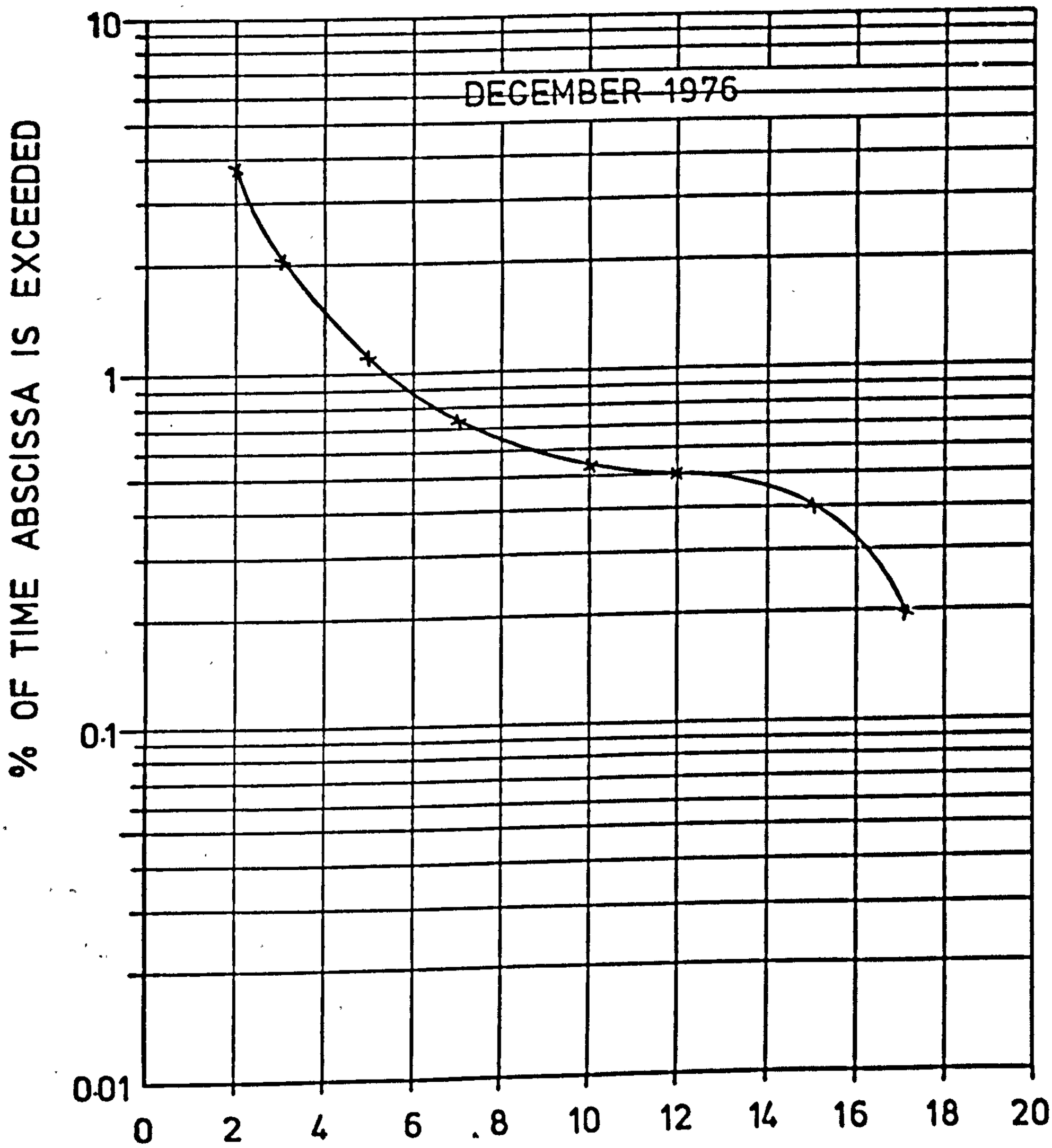

Fig. 9.12 Distribution of 36 GHz attenuation in December 1976.

rainfall exceeded 20 dB for only 31 minutes, of which 15 minutes occurred in the month of October,1976, that is, 48% of the time during which the attenuation was greater than 20 dB occurred in one month. In December 1976 the highest observed attenuation was 17 dB. However, 67% of the total time during which the attenuation exceeded 17 dB occurred in December 1976.

Clearly, the fading distributions shown in Figures 9.10 9.11 and 9.12 indicate that the system is not suitable for trunk telecommunications links which normally have longer propagation paths than in this experiment and usually operate with a fading margin of about 30 dB. However, it would be useful for local distribution services, such as high speed data links in an urban area where the large bandwidth potential could be exploited and the reliability requirements are less stringent or secure low speed data links between telephone exchanges. For this reason, the duration of individual fades may be of interest. Figure 9.13 shows the distribution of fade durations. The curves apply to fades of 5 dB, 10 dB and 15 dB; the number of events that contribute to each curve is shown in brackets. It can be seen that during the period of the measurements, fades greater than 5 dB occurred 248 times, fades greater than 10 dB occurred 75 times and 15 dB 27 times. There were only 7 occasions where the fades were greater than or equal to 20 dB. These are tabulated in Table 9.1. The longest duration was approximately 10 minutes.

Based on the distribution curves shown, the reliability of a communications system at 36 GHz in central London area was

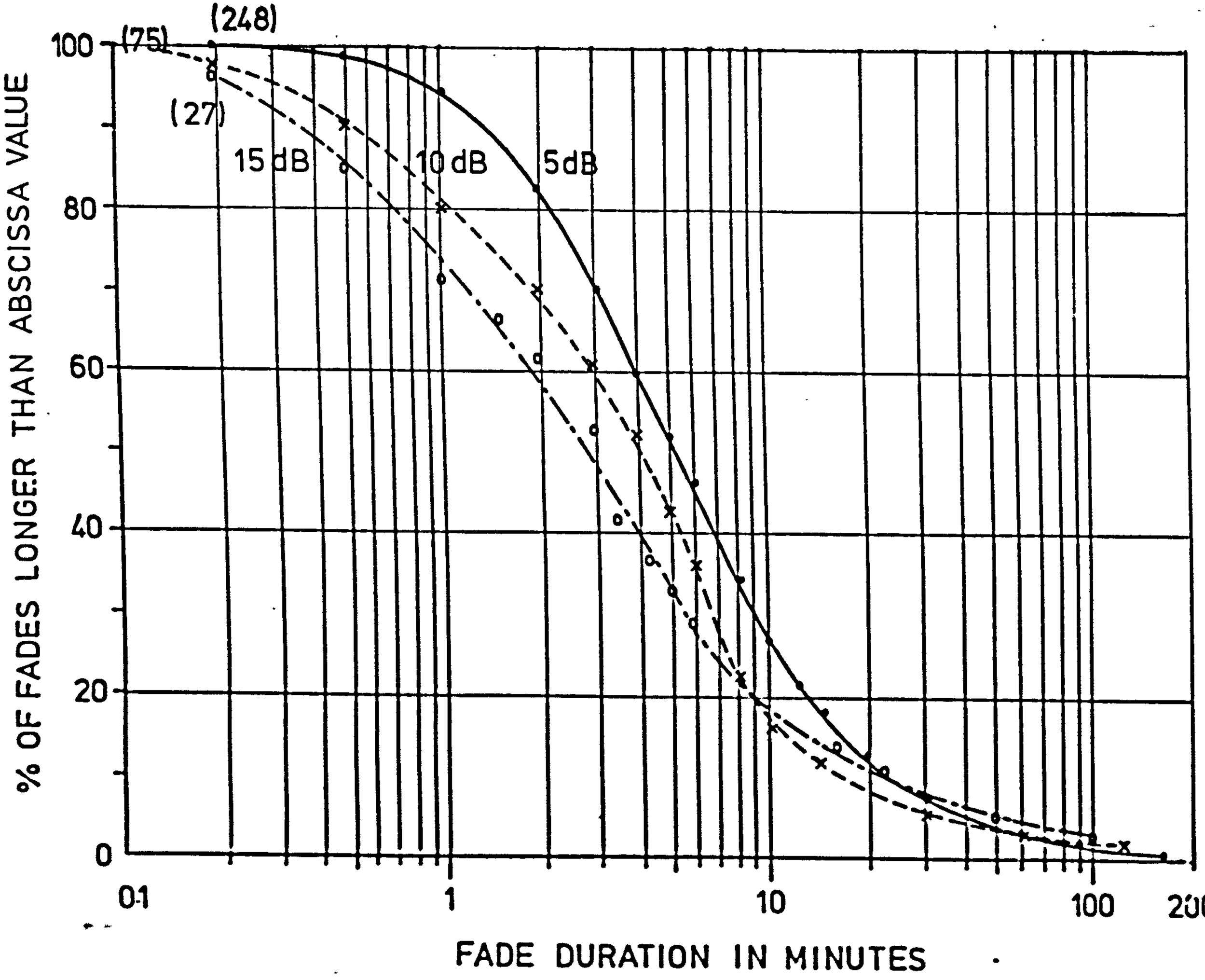

Fig. 9.13 Distribution of fade duration.

found to be better than 99.995% with a transmitting power of 15 mW (Section 3.1.1) and a propagation path of 4.1 Km if a fading margin of 20 dB is chosen. The period of measurement covered the long, hot and dry summer of 1976 and also the very wet winter of 1976-77. Normally, a fading margin of 30 dB is used for most design, in which case the reliability of the system will be much better. This leads to the conclusion that a millimetre wavelength telecommunications system at 36 GHz is very feasible for short paths of a few kilometres.

Table 9.1 Distribution of fades greater than or equal to 20 dB

Duration of fades (min.)	No. of events
0.5	1
1	1
2	1
3	1
5	1
9.5	1
10	1

CHAPTER 10 GENERAL CONCLUSIONS

The object of this work has been to study the propagation characteristics of millimetre waves through the atmosphere in a town environment. One aspect of the work was to test experimentally the existing theories of wave propagation through a turbulent medium of which Tatarski's theory forms the basis. Another aim has been to gather information of possible use to the communication engineers and to identify possible problems in the use of millimetre waves for communication systems along a link in a town environment. Some success has been achieved in both of these aims and the experimental results are summarised as follows:

The log amplitude fluctuations at 8.33 mm and 2.73 mm wavelengths were found experimentally to have a log-normal distribution. The physical size of the outer scale of turbulence L_o plays an important role in millimetre wavelength amplitude scintillations. When L_o is larger than the first Fresnel zone size $(\lambda L)^{1/2}$, the log-amplitude variances have a $k^{7/6}$ wave number dependence whereas when L_o is smaller than $(\lambda L)^{1/2}$, they have a k^2 dependence. These results agree very well with Tatarski's prediction of wave amplitude fluctuations in a turbulent medium.

Investigation of amplitude scintillation spectra revealed that the spectra usually followed a -8/3 power law,

indicating that the "two-thirds" law of the Kolmogorov spectrum of turbulence was operative during the course of the experiments on most occasions.

The amplitude scintillations were found to be caused by uniform motion of the atmosphere across the propagation path by wind, as predicted by Taylor's "frozen atmosphere" hypothesis, rather than the internal motions of the atmosphere. The normalized spectral density of a certain spectral frequency was found to be related to the transverse wind speed across the path by a 5/3 power law. Wind speed deduced from amplitude scintillation spectral measurements agreed within 20% of the direct measurements, thus suggesting the feasibility of using millimetre wave propagation for remote wind speed probing.

Direct measurements of the refractive index by radio refractometer gave evidence of the "two-thirds" law of Kolmogorov spectrum of turbulence for refractive index. Results are presented of the determination of the atmospheric refractive index structure parameter C_n^2 deduced from amplitude scintillation measurements and from the refractive index frequency spectrum computed from refractivity measurements. The two methods of measurement agree within 21% and further confirms the applicability of Tatarski's theoretical predictions to millimetre wavelengths.

Anomalous large amplitude fluctuations were found to be associated with propagation in town environment. These large

fluctuations may be a contributory cause to the error rate of a digital communication system. Further studies are recommended along an appropriate path in a town environment to investigate whether or not the performance of a digital system would be significantly degraded.

Long term statistics of the refractive index variations in London area are also given and it has been shown that the transit-time variations due to these refractive index changes, under most circumstances, do not significantly affect a digital transmission system for path length of several kilometres.

Attenuation due to fog was found to be fairly small; only of the order of 0.6 dB maximum on the 36 GHz link. Agreements and discrepancies between experimental and theoretical measurements were also observed. Discrepancies might be mainly due to error in the estimation of visual range and non-uniformity of fog along the entire propagation path.

Although multipath fading is expected to be rare on a short hop propagation path, it is suspected that it did occur on some occasions. For one event, the possibility of multipath effects was supported by meteorological evidence.

Results of the rainfall attenuation on the 110 and 36 GHz links have been presented. A discrepancy of less than 20% between the experimentally measured and theoretically predicted attenuations was obtained. There is a tendency for the observed

attenuation to be higher than predicted values. This might be due to the lack of homogeneity in rainfall intensity along the propagation path and shortcomings in the experimental techniques. However dual frequency measurement on the two links gave results which seem to be consistent with computations based on the Laws-Parsons raindrop size distribution indicating that this distribution adequately represents the rain on a terrestrial microwave communication path.

Statistics for 16 months on the 36 GHz link have showed that, with a transmitting power of 15 mW, the reliability of the link is as high as 99.995% for a fading margin of 20 dB. This further confirms that the use of a frequency of 36 GHz is practical for short paths of several kilometres.

APPENDICES

APPENDIX

Appendix 3.1 Stability of the automatic frequency control system of the 36 GHz receiver.

Assuming linear operation for the automatic frequency control system, it can be represented in the simple block diagram form as shown in Figure A 3.1a and Figure A3.1b where

R(s) is the reference signal frequency

C(s) is the output signal frequency

$G_1(s)$ is the discriminator characteristic

$G_2(s)$ is the gain of the amplifier integrator

$G_3(s)$ is the transfer function for conversion of control voltage into frequency

G(s) is the product of $G_1(s)$; $G_2(s)$ and $G_3(s)$

E(s) is the error signal

M(s) is the closed loop transfer function

Therefore, the closed loop transfer function is given by

$$M(s) = \frac{C(s)}{R(s)} = \frac{G(s)}{1 + G(s)} \qquad \text{A 3.1.1}$$

For our case, $G_1(s)$ = 0.08 volt/MHz in the range of 27 MHz to 33 MHz;

$$G_2(s) = \frac{1}{R_1 C \left(s + \frac{1}{R_2 C} \right)} \qquad \text{A 3.1.2}$$

where R_1 is the input resistance of the integrator

R_2 and C are the feedback resistance and capacitance of the integrator.

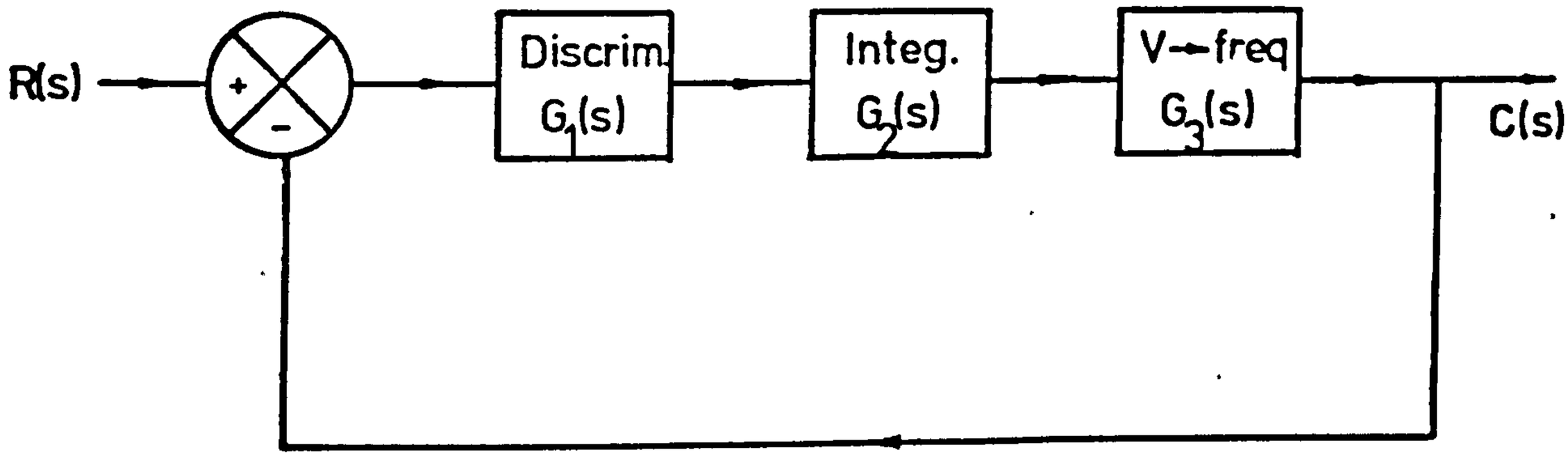

(a)

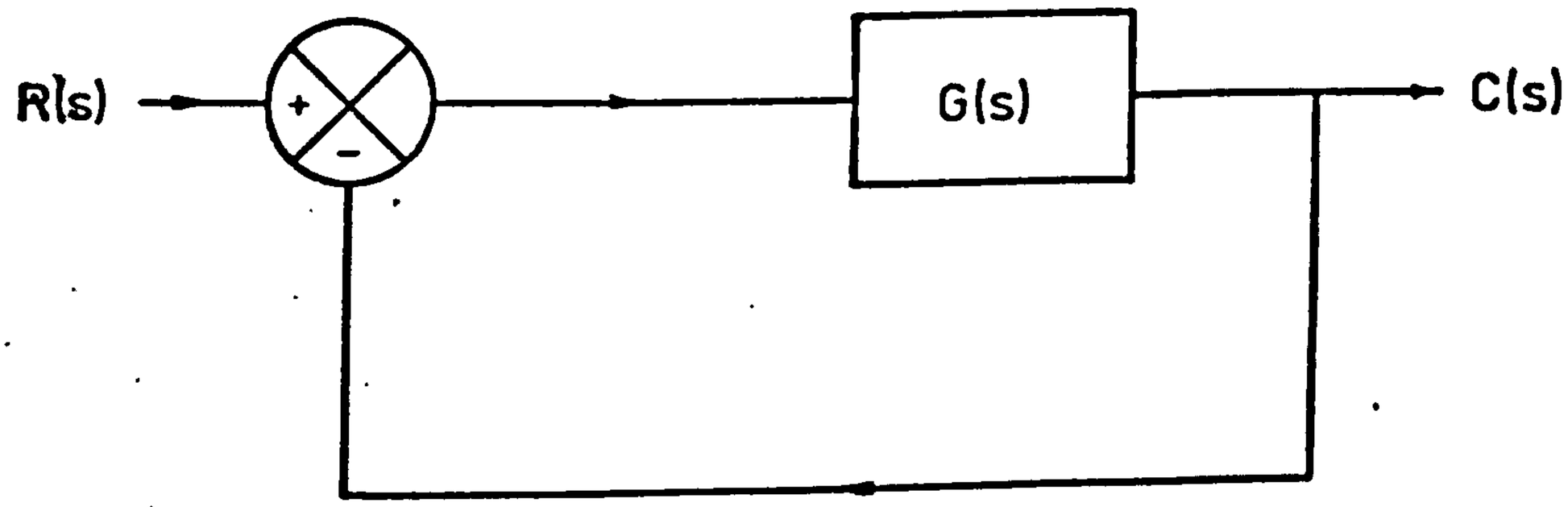

(b)

Fig. A 3.1 Automatic frequency control system

$G_3(s)$ = 100 MHz/volt with centre frequency at about 36 GHz

Therefore G(s) is given by

$$G(s) = \frac{8}{R_1 C \left(s + \frac{1}{R_2 C} \right)} \qquad \text{A 3.1.3}$$

Since R_2 and C are always real and positive, therefore the root of the characteristic equation 1 + G(s) of the closed loop transfer function always lies on the right half s-plane. Thus the system is always stable (Kuo 1967).

Appendix 3.2 Circuit diagram of differential temperature head amplifier.

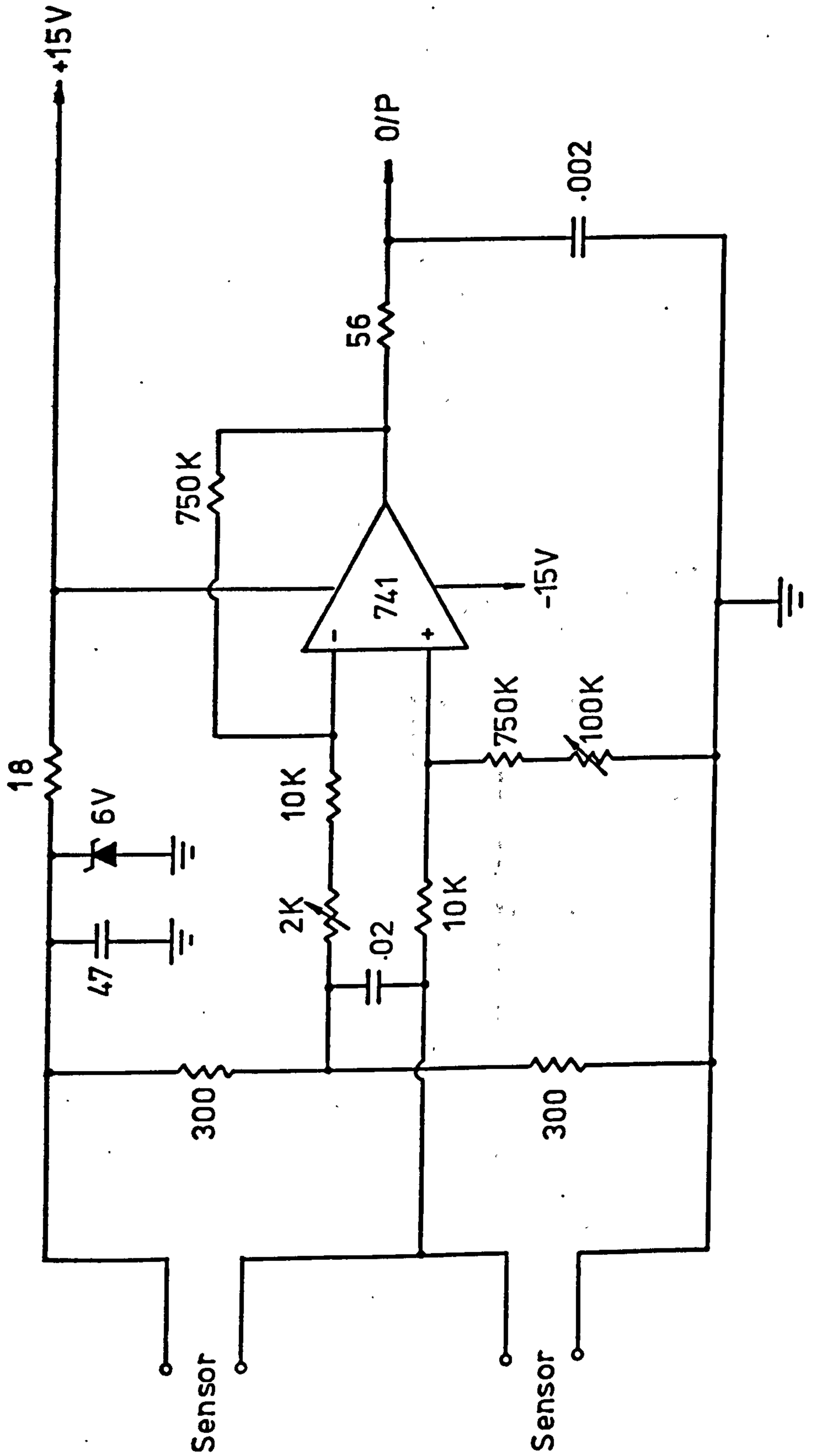

Fig A3.2 Differential temperature head amplifier.

Appendix 3.3 Block diagrams of the U.C.L. Radio Refractometer.

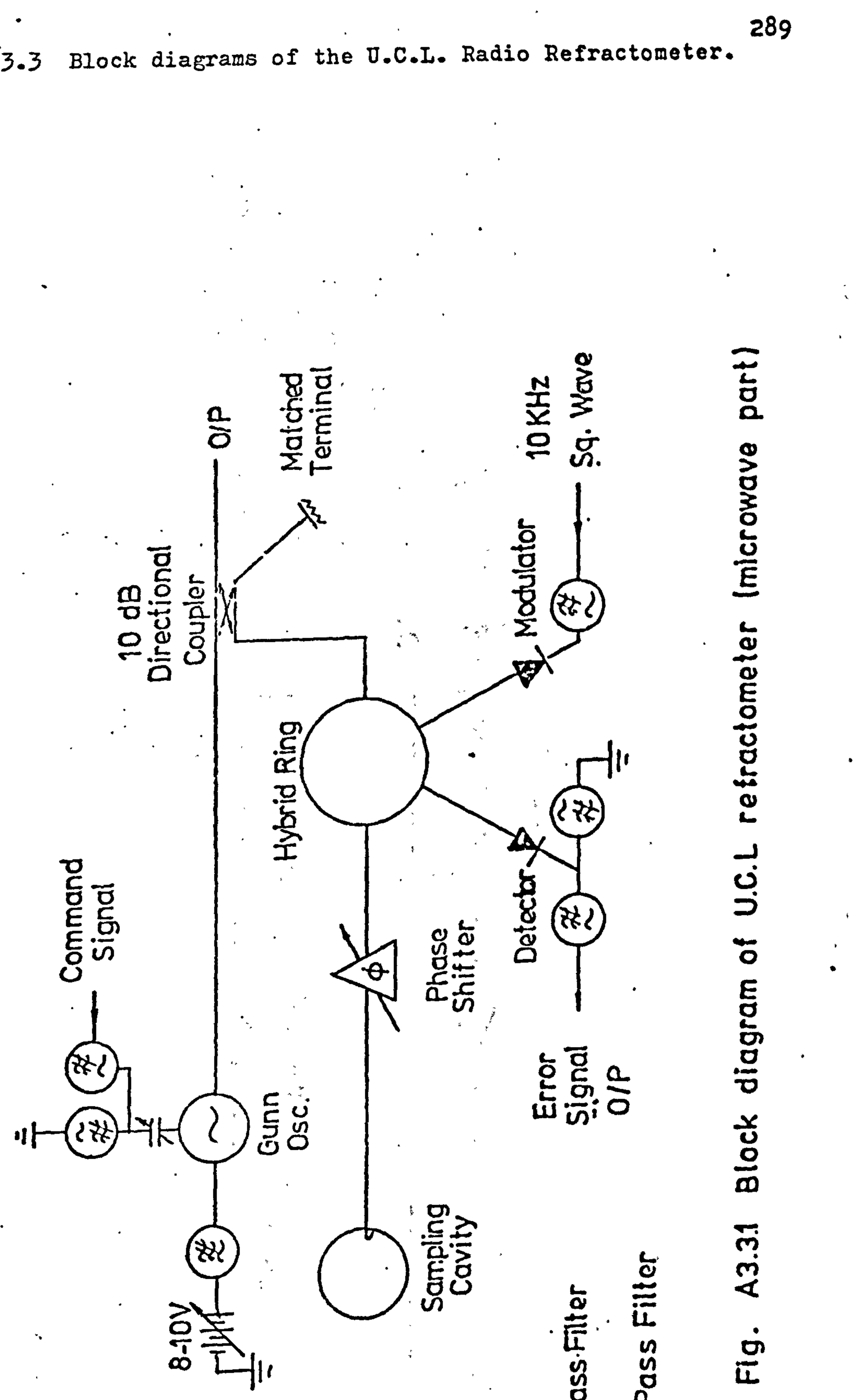

Fig. A3.31 Block diagram of U.C.L refractometer (microwave part)

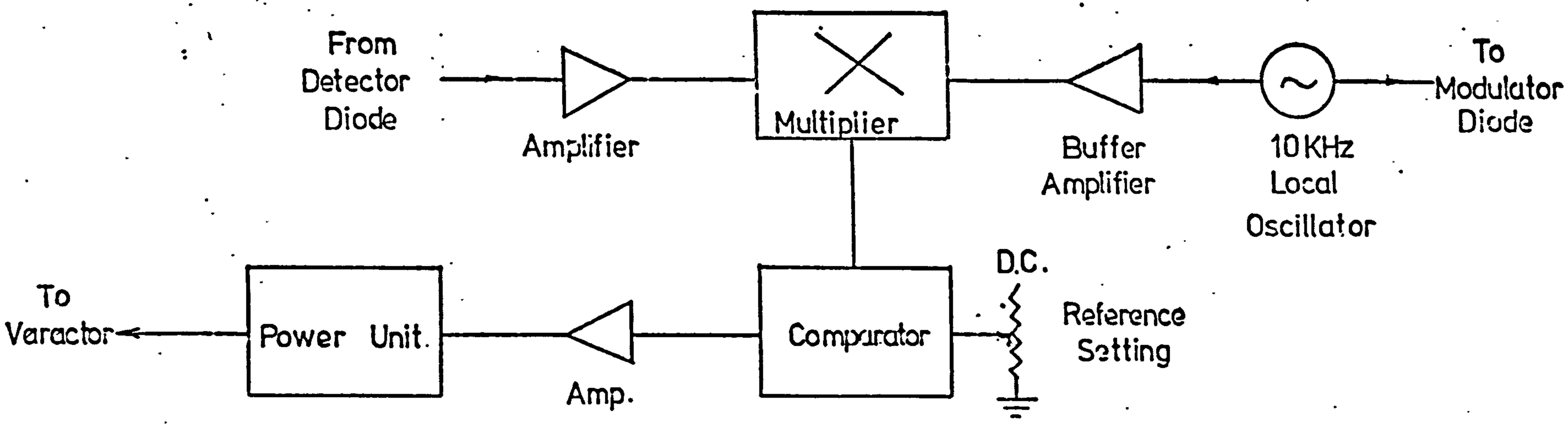

Fig. A3.3.2 Block diagram of U.C.L refractometer (electronic part)

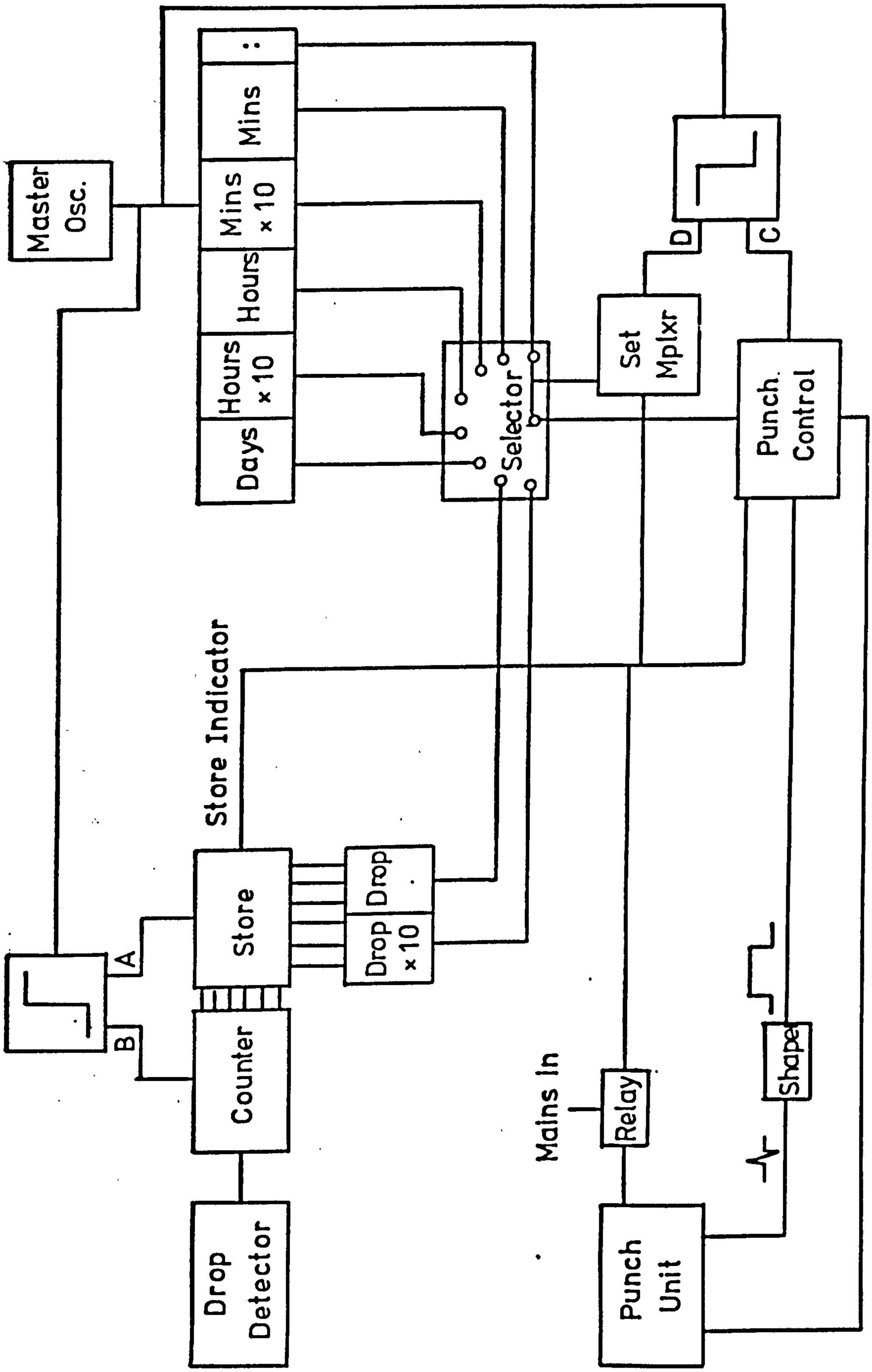

Fig. A 3.4 Block diagram of raingauge.

Appendix 4.1 Design of the Butterworth low-pass filter

To synthesize the Butterworth low-pass filter with the amplitude characteristic

$$|G(\omega)|^2 = \frac{1}{\left[1 + \frac{\tan\frac{\omega T}{2}}{\tan\frac{\omega_c T}{2}}\right]^{2n}} \qquad \text{A 4.1.1}$$

it is necessary to determine the location of the poles on the z^{-1} plane.

$$\text{Let } p = \frac{1 - z^{-1}}{1 + z^{-1}} \qquad \text{A 4.1.2}$$

where $p = u + jv$. Since A 4.1.1 is the frequency response, we put, then, $z^{-1} = e^{-j\omega T}$, hence, $p = -j \tan\frac{\omega T}{2}$. On the p-plane, the poles of equation A 4.1.1 will be located at the roots of the equation

$$\left(\frac{jp}{v_c}\right)^{2n} + 1 = 0 \qquad \text{A 4.1.3}$$

where $v_c = \tan\frac{\omega_c T}{2}$ and ω_c is the cutoff frequency.

The roots are given by

$$p_r = v_c\, e^{j\left(\frac{2r+1}{2n}\right)\pi} \qquad r = 0,1,2, \ldots , (2n-1)$$

for n = even

$$p_r = v_c\, e^{j\left(\frac{r}{n}\right)\pi} \qquad r = 0,1,2, \ldots , (n-1)$$

for n = odd

Therefore,

$$u_r = v_c \cos(\frac{2r+1}{2n})\pi \quad \text{and} \quad v_r = v_c \sin(\frac{2r+1}{2n})\pi$$

$$r = 0,1,2, \ldots , (2n-1)$$

or $$u_r = v_c \cos(\frac{r}{n})\pi \quad \text{and} \quad v_r = v_c \sin(\frac{r}{n})\pi$$

$$r = 0,1,2, \ldots , (n-1)$$

Let $z^{-1} = x + jy$, then

$$z_r^{-1} = \frac{1 - p_r}{1 + p_r}$$

Hence,

$$x_r = \frac{1 - v_c^2}{1 + 2u_r + v_c^2}$$

$$y_r = \frac{-2v_r}{1 + 2u_r + v_c^2}$$

Once the roots of z^{-1} are determined, those lie outside the unit circle are chosen to form the digital filter transfer function:

$$G(z^{-1}) = \frac{(1 + z^{-1})^n}{\prod_{r=1}^{n} \left[z^{-1} - z_r\right]} \qquad \text{A 4.1.4}$$

The term $(1 + z^{-1})^n$ is introduced because at frequencies $\frac{(2n+1)}{2}(\frac{2\pi}{T})$, $G(\omega)$ is zero, that is, the transfer function should have a nth order zero.

The coefficients for the digital filter realization can be computed by comparing equation A 4.1.4 with the general filter equation

$$y_k = a_o x_k + \ldots\ldots\ldots + a_n x_{k-n} - (b_1 y_{k-1} + b_2 y_{k-2} + \ldots + b_m y_{k-m})$$

Design of a 5 Hz low-pass Butterworth filter.

Cut-off frequency $f_c = 5$ Hz

Sampling frequency $f_s = 40$ Hz

No of poles $n = 4$

Therefore, the attenuation at 7 Hz is

$$10 \log_{10} \left[1 + \left(\frac{\tan \frac{2 \times 7}{40 \times 2}}{\tan \frac{2 \times 5}{40 \times 2}}\right)^8\right] = 13.8 \text{ dB}$$

and

$$v_c = \tan \left(\frac{\omega_c T}{2}\right) = 0.4142$$

The poles on the p-plane are thus given by

r	u_r	v_r
0	0.382671	0.158506
1	0.158506	0.382671
2	-0.158506	0.382671
3	-0.382671	0.158506

4	-0.382671	-0.158506
5	-0.158506	-0.382671
6	0.158506	-0.382671
7	0.382671	-0.158506

The poles on the z^{-1} plane are:

r	x_r	y_r
0	0.427713	0.163669
1	0.556532	0.514145
2	0.969444	0.895608
3	2.039384	0.780395
4	2.039384	-0.780395
5	0.969444	-0.895608
6	0.556532	-0.514145
7	0.427713	-0.163669

Therefore the poles for stable design are:

$$0.969444 \pm j0.895608$$

and $$2.039384 \pm j0.780395$$

Thus the transfer function $G(z^{-1})$ is given as:

$$G(z^{-1}) = \frac{0.0102086(1+4z^{-1}+6z^{-2}+4z^{-3}+z^{-4})}{0.120399z^{-4}-0.724518z^{-3}+1.735945z^{-2}-1.968489z^{-1}+1}$$

Hence, the design coefficients are:

$$a_0 = 0.0102086$$

$$a_1 = 0.0408344$$

$$a_2 = 0.0612516$$

$$a_3 = 0.0408344$$

$$a_4 = 0.0102086$$

$$b_1 = -1.968489$$

$$b_2 = +1.735945$$

$$b_3 = -0.724518$$

$$b_4 = +0.120399$$

Appendix 4.2 The Fast Fourier Transform program

```
LOGIN:4
PASSWORD:
<>EDIT.FASTF
EDITAOF 3
T*
      SUBROUTINE FASTF(AX,AY,ISIZE)
      DIMENSION AX(ISIZE),AY(ISIZE)
       INTEGER L(12)
       EQUIVALENCE (L1,L(1)),(L2,L(2)),(L3,L(3)),(L4,L(4)),(L5,L(5))
      EQUIVALENCE (L6,L(6)),(L7,L(7)),(L8,L(8)),(L9,L(9))
      EQUIVALENCE (L10,L(10)),(L11,L(11)),(L12,L(12))
      PIE2=8.0*ATAN(1.0)
       N=IABS(ISIZE)
       IF(N-4)14,11,11
11    IFACC=1
      IFACA=N/4
      IF(ISIZE)62,12,12
62     DO 17 K=1,N
17    AY(K)=-AY(K)
12    ITIME=0
16    IFCAB=IFACA*4
      ITIME=ITIME+2
      DO 80 LITLA=1,IFACA
      DO 82 I0=LITLA,N,IFCAB
      I1=I0+IFACA
      I2=I1+IFACA
      I3=I2+IFACA
      XS0=AX(I0)+AX(I2)
      XS1=AX(I0)-AX(I2)
      YS0=AY(I0)+AY(I2)
      YS1=AY(I0)-AY(I2)
      XS2=AX(I1)+AX(I3)
      XS3=AX(I1)-AX(I3)
      YS2=AY(I1)+AY(I3)
      YS3=AY(I1)-AY(I3)
      AX(I0)=XS0+XS2
      AY(I0)=YS0+YS2
      X1=XS1+YS3
      Y1=YS1-XS3
      X2=XS0-XS2
      Y2=YS0-YS2
      X3=XS1-YS3
      Y3=YS1+XS3
      IF(LITLA-1)14,66,64
65    AX(I2)=X1
      AY(I2)=Y1
      AX(I1)=X2
      AY(I1)=Y2
      AX(I3)=X3
      AY(I3)=Y3
      GO TO 82
64    AX(I2)=X1*CW1+Y1*SW1
      AY(I2)=Y1*CW1-X1*SW1
      AX(I1)=X2*CW2+Y2*SW2
      AY(I1)=Y2*CW2-X2*SW2
      AX(I3)=X3*CW3+Y3*SW3
      AY(I3)=Y3*CW3-X3*SW3
```

```
 82   CONTINUE
      IF(LITLA-IFACA)65,80,14
 65   CW1=COS(PIE2*FLOAT(LITLA)/FLOAT(IFCAB))
      Z=1.-CW1*CW1
      Z=ABS(Z)
      SW1=SQRT(Z)
      CW2=CW1*CW1-Z
      SW2=2.*CW1*SW1
      CW3=CW1*CW2-SW1*SW2
      SW3=CW1*SW2+CW2*SW1
 80   CONTINUE
      IF(IFACA-1)21,21,67
 67   IFACC=IFACC*4
      IFACA=IFACA/4
      IF(IFACA)14,68,16
 68   DO 40 K=1,N,2
      I=K+1
      TEMPR=AX(K)+AX(I)
      AX(I)=AX(K)-AX(I)
      AX(K)=TEMPR
      TEMPR=AY(K)+AY(I)
      AY(I)=AY(K)-AY(I)
 40   AY(K)=TEMPR
      ITIME=ITIME+1
 21   IF(ISIZE)69,166,18
 69   DO 19 K=1,N
 19   AY(K)=-AY(K)
      GO TO 166
 18   Z=SQRT(FLOAT(N))
      DO 177 K=1,N
      AX(K)=AX(K)/Z
177   AY(K)=AY(K)/Z
166   II=1
      DO 101 K=1,ITIME
      II=II*2
101   L(K)=II
      DO 102 K=ITIME,11
102   L(K+1)=1
      II=1
      DO 103 J1=1,2
      DO 103 J2=J1,L2,L1
      DO 103 J3 =J2,L3,L2
      DO 103 J4=J3,L4,L3
      DO 103 J5=J4,L5,L4
      DO 103 J6=J5,L6,L5
      DO 103 J7=J6,L7,L6
      DO 103 J8=J7,L8,L7
      DO 103 J9=J8,L9,L8
      DO 103 J10=J9,L10,L9
      DO 103 J11=J10,L11,L10
      DO 103 J12=J11,L12,L11
      IF(II-J12)108,103,103
108   TEMPR=AX(II)
      AX(II)=AX(J12)
      AX(J12)=TEMPR
      TEMPR=AY(II)
      AY(II)=AY(J12)
      AY(J12)=TEMPR
103   II=II+1
 14   RETURN
      END
```

Appendix 5.1 Conversion of unit of the amplitude fluctuations equation.

$$0.31\ C_n^2\ k^{7/6}\ L^{11/6}$$

$$= \left[\ln \frac{A}{A_o}\right]^2$$

$$= \overline{\left[\frac{\log_{10} \frac{A}{A_o}}{\log_{10} e}\right]^2}$$

$$= \overline{\left[\frac{\log_{10} (\frac{P}{P_o})^{1/2}}{\log_{10} e}\right]^2}$$

$$= \left[\frac{\sigma^2}{(20\log_{10} e)^2}\right]$$

Therefore,

$$\sigma^2 = (20\log_{10} e)^2 \times 0.31\ C_n^2\ k^{7/6}\ L^{11/6}$$

$$= 23.39\ C_n^2\ k^{7/6}\ L^{11/6}\ (dB^2)$$

A_o = mean amplitude; A = instantaneous amplitude;

P_o = mean power at the receiver; P = instantaneous power received.

REFERENCES

Chapter 1

Bean, B.R. and Dutton, E.J. (1968): "Radio meteorology". Dover.

CCIR (1975): Vol.V Report 233-3, Geneva

Chernov, L.A. (1960): "Wave propagation in a random medium". Dover.

Heaviside, O.(1902): "Theory of Electric Telegraphy". Encyclopaedia Britannica, 10-ed.

Lane, J.A., Gordon-Smith, A.C. and Zavody, A.M. (1967): "Absorption and scintillation effects at 3 mm wavelength on a short line-of-sight radio link". Electronics Lett. Vol.5, No. 5, pp185-6.

Lee, R.W. and Harp, J.C. (1969): "Weak scattering in random media, with applications to remote probing". Proc.IEEE, Vol.57, No.4, pp375-406.

Lee, R.W. and Waterman, A.T. (1968): "Space correlations of 35 GHz transmissions over a 28 km path". Radio Science, Vol. 3 No. 2, pp135-139.

Llewellyn Jones, D.T. and Zavody, A.M. (1973): "Rainfall attenuation studies at 110 GHz". IEE Conf. Publ. No.98, pp35-44.

Marconi, G. (1901): "Editorial comment". Elect. World 38, p1023.

Matthews, P.A. (1965): "Radio waves propagation at VHF and above" Chapman and Hall Ltd.

Medhurst, R.G. (1965): "Rainfall attenuation of centimetre waves: comparison of theory and measurements". IEEE Tran. AP13 pp550-564.

Norbury, J.R. and White, W.J.K. (1973): "Correlation between measurements of rainfall rate and microwave attenuation at 36 GHz". IEE Conf. Publ. No. 98, pp45-51.

Saxton, J.A.,Lane, J.A., Meadows, R.W. and Matthews, P.A. (1964): "Layer structure of the troposphere". Proc. IEE Vol.111 No. 2, p275.

Smith, E.K. and Weitraub, S. (1953): "The constants in the equation for atmospheric refractive index and radio frequencies" Proc. IRE, 41, pp1035-1037.

Special Issue on "Millimetre waves and Beyond" (1966): Proc. IEEE 54, Pt.4, pp447-718.

Straiton, A.W. and Tolbert, C.W. (1960): "Anomalies in the absorption of radio waves by atmospheric gases". Proc. IRE 48 p989.

Tatarski, V.I. (1961): "Wave propagation in a turbulent medium" Dover, New York.

Tolbert, C.W. and Straiton, A.W. (1957): "Experimental measurements of the absorption of millimetre radio waves over extended ranges". IRE Trans. AP 5, p239.

Zennecks, J. (1907): "Uber die Fortpfangzung ebener electromagnetisseta Weller einer ebenen Leiterfache und ihre beziehung zur Porachtlosen Telegraphie". Am. Phys. Lpz. (4), 23, p846.

Chapter 2

Chernov, L.A. (1960): "Wave propagation in a random medium". Dover.

Clifford, S.F. and Strohbehn, J.W. (1970): "The theory of microwave line-of-sight propagation through a turbulent atmosphere". IEEE Trans. AP-18, 2, pp264-274.

Landau, L.D. and Lifshitz, E.M. (1959): "The classical theory of fields". Addison-Wesley, Reading, Mass.

Lee, R.W. and Harp, J.C. (1969): "Weak scattering in random media, with applications to remote probing". Proc. IEEE Vol. 57 No. 4, pp375-406.

Liu, C.C. (1964): "Statistical theory of turbulence". Princeton University Press, Princeton, N. Jessey.

Lumley, J.C. and Panofsky, H.A. (1964): "The structure of atmospheric turbulence". Interscience, N.Y.

Strohbehn, J.W. (1968): "Line-of-sight wave propagation through the turbulent atmosphere". Proc. IEEE Vol. 56, No.8 pp1301-1318.

Strohbehn, J.W. and Clifford, S.F. (1967): "Polarization and angle of arrival fluctuations for a plane wave propagated through a turbulent medium". IEEE Trans. AP-15, pp416-421.

Tatarski, V.I. (1961a): "Wave propagation in a turbulent medium" Dover, N.Y., Chapters 2 and 3.

Tatarski, V.I. (1961b): "Wave propagation in a turbulent medium" Dover, N.Y., Chapter 6.

Tatarski, V.I. (1961c): "Wave propagation in a turbulent medium" Dover, N.Y., Chapter 4.

Tatarski, V.I. (1961d): "Wave propagation in a turbulent medium" Dover, N.Y., Chapter 7.

Taylor, L.S. (1968a): "Validity of ray-optics calculations in a turbulent atmosphere". J. Opt. Soc. Am. 58:57.

Taylor, L.S. (1968b): "Validity of ray-optics in a turbulent atmosphere". J. Opt. Soc. Am. 58:57.

Tennekes, H. and Lumley, J.L. (1973): "A first course in turbulence". MIT Press, U.S.A.

Chapter 3

Chan, C.K. (1974): "An expendable microwave radio refractometer". Ph.D. Thesis, University of London.

Kuo, B.C. (1967): "Automatic control system". Prentice Hall.

Mavrokoukoulakis, N.D. (1977): "Clear-air atmospheric propagation at millimetric wavelengths." Ph.D. Thesis, University of London.

Poskitt, G. (1974): "An electronic raingauge with paper tape output". U.C.L. Report.

Vilar, M.E. (1972): "Scintillation phenomena in millimetric radio-wave propagation". Ph.D. Thesis, University of London.

Chapter 4

Blackman, P.F. (1975): "Introduction to sampling and z transform" from 'Introduction to digital filtering'. Wiley-Interscience Publ.

Coates, R. (1975): "Fourier transforms methods" from 'Introduction to digital filtering'. Wiley-Interscience Publ.

Constantinides, A.G. (1975): "Direct synthesis of digital filters" Wiley-Interscience.

Constantinides, A.G. (1975): "General characteristics of digital filters" from 'Introduction to digital filtering'. Wiley Interscience.

Kreyszig, E. (1962): "Advanced engineering mathematics" Wiley.

Mavrokoukoulakis, N.D. (1977): "Clear-air atmospheric propagation at millimetric wavelengths". Ph.D. Thesis, University of London.

Chapter 5

Fried, D.L., Mevers, G.E. and Keister, M.P. (1967): "Measurements of Laser scintillation in the atmosphere". J. Opt. Soc. Am. Vol. 57, pp787-797.

Gjessing, D.T., Kjelaas, A.G. and Golton, E. (1972): "Small scale atmospheric structure deduced from measurements of temperature, humidity and refractive index". Boundary-Layer Meteoro. 1972, pp475-492.

Strohbehn, J.W. (1968): "Line-of-sight wave propagation through the turbulent atmosphere". Proc. IEEE Vol. 56, No. 8 pp1301-1318.

Tatarski, V.I. (1961a): "Wave propagation in a turbulent medium" Dover, N.Y., Chapter 1.

Tatarski, V.I. (1961b): "Wave propagation in a turbulent medium" Dover, N.Y., Chapter 7.

de Wolf, D.A. (1967): "Multiple scattering in a random continuum" Radio Science Vol. 2, pp1379-1392.

de Wolf, D.A. (1968): "Saturation of irradiance fluctuations due to turbulent atmosphere". J. Opt. Soc. Am. Vol. 58, pp461-466.

Chapter 6

Lawrence, R.S., Ochs, G.R. and Clifford, S.F. (1972): "Use of scintillations to measure average wind across a light beam". Appl. Opt. Vol. 11, 2, pp239-243.

Lawrence, R.S. and Strohbehn, J.W. (1970): "A survey of clear-air propagation effects relevant to optical communications" Proc. IEEE, Vol. 58, No. 10, pp1523-1545.

Lee, R.W. and Waterman, A.T. (1968): "Space correlation of 35 GHz transmissions over a 28 km path". Radio Science, Vol.3 No. 2, pp135-139.

Lumley, J.L. and Panofsky, H.A. (1964): "The structure of atmospheric turbulence". Interscience Publishers.

Ochs, G.R., Clifford, S.F. and Ting-i Wang (1976): "Laser wind sensing: the effects of saturation of scintillation" Appl. Opt. Vol. 15, No. 2, pp403-408.

Shen, Liang-chi (1970): "Remote probing of atmosphere and wind velocity by millimetrer waves". IEEE Trans. AP-18, 4 pp493-497.

Special Issue on remote environment sensing, Proc. IEEE. Vol. 57, pp371-742, 1969.

Tatarski, V.I. (1961a): "Wave propagation in a turbulent medium" Dover, N.Y., Chapter 12.

Tatarski, V.I. (1961b): "Wave propagation in a turbulent medium" Dover, N.Y., Chapter 7.

Chapter 7

Bean, B.R. and Dutton, E.J. (1968): "Radio Meteorology". Dover.

Gjessing, D.T., Kjelaas, A.G. and Golton, E. (1972): "Small scale atmospheric structure deduced from measurements of temperature, humidity and refractive index". Boundary-Layer Meteoro. 1972, pp475-492.

Kaimal, J.C. (1973): "Turbulence spectra, length scales and structure parameters in the stable surface layer". Boundary-Layer Meteoro. 4, 1973, pp289-309.

Mavrokoukoulakis, N.D. (1977): "Clear-air atmospheric propagation at millimetric wavelengths". Ph.D. Thesis, University of London.

Pierce, J.R. (1969): "Synchronizing digital networks". B.S.T.J. 48, No. 3, pp615-636.

Chapter 8

Lane, J.A. (1968): "Small scale variations of radio refractive index in the troposphere". Proc. IEE Vol. 115, No. 9 pp1227-1239.

Lawrence, R.S. and Strohbehn, J.W. (1970): "A survey of clear-air propagation effects relevant to optical communications" Proc. IEEE Vol. 58 No. 10, pp1523-1545.

Radford, W.H. (1938): "Papers on Phys, Oceangr. and Met." M.I.T. and Woods Hole Oceangraphic Institute 6, No. 4.

Ryde, J.W. (1940): "The attenuation and Radar Echoes produced at centimetre wavelengths by various meteorological phenomena". 'Meteoro. factors in radio wave propagation' Physical Society London, p169.

Ruthroff, C.L. (1971): "Multipath fading on line-of-sight microwave systems as a fraction of path length and frequency" B.S.T.J., Vol.50, No.7.

Saxton, J.A, and Hopkins, H.G. (1951): "Some adverse influence of meteorological factors on marine navigational radar". Proc. IEE, 98, Pt. III, pp26-36.

Chapter 9

Best, A.C. (1957): "Physics on meteorology". Pittman and Sons Ltd.

Bodtmann, W.F. and Ruthroff, C.L. (1974): "Rain attenuation on short radio paths; theory, experiment and design". B.S.T.J., Vol. 53, No. 7, pp1329-1349.

Eedi, F. (1975): "Attenuation versus rain rate". Contribution to Second Annual Report of the Management Committee for the Implementation of a European Project in the Field of Telecommunications on "Influence of atmospheric conditions on EM wave propagation at frequencies above 10 GHz.

Gunn, K.L.S. and East, T.W.R. (1954): "The microwave properties of precipitation particles". J. Roy. Met. Soc., Vol. 80.

Gunn, R. and Kinzer, G.D. (1946): "The terminal velocity of fall for water droplets in stagnant air". J. of Meteoro., Vol. 6.

Joss, J. et al. (1968): "The variation of raindrop size distribution". Proc. Int. Cong. Cloud Physics, Toronot, 1968.

Laws, J.O. and Parsons, D.A. (1943): "The relation of raindrop size to intensity". Trans. of Am. Geographical Union, Vol. 24.

Llewellyn Jones, D.T. and Zavody, A.M. (1973): "Rainfall attenuation studies at 110 GHz". IEE Conf. Publ. No. 98 on 'Propagation of radio waves at frequencies above 10 GHz'. 1973.

Marshall, J.S., Palmer, W.M.K. (1948): "The distribution of rain-drop with size". J. Meteoro., Vol. 5, 1948.

Matthews, P.A. (1965): "Radio wave propagation at VHF and above". Chapman and Hall Ltd. London.

Medhurst, R.G. (1965): "Rainfall attenuation of centimetric waves: comparison of theory and measurements". IEEE Trans. AP-13 No. 4.

Norbury, J. R. and White, W.J.K. (1972): "Microwave attenuation at 35.8 GHz due to rainfall". Electron. Lett., Vol. 8, No.4

Norbury, J.R. and White, W.J.K. (1973): "Correlation between measurements of rainfall rate and microwave attenuation at 36 GHz". IEE Conf. Publ. No. 98 on 'Propagation of radio waves at frequencies above 10 GHz".

Ryde, J.W. and Ryde, D. (1944): "Attenuation of centimetric waves by rain, hail, clouds". Report 8516, GEC research Lab.

Sander, J. (1975): "Rain attenuation of millimetric waves at λ=5.77, 3.3 and 2mm". IEEE Trans. AP-23, No. 2.

Semplak, R.A. (1971): "Dual frequency measurements of rain-induced microwave attenuation on a 2.6 kilometres propagation path". B.S.T.J., Vol.50, No.8.

Setzer, D.E. (1970): "Computed transmission through rain at micro-wave and visible frequencies". B.S.T.J., Vol. 49, No. 8.

Tahim, K.S. (1975): "Radio-relay system operating at frequencies above 15 GHz; propagation characteristics and system design". M.Sc. Report, U.C.L.

Weibel, G.E. and Dressel, H.O. (1967) : "Propagation studies in millimeter-wave link systems". Proc. IEEE Vol. 55, No. 4, pp497-513.